The Electrosolvation Force: A New Paradigm in Interparticle Interactions



Sida Wang

Corpus Christi College
University of Oxford
Hilary 2025

This thesis is submitted to the Department of Physical & Theoretical Chemistry, University of Oxford, in partial fulfilment of the requirements for the degree of *Doctor of Philosophy*

This thesis is dedicated to the memory of my grandmothers

曲俊英 & 來永秀

Abstract

Understanding forces governing the behaviour of particles in solution is fundamental across a wide range of subjects such as biology, material science and nanotechnology. Interparticle interactions play a crucial role in processes such as crystallization, self-assembly and biomolecular folding, where higher-ordered structures are formed from the precise interplay of fundamental building blocks. Traditionally, we learned from electromagnetism that like-charged objects repel, a principle long assumed to hold true in solutions, especially in dilute electrolyte systems. However, recent studies suggest that this perspective may be overly simplistic; specifically, the solvent — traditionally considered a continuum — has now been demonstrated to exert a dynamic and often counterintuitive role at the molecular level, even reversing the expected electrostatic repulsion between particles of like charge.

This thesis explores the like-charge attraction phenomenon across a broad range of solvents, co-solvents, and particle surface chemistries. Through rigorous experimental measurements and computational simulations, we establish the generality of this anomalous attraction. We highlight the observation of a strong, asymmetrical and long-ranged attractive component between like-charged particles that cannot be explained by conventional DLVO theory. The concept of electrosolvation is proposed, where 'electro-', refers to the fundamentally electrical nature of this contribution to the free energy, driven by the sign of charge of the objects; and '-solvation' indicates the solvent or solvation-mediated nature of the interaction. Our findings provide a novel perspective in understanding and controlling interparticle interactions in both natural processes and industrial applications.

Acknowledgements

Thank you, Prof. Madhavi Krishnan, for offering me the life-changing opportunity to immerse myself in the world of science at Oxford during the last few years of my twenties. It has been the best years of my life — though you have told me that the best is yet to come. I cherished every little moment we spent together unravelling the forces that shaped our world and marvelling at the greatness of nature. More importantly, I have learnt to become a better person, a more important lesson for life.

I would also like to express my appreciation to my current and former colleagues, Rowan, Sushanta, Xin, Tim, Katharina, Ali, Ollie, Julia, Dimitrios, Pawel, Pedro, Gunnar, Narain and Maria for your generous support in my research and the inspiring conversations we have shared. To the part II students, Mel, Rob, Beth, Jiajie and Angela, I will always cherish the days we spent working side by side in the lab and the joy you brought to the group.

最重要的，我想感謝我的家人們，特別是我的母親，張麗紅，和父親，王岩，感謝你們無條件的愛與支持。你們犧牲了許多得以讓我擁有現在的美好生活，我都牢記在心。謝謝我的爺爺，王建基，你是我們大家庭的榜樣，鼓勵著我們闖蕩世界。正是你們的以身作則，讓我成爲了一個積極向上、自信堅韌的人。

List of Publications

This thesis is based on the work contained in the following research papers:

- **A charge-dependent long-ranged force drives tailored assembly of matter in solution**
  S. Wang*, R. Walker-Gibbons*, B. Watkins, M. Flynn, & M. Krishnan
  Nature Nanotechnology, 19, 485–493 (2024).
  **contributed equally*

- **Chemical control of colloidal self-assembly driven by the electrosolvation force**
  S. Wang*, R. Walker-Gibbons*, B. Watkins, B. Lin & M. Krishnan,
  Nature Communications (to appear)
  **contributed equally*

- **Strongly attractive pair potentials between like-charged particles in fluids**
  S. Wang, R. Walker-Gibbons & M. Krishnan
  status: unpublished

Contents

Chapter 1	Introduction	*1*
Chapter 2	A charge-dependent long-ranged force drives tailored assembly of matter in solution	*13*
Chapter 3	Chemical control of colloidal self-assembly driven by the electrosolvation force	*117*
Chapter 4	Strongly attractive pair potentials between like-charged particles in fluids	*221*
Chapter 5	Conclusion	*241*
	References	*249*

1

Introduction

History of the like-charge attraction phenomenon

Since Coulomb's description of electrostatics in 1785, it has become well known that two negatively charged objects that approach in air will repel. It is also expected that, intuitively, the same pair of objects submerged in water would repel too, and the effect should be symmetrical regardless of the sign of charge. Such a description of electrostatic interactions has been well established in the Poisson-Boltzmann (PB) theory, first developed by Gouy and Chapman in the 1910s [1,2]. A description of the electrostatics in linear regime is added to the van der Waals interaction in the DLVO theory (developed by Derjaguin and Landau, Verwey and Overbeek in the 1940s), which also clearly indicates that two similarly charged surfaces in dilute electrolytes should experience a repulsion that monotonically decays with separation, with the van der Waals (vdW) attraction dominating at very short range [3-6]. But within the PB theory the interaction between like-charged particles is expected to be purely repulsive, no matter the sign of charge [7-10]. Nonetheless, experimental studies as early as the 1920s have shown evidence that departed from theoretical predictions. Findings such as the spontaneous

formation of order structures, or 'tactoids' of vanadium oxide and uniform special arrangement of disk-shaped iron oxide in large separation, as well as hexagonal close-packed arrangement of tobacco virus crystals all indicated the presence of a *'long range attractive forces, which under some conditions can outweight the effect of repulsive forces*', suggested by Langmuir [11-16]. Rosalind Franklin also pointed to such long-ranged attractive force during her study of Tipula iridescent virus crystals where the virus particles were held together at large separations, two times the size of the virus themselves [17]. Various studies in recent years also suggested experimental evidence for a long-ranged attractive force between like-charged objects, such as ordered arrangements of polymer, liposome, and tRNA, DNA stretching, biomolecular condensation and phase segregation [18-26].

A more systematic route of examining the like-charge attraction phenomenon was carried out by direct observation of charged microspheres since 1970s, which was an ideal and simple model for colloidal studies [27]. Kose *et al.* first directly observed hexagonally ordered structures with large spacings after diluting latex microspheres in deionized water, using a metallurgical microscope (Fig. 1) [28]. Their finding was later confirmed by other studies in the 1980s [29-31]. In 1994, Ito *et al.* directly observed the void structures in solution between negatively charged polystyrene particles through confocal laser scanning microscope. The presence of voids further confirmed the existence of attractive potentials, ruling out the possible artifact originated from interfaces [32]. In the same year, Kepler and Fraden developed a technique for the measurement of pair potentials between colloidal particles using digital video microscopy. A long-ranged (up to 2 μm in interparticle separation) weak attraction (~0.2 $k_B T$) was measured between negatively charged submicron polystyrene particles in deionized water (DI) [33]. Grier and his colleagues confirmed such long-ranged attraction by studying negatively charged polystyrene sulphate particles in DI, the pair potential was measured using optical tweezers [34,35]. Both studies concluded that such attraction is much longer ranged than van der Waals attraction, where the DLVO theory fails to explain for low ionic strength solutions. Their studies suggested that the observed like-charge attraction was originated

from wall confinement, however it has been shown that confinement alone cannot produce such effective attraction on the bases of PB theory [7-10,36,37]. Others criticized the possible experimental artifacts, but later clarified by Polin *et al.* through artifact-corrected video microscopy measurement [38-40]. Several other explanations have been put forward, such as ion-induced effective potential, wall-induced effects, ion correlation, image charge effect, nonequilibrium hydrodynamics, fluctuation in ion, many-body effects, charge inversion and attraction between metal particles distribution [41-54]. However, these explanations do not capture the experimental observations.

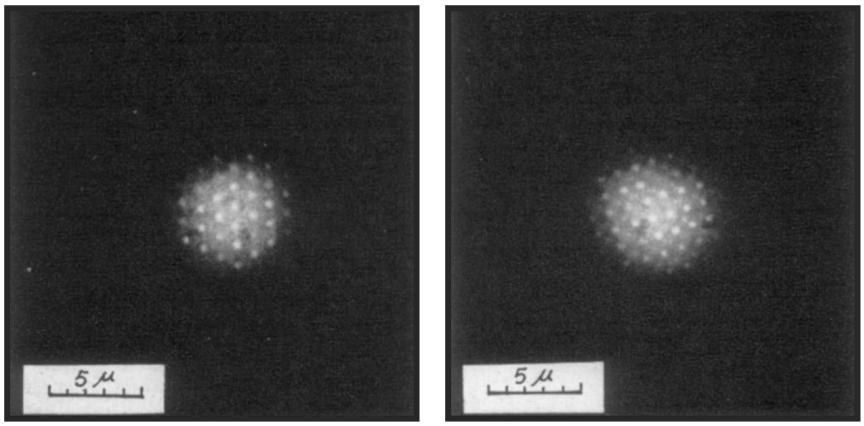


Figure 1. Ordered structures of sub-micron polystyrene particles with large spacings, adopted from Kose *et al.* [28]. The particles having an average diameter of 341 nm and a number density of 5.6 vol%, were deionized and diluted in DI water. The sample was observed in an enclosed glass observation cell under a metallurgical microscope. Left and right images display hexagonal and cubic arrangements, respectively.

More recent studies by Groves *et al.* provided hints at the mysteries long-ranged attraction, by coating micron-sized silica particles with charged lipid membranes [55,56]. It was found that like-charge attraction appeared only in systems where particles are negatively charged, whereas no attraction was found among positively charged particles (Fig. 2) [57]. Particles coated with negatively charged lipids self-organized into hexagonally packed clusters in DI water (~5 μM), indicated by a strong peak in the radial distribution function, $g(r)$, and an averaged intersurface separation of nearly 1 μm. Such attraction must be associated with a deep minimum in potential energy, which was

inferred to be around 5 $k_B T$ [58]. Along with its asymmetrical and long-ranged properties, all theories made prior failed to capture these characteristics.

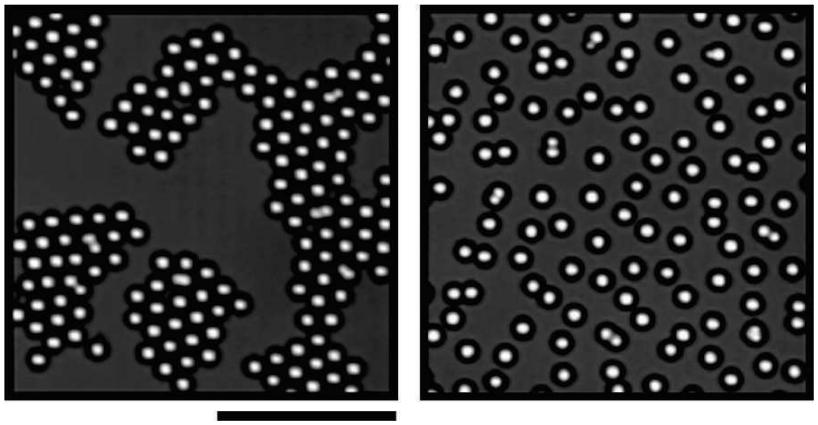


Figure 2. Optical microscopy images of particles coated with negatively and positively charged lipids, adopted from Groves *et al.* [57]. Silica particles with an average diameter of 6.54 µm were coated with lipid bilayers submerged in DI water, levitating above a similarly coated surface. Left: particles coated with negatively charged lipids forming hexagonally packed clusters with large intersurface separation (~1 µm), indicating a long-ranged attraction, right: particles coated with positively charged lipids are well dispersed without cluster formation, indicating a net repulsive system. Scale bar 60 µm.

An additional contribution to the interparticle interaction

A new theory was developed by Krishnan *et al.* in 2020 which provided an explanation for the asymmetrical behaviour of the long-ranged attraction between like-charged objects in dilute aqueous solutions containing monovalent salts. According to this model, there is an additional contribution to the traditional counterion-governed repulsion between two like-charged particles. This contribution is not contained within the PB theory, and arises from excess free energy of interfacial water molecules at a charged surface [58,59]. It is important to note that PB theory, and the related DLVO theory which incorporates an attraction due to the vdW force, rely on a description of the medium that entails a dielectric *constant* everywhere, overlooking molecular-level effects such as net orientation or a "pre-polarisation" at an interface. We have introduced the term '*electrosolvation*' force to describe an electrically influenced, solvation related contribution to the interparticle interaction. '*Electro-*', referring to the fact that this

phenomenon is fundamentally electrical in nature, driven by the sign of charge of the objects; and *'-solvation'* indicates the solvent or solvation dependent nature of the interaction.

It is well known that two like-charged objects approaching in solution experience a net reduction in charge that minimizes the free energy of the system through the process of 'charge regulation' [60]. However, a reduction in particle charge cannot render the interparticle interaction repulsive. We postulate that there is an "excess" free energy that arises from the coupling of the particle charge and the dipolar interfacial layer which does not appear in the traditional continuum view of water. Most importantly, calculations using the model revealed that this contribution can be large enough to compete with and even overcome the weak double layer repulsion at long range. Superimposing the traditionally expected electrostatic repulsion and the electrosolvation force, it is possible to produce a net potential at long range that is either attractive or repulsive, depending on the specific combination of particle charge and solvent, and other experimental conditions (Fig. 3).

To write the total interaction potential U^*_{tot} that describes the approach of two spherical particles of radius R from large separation to an interparticle separation distance $x = r - 2R$ in solution, we add the suggested electrosolvation free energy to the traditional DLVO contribution, such that

$$U^*_{\mathrm{tot}}(x) = U_{\mathrm{DLVO}}(x) + \Delta F_{\mathrm{int}}(x) = U_{\mathrm{vdW}}(x) + \Delta F_{\mathrm{el}}(x) + \Delta F_{\mathrm{int}}(x) \qquad (1.1)$$

where U_{vdW} is the van der Waals (vdW) contribution. ΔF_{el} is the traditional electrostatic free energy given by $\Delta F_{\mathrm{el}} = A \exp(-\kappa_1 r)/r$, where $A>0$ indicates monotonic repulsion and $\kappa_1 \approx \kappa = \sqrt{2e^2 N_{\mathrm{A}} c_0/\varepsilon\varepsilon_0 k_{\mathrm{B}} T}$, the inverse Debye screening length. Here ε denotes the dielectric constant of a solvent containing a molar concentration of c_0 monovalent ions, where e, N_{A}, ε_0, k_{B}, and T are the elementary charge, Avogadro's number, permittivity of free space, Boltzmann's constant and absolute temperature, respectively. ΔF_{int} is the electrosolvation (or interfacial solvation) free energy contribution resembling a Yukawa potential form, $\Delta F_{\mathrm{int}} = B \exp(-\kappa_2 r)/r$,

where κ_2 is the effective screening length due to electrosolvation ($\kappa_2 < \kappa_1$) and B can be either positive or negative depending on the sign of the particle charge and the orientation of interfacial solvent molecules. For large microspheres interacting at long distances ($R \gg \kappa^{-1}$, $\kappa x > 2$), the vdW contribution can be neglected and the total interaction is simplified to

$$U_{\mathrm{tot}}(x) = \Delta F_{\mathrm{el}}(x) + \Delta F_{\mathrm{int}}(x) \approx A \exp(-\kappa_1 x) + \ B \exp(-\kappa_2 x) \tag{1.2}$$

Specifically, the electrosolvation free energy per unit area f_{int} can be obtained through molecular dynamics (MD) simulations where the *excess* electrical potential due to interfacial solvent orientation, $\varphi_{\mathrm{int}}(\sigma)$, is calculated as function of charge density σ:

$$f_{\mathrm{int}}(\sigma) = \int_0^{\sigma} \varphi_{\mathrm{int}}(\sigma)\ \mathrm{d}\sigma \tag{1.3}$$

Importantly, at a weakly charged or even uncharged surface where $\varphi_{\mathrm{int}}(\sigma \approx 0) \approx \varphi_0$, a non-zero excess electrical potential can arise from the preferential orientation of interfacial solvent molecules (e.g. water). This results in an asymmetric interaction potential which leads to the observed charge-asymmetry of like-charge attraction phenomenon. Furthermore, σ at position $\boldsymbol{R}$ on the particle surface is a function of interparticle separation x due to charge regulation. Thus, the following surface integral yields the total electrosolvation free energy $F_{\mathrm{int}}(x)$ for the interaction:

$$F_{\mathrm{int}}(x) = \int_S f_{\mathrm{int}}(\sigma(\boldsymbol{R}, x))\ \mathrm{d}A \tag{1.4}$$

The model further suggests that the coefficient B may be given by

$$B \propto ez\varphi_{\mathrm{int}}\Gamma R^2 \frac{\mathrm{d}\alpha}{\mathrm{d}\psi_{\mathrm{s}}}\psi_{\mathrm{s}} \tag{1.5}$$

where

$$\alpha = \frac{1}{1 + 10^{z(\mathrm{p}H - \mathrm{p}K)}\ \exp(z\psi_{\mathrm{s}})} \tag{1.6}$$

is the ionization probability of an ionisable surface group with number density Γ and valency $z = \pm 1$. $\frac{\mathrm{d}\alpha}{\mathrm{d}\psi_{\mathrm{s}}}$ can be considered as a measure of the ability of the particle to charge regulate and is largest when $pK + 0.2 \lesssim \mathrm{p}H \lesssim \mathrm{p}K + 2.5$ for negatively charged particles. Further details will be addressed in the context of experiments in the following chapters.

To summarise, the electrosolvation model suggests that for two particles carrying negative ionizable surface groups ($\psi_s < 0$, $z\frac{d\alpha}{d\psi_s} < 0$) approaching in water ($\varphi_{int} < 0$), a negative value of B term is expected. The electrosolvation contribution can compete with and even overcome the electrostatic repulsion which results in a deep and long-ranged minima in the pair potential. Conversely, for particles carrying positive ionizable surface groups ($\psi_s > 0$, $z\frac{d\alpha}{d\psi_s} < 0$) suspended in water ($\varphi_{int} < 0$), a positive B term is expected, suggesting monotonic repulsion which behaves as the DLVO model predicted.

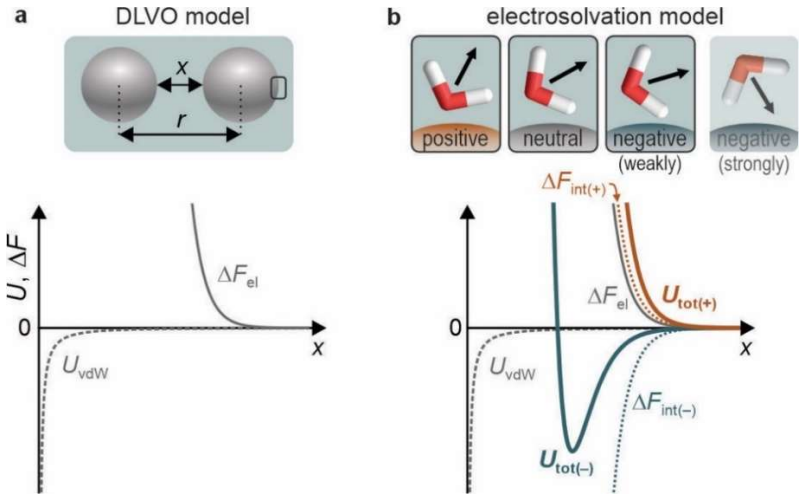


Figure 3. The DLVO model and electrosolvation model. (**a**) The DLVO model assumes a continuous and homogeneous solvent system where particles are balanced by van der Waals contribution U_{vdW}, and double layer repulsion ΔF_{el}. (**b**) The electrosolvation model takes into account of energy contribution from interfacial solvent molecules, which can compete with the electrostatics and result in an overall attractive ($U_{tot(-)}$) or repulsive ($U_{tot(+)}$) potential between like-charged particles, capturing the asymmetry phenomenon observed in experiments. Schematic demonstrates the preferential orientation of solvent water molecules at a solid-liquid interface. Close to a neutral surface, water molecules on average point the hydrogen atoms slightly towards the bulk, resulting in a net dipole moment (arrow) pointing away from the interface. At a weakly negatively charged surface, this orientation remains largely the same, giving rise to an electrosolvation free energy contribution that decreases with decreasing separation due to charge regulation ($\Delta F_{int} < 0$). At a positively charged surface however, the same water dipole orientation results in a positive electrosolvation contribution that increases with decreasing separation ($\Delta F_{int} > 0$) [58,59]. The symmetry-broken net orientation of water (or solvent dipoles) at the interface is therefore responsible for breaking the charge inversion symmetry of the interaction between particles in solution.

Experimental approach

Experiments described in the following three chapters were conducted in similar methodologies, specific details can be found in the methods section of each chapter. In general, to examine the interparticle interactions in solutions, a bright-field microscope was assembled. The setup consists of a collimated light-emitting diode (LED) light source, a pitch and roll platform supporting the observation cell, an objective lens and a charge-coupled device (CCD) camera for image acquisition (Fig. 4). The dilute particle suspension of interest is contained and sealed in the observation cell. Consecutive snapshots of particle interactions are recorded once all particles in solution settles under gravity to the bottom of the cell and stabilizes. Particle coordinates are localized and interparticle separations are measured to construct the radial probability density function, $g(r)$.

The underlying pair potential, $U(r)$, is inferred from iterative Brownian dynamic (BD) simulations, assuming pairwise additivity of particle interactions within clusters, where r is the centre-to-centre distance between particles. Additionally, direct measurement of pair interaction potential is conducted via single-particle tracking of isolated pairs using the Boltzmann inversion relation:

$$U(x) = -k_{\mathrm{B}}T \ln [P(x)] \tag{1.7}$$

where $P(x)$ is the probability density function of separation distance between two interacting particles, k_{B} is the Boltzmann constant and T is the absolute temperature.

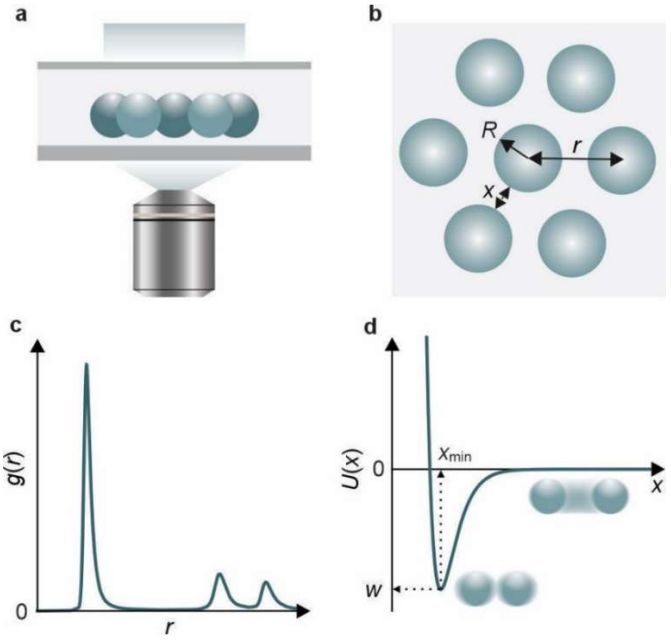


Figure 4. Overview of the experimental setup. (**a**) Schematic representation of a microsphere suspension levitating in an observation cell under the microscope. (**b**) Top view of the interacting particles of averaged radius R forming a cluster in hexagonal arrangement, with a centre-to-centre separation distance $r = x + 2R$. (**c**) Radial distribution profile, $g(r)$, of a typical cluster-forming colloidal suspension system obtained from experiments. (**d**) Corresponding pair interaction potential, $U(x)$, inferred from BD simulation displaying a minimum characterized by the well depth w and the location $x_{\min}$.

Thesis outline

This thesis is dedicated to the century-old and long-debated problem of like-charge attraction. The experiment-orientated studies presented herein provided compelling evidence for the existence of an additional component that is absent from the classical view of interparticle interactions in solution. The properties of this additional contribution, the electrosolvation force, are examined and quantified through a series of finely controlled experiments described in the following three chapters:

Chapter 2: A charge-dependent long-ranged force drives tailored assembly of matter in solution

This study investigated the long-ranged attraction characterized by clusters (or crystalline structures) formation among various types of negatively charged particles in aqueous solutions, and its correlation with ionic strength and pH. The charge-dependent nature of the attraction is explored by alternating signs of the particle surface charge. In water, negatively charged particles exhibit attraction, while positively charged particles repel, demonstrating that the attraction is asymmetric with respect to the sign charge in the system. The generality of like-charge attraction is examined between chemically dissimilar particles, highlighting the importance of physical electrical charge-state over specific chemical properties, further extending to macromolecules. Importantly, the switching of the 'charge-asymmetry' is demonstrated, showing attraction between positively charged particles and the absence of attraction among negatively charged particles in non-aqueous solvent systems. This study offered compelling evidence supporting the emerging concept of the electrosolvation force, suggesting a major conceptual departure from the traditional DLVO picture.

Chapter 3: Chemical control of self-assembly by the electrosolvation force

This chapter describes the systematic exploration of the influence of solvents, osmolytes and surfactants on the long-ranged attractive interaction between like-charged particles. The solvation-governed nature of the attraction is demonstrated across a broader range of simple solvents and solvent mixtures. The role of interfacial molecular

dipole orientation and surface adsorption is studied through the addition of various small neutral molecules, such as zwitterionic amino acids. Significant weakening of the long-ranged attraction is observed upon the addition of 'interfacially disruptive' molecules at low concentrations, as confirmed by Molecular dynamics (MD) simulation. This study provides further strong evidence of the importance of surface and interfacial molecular orientation in modulating the magnitude of the proposed electrosolvation force.

Chapter 4: Strongly attractive pair potentials between like-charged particles in fluids

This chapter quantitatively investigates the characteristics of like-charge attraction through direct measurements of pair potentials between isolated pairs of particles. In line with the previous cluster-formation experiments, strong and long-ranged attraction is measured between negatively charged particles in water and positively charged particles in heptanol. Additionally, the effect of ionic strength and particle size are examined. Notably, the measured effective screening length that governs the attractive component of the pair potential was found to be approximately one order of magnitude larger than the nominal Debye length. Our findings call for a re-evaluation of the current continuum model of electrostatic interactions and a necessity for the theory to incorporate 'non-local' effects in the solvent medium.

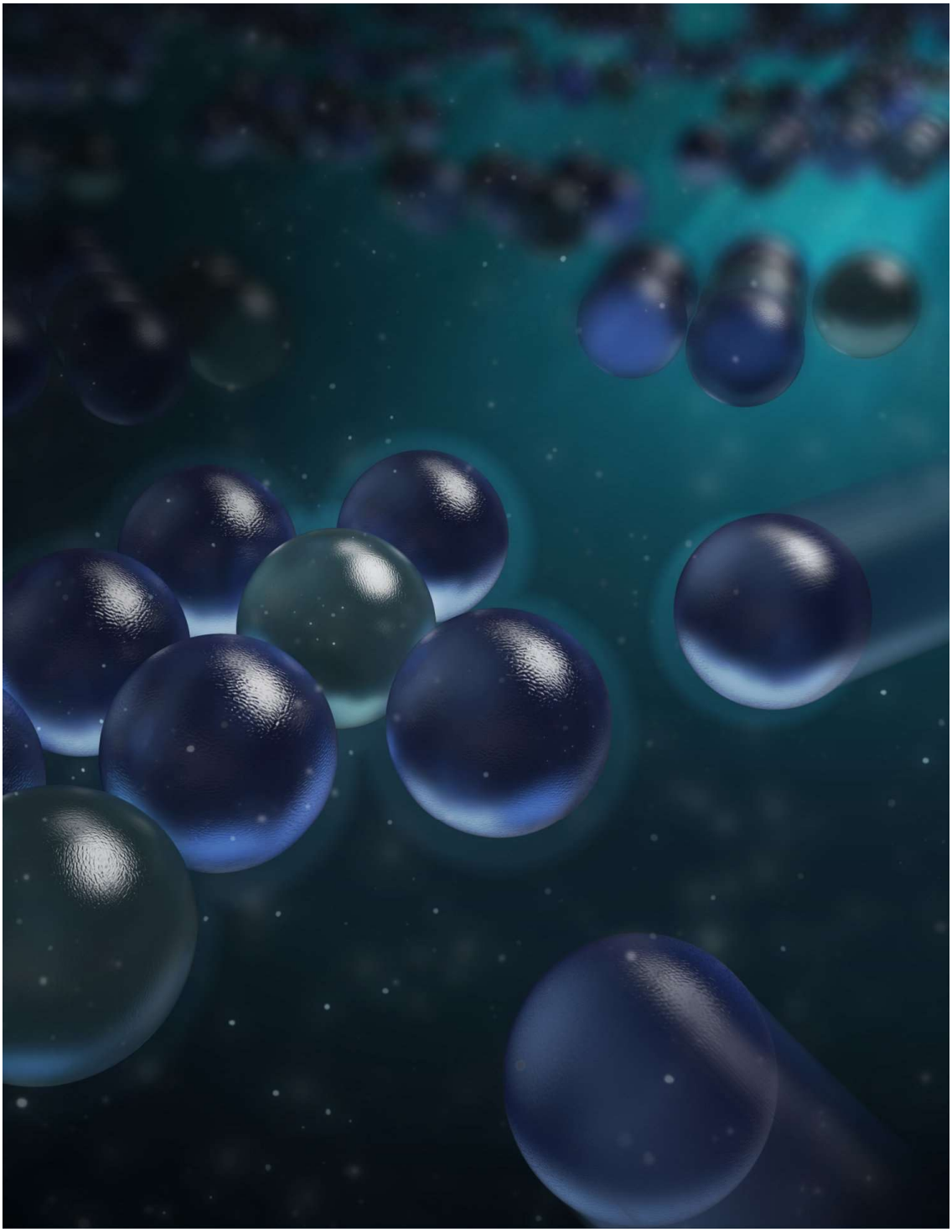


Figure 5. An artwork demonstrating cluster formation between like-charged particle in solution.

2

A charge-dependent long-ranged force drives tailored assembly of matter in solution

The conundrum of the like-charge attraction phenomenon has persisted for nearly a century, with numerous experimental evidences reported across a wide range of systems—from biomolecules to polyelectrolytes, and from colloidal nanoparticles to microspheres [11,12,14,16,17,28,29,33,35,57]. Due to the relatively weak magnitude of the attraction, arguably due to the use of rather small particles in those experiments, attempted measurements in such systems were often confounded by experimental artifacts in direct microscopy-based measurements [37-39]. Nonetheless, in 2009, Groves *et al.* demonstrated the asymmetrical behaviour of the like-charge attraction using charged lipid-coated silica microspheres [57]. Their study showed that particles with negatively charged lipid-coated surfaces attracted each other strongly in aqueous solutions, while positively charged particles repelled. Imaging artifacts were clearly absent from measurements, however, there remained no credible theoretical explanation for the observations.

The establishment of the interfacial solvation (or electrosolvation) model offered a mechanism to describe the asymmetrical attraction between like-charged particles by accounting for the additional contribution from interfacial solvent molecules, which was disregarded in the traditional electrostatic description that treats solvent as a continuum [58,59]. Understanding the interplay between specific surface chemistry and the structure of interfacial solvent thus becomes crucial, as suggested by our model. Therefore, new experimental studies are needed to systematically examine the characteristics of this asymmetrical attractive force, focusing on solvent properties such as ionic strength and pH, as well as surface properties such as species of ionizable groups.

With the advancement in digital video microscopy and particle tracking algorithms, direct observation of self-interacting colloidal microspheres levitating on a two-dimensional plane enables the accurate localization of individual microspheres with nanometre-level precision [33,56,57,61,62]. Individual particle trajectories can be localized to determine the radial distribution function $g(r)$. Furthermore, the underlying pair interacting potential can be conveniently inferred through BD simulations [63].

This chapter presents the published peer reviewed article titled "*A charge-dependent long-ranged force drives tailored assembly of matter in solution*". The aim of this study is to provide further experimental evidence of like-charge attraction and to examine the mechanism proposed in the electrosolvation model. The asymmetrical property of the attractive potential is demonstrated in particles carrying a range of different surface functional groups, such as silanol, carboxyl, amino, polypeptides and polyelectrolytes. We found that particles with negatively charged surfaces rapidly self-assembled into ordered clusters at large interparticle separations in aqueous solutions, indicating a strong attractive potential on the order of a few $k_{\mathrm{B}}T$, while positively charged particles remained dispersed, indicative of monotonic repulsion. We further investigated the influence of surface charge density on cluster formation through pH change, where the ionizable surface groups on the particle surface are directly related to solution pH through their pK values. The generality of like-charged attraction is demonstrated by the mixing of chemically dissimilar particles. The observed cluster

formation emphasizes the importance of charge state to attraction rather than specific surface chemistry. Importantly, by examining the other side of the asymmetry, we find that particles with positive surface charge attract in alcohols whereas negatively charged particles repel. This behaviour is well captured by the electrosolvation model through the study of the interfacial molecular orientation in MD simulation. Furthermore, by treating macromolecules as charged nanospheres, we provided a calculation suggesting that the electrosolvation force could play a role in explaining the phase separation of proteins carrying a net negative charge. This study demonstrates clear experimental evidence of a long-ranged asymmetrical attraction that is effectively described by the electrosolvation model, indicating a departure from the traditional view of interparticle interactions.

paper:

A charge-dependent long-ranged force drives tailored assembly of matter in solution

nature nanotechnology

Article

https://doi.org/10.1038/s41565-024-01621-5

A charge-dependent long-ranged force drives tailored assembly of matter in solution

Received: 22 November 2023

Accepted: 25 January 2024

Published online: 1 March 2024

Check for updates

Sida Wang[1,3], Rowan Walker-Gibbons[1,3], Bethany Watkins[1], Melissa Flynn[1] & Madhavi Krishnan[1,2]

The interaction between charged objects in solution is generally expected to recapitulate two central principles of electromagnetics: (1) like-charged objects repel, and (2) they do so regardless of the sign of their electrical charge. Here we demonstrate experimentally that the solvent plays a hitherto unforeseen but crucial role in interparticle interactions, and importantly, that interactions in the fluid phase can break charge-reversal symmetry. We show that in aqueous solution, negatively charged particles can attract at long range while positively charged particles repel. In solvents that exhibit an inversion of the net molecular dipole at an interface, such as alcohols, we find that the converse can be true: positively charged particles may attract whereas negatives repel. The observations hold across a wide variety of surface chemistries: from inorganic silica and polymeric particles to polyelectrolyte- and polypeptide-coated surfaces in aqueous solution. A theory of interparticle interactions that invokes solvent structuring at an interface captures the observations. Our study establishes a nanoscopic interfacial mechanism by which solvent molecules may give rise to a strong and long-ranged force in solution, with immediate ramifications for a range of particulate and molecular processes across length scales such as self-assembly, gelation and crystallization, biomolecular condensation, coacervation, and phase segregation.

The delicate interplay of interactions between objects in the fluid phase influences the behaviour, organization and properties of systems from nanometric to more macroscopic size and length scales and thus underpins a wealth of natural phenomena. Our understanding and intuition of the interaction between electrically charged particles in solution is grounded in a central principle from classical electromagnetics which dictates that the force between charges of the same sign is not only repulsive at all separations but is also symmetric with respect to the sign of the charge. For example, because like-charged objects in vacuum are expected to repel regardless of whether the sign of the charge they carry is positive or negative, the expectation is that like-charged particles in solution must also monotonically repel, particularly at long range where the van der Waals (vdW) attraction is too weak to substantially influence the overall interaction. This view is a hallmark of the Derjaguin–Landau–Verwey–Overbeek (DLVO) theory, a cornerstone of colloid science[1–3].

Nonetheless, clear and well-founded exceptions to the rule exist in the presence of multivalent ions[4,5] and in particular regimes involving high magnitudes of electrical charge and in low dielectric constant media[6]. But over the decades, consistent reports of attraction between like-charged particles from the nanometre to micrometre scales in size and range, for example, nucleic acids, liposomes, polymers and colloidal particles in aqueous media containing low concentrations of monovalent salt—where DLVO theory is expected to hold—have evaded explanation[7–17]. Not surprisingly, this persistent divergence between experiment and theory has received considerable attention in the theoretical literature[6,18–23].

[1]Physical and Theoretical Chemistry Laboratory, Department of Chemistry, University of Oxford, Oxford, UK. [2]The Kavli Institute for Nanoscience Discovery, Oxford, UK. [3]These authors contributed equally: Sida Wang, Rowan Walker-Gibbons. e-mail: madhavi.krishnan@chem.ox.ac.uk

https://doi.org/10.1038/s41565-024-01621-5

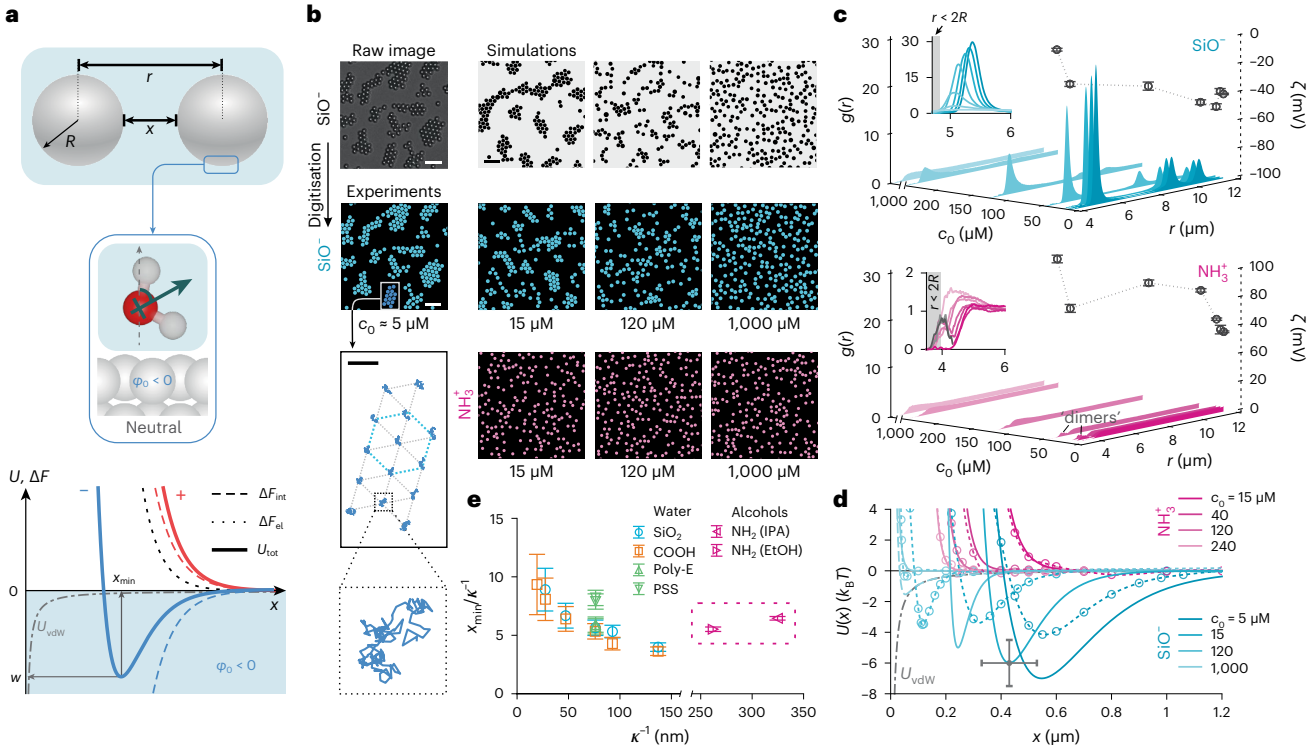


Fig. 1 | Interparticle interactions in solution can break charge-reversal symmetry. a, Schematic representations of two interacting spheres (top), and of the dominant average orientation of water molecules near an uncharged surface (middle). Bottom: Various contributions to the total interaction free energy for positively (red lines) and negatively charged (blue lines) particles: electrostatic repulsion, ΔF_{el} (black dotted line; applies to both signs of charge); interfacial solvation contribution, ΔF_{int}, depends on the sign of charge (dashed lines); total interaction energy, $U_{tot} = \Delta F_{el} + \Delta F_{int}$ (solid lines); and the vdW contribution, U_{vdW} (dashed-dotted grey line; applies to both cases). For $\varphi_0 < 0$ (for example, in water) negatively charged particles may display a minimum in U_{tot} of depth w at a separation x_{min} (solid blue line), and positively charged particles repel monotonically (red solid line) (Supplementary Information, section 3.1). **b**, Negatively charged silica particles (SiO^-, blue circles, $R = 4.82$ μm) form hcp clusters in water depending on salt concentration, c_0 (middle row). Scale bars, 20 μm. Inset, bottom left: trajectories of particles in a single cluster over a period of 30 s. Scale bar, 5 μm. Positively charged aminated silica particles (NH_3^+, pink circles, $R = 3.92$ μm) in water do not form clusters regardless of c_0 (bottom row). Images acquired using bright-field microscopy (Supplementary Figs. 3 and 25) and digitized to facilitate presentation. BD simulation snapshots for SiO^- particle interactions (top). **c**, Measured radial probability density functions, $g(r)$, for SiO^- (top) and NH_3^+ particles (bottom), including measured zeta potentials (ζ; circular symbols) for varying c_0. Error bars denote ±s.d for three measurements. Insets: the small peak around $2R$ reflects particle 'dimers' in the sample. **d**, Inferred pair-interaction potentials, $U(x)$ (solid lines), for SiO^- (blue) and NH_3^+ particles (pink). Calculated $U_{tot}(x)$ curves as described in ref. 27 and Supplementary Information, sections 3.2 and 3.3 (dashed lines with symbols; see Supplementary Table 1 for parameter values). Error bars denote estimated uncertainties of ±100 nm on particle diameter and $\pm 1.5 k_B T$ in w (Supplementary Fig. 18). **e**, Plot of x_{min} versus κ^{-1} for various negative particles in water and positive particles in alcohols shows that $x_{min} \approx 5 - 10\kappa^{-1}$ (Fig. 5). Errors bars represent an uncertainty of ≈50 nm in x, averaged over all particle types.

Standing theories invoke a continuum description of the solvent which overlooks finer-grained detail such as the molecular nature of the solvent, and its structure and interactions, particularly at an interface with a molecule or a particle[1,2]. Despite the general success of classical mean-field, continuum theories[3], it is becoming increasingly clear that the molecular nature of water ought to play a defining role in a host of interfacial phenomena in the aqueous phase[24–26]. We recently suggested that the behaviour of the molecular solvent at an interface can make a substantial contribution to the total interaction free energy of two approaching objects carrying electrical charge[27,28] (Fig. 1a). In particular, for charged matter in water, our model suggested that this contribution could be large enough not only to counteract the interparticle Coulombic repulsion but could even overwhelm it, changing the sign of the interparticle force for negatively charged particles, turning it net attractive. The orientational behaviour of the interfacial solvent could therefore be viewed as a store of free energy that can be tapped by the interparticle interaction, even at large separations (Fig. 1a). We further suggested that this interfacial free energy contribution results in a force whose sign and magnitude may be given in terms of an interfacial electrical potential, φ_0, that depends on the nature of the solvent, with $\varphi_0 < 0$ for water at an interface (refs. 27–29) (Fig. 1a; see Supplementary Information, section 3.1 for details).

The main experimental trends suggested by the interfacial solvation model are: (1) the breaking of charge-reversal symmetry in interparticle interactions, for example, negatively charged particles may attract in water, whereas positive particles repel; (2) the use of a different solvent may reverse this trend, that is, positive particles may attract whereas negatives repel; and (3) the magnitude of the solvation contribution to the interparticle interaction should depend strongly on the pH in solution. Here we report on comprehensive experimental tests of the contribution of the interfacial solvent to long-range interactions in solution. We demonstrate that the solvent can make a large contribution to the interparticle interaction and can counterintuitively drive the spontaneous formation of ordered assemblies of like-charged particles in solution. Furthermore, both the sign and magnitude of this free-energy contribution can have a decisive impact on the ability of a system of particles to self-assemble, and crucially we show that they are both amenable to careful tuning using a variety of particle- and solution-dependent parameters.

Measuring interparticle interactions in a two-dimensional suspension

We performed a range of experiments on two-dimensional (2D) suspensions of colloidal particles in solution and examined the dependence of the interparticle interaction on system properties such as pH and ionic strength of the electrolyte, particle charge and chemistry, and on the solvent molecular structure. We observed the spatial structure of the suspension using bright-field optical microscopy (Supplementary Information, section 1.5 and Supplementary Fig. 3) and constructed radial probability density distributions, $g(r)$, from the spatial coordinates of particles in a series of images. To infer the form of the underlying interparticle interaction, we performed Brownian dynamics (BD) simulations of interparticle interactions with various input potentials, $U(x)$, assuming pairwise additivity of the interactions, and generated simulated $g(r)$ functions (Supplementary Information, sections 2.1 and 3.4). Here, r denotes the interparticle separation between spheres of radius R, at an intersurface separation x (Fig. 1a). An iterative process permitted us to identify pair-potentials that were qualitatively consistent with the experimental data (Fig. 1b, top row; Supplementary Figs. 18–24 and Supplementary Tables 2–12). We also compared these experimentally inferred pair-potentials with a total interaction free energy, $U_{tot}(x)$, calculated for a pair of identical particles using the interfacial solvation model[27] (dashed lines with symbols in Figs. 1, 2 and 5, see Supplementary Information, sections 3.2 and 3.3). As implied by Supplementary Information equations (5)–(9), varying the value of $p = pK - pH$ in the theoretical model may result in a calculated $U_{tot}(x)$ that is purely repulsive, purely attractive, or a non-monotonic function displaying a minimum of depth w at an intersurface separation x_{min}. Parameter values for all calculated curves in this study are given in Supplementary Table 1.

Negative particles attract and positives repel in water

We first examined a system of colloidal silica particles of nominal diameter 4.82 μm dispersed in deionized water with an estimated background ionic strength of $c_0 = 5$ μM. The measured electrical potential (zeta potential) in the vicinity of the particle surface, $\zeta \approx -40$ mV, is indicative of a strongly negative surface charge arising from a high density of ionized surface silanol groups. DLVO theory predicts strong interparticle repulsions under these conditions, implying the observation of a randomly dispersed 2D distribution of particles. In marked departure from this intuitive expectation, we noted that the particles spontaneously self-assembled into stable, slowly reorganizing, hexagonally close packed (hcp) clusters characterized by an intersurface separation of the order of $x \approx 0.5\ \mu m \approx 5\kappa^{-1}$, sharing similarities with previous reports[12,30,31] (Fig. 1b, middle panels, and Supplementary Video 1). Here κ^{-1} is the Debye length which is a measure of the spatial decay rate of the magnitude of electrostatic interactions, and in a solution of monovalent ions can be given in nanometers by $\kappa^{-1} \approx 0.304/\sqrt{c_0}$, with c_0 in M. The spatial structure of the clusters, and the presence of large voids between clusters, implies the presence of a strong, long-ranged attractive interaction between particles of like charge. This attraction is counteracted by a repulsion at shorter range, giving rise to a stable pair-potential minimum at comparatively large separations[13]. The measured $g(r)$ profiles present periodic peaks of diminishing height, reflecting the ordered internal structure of finite-sized clusters—a characteristic signature of attractive interparticle interactions in solution (Fig. 1c, top panel). Simulations of interparticle interactions (snapshots in Fig. 1b, top row) and the corresponding inferred $U(x)$ agree with calculated $U_{tot}(x)$ curves which capture both the experimentally inferred location of the minima, $x_{min} \approx 2 - 10\kappa^{-1}$, and their depth, $|w| \approx 4k_BT$ (Fig. 1d)[27,28] (Supplementary Information, section 3.2). Here κ_B is Boltzmann's constant and T is the absolute temperature. Experiments performed for $c_0 = 5$ μM–1 mM on negatively charged silica and carboxylated particles displayed similar trends.

Interaction potentials measured for isolated pairs of interacting particles display good agreement with the w and x_{min} values inferred from the ensemble experiments (Extended Data Fig. 1a–d, Supplementary Fig. 12 and Supplementary Information, section 4.2). This confirms that the observed cluster formation stems from a pair-potential that indeed carries a substantial attractive component, rather than from collective interactions in a system of purely repulsive particles[20]. Furthermore, in contrast to previous suggestions concerning like-charge attraction, we find that the long-ranged attraction is unaffected by the surface properties of the underlying coverglass[15,32,33] (Extended Data Fig. 1a–d and Supplementary Information, section 4.4) which agrees with previous measurements of attractive pair interactions in bulk solution and with theoretical expectations from the interfacial solvation model[17]. Note that optical image processing artefacts play no role in our measurements of pair-interaction minima[34] (Extended Data Fig. 1e–h, and Supplementary Information, section 4.3).

Turning to experiments on positively charged aminated silica particles under the same conditions, we found that particles remained randomly dispersed in solution as expected for a purely repulsive interparticle interaction (Fig. 1b, lowest row and Supplementary Video 1). The measured $g(r)$ profiles were relatively featureless, and categorically devoid of the periodic structure characteristic of ordered clusters (Fig. 1c, lower panel). The corresponding $U(x)$ profiles imply monotonically decaying repulsions in good agreement with the profiles calculated from the interfacial solvation model (Fig. 1d). The conspicuous absence of a long-ranged minimum in $U(x)$ for positive particles contrasts with the strong attraction observed for negative particles, and suggests that the solvent is responsible for this striking qualitative departure from the expectation of charge-reversal symmetry in interparticle interactions.

pH controls the magnitude of the long-ranged force

Next we explored the influence of pH on the interaction between silica particles. Silica surfaces carry a variety of ionizable silanol groups that are characterized by different number densities and highly disparate pK values between 2 and 11 which implies a wide range of pH over which the surface ionizable groups may undergo a change in α, their extent of ionization[35–37]. We examined cluster formation in silica at a fixed ionic strength with pH varying from 4 to 10 and inferred the value of w in each case. While $w < 0$ denotes the depth of the minimum in an attractive pair-potential, we take $w = 0$ for a purely repulsive pair-potential. For silica, we found that although the magnitude of w decreased markedly with increasing pH, it remained substantial ($|w| \approx 2k_BT$) even at high pH > 9 (Fig. 2d and Supplementary Video 2). This occurs despite the fact that the electrostatic interaction, ΔF_{el}, is expected to grow in magnitude with increasing pH, progressively counteracting an attractive interfacial contribution that we expect to simultaneously weaken as $\frac{d\alpha}{d\psi_s} \to 0$. Here ψ_s denotes the electrical surface potential of the particle (see Supplementary Information, section 3.1 for details). Importantly, we found that the observations can be qualitatively explained within the interfacial solvation model (Fig. 2a,d, top panels, Supplementary Information, section 3.5 and Supplementary Video 2).

To quantitatively explore the effect of pH, we examined the behaviour of carboxylated melamine resin (COOH) particles where the charge arises from carboxyl groups characterized by a nominal pK ≈ 4.5. We observed a clear maximum $|w|$ in the range of $pK < pH < pK + 3$, in qualitative agreement with the trend expected for $\frac{d\alpha}{d\psi_s}$, as given by Supplementary Information equation (9) and discussed further in the Supplementary Information (Fig. 2a,d, middle panels, Supplementary Information, section 3.5 and Supplementary Video 3).

https://doi.org/10.1038/s41565-024-01621-5

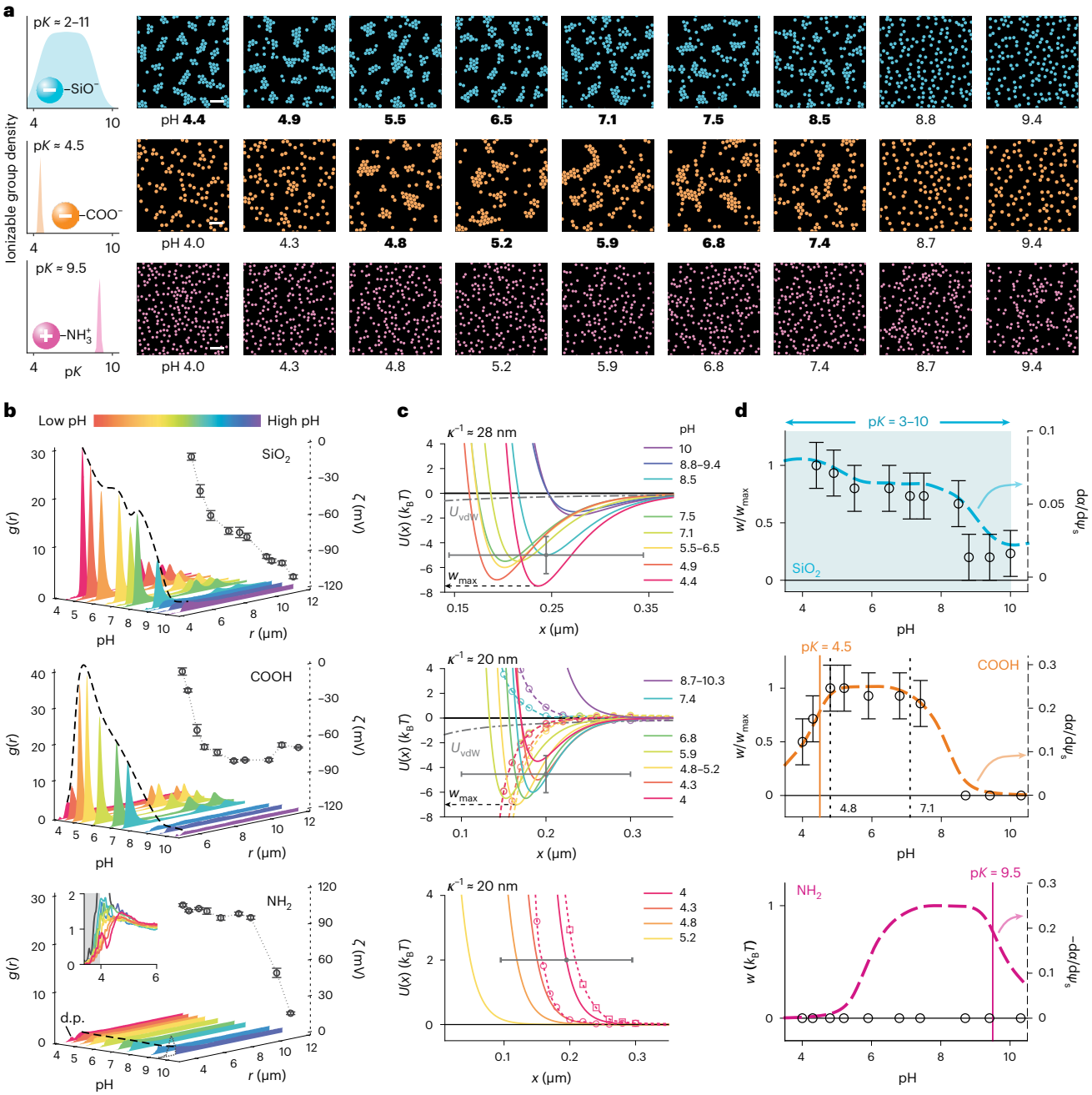


Fig. 2 | Tuning the interparticle interaction using the pH in solution. **a**, Snapshots of colloidal suspension structure as a function of pH for silica particles (top), carboxylic acid particles (middle) and aminated silica particles (bottom), holding salt concentration constant in each data series: c_0 = 0.12 mM (SiO_2), 0.25 mM (COOH) and 0.25 mM (NH_2). Scale bars, 20 μm. Bold values indicate the pH at which hcp cluster formation is observed. **b**, Radial probability density functions $g(r)$ (curves) and measured zeta (ζ) potentials (symbols) as a function of pH for all three particle types. Error bars represent mean ± s.d. from three measurements. The increasing height of the 'dimer-peak' (d.p.) with increasing pH for positive particles is indicative of increased sticking of particles due to discharging of the basic ionizable groups (bottom panel). **c**, $U(x)$ profiles inferred from measured $g(r)$ profiles (solid lines; Supplementary Figs. 20–22 and Supplementary Tables 4–8), theoretical $U_{tot}(x)$ curves (dashed lines with symbols) calculated as described in ref. 27 and Supplementary Information, sections 3.2 and 3.3 (see Supplementary Table 1 for parameter values), and U_{vdW} contribution for comparison (dashed-dotted grey line). w_{max} denotes the maximum inferred depth of the experimentally observed minimum in each case. Error bars denote estimated uncertainties of ±100 nm in particle diameter and $\pm 1.5 k_B T$ in w (Supplementary Figs. 20–22). **d**, Plots comparing trends as a function of pH in the experimentally inferred quantity w/w_{max} (symbols, left axis) with that of $\frac{d\alpha}{d\psi_S}$ determined using Supplementary Information equation (9) (dashed curves, right axis). See Supplementary Fig. 25 for all raw image data.

Next, we examined the behaviour of positively charged aminated silica particles carrying a high density of amino groups (NH_2) of nominal p$K \approx 9.5$. We did not observe cluster formation in positive particles over the entire range of pH (Fig. 2a, bottom panel and Supplementary Video 4). In fact the $g(r)$ curves reflected robust interparticle repulsions at large distances that were strongest at low values of pH ≈ 4 (Fig. 2b,

https://doi.org/10.1038/s41565-024-01621-5

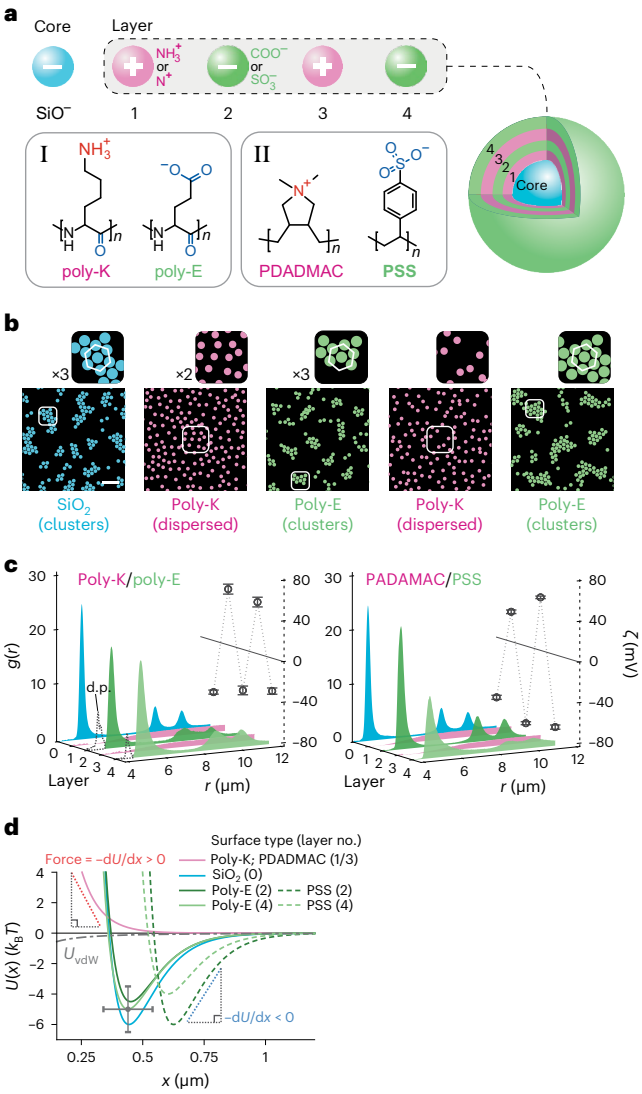


Fig. 3 | The sign of the long-ranged force depends on the sign of charge of the interacting particles. a, Top: schematic depiction of a sequentially coated silica particle displaying four serial layers with alternating sign of coating charge. Bottom: chemical structures of charged polypeptides (poly-K and poly-E) and polyelectrolytes (PDADMAC and PSS) used for layer-by-layer coating of silica particles. **b**, Images of particle suspension structure following each coating procedure using charged polypeptides. Scale bar, 20 μm. See Supplementary Figs. 23 and 25 for polyelectrolyte data, including PEI/PSS coatings, and raw images. **c**, Radial probability density functions $g(r)$ and measured zeta potentials as a function of coating or layer number for polypeptide (left) and polyelectrolyte coatings (right). Error bars represent mean ± s.d. from three measurements. The alternating sign of zeta-potential values for each new coating layer confirms the change in sign of the particle charge. **d**, $U(x)$ profiles inferred from measured $g(r)$ profiles for particles with positively charged (pink curve) and negatively charged coatings (blue and green curves) with layer numbers in parentheses (Supplementary Fig. 23 and Supplementary Tables 9–11). At long range ($x \gtrsim 5\kappa^{-1}$), negatively charged particles (charge density $\sigma < 0$) display an attraction which implies that the interparticle force is attractive, that is, $-\frac{dU(x)}{dx} < 0$, whereas the converse is true for positively charged particles ($\sigma > 0$) where we infer $-\frac{dU(x)}{dx} > 0$ for all separations, which agrees qualitatively with DLVO theory. All experiments were performed at $c_0 = 15$ μM. Error bars denote estimated uncertainties of ±100 nm in particle diameter and $\pm 1.5 k_B T$ in w (Supplementary Fig. 23).

bottom panel). Under more alkaline conditions given by $7 < \text{pH} < \text{p}K \approx 9$, the net charge on the particles decreases due to gradual deprotonation of the amino groups. This discharging of the amino groups correlates with a reduction in measured zeta potential and a consequent weakening of the interparticle repulsion (Fig. 2b, bottom panel), but the formation of stable, ordered clusters was never observed (Fig. 2a–c). This range of pH values ($7 < \text{pH} < 9$) may be contrasted with the equivalent pH range of 5–7 for carboxyl particles where we in fact observed the most stable clusters characterized by the deepest minima in interaction energy (largest $|w|$) generated by the long-ranged attractive force. We obtained similar results for silica particles coated with positively charged polyelectrolytes such as polyethyleneimine (PEI) (Supplementary Fig. 16). Thus we find that the measured pH dependence of interparticle interactions—for both signs of particle charge and a range of surface chemistries—carries key signatures of the solvation free-energy contribution, furnishing crucial validation of an interaction mechanism invoking charge-dependent solvent structuring at the solid–liquid interface.

Sequential switching between attraction and repulsion

To further probe the influence of surface chemistry on the interparticle interaction we examined the behaviour of negatively charged polystyrene sulfonate (PSS) surfaces. Isolated styrene sulfonic acid groups are highly acidic in free solution ($\text{p}K < -0.5$) but are expected to be characterized by $\text{p}K \approx 3$ in the context of a polymer backbone[38]. We produced PSS-coated silica particles using the layer-by-layer polyelectrolyte film deposition method[39]. We first coated silica particles with a layer of positively charged poly(diallyldimethylammonium chloride) (PDADMAC) polymer, which switched the sign of the zeta potential from $\zeta \approx -50$ mV to $\zeta \approx +40$ mV. PDADMAC-coated silica particles in solution no longer formed clusters (Fig. 3). We then further coated PDADMAC-coated silica particles with a layer of PSS, which altered the zeta potential from approximately +40 mV to −70 mV. We found that the system of PSS-coated particles formed stable clusters in solution at pH 5–6 ($\approx \text{p}K + 2.5$), indicating the reappearance of long-ranged interparticle attractions, similar to uncoated silica particles. We then proceeded to sequentially coat these PSS particles with alternating layers of PDADMAC and PSS, confirming the sign of the particle charge after each coating procedure using zeta potential measurements. We consistently found that the long-ranged interparticle attraction could be switched on and off depending on the sign of charge of the most recent surface coating. Data from four layers of sequential coating are presented in Fig. 3 (Supplementary Video 5). Similar results were obtained with alternating coatings of positively charged PEI and negatively charged PSS (Supplementary Figs. 23 and 25). All polyelectrolyte coating experiments were performed at $c_0 = 15$ μM (Fig. 3 and Supplementary Fig. 23).

To continue exploring the generality of the 'like-charge self-assembly' phenomenon we turned our attention to the examination of the interactions of polypeptide surface coatings on silica particles. Poly-L-lysine hydrobromide (poly-K) and poly-L-glutamic acid sodium salt (poly-E) polypeptides are routinely used as surface coatings, generating positively and negatively charged surfaces on account of their ionized amino (NH_3^+; $\text{p}K \approx 10$) and carboxyl (COO^-; $\text{p}K \approx 4.5$) side-chain groups, respectively. Here again we found that whereas positively charged lysine surfaces repelled as expected (similar to PEI- and PDADMAC-coated particles), poly-E surfaces displayed long-ranged attractions similar to our carboxyl particles (Fig. 3d). Once again we were able to repeatedly alternate between attractions and repulsions in the particle suspension by sequentially coating the particles with poly-K and poly-E layers, a finding that carries strong implications for interactions in proteins.

The above experiments show that negatively charged silica surfaces ($\text{p}K \approx 2$–11), carboxylated melamine resin particles ($\text{p}K \approx 4.5$),

https://doi.org/10.1038/s41565-024-01621-5

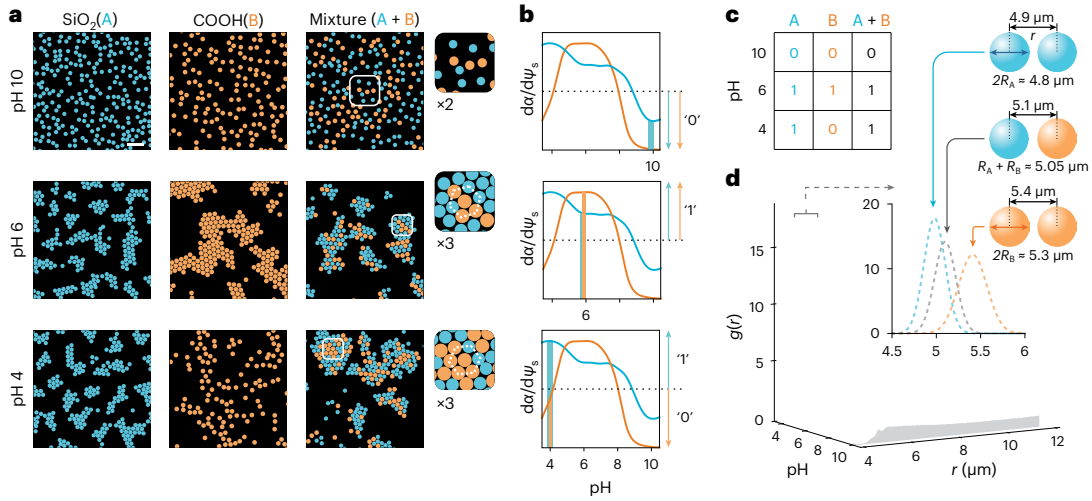


Fig. 4 | Cluster formation in chemically dissimilar particles. a, Structure of suspensions of pure SiO_2 particles, COOH particles and equimolar mixtures of the two species in solution at pH values 4, 6 and 10, corresponding to salt concentrations c_0 = 0.29, 0.01 and 0.13 mM, respectively. hcp clusters containing both particle species form even under conditions where one of the particle species does not display substantial self-attraction (pH 4 for this system, bottom panels). Scale bar, 20 μm. **b**, Plots of normalized $\frac{d\alpha}{d\psi_S}$ versus pH for SiO_2 (blue curve) and COOH (orange curve) from Fig. 2, with a dotted black line indicating a threshold level above which we regard $\frac{d\alpha}{d\psi_S}$ to be high, taking a binarized value of 1, which is accompanied by the formation of strong and stable same-species clusters as shown in Fig. 2. For low values of $\frac{d\alpha}{d\psi_S}$ we expect no cluster formation and assign this state and cluster formation outcome a value of 0. **c**, Truth table for the outcome of cluster formation in mixtures (column 3) depending on the binarized values of $\frac{d\alpha}{d\psi_S}$ for the individual pure species (columns 1 and 2). A value of 1 indicates the formation of mixed clusters containing both particle species, and 0 reflects no cluster formation. **d**, Radial probability distributions $g(r)$ for the three mixtures in **a**, displaying clear peak signatures of all three expected nearest-neighbour distances in the cross-species hcp clusters, that is, $r_{AA} > 2R_A$, $r_{AB} > R_A + R_B$, $r_{BB} > 2R_B$ (inset).

polystyrene sulfonate (p$K \approx 3$) and polyglutamate (p$K \approx 4.5$) coated polypeptide surfaces suspended in water support long-ranged interparticle attractions when the pH of the solution lies within a range of about 3 units above the pK of the ionizable groups. In contrast, positively charged particles display robust repulsions regardless of surface chemistry, and no evidence of a long-ranged attraction over the entire range of pH tested.

'Chemical logic' in cluster formation

Next, we performed experiments on mixtures of particles of different surface chemistry and observed the nature of the crystallites formed. Suspensions containing both COOH particles and SiO_2 particles displayed no cluster formation at high pH values, similar to each of the pure species, as expected (Fig. 4a, top). At pH values where each species is known to form clusters in the pure state (Fig. 2), we found that the mixture also formed hcp clusters composed of both species of particle with signatures in the $g(r)$ reflecting both particle sizes (Fig. 4a, middle and Fig. 4d). We then performed experiments at pH ≈ 4 where pure COOH particles do not form clusters, but SiO_2 particles do cluster. Interestingly, we found that rather than exclude the non-cluster-forming COOH species, the system displayed stable hcp clusters containing both types of particles (Fig. 4a, bottom and Supplementary Video 6). All these observations can be explained within the proposed interfacial solvation model of interparticle interactions (Supplementary Information, section 3.6). Specifically, it appears sufficient for one species of particle to be in the charge-regulating regime $\left(\frac{d\alpha}{d\psi_s} \neq 0\right)$ for an attraction between chemically dissimilar like-charged particles to manifest (Fig. 4b,c).

Thus we show that similar or identical chemistry is not a requirement for interparticle attraction, but that the electrical charge-state of the groups underpins a force with a general and tunable character that holds in a broad sense. Simply put, chemical properties of the particle may enter the physics of the interaction via the pK of the ionizable groups. These observations could carry implications for the biological phase separation problem, for example, where strongly acidic RNA molecules participate in cluster formation in mixtures involving other charged molecular species such as proteins[40,41]. To emphasize the connection with the biomolecular condensation problem, the silica particles in the clusters (Fig. 4a, bottom) may be seen to act as the 'scaffold', while the carboxyl particles act as 'clients'[42].

Negative self-attraction in water changes sign in alcohols

The question then naturally arises as to whether the type of charge asymmetry observed for the interparticle interaction in water could be altered in a different solvent on account of differences in molecular orientational behaviour at an interface. We first confirmed that positively charged amine-derivatized silica particles suspended in ethanol and isopropanol (IPA) displayed positive zeta potentials (Fig. 5c). We recall that these particles remained well dispersed when suspended in water (Figs. 1 and 2). In ethanol and IPA however, we found that positively charged particles formed stable crystalline clusters, displaying $g(r)$ distributions reminiscent of attractive interactions generally encountered for negatively charged silica particles in water (Fig. 5b,c and Supplementary Video 7). Negatively charged carboxylated particles, on the other hand, remained well dispersed in both alcohols, did not form clusters and qualitatively echoed observations on positively charged particles in water.

Molecular simulations of ethanol and IPA indeed show that the normal component of the average molecular dipole can be inverted with respect to that of molecular water at a neutral surface; that is, interfacial molecules orient such that their comparatively hydrophobic methyl ($-CH_3$) groups point towards a neutral surface (Fig. 5a and Supplementary Fig. 8b; Supplementary Information, section 2.2)[43]. This molecular orientation gives an interfacial

https://doi.org/10.1038/s41565-024-01621-5

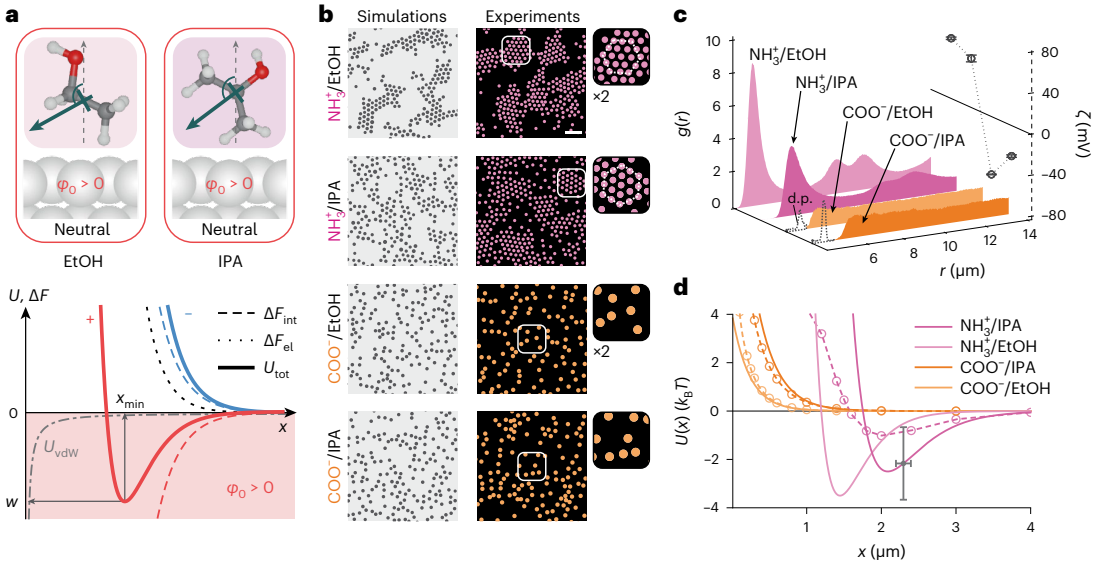


Fig. 5 | Negative self-attraction in water switches to positive self-attraction in alcohols. a, Top: MD simulations of ethanol and IPA at an uncharged surface show that these molecules orient on average with their methyl groups pointing slightly towards the interface and their electronegative oxygen atoms pointing towards the bulk, giving an interfacial potential $\varphi_0 > 0$. Unlike water, the average interfacial molecular dipole moment (green arrow) points towards the surface. Bottom: various contributions to the total interaction free energy for positive (red lines) and negative (blue lines) particles: electrostatic repulsion, ΔF_{el} (black dotted line; applies to both signs of charge); interfacial solvation contribution, ΔF_{int} (dashed line, different for positive and negative); total interaction energy, $U_{tot} = \Delta F_{el} + \Delta F_{int}$ (solid lines); and the vdW contribution, U_{vdW} (dashed-dotted grey line; applies to both cases). When $\varphi_0 > 0$, positively charged particles may display a minimum in U_{tot} at an interparticle separation x_{min} (solid red line), whereas negatively charged particles repel monotonically, displaying no minimum (solid blue line) (Supplementary Information, section 3.1). **b**, Right: experiments show that positively charged aminated silica particles (pink) form hcp clusters, whereas negatively charged carboxylated particles (orange) do not form clusters in alcohols. Scale bar, 20 μm. See Supplementary Fig. 25 for raw images. Left: BD simulations with appropriate input pair-interaction potentials recover the experimentally observed suspension structure. **c**, Measured radial probability density functions, $g(r)$, for positively charged particles (shades of pink) and negatively charged particles (shades of orange) in alcohols, including measured zeta potentials (circular symbols) for each case. Error bars denote ±s.d for three measurements. Experiments correspond to measured values of $c_0 \approx 0.4$ μM (see Supplementary Table 12 for details). **d**, Pair interaction potentials inferred for the experimental data from BD simulations (solid lines) for negative particles (orange) and positive particles (pink) (see Supplementary Fig. 24 and Supplementary Table 12 for details). Calculated $U_{tot}(x)$ curves as described in ref. 27 and Supplementary Information, sections 3.2 and 3.3 (dashed lines with symbols; see Supplementary Table 1 for parameter values). Error bars denote estimated uncertainties of ±100 nm in particle diameter and $\pm 1.5 k_B T$ in w (Supplementary Fig. 24).

solvation potential at zero surface charge that has a positive sign, that is, $\varphi_0 > 0$, which would suggest attraction between positive particles in our model. Attempts to experimentally probe the interfacial electrical potential have indeed suggested similar orientational behaviour and an inversion in sign of φ_0 for alcohols at interfaces compared to water[44–46]. Furthermore, the experimentally inferred $U(x)$ curves are qualitatively captured by calculations of $U_{tot}(x)$, as shown in Fig. 5d, yielding physically plausible model parameters (Supplementary Video 7, Supplementary Information, section 3.3 and Supplementary Table 1).

Interfacial solvation and biomolecular condensation

Finally, inspired by the spontaneous formation of tuneable clusters in like-charged microspheres in solution, we examine the implications of this long-ranged solvation force for the formation of reversible condensates at the molecular scale under physiological conditions, broadly encountered, for example, in the liquid–liquid phase-segregation problem in biology. We constructed a simple model of a protein as a sphere carrying surface-ionizable groups exposed to the solvent (Fig. 6a) and examined the pair-interaction energy, $u(x)$, of two spherical, charged molecules carrying five ionizable glutamic acid groups (pK = 4.5), immersed in an electrolyte containing monovalent salt at a concentration in the range c_0 = 10 mM–1 M in the pH range 5.5–8 (Fig. 6, Supplementary Fig. 10 and Supplementary Information, section 3.7). We analysed the sign and magnitude of the total interaction potential, $u^*_{tot}(x)$, given by Supplementary Information equation (5), at a nominal intersurface distance of x = 1 nm between the molecules.

We noted that the interparticle electrostatic repulsion, reflected in ΔF_{el}, is expected to be substantial over the range of pH and salt concentration considered since the molecules carry substantial net charge (of the same sign) (Fig. 6b). Interestingly, upon adding the interfacial contribution to the total free energy we found that the interaction could be expected to turn distinctly attractive (that is, $u^*_{tot} < 0$ relative to infinite separation), particularly at lower ionic strength and at pH values higher than the pK of the charged groups (Supplementary Fig. 10 and Supplementary Information, section 3.7). We then estimated the profile of a coexistence curve demarcating parts of the parameter space where phase separation may occur from regions where the molecules remain well dispersed. We found that the interfacial model suggests the counterintuitive formation of condensates of like-charged molecules at salt concentrations up to $c_0 \sim 0.5$ M and at pH values as high as ≈6.5 (Fig. 6c, right panel and Supplementary Information, section 3.7). Such behaviour has in fact been reported for proteins carrying net negative charge[42,47], for example, the negatively charged wild-type yeast protein Sup35 which carries a net excess of six acidic amino acids (aspartic and glutamic acids) over the number of basic side chains (lysine and arginine) in the domain that controls its phase-segregation response (Supplementary Fig. 10l)[47]. A DLVO-type model of the same interaction, however, would not capture the experimental trends reported for Sup35 (Fig. 6c, left panel and Supplementary Information, section 3.7).

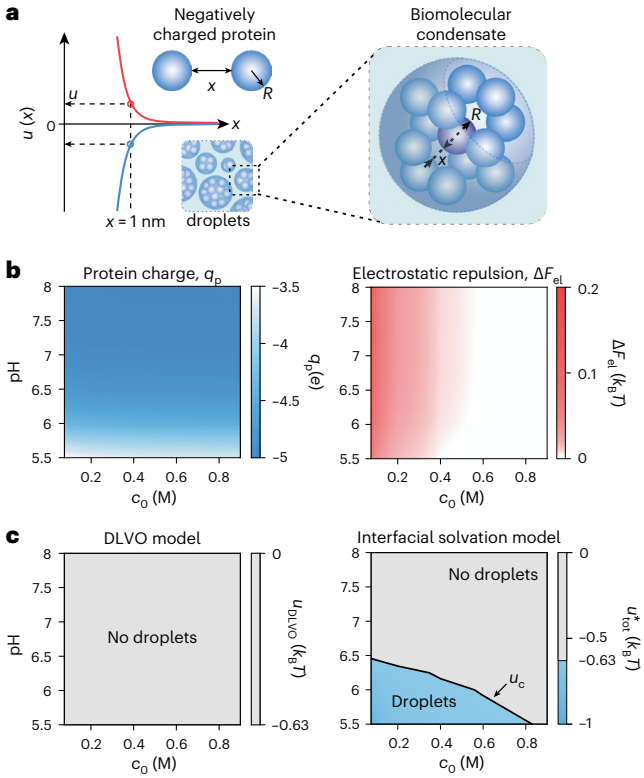


Fig. 6 | The charge-dependent solvation force can drive the formation of biomolecular condensates. a, Schematic representation of biomolecular condensate droplets formed from protein molecules depicted as spheres of radius $R = 2.5$ nm carrying a negative electrical charge equivalent to a net surplus of five glutamic acid groups. Blue and red lines present two possible, qualitatively different interaction potentials $u(x)$ (for example, $u_{DLVO}(x)$ or $u^*_{tot}(x)$) for a pair of interacting molecules where u is the value of interaction energy at an intersurface separation of $x = 1$ nm in either scenario. **b**, Left: the calculated molecular charge attains its maximum value of $q_p = -5e$ at pH > 6.5 and remains substantially negative over a broad range of pH values. Right: calculation of the electrostatic interaction energy ΔF_{el} ($x = 1$ nm) suggests a net repulsive interaction between two molecules for the relevant pH and c_0 range. **c**, Left: applying a pairwise interaction energy threshold for droplet formation of $u \lesssim u_c = -0.63 k_B T$ to the calculated value of $u_{DLVO} = \Delta F_{el} + u_{vdW}$ we obtain no indication of phase separation from a DLVO perspective. Right: inclusion of the solvation free-energy contribution in the interaction potential $u^*_{tot} = u_{DLVO} + \Delta F_{int}$ yields a coexistence curve (black line) which displays pH and salt concentration dependence of droplet formation similar to the experimental observations (see Supplementary Information, section 3.7 for details).

Conclusion

This study provides compelling evidence for a profoundly different view of interparticle and intermolecular interactions with general implications for self-assembly and clustering of matter in solution, relevant even, for example, to the origin of life[48]. The concerted action of electrical charge at an interface and the local interfacial solvation structure can give rise to an 'electrosolvation force' between objects in solution. As a rule of thumb, interparticle attraction between identical, nominally repulsive particles may be expected when the sign of the interfacial electrical potential, φ_0, in a particular solvent matches that of the sign of charge of the particle. The observations call for a re-evaluation of archetypal notions in biomolecular interactions, for example, that negatively charged poly-E stretches in proteins repel unequivocally in solution, which does not necessarily hold depending on the pH in solution (Fig. 2, middle panels). Like-charged molecules in solution may in fact experience a counterintuitive strong and long-ranged attraction, even under physiological conditions. These results have further ramifications for interactions in solvent mixtures, and in solutions containing additives such as zwitterions, osmolytes, polyols or other overall electrically neutral molecules that are not expected to strongly influence the electrostatic interaction per se[49]. Net-neutral molecular species in solution may alter the interfacial solvation structure due to the pure electrolyte and thus modify the total interaction between charged particles. The concept invoked here for longer-ranged interparticle and intermolecular interactions may well be found to hold for intramolecular interactions and conformational changes associated with nanometre-scale processes such as biomolecular folding. Finally, our findings provide evidence for the ability to probe the sign and magnitude of the interfacial electrical potential due to the solvent, previously believed to be immeasurable[44,45,50].

Online content

Any methods, additional references, Nature Portfolio reporting summaries, source data, extended data, supplementary information, acknowledgements, peer review information; details of author contributions and competing interests; and statements of data and code availability are available at https://doi.org/10.1038/s41565-024-01621-5.

References

1. Derjaguin, B. V. & Landau, L. Theory of the stability of strongly charged lyophobic sols and of the adhesion of strongly charged particles in solutions of electrolytes. *Acta Physicochim. (USSR)* **14**, 30–59 (1941).
2. Verwey, E. J. W. & Overbeek, J. T. G. *Theory of the Stability of Lyophobic Colloids* (Elsevier, 1948).
3. Trefalt, G., Palberg, T. & Borkovec, M. Forces between colloidal particles in aqueous solutions containing monovalent and multivalent ions. *Curr. Opin. Colloid Interface Sci.* **27**, 9–17 (2017).
4. Rau, D. C. & Parsegian, V. A. Direct measurement of the intermolecular forces between counterion-condensed DNA double helices. Evidence for long range attractive hydration forces. *Biophys. J.* **61**, 246–259 (1992).
5. Kjellander, R., Marcelja, S., Pashley, R. M. & Quirk, J. P. Double-layer ion correlation forces restrict calcium clay swelling. *J. Phys. Chem.* **92**, 6489–6492 (1988).
6. Levin, Y. Electrostatic correlations: from plasma to biology. *Rep. Prog. Phys.* **65**, 1577–1632 (2002).
7. Haro-Perez, C. et al. Dynamic arrest in charged colloidal systems exhibiting large-scale structural heterogeneities. *Phys. Rev. Lett.* **102**, 018301 (2009).
8. Krishnan, M., Moench, I. & Schwille, P. Spontaneous stretching of DNA in a two-dimensional nanoslit. *Nano Lett.* **7**, 1270–1275 (2007).
9. Klug, A., Franklin, R. E. & Humphreysowen, S. P. F. The crystal structure of tipula iridiscent virus as determined by Bragg reflection of visible light. *Biochim. Biophys. Acta* **32**, 203–219 (1959).
10. Kepler, G. M. & Fraden, S. Attractive potential between confined colloids at low ionic-strength. *Phys. Rev. Lett.* **73**, 356–359 (1994).
11. Grier, D. G. A surprisingly attractive couple. *Nature* **393**, 621–623 (1998).
12. Baksh, M. M., Jaros, M. & Groves, J. T. Detection of molecular interactions at membrane surfaces through colloid phase transitions. *Nature* **427**, 139–141 (2004).
13. Ito, K., Yoshida, H. & Ise, N. Void structure in colloidal dispersions. *Science* **263**, 66–68 (1994).
14. Matsuoka, H., Schwahn, D. & Ise, N. Observation of cluster formation in polyelectrolyte solutions by small-angle neutron scattering. 1. A steep upturn of the scattering curves from solutions of sodium poly(styrenesulfonate) at scattering vectors below 0.01 $Å^{-1}$. *Macromolecules* **24**, 4227–4228 (1991).

15. Larsen, A. E. & Grier, D. G. Like-charge attractions in metastable colloidal crystallites. *Nature* **385**, 230–233 (1997).
16. Musheev, M. U., Kanoatov, M., Retif, C. & Krylov, S. N. Stable DNA aggregation by removal of counterions. *Anal. Chem.* **85**, 10004–10007 (2013).
17. Tata, B. V. R., Mohanty, P. S. & Valsakumar, M. C. Bound pairs: direct evidence for long-range attraction between like-charged colloids. *Solid State Commun.* **147**, 360–365 (2008).
18. Langmuir, I. The role of attractive and repulsive forces in the formation of tactoids, thixotropic gels, protein crystals and coacervates. *J. Chem. Phys.* **6**, 873–896 (1938).
19. Sogami, I. & Ise, N. On the electrostatic interaction in macroionic solutions. *J. Chem. Phys.* **81**, 6320–6332 (1984).
20. vanRoij, R. & Hansen, J. P. Van der Waals-like instability in suspensions of mutually repelling charged colloids. *Phys. Rev. Lett.* **79**, 3082–3085 (1997).
21. Sader, J. E. & Chan, D. Y. C. Long-range electrostatic attractions between identically charged particles in confined geometries: an unresolved problem. *J. Colloid Interface Sci.* **213**, 268–269 (1999).
22. Ray, J. & Manning, G. S. Formation of loose clusters in polyelectrolyte solutions. *Macromolecules* **33**, 2901–2908 (2000).
23. Chremos, A. & Douglas, J. F. Communication: Counter-ion solvation and anomalous low-angle scattering in salt-free polyelectrolyte solutions. *J. Chem. Phys.* **147**, 241103 (2017).
24. Gonella, G. et al. Water at charged interfaces. *Nat. Rev. Chem.* **5**, 466–485 (2021).
25. Nagata, Y., Ohto, T., Backus, E. H. G. & Bonn, M. Molecular modeling of water interfaces: from molecular spectroscopy to thermodynamics. *J. Phys. Chem. B* **120**, 3785–3796 (2016).
26. Kung, W., González-Mozuelos, P. & De La Cruz, M. O. Nanoparticles in aqueous media: crystallization and solvation charge asymmetry. *Soft Matter* **6**, 331–341 (2010).
27. Kubincová, A., Hünenberger, P. H. & Krishnan, M. Interfacial solvation can explain attraction between like-charged objects in aqueous solution. *J. Chem. Phys.* **152**, 104713 (2020).
28. Behjatian, A., Walker-Gibbons, R., Schekochihin, A. A. & Krishnan, M. Nonmonotonic pair potentials in the interaction of like-charged objects in solution. *Langmuir* **38**, 786–800 (2022).
29. Walker-Gibbons, R., Kubincová, A., Hünenberger, P. H. & Krishnan, M. The role of surface chemistry in the orientational behavior of water at an interface. *J. Phys. Chem. B* **126**, 4697–4710 (2022).
30. Winter, E. M. & Groves, J. T. Surface binding affinity measurements from order transitions of lipid membrane-coated colloidal particles. *Anal. Chem.* **78**, 174–180 (2006).
31. Gomez, E. W., Clack, N. G., Wu, H. J. & Groves, J. T. Like-charge interactions between colloidal particles are asymmetric with respect to sign. *Soft Matter* **5**, 1931–1936 (2009).
32. Polin, M., Grier, D. G. & Han, Y. Colloidal electrostatic interactions near a conducting surface. *Phys. Rev. E* **76**, 041406 (2007).
33. Crocker, J. C. & Grier, D. G. When like charges attract: the effects of geometrical confinement on long-range colloidal interactions. *Phys. Rev. Lett.* **77**, 1897–1900 (1996).
34. Baumgartl, J. R., Arauz-Lara, J. L. & Bechinger, C. Like-charge attraction in confinement: myth or truth? *Soft Matter* **2**, 631 (2006).
35. Darlington, A. M. & Gibbs-Davis, J. M. Bimodal or trimodal? The influence of starting pH on site identity and distribution at the low salt aqueous/silica interface. *J. Phys. Chem. C.* **119**, 16560–16567 (2015).
36. Macias-Romero, C., Nahalka, I., Okur, H. I. & Roke, S. Optical imaging of surface chemistry and dynamics in confinement. *Science* **357**, 784–787 (2017).
37. Ninham, B. W. & Parsegian, V. A. Electrostatic potential between surfaces bearing ionizable groups in ionic equilibrium with physiologic saline solution. *J. Theor. Biol.* **31**, 405–428 (1971).
38. Dong, H. T., Du, H. B., Wickramasinghe, S. R. & Qian, X. H. The effects of chemical substitution and polymerization on the pK(a) values of sulfonic acids. *J. Phys. Chem. B* **113**, 14094–14101 (2009).
39. Decher, G. Fuzzy nanoassemblies: toward layered polymeric multicomposites. *Science* **277**, 1232–1237 (1997).
40. Polymenidou, M. The RNA face of phase separation. *Science* **360**, 859–860 (2018).
41. Wadsworth, G. M. et al. RNAs undergo phase transitions with lower critical solution temperatures. *Nat. Chem.* **15**, 1693–1704 (2023).
42. Parchure, A. et al. Liquid–liquid phase separation facilitates the biogenesis of secretory storage granules. *J. Cell Biol.* **221**, e202206132 (2022).
43. Reif, M. M. & Hünenberger, P. H. Origin of asymmetric solvation effects for ions in water and organic solvents investigated using molecular dynamics simulations: the Swain acity–basity scale revisited. *J. Phys. Chem. B* **120**, 8485–8517 (2016).
44. Paluch, M. Electrical properties of free surface of water and aqueous solutions. *Adv. Colloid Interface Sci.* **84**, 27–45 (2000).
45. Randles, J. E. B. Structure at the free surface of water and aqueous electrolyte solutions. *Phys. Chem. Liq.* **7**, 107–179 (1977).
46. Trasatti, S. Interfacial behaviour of non-aqueous solvents. *Electrochim. Acta* **32**, 843–850 (1987).
47. Franzmann, T. M. et al. Phase separation of a yeast prion protein promotes cellular fitness. *Science* **359**, 47–54 (2018).
48. Poudyal, R. R., Pir Cakmak, F., Keating, C. D. & Bevilacqua, P. C. Physical principles and extant biology reveal roles for RNA-containing membraneless compartments in origins of life chemistry. *Biochemistry* **57**, 2509–2519 (2018).
49. Govrin, R., Schlesinger, I., Tcherner, S. & Sivan, U. Regulation of surface charge by biological osmolytes. *J. Am. Chem. Soc.* **139**, 15013–15021 (2017).
50. Lyklema, J. H. Interfacial potentials: measuring the immeasurable? *Substantia* **1**, 75–93 (2017).

Publisher's note Springer Nature remains neutral with regard to jurisdictional claims in published maps and institutional affiliations.

Open Access This article is licensed under a Creative Commons Attribution 4.0 International License, which permits use, sharing, adaptation, distribution and reproduction in any medium or format, as long as you give appropriate credit to the original author(s) and the source, provide a link to the Creative Commons licence, and indicate if changes were made. The images or other third party material in this article are included in the article's Creative Commons licence, unless indicated otherwise in a credit line to the material. If material is not included in the article's Creative Commons licence and your intended use is not permitted by statutory regulation or exceeds the permitted use, you will need to obtain permission directly from the copyright holder. To view a copy of this licence, visit http://creativecommons.org/licenses/by/4.0/.

© The Author(s) 2024

Methods

Experimental methods

Preparation of particle suspensions for microscopy measurements. In our experiments we study the behaviour of three distinct types of microspheres with different surface chemistries. The three main classes of particle involve SiO_2 particles (Bangs Laboratories), amine-derivatized silica particles (NH_2–SiO_2, referred to as 'NH_2' or 'NH_3^+' in the text) (microParticles) with an estimated NH_2 group content of >30 μmol g^{-1}, and carboxylated melamine formaldehyde (COOH–MF, referred to as 'COOH' or 'COO^-' in the text) particles (microParticles) with a carboxyl group content of 400 μmol g^{-1}. The particle size distributions provided by the manufacturer are shown in Supplementary Fig. 1.

For experiments on SiO_2 and COOH particles in aqueous solution, particles were first rinsed (centrifuged and resuspended) in deionized water. Next, they were incubated in 5 mM NaOH (99.99%, Alfa Aesar) solution for 10 min. Following this, they were centrifuged and resuspended in aqueous electrolyte of the required ionic strength around six times until the measured electrical conductivity of the supernatant solution converged to that of the pure electrolyte. Note that in general NaOH treatment is not essential, and overnight exposure to deionized water with subsequent rinsing in deionized water is an equally effective treatment prior to clustering experiments (Supplementary Fig. 11). However, NaOH pretreatment was necessary to observe strong clustering in COOH particles.

NH_2–SiO_2 particles were first rinsed in deionized water and then resuspended multiple times in aqueous electrolyte solution until the measured supernatant conductivity converged to that of the pure electrolyte. The suspension was further sonicated for cases in which a large population of 'sticking' particles were observed. The presence of stuck particles in the experimental data gives rise to small 'dimer' peaks at interparticle separations $2R$ in the measured $g(r)$ which cannot be entirely eliminated (indicated as 'd.p.' in Figs. 2b, 3c and 5c). In experiments on mixtures of SiO_2 and COOH particles (Fig. 4), the two types of particles were initially mixed at a 1:1 ratio, then incubated in 10 mM NaOH solution for 10 min. Thereafter the procedures were the same as described above.

For experiments on colloidal dispersions in alcohols, NH_2–SiO_2 particles were first centrifuged and resuspended in deionized water, followed by resuspension in either ethanol (≥99.8%, Sigma-Aldrich) or IPA (≥99.5%, Sigma-Aldrich). The process of centrifugation and resuspension was repeated multiple times until the value of the supernatant conductivity converged to that measured for the pure alcohol. COOH particles were first centrifuged and resuspended in deionized water, followed by resuspension in ethanol, and final resuspension in either ethanol or IPA for measurements.

Preparation and characterization of electrolyte solutions. For experiments examining the dependence of interparticle interactions on the ionic strength of the electrolyte (Fig. 1), various concentrations of NaCl (99.998%, Alfa Aesar) solution were prepared in deionized water; the measured conductivity of these solutions corresponds to a background concentration of monovalent ions of $c_0 \approx 5$ μM. The ionic strength of the various electrolyte solutions in our experiments was determined from measurements of electrical conductivity, s, performed with a conductivity meter (inoLab Cond 7110). A calibration curve of standard solutions was used for this purpose (Supplementary Fig. 2).

To convert the measured electrical conductivity to a background salt concentration in alcohols, we used the same calibration relationship as for aqueous electrolytes as shown in Supplementary Fig. 2, but corrected the inferred concentrations for the viscosity of the alcohol as suggested in previous work[51] (the viscosity values used for ethanol and IPA were 1.1 cP and 2.4 cP, respectively, see Supplementary Information, section 1.2).

In experiments exploring the pH dependence of interparticle interactions (Fig. 2), the pH of the electrolyte was adjusted to the desired value by adding either HCl (99.999%, Alfa Aesar) or a Tris buffer (≥99.9%, Carl Roth), to deionised water. Addition of acid or buffering agent to deionized water raised the conductivity of the solution to a value between 1 and 30 μS cm^{-1} (0.01–0.25 mM) depending on the target pH value. For experiments performed at variable pH, ionic strength in the electrolyte was maintained constant (to within ±0.02 mM) across the entire range of pH in a given experimental series via the addition of a variable amount of NaCl. The pH value of the aqueous solution was taken as the mean value of three consecutive measurements using a pH meter (Horiba PH-33). The pH of pure alcohol samples was inferred by extrapolation of pH values measured for water–alcohol mixtures (Supplementary Fig. 2b).

Layer-by-layer coating of silica particles with polypeptides and polyelectrolytes. In the experiments presented in Fig. 3, we used alternating coatings of positively and negatively charged polyelectrolytes on plain SiO_2 particles. Coatings were applied in the following pairs of combinations of positively and negatively charged polyelectrolytes: poly-K (M_r, ≥300,000; Sigma) and poly-E (M_r, 50,000–100,000; Sigma); PDADMAC (M_r, 200,000–350,000; Aldrich) and PSS (M_r, ~70,000; Aldrich), and finally, PEI (M_r, ~750,000; Sigma) and PSS.

To coat the particles, plain SiO_2 particles were first centrifuged and resuspended in deionized water, followed by incubation in 5 mM NaOH solution for 10 min, resuspension in deionized water, and repetition of the resuspension process until the supernatant conductivity converged to that of deionized water. The rinsed particles were then incubated in the polyelectrolyte solution at 0.1% w/v for 20 min with occasional vortexing to improve mixing. The coated particles were centrifuged and resuspended in deionized water to remove any excess polymer and the resuspension procedure repeated until the conductivity of the supernatant no longer changed. Subsequent layers of polymer coatings were applied by repeating the coating procedure described above with the corresponding oppositely charged polyelectrolyte. The sign of the surface charge of each coating layer was confirmed by zeta-potential measurements (Zetasizer Nano Z, Malvern Panalytical).

Cuvette preparation and sample loading. We used a glass cuvette with a polished flat-well of 1 mm depth (20/C/G/1, Starna Scientific), as shown in Supplementary Fig. 3b, for all video microscopy measurements. The cuvette was cleaned with piranha solution (3:1 mixture of concentrated sulfuric acid and 30 wt% hydrogen peroxide solution) and then rinsed thoroughly with deionized water. A glass cuvette naturally provides a negatively charged surface in water, ethanol and IPA for experiments with negatively charged particles. For experiments with positively charged particles, the entire cuvette was coated with 1% w/v PEI solution, rinsed and dried under nitrogen to provide a thin layer of positively charged polymer coating. To load the cuvette, the prepared particle solution was carefully pipetted into the well and sealed with the cover slide such that the device was free of air bubbles and held together by capillary force.

Microscopy. The optical microscope was constructed using a 470 nm light-emitting diode (LED) (M470L4, ThorLabs), a 10× objective (Olympus UPlanSApo) and a charge-coupled device camera (DCU223M, ThorLabs) for recording images (Supplementary Fig. 3). The sample holder was placed onto a carefully balanced pitch and roll platform (AMA027, ThorLabs). Following complete settling of particles in suspension to a plane near the bottom surface of the cuvette, which typically takes about 2 min, the focus was adjusted such that a clear intensity maximum was observed for all particles. All measurements were performed after complete settling. The intensity of the LED was adjusted such that the intensity maxima of illuminated particles did not exceed the saturation value of the camera, enabling accurate particle localization.

Video recording and data processing. Sequential images of the 2D suspension of colloidal particles were taken with ThorCam software at a constant frame rate of 5, 10 or 30 frames per second for 150–500 frames using an exposure time of ≈ 0.5 ms. The images were processed based on the radial symmetry method using the TrackNTrace particle-tracking framework, where the particle centre maximum is detected[52,53]. The localization precision for a static SiO_2 particle during a 100 s measurement at an exposure time of ≈ 0.5 ms was found to be <20 nm, as shown in Supplementary Fig. 4. In the analysis of experimental images, coordinates of all particle centres were extracted from the recorded frames, and the radial distribution function curve $g(r)$ calculated and averaged over all images. To clearly distinguish between experiments on particles with different signs of particle charge in three different solvents, the recorded images were digitized and false-coloured (Supplemenetary Information, section 1.6 and Supplementary Fig. 3). The average particle detection efficiency over all experiments was >98%.

Simulation methods

BD simulations of interparticle interactions. We performed BD simulations of a 2D distribution of spheres interacting via an appropriately chosen input potential using the BROWNIAN package in the LAMMPS software[54]. We inferred the required pair-interaction potentials, $U(x)$, underpinning the experimental data by varying the input potential to the BD simulations. We thus generated simulated radial probability distribution functions, $g(r)$s, that matched the experimentally measurements. Validation and further discussion of the BD simulation set-up and approach are provided in Supplementary Information, section 2.1. Example input and necessary simulation files are provided in our Figshare repository, available at: https://doi.org/10.6084/m9.figshare.c.6132003.

We assumed a pairwise interaction potential $U(x)$ of the form: $U(x) = Ae^{-\kappa_1 x} + Be^{-\kappa_2 x} + U_{vdW}$. Here the first term represents the overall repulsive electrostatic free energy of interaction, $\Delta F_{el}(x) = A\ \exp(-\kappa_1 x)$, with $A > 0$ and the second term, $\Delta F_{int}(x) = B\ \exp(-\kappa_2 x)$, denotes the free-energy contribution arising from interfacial solvation[2]. Note that $\kappa_2 < \kappa_1 \approx \kappa$. The third term represents the vdW attraction between silica particles in solution, for which we have used the expression in ref. 55.

BD simulations were performed by taking into account the experimentally determined polydispersity in particle size as shown in Supplementary Fig. 1. This implies that at the simulation level a variable particle radius is taken into account to the lowest level of approximation (that is, the interaction potential remains fixed and independent of the size of the particles, which would not be true in practice). Using a value of the Hamaker constant $A_H = 2.4$ zJ we found that U_{vdW} made a small contribution (≈ $-0.5k_BT$) to the total interaction energy at large separations, $x \geq 0.2$ µm, that is, for the majority of experiments in this work[56,57]. However, for experiments at higher salt concentrations ($c_0 \approx 1$ mM; Fig. 1d), the vdW interaction can make a more substantial contribution (≈ $-1k_BT$) to the interaction at separations $x \approx 0.1$ µm, and for this reason it was included in our expression for $U(x)$ when modelling these measurements.

The experimentally measured $g(r)$ curve provides an estimate of the the location of the minimum in the pair potential x_{min}. In Supplementary Information equation (6), the screening length $\kappa_1^{-1} = \kappa^{-1}$, which is known from the measured salt concentration. We then use a trial value of the interaction free energy at the minimum, $U(x_{min}) = w < 0$, to obtain initial values for the parameters A and B as inputs for the pair-interaction potential, $U(x)$, using Supplementary Information equation (4), where we have taken $\kappa_2/\kappa_1 \approx 0.95$, as suggested in ref. 28. We note, however, that this ratio is not a strict requirement and that we may also treat it as a free parameter which yields an alternate set of parameters A, B, κ_1 and κ_2 that can provide equally good qualitative agreement with the experimental data (see, for example, Supplementary Table 5).

Particle configurations for the BD simulations were initialized via random particle placement in a 200 × 200 µm² simulation box that reproduced the experimental particle density (≈ 0.008 particles µm^{-2}). The polydispersity of the simulated colloids was drawn from the manufacturer's size distribution for each particle type, as shown in Supplementary Fig. 1. Periodic boundaries were applied in the x,y dimensions while the z dimension was held finite. The z coordinate of the colloids were fixed at a constant height throughout the simulation, ensuring a 2D system and thus mimicking the experiment. BD simulations were performed assuming that the interactions between the particles may be regarded as pairwise additive (discussed further in the main text and in Supplementary Information, section 3.4)

Convergence of the potential energy per particle in our BD simulations was monitored over time (Supplementary Fig. 5). Particle positions used for the calculation of the final simulated $g(r)$s were collected once the value of the potential energy reached a stationary value, after ≈ 30 min of simulation time in a run involving a strongly attractive $U(x)$ of a well depth of several k_BT (Supplementary Fig. 5). Agreement between the simulated and the experimental $g(r)$s was assessed for a trial input pair-interaction potential $U(x)$ and the value of the well depth w adjusted in subsequent BD simulations if required, to obtain a final simulated best match with the experimental data. This procedure permitted us to infer the functional form of an underlying pair-interaction potential $U(x)$ capable of capturing the experimentally measured $g(r)$.

Molecular dynamics simulations of alcohols at interfaces. The excess electrical potential due to the orientation of solvent molecules at an interface, φ_0 or φ_{int}, is required as an input to the interfacial solvation model to calculate theoretical $U_{tot}(x)$ curves (Supplementary Information, section 3.2). To estimate $\varphi_{int}(\sigma)$ as a function of surface electrical charge density, σ, we performed molecular dynamics (MD) simulations with the GROMACS MD code[58]. We examined the behaviour of a solvent phase in contact with a model surface composed of oxygen atoms in a parallel-plate capacitor set-up, as described extensively in previous work[27,29]. Example input files, force-field parameters and code for the analysis of the simulations performed in this study are available in our Figshare repository: https://doi.org/10.6084/m9.figshare.c.6132003.

Prior to running MD simulations in the capacitor set-up, we first ran preliminary simulations of a box of 7,500 IPA molecules, without the capacitor wall atoms, under constant pressure, maintained with the Parrinello–Rahman pressure-coupling method. The length of the box in z was allowed to fluctuate while keeping the x,y dimensions fixed to those of the capacitor walls of fixed area. This equilibrated slab of solvent was then sandwiched between capacitor plates comprised of positionally restrained oxygen atoms that only support Lennard–Jones interactions (Supplementary Fig. 7). In our simulations, IPA molecules were parametrized with the CHARMM36 force field[59]. As in previous work, the plates are ≈ 10×10 nm² in area and are separated by ≈ 8 nm of solvent medium in the z direction[27,29]. This ensures that any oscillations in the solvent density or dipole moment profiles attain bulk-like properties at a location z_{mid} in the middle of the capacitor. A subset of the atoms belonging to the first layer in each wall (in direct contact with the solvent) was randomly assigned a positive (left plate) or a negative charge (right plate) to generate an electric field of specific strength in the box while maintaining electroneutrality within the box. The capacitor system simultaneously yields estimates of $\varphi_{int}(\sigma)$ for both positive and negative values of σ and provides a well-defined system for comparing solvation at a macroscopic surface with a continuum electrostatics model.

Next, a second round of equilibration was carried out for the entire capacitor system, including the capacitor walls, and consisted of a short NVT run with a velocity-rescaling thermostat, followed by 500 ps in an NPT ensemble where only the z dimension of the box was allowed to fluctuate, keeping the the x,y dimensions fixed. This ensured that solvent molecules were maintained at the correct density throughout

the simulation box. Following this procedure, production MD runs of 20 ns duration were performed in an NVT ensemble with trajectory frames written every 20 ps. The particle mesh Ewald method was used to evaluate the long-range electrostatic interactions using a 1 Å grid spacing and a short-range cut-off of 12 Å. The Lennard–Jones interactions were smoothed over the range of 10–12 Å using the force-based switching function. We scaled the z dimension of the box by a factor 2 for Ewald summation only and applied the 3dc correction of Yeh and Berkowitz to remove artificial polarization induced by neighbouring image dipoles[60]. The orientation of solvent molecules as a function of distance from the walls was analysed to yield $\varphi_{int}(\sigma)$ values that were used in the calculation of the interfacial free energy term, ΔF_{int}, as previously described[27–29].

Data availability

Raw experimental data are available from our Figshare repository at: https://doi.org/10.6084/m9.figshare.c.6132003.

Code availability

Simulation files and code used to analyse the experimental and simulated data are available from our Figshare repository at: https://doi.org/10.6084/m9.figshare.c.6132003.

References

51. Kokot, G., Bespalova, M. I. & Krishnan, M. Measured electrical charge of SiO_2 in polar and nonpolar media. *J. Chem. Phys.* **145**, 194701 (2016).
52. Stein, S. C. & Thiart, J. TrackNTrace: a simple and extendable open-source framework for developing single-molecule localization and tracking algorithms. *Sci. Rep.* **6**, 37947 (2016).
53. Parthasarathy, R. Rapid, accurate particle tracking by calculation of radial symmetry centers. *Nat. Methods* **9**, 724–726 (2012).
54. Thompson, A. P. et al. LAMMPS—a flexible simulation tool for particle-based materials modeling at the atomic, meso, and continuum scales. *Comput. Phys. Commun.* **271**, 108171 (2022).
55. Hamaker, H. C. The London–van der Waals attraction between spherical particles. *Physica* **4**, 1058–1072 (1937).
56. Valmacco, V. et al. Dispersion forces acting between silica particles across water: influence of nanoscale roughness. *Nanoscale Horiz.* **1**, 325–330 (2016).
57. Ackler, H. D., French, R. H. & Chiang, Y.-M. Comparisons of Hamaker constants for ceramic systems with intervening vacuum or water: from force laws and physical properties. *J. Colloid Interface Sci.* **179**, 460–469 (1996).
58. Abraham, M. J. et al. GROMACS: high performance molecular simulations through multi-level parallelism from laptops to supercomputers. *SoftwareX* **1–2**, 19–25 (2015).
59. Vanommeslaeghe, K. et al. CHARMM general force field: a force field for drug-like molecules compatible with the CHARMM all-atom additive biological force fields. *J. Comput. Chem.* **31**, 671–690 (2009).
60. Yeh, I.-C. & Wallqvist, A. On the proper calculation of electrostatic interactions in solid-supported bilayer systems. *J. Chem. Phys.* **134**, 055109 (2011).
61. Yücel, H. & Okumuşoğlu, N. T. A new tracking algorithm for multiple colloidal particles close to contact. *J. Phys. Condens. Matter* **29**, 465101 (2017).

Acknowledgements

The authors thank P. Hünenberger, R. Netz, H. Frost, A. Baldwin and C. Robinson for stimulating discussions, and A. Lawrence for early contributions to experiments. Funding was provided by the European Research Council (ERC) under the European Union's Horizon 2020 research and innovation programme number 724180.

Author contributions

S.W. performed all experiments. R.W.-G. performed and analysed simulations. S.W. and R.W.-G. analysed the data and participated in manuscript preparation. B.W. and M.F. contributed to experiments. M.K. designed the research, performed theoretical modelling and wrote the manuscript.

Competing interests

The authors declare no competing interests.

Additional information

Extended data is available for this paper at https://doi.org/10.1038/s41565-024-01621-5.

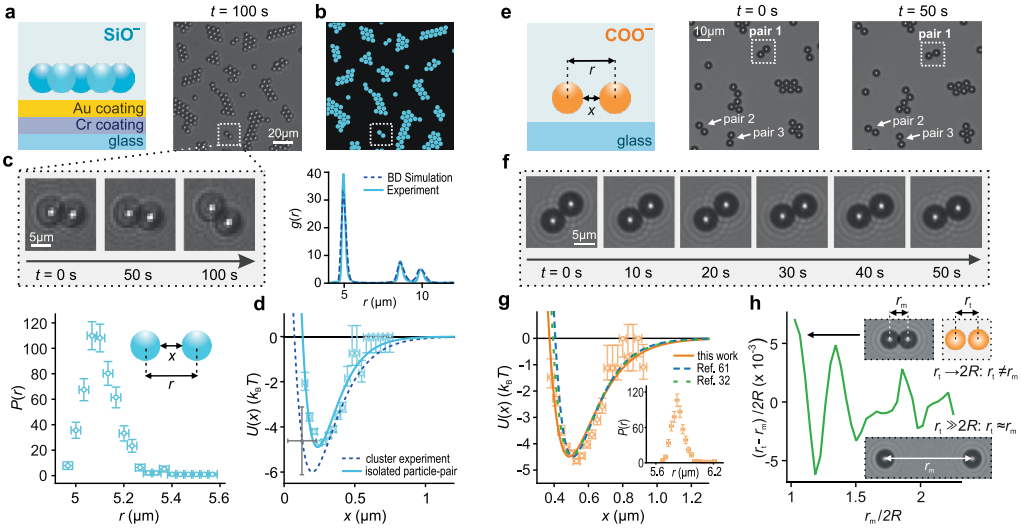
Supplementary information The online version contains supplementary material available at https://doi.org/10.1038/s41565-024-01621-5.

Correspondence and requests for materials should be addressed to Madhavi Krishnan.

Peer review information *Nature Nanotechnology* thanks the anonymous reviewer(s) for their contribution to the peer review of this work.

Reprints and permissions information is available at www.nature.com/reprints.

https://doi.org/10.1038/s41565-024-01621-5



Extended Data Fig. 1 | Direct measurement of pair-interaction potentials on isolated pairs of negatively charged particles in water. (**a**) Schematic representation of the experimental system displaying a cluster of SiO_2 particles of diameter $2R = 4.82$ μm in suspension above the underlying coverglass. The glass surface is coated with a 5 nm thick chrome (Cr) film followed by a 10 nm thick gold (Au) film in order to suppress any electrostatic contribution from the glass, similar to ref. 32 (left). Microscopy image of clusters of silica particles formed above the Au-coated surface, indicating an isolated pair of attracting particles (right). (**b**) Digitised image of clusters (top) accompanied by plot of measured and simulated $g(r)$ distributions (solid and dashed lines respectively) (bottom). Experiments that display particle clustering often contain isolated, strongly interacting 'bound pairs' of particles located several micrometres from other neighbouring particles (white box). (**c**) Time series of snapshots of an isolated pair of interacting particles acquired over a typical period of 100 s (top) and corresponding measured probability density distribution, $P(r)$, of the interparticle separation, r (bottom; see Supplementary Section 4.2). Error bars reflect a spatial localisation accuracy of ≈20 nm in r and a shot-noise error estimate on $P(r)$ (described in Supplementary Sections 1.6 and 4.2). (**d**) $U(x)$ profiles inferred from both types of measurement: isolated pair $P(r)$ measurement (symbols and solid fit line) and cluster-based $g(r)$ (dashed line) measurements (see Supplementary Section 4.2). The $U(x)$ data corresponding to the $P(r)$ measurements (blue symbols) are fit to Eq. S6 (Supplementary Fig. 14). The directly measured $U(x)$ profile for the isolated pair is in good agreement with that inferred from the cluster-formation experiment. (see Supplementary Fig. 14). Grey error bars denote an estimated uncertainty of $\pm 1.5\, k_B T$ in the overall process. The horizontal error bar captures the overall uncertainty in measured interparticle separation (arising from the particle size dispersion and localisation error, see Supplementary Section 1.6). (**e**) Schematic of a pair of COOH particles with centre-to-centre distance and intersurface separation denoted by r and x respectively (left). Experiments on a dilute suspension of particles (approximately factor 2 lower than for the cluster experiments) display a large number of isolated, strongly interacting 'bound pairs' of particles located several micrometres from other neighbouring particles as indicated (right). (**f**) Digital video microscopy snapshots of a single pair of interacting COOH particles of diameter $2R = 5.29$ μm over a period of 50 s. The particle images are characterised by a bright intense region at the centre, surrounded by a dark ring and associated diffraction pattern. (**g**) $P(r)$ plot of an interacting pair of particles (inset) determined using the TrackNTrace particle tracking code employing the radial symmetry method[52], that is the particle tracking method used in all experiments in this work. $U(x)$ data corresponding to measured $P(r)$ (symbols) accompanied by a fit curve (solid orange line). Error bars on $U(x)$ values for each of the measured points are derived from a shot-noise estimate (see Supplementary Section 4.2). The solid orange line may be compared with fits to $U(x)$ data obtained by applying two different corrections to the measured interparticle distances, r, according to ref. 61 (blue dashed line) and ref. 32 (green dashed line). All fits of $U(x)$ data are to the form of Eq. S6 and details are outlined in Supplementary Fig. 13. Good agreement between the various curves shows that particle-tracking correction methods have a negligible effect on the inferred well depth w and x_{min} values of the underlying pair interaction potential. (**h**) Plot of the expected difference r_t-r_m between the true and measured interparticle separation as a function of r_m, for our experimental system, using the method of ref. 32 (see Supplementary Section 4.3). The maximum error in the inferred interparticle distance r_t-$r_m = 37$ nm is comparable with the localisation accuracy and occurs at an interparticle separation corresponding to the distance of nearest approach $r_t = 2R$.

Supplementary Information

A charge-dependent long-ranged force drives tailored assembly of matter in solution

Sida Wang†[1], Rowan Walker-Gibbons†[1], Bethany Watkins[1], Melissa Flynn[1], & Madhavi Krishnan*[1,2]

† these authors contributed equally
[1]Physical and Theoretical Chemistry Laboratory, Department of Chemistry, University of Oxford, South Parks Road, Oxford OX1 3QZ, United Kingdom
[2]The Kavli Institute for Nanoscience Discovery, Sherrington Road, Oxford OX1 3QU, United Kingdom.
*correspondence to madhavi.krishnan@chem.ox.ac.uk

Table of Contents

S1 Supplementary experimental methods 6
S1.1 Preparation of particle suspensions for microscopy measurements 6
S1.2 Electrolyte solution preparation and measurements of solvent properties 7
S1.3 Layer-by-layer coating of silica particles with polypeptides and polyelectrolytes 9
S1.4 Cuvette preparation and sample loading 10
S1.5 Microscopy 10
S1.6 Video Recording and data processing 11
S2 Supplementary simulation methods 14
S2.1 Brownian Dynamics (BD) simulations of interparticle interactions 14
S2.2 Molecular Dynamics (MD) simulations of alcohols at interfaces 18
S3 Supplementary calculation methods 21
S3.1 A brief overview of the interfacial solvation model of interparticle interactions 21
S3.2 Summary of the approach to calculating the total interparticle interaction 25
S3.3 Discussion on parameter values used in the theoretical modelling of the experimentally inferred interaction potentials 29
S3.4 Considerations in comparing the results of pair-interaction-based theory and simulation procedures with an experiment involving an ensemble of interacting particles 33
S3.5 Analysing the pH response of particle cluster formation 35
S3.6 Cluster formation in mixtures of chemically dissimilar particles 40
S3.7 Protein pair-interaction modelling and calculation of a protein phase separation response as a function of pH and salt concentration 42
S4 Supplementary Results 50
S4.1 Interactions in silica particles in water without prior treatment with NaOH 50
S4.2 Direct measurements of interaction potentials for pairs of isolated particles 50
S4.3 Optical artifacts in particle tracking do not influence the measurements 52
S4.4 The long-range attraction is not influenced by surface charge on the neighbouring coverglass surface 54
S4.5 Ionic strength dependence of cluster formation for COOH particles in aqueous solution 55
S4.6 pH dependence of the interactions of PEI-coated silica particles 56
S4.7 Ionic-strength dependent swelling of positively charged polyelectrolyte coatings detected in $g(r)$ measurements 56
S5 Data Processing & Analysis 59
S5.1 Matching experimentally measured $g(r)$s with those from BD simulations 59
S5.2 Overview of all experimental snapshots and corresponding digitized images 66
S6 Supplementary Tables 72
References 78

List of Figures

Fig. S1. Probability distributions of particle diameter for each particle type studied in experiments. 6
Fig. S2. Calibration curves underlying salt concentration and pH measurements. 9
Fig. S3. Experimental set-up for measurements on 2-d colloidal dispersions. 11
Fig. S4. Spatial localization accuracy of a single immobilized SiO_2 particle..... 12
Fig. S5. Convergence of the potential energy per particle, PE/N, over the course of a BD simulation..... 16
Fig. S6. Influence of the particle polydispersity on the $g(r)$ inferred from a BD simulation..... 18
Fig. S7. MD simulations of isopropanol in a capacitor setup: calculation of $\varphi_{\mathrm{int}}(\sigma)$ for an alcohol at an interface. 20
Fig. S8. Schematic depiction of the qualitative average orientation of a solvent molecule at the solid-liquid interface. 28
Fig. S9. ζ potentials for SiO_2 and COOH particles 37
Fig. S10. Biomolecular condensate formation from protein molecules 47
Fig. S11. Interaction of silica particles in deionised water prepared without prior NaOH treatment. 50
Fig. S12. Direct measurement of pair-interaction potentials for COOH particles. 51
Fig. S13. Application of particle tracking corrections and their effect on the measured pair interaction potentials $U(x)$. 53
Fig. S14. Examining the effect of coating the underlying coverglass of the experimental cell with thin metal films. 54
Fig. S15. Ionic strength dependence of the interactions of COOH particles in aqueous electrolyte..... 56
Fig. S16. pH dependence of the interactions of PEI-coated silica particles in aqueous electrolyte at constant salt concentration 56
Fig. S17. Interactions of PDADMAC coated silica particles in electrolytes with different salt concentrations..... 58
Fig. S18. Matching of the experimental radial probability distribution functions $g(r)$s with those from BD simulations for experiments that vary the salt concentration c_0 for SiO_2 particles in water. 59
Fig. S19. Matching the experimental radial probability distribution functions with those from BD simulations for experiments varying the salt concentration for NH_2-SiO_2 particles in water. 60
Fig. S20. Matching the experimental radial probability distribution functions with those from BD simulations for experiments varying the pH for SiO_2 particles in water..... 61
Fig. S21. Matching the experimental radial probability distribution functions with those from BD simulations for experiments varying the pH for COOH particles in water ...62
Fig. S22. Matching the experimental radial probability distribution functions with those from BD simulations experiments varying the pH for NH_2-SiO_2 particles in water. 63

Fig. S23. Matching the experimental radial probability distribution functions with those from BD simulations for the polyelectrolyte coating experiments 64
Fig. S24. Matching the experimental radial probability distribution functions $g(r)$s with those from BD simulations for experiments in alcohols. 65
Fig. S25. Overview of all experimental snapshots and corresponding digitized images. 68
Fig. S26. Full-scale experimental snapshot of silica particles suspended in DI water. .. 69
Fig. S27. Full-scale experimental snapshot of carboxylated particles suspended in DI water. 70
Fig. S28. Full-scale experimental snapshot of aminated silica particles suspended in ethanol. 71

List of Tables

Table S1. Parameter values used in PB-interfacial solvation model calculations.....72
Table S2. BD simulation parameter values used to model experiments that examine the salt concentration dependence of cluster formation for SiO_2 particles in water 73
Table S3. BD simulation parameter values used to model experiments that examine the salt concentration dependence of interparticle interactions for NH_2-SiO_2 particles in water 73
Table S4. BD simulation parameter values used to model experiments that examine the pH dependence of cluster formation for SiO_2 particles in water 74
Table S5. Alternative set of parameters for the experiments varying pH for SiO_2 particles in water 74
Table S6. BD simulation parameter values used to model experiments that examine the pH dependence of cluster formation for COOH particles in water 75
Table S7. Alternative set of parameters for the experiments varying the pH for COOH particles in water 75
Table S8. BD simulation parameter values used to model experiments that examine the pH dependence of interparticle interactions for NH_2-SiO_2 particles in water 76
Table S9. BD simulation parameter values used to model experiments that examine the dependence of cluster formation on the charge of the polypeptide coating layer (poly-K/poly-E) displayed in Fig. 3c 76
Table S10. BD simulation parameter values used to model experiments that examine the dependence of cluster formation on the charge of the polyelectrolyte coating layer (PDADMAC/PSS) displayed in Fig. 3c.....76
Table S11. BD simulation parameter values used to model experiments that examine the dependence of cluster formation on the charge of the polyelectrolyte coating layer (PEI/PSS).....77
Table S12. BD simulation parameter values used to model experiments that examine the dependence of cluster formation on the sign of the charge of the particle in ethanol and isopropanol 77

S1 Supplementary experimental methods

S1.1 Preparation of particle suspensions for microscopy measurements

In our experiments we study the behaviour of three distinct types of microspheres with different surface chemistries. The 3 main classes of particle involve SiO_2 particles (Bangs Laboratories), amine derivatized silica particles (NH_2-SiO_2, referred to as "NH_2" or "NH_3^+" in the main manuscript) (microParticles GmbH) with an estimated NH_2 group content of >30 µmol/g, and carboxylated melamine formaldehyde (COOH-MF, referred to as "COOH" in the manuscript) particles (microParticles GmbH) with a carboxyl group content of 400 µmol/g. The particle size distributions provided by the manufacturer are shown in Fig. S1.

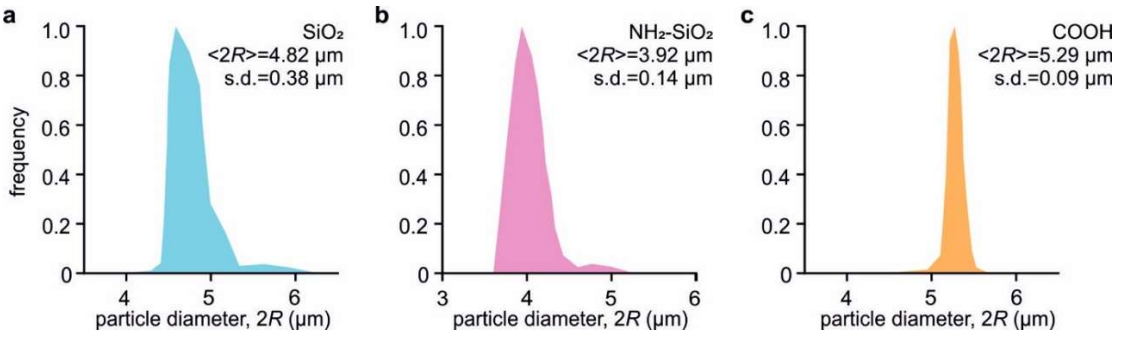


Fig. S1. Probability distributions of particle diameter for each particle type studied in experiments. (**a**) SiO_2, (**b**) NH_2-SiO_2 and (**c**) COOH particles. The distributions are taken from the manufacturer's measurements based on the Coulter principle. The mean and standard deviation (s.d.) of the particle diameter distributions are quoted in the inset. BD simulations of interparticle interactions (see Section S2.1) draw from these particle diameter distributions.

For experiments on SiO_2 and COOH particles in aqueous solution, particles were first centrifuged and resuspended in deionized water. Next, they were incubated in 5mM NaOH (99.99%, Alfa Aesar) solution for 10 minutes. Following this, they were centrifuged and resuspended in aqueous electrolyte of the required ionic strength around six times until the measured electrical conductivity of the supernatant solution converged to that of the pure electrolyte. Note that in general NaOH treatment is not essential and overnight exposure to DI water and rinsing in DI water are equally effective treatments prior to clustering experiments (see Fig. S11). However, NaOH pre-treatment was

necessary in order to observe strong clustering in COOH particles. This is likely because a basic solution favours deprotonation of weakly acidic groups.

NH_2-SiO_2 particles were first washed in deionized water and then resuspended multiple times in aqueous electrolyte solution until the measured supernatant conductivity converged to that of the pure electrolyte. The suspension was further sonicated for cases in which a large population of 'sticking' particles were observed. The presence of stuck particles in the experimental data gives rise to small "dimer" peaks at interparticle separations $2R$ in the measured $g(r)$ which cannot be entirely eliminated (indicated as 'd.p.' in Fig. 2b, Fig. 3c, Fig. 5c).

In experiments on mixtures of SiO_2 and COOH particles (Fig. 4), the two types of particles were initially mixed at a 1:1 ratio, then incubated in 10 mM NaOH solution for 10 minutes. Thereafter the procedures were the same as described above.

For experiments on colloidal dispersions in alcohols, NH_2-SiO_2 particles were first centrifuged and resuspended in deionized water, followed by resuspension in ethanol (≥99.8%, Sigma-Aldrich) or isopropanol (≥99.5%, Sigma-Aldrich). The process of centrifugation and resuspension was repeated multiple times until the value of the supernatant conductivity converged to that measured for the pure alcohol. COOH particles were first centrifuged and resuspended in deionized water, followed by resuspension in ethanol, and final resuspension in either ethanol or isopropanol for measurements.

S1.2 Electrolyte solution preparation and measurements of solvent properties

For experiments examining the dependence of interparticle interactions on the ionic strength of the electrolyte (Fig. 1), various concentrations of sodium chloride (NaCl, 99.998%, Alfa Aesar) solution were prepared in deionised water, whose measured conductivity corresponds to a background concentration of monovalent ions of $c_0 \approx 5\ \mu M$. The ionic strength of the various electrolyte solutions in our experiments was determined using measurements of electrical conductivity, s, performed using a conductivity meter (inoLab® Cond 7110). A calibration curve of standard solutions was

used for this purpose (Fig. S2). For water, we may estimate the theoretically expected slope, a, in the equation $c_0 = as$ using the expression $a = 4\pi\eta a_{\mathrm{h}}/e^2 N_A$ where $\eta = 0.89\,\mathrm{cP}$ is the viscosity of water at a temperature of 298 K, a_{h} is the average hydrodynamic radius of the ions in solution, e the elementary charge and N_{A} the Avogadro number[1]. Using ionic radii 1.01 Å and 1.82 Å for Na^+ and Cl^- ions given in Ref. 2, this expression yields a value of a =102.4 $\mathrm{kg\,mol\,A^{-2}\,s^{-3}}$, which is only about 30% larger than the experimentally measured value for water of 77.5 $\mathrm{kg\,mol\,A^{-2}\,s^{-3}}$as shown in Fig. S2a.

In order to convert the measured electrical conductivity to a background salt concentration in alcohols, we used the same calibration relationship as for aqueous electrolytes as shown in Fig. S2, but corrected the inferred concentrations for the viscosity of the alcohol as suggested in previous work[1] (viscosity values used for ethanol and isopropanol were 1.1 cP and 2.4 cP respectively). This procedure assumes that the hydrodynamic radii for the ionic species are identical in both water and alcohols, and it is possible therefore that our experimentally inferred salt concentration values in alcohols are not highly accurate.

In experiments exploring the pH dependence of interparticle interactions (Fig. 2), the pH of the electrolyte was adjusted to the desired value by adding either hydrochloric acid (HCl, 99.999%, Alfa Aesar) or a buffering agent tris(hydroxymethyl)aminomethane (TRIS, ≥99.9%, Carl Roth) to deionised water. Addition of acid or buffering agent to deionised water raised the conductivity of the solution to a value between 1 and 30 $\mu\mathrm{S/cm}$ (0.01 to 0.25 mM) depending on the target pH value. For experiments performed at variable pH, the ionic strength in the electrolyte was maintained constant (to within ±0.02 mM) across the entire range of pH in a given experimental series via the addition of a variable amount of NaCl. The pH value of the aqueous solution was taken as the mean value of three consecutive measurements using a pH meter (Horiba PH-33). The pH of pure alcohol samples was inferred by extrapolation of pH values measured for water-alcohol mixtures (Fig. S2b).

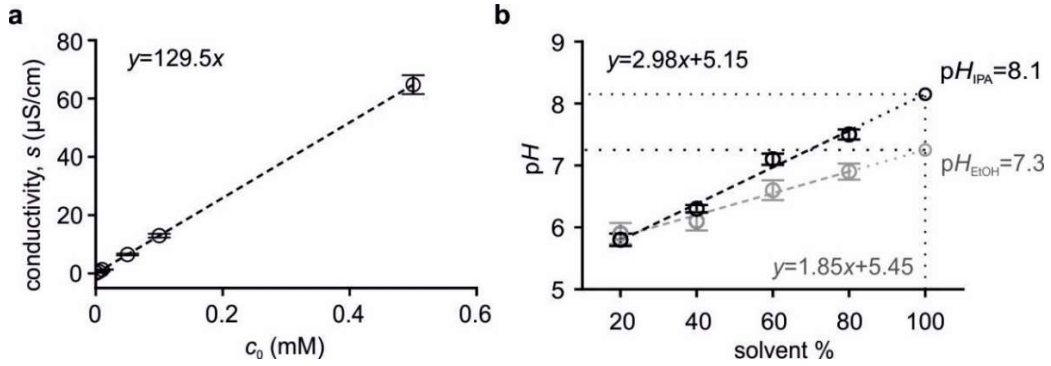


Fig. S2. Calibration curves underlying salt concentration and p*H* measurements. (**a**) Dependence of NaCl solution conductivities on salt concentrations of standard solutions. Data are presented as measured values ± 5% instrumental error. (**b**) Measurement of the p*H* of alcohol-water mixtures for ethanol (EtOH -grey) and isopropanol (IPA - black) mixtures. Data are presented as averaged values ± S.D. of three set of measurements.

S1.3 Layer-by-layer coating of silica particles with polypeptides and polyelectrolytes

In the experiments presented in Fig. 3, we used alternating coatings of positively and negatively charged polyelectrolytes on plain SiO_2 particles. Coatings were applied in the following pairs of combinations of positively and negatively charged polyelectrolytes: poly-L-lysine hydrobromide (poly-K, Molecular weight ≥300,000, Sigma) and poly-L-glutamic acid sodium salt (poly-E, mol. wt. 50,000-100,000, Sigma); poly(diallyldimethylammonium chloride) (PDADMAC, mol. wt. 200,000-350,000, Aldrich) and poly(sodium 4-styrenesulfonate) solution (PSS, mol. wt. ~70,000, Aldrich), and finally poly(ethyleneimine) solution (PEI, mol. wt. ~750,000, Sigma) and PSS.

In order to coat the particles, plain SiO_2 particles were first centrifuged and resuspended in deionised water, followed by incubation in 5 mM NaOH solution for 10 minutes, resuspension in deionised water, and repetition of the resuspension process until the supernatant conductivity converged to that of deionised water. The washed particles were then incubated in the polyelectrolyte solution at 0.1% w/v for 20 minutes with occasional vortexing to improve mixing. The coated particles were centrifuged and resuspended in deionised water to remove any excess polymer and the resuspension procedure repeated until the conductivity of the supernatant no longer changed. Subsequent layers of polymer coatings were applied by repeating the coating procedure

described above with the corresponding oppositely charged polyelectrolyte. The sign of the surface charge of each coating layer was confirmed by zeta potential measurements (Zetasizer Nano Z, Malvern Panalytical).

S1.4 Cuvette preparation and sample loading

We used a glass cuvette with a polished flat-well of 1 mm depth (20/C/G/1, Starna Scientific), as shown in Fig. S3b for all video microscopy measurements. The cuvette was cleaned with piranha solution (3:1 mixture of concentrated sulfuric acid and 30 wt. % hydrogen peroxide solution) and then rinsed with deionised water thoroughly. A glass cuvette naturally provides a negatively charged surface in water, ethanol and isopropanol for experiments with negatively charged particles. For experiments with positively charged particles, the entire cuvette was coated with 1% w/v PEI solution, rinsed and dried under N_2 to provide a thin layer of positively charged polymer coating.

To load the cuvette, the prepared particle solution was carefully pipetted into the well and sealed with the cover slide such that the device was air-bubble-free and held together by capillary force.

S1.5 Microscopy

The optical microscope was constructed using a 470 nm collimated LED light (M470L4, ThorLabs), a 10x objective (Olympus UPlanSApo) and a CCD camera (DCU223M, ThorLabs) for recording images (Fig. S3). The sample holder was placed onto a carefully balanced pitch, roll and tilt platform (AMA027, ThorLabs). Follwing complete settling of particles in suspension to a plane near the bottom surface of the cuvette, which takes about 2 mins typically, the focus was adjusted such that a clear intensity maximum was observed for all particles. All measurements were performed after complete settling. The LED light intensity was adjusted such that the intensity maxima of illuminated particles did not exceed the saturation value of the camera, enabling accurate particle localization. In general, in the experiments where particles form clusters, we initially note the formation of small clusters characterised by strong interparticle interactions. With the

passage of time (several tens of minutes), clusters could be found to grow in size, but the strength of the interparticle interactions may also alter as the pH and ionic strength of the solution can change.

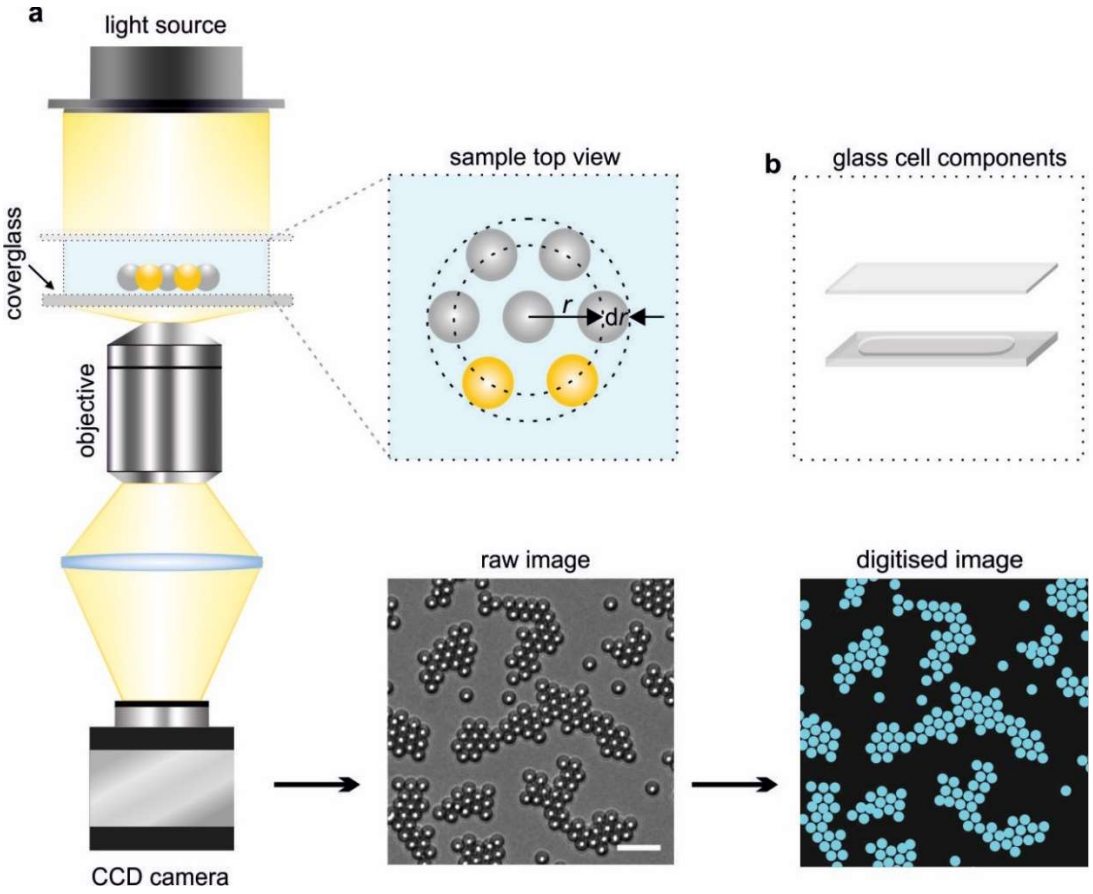


Fig. S3. Experimental set-up for measurements on 2-d colloidal dispersions. (**a**) Colloidal particles levitating above the coverglass surface are illuminated and imaged on to a CCD camera for a period of 30 seconds (scale bar: 20 μm. Particle coordinates are extracted using single particle tracking software (see Section S1.6). This information is used to generate probability density function, $g(r)$, profiles as well as digitised images. In the digitised microscopy images, particles are represented as coloured discs of uniform diameter $2R$ on a black background (see Section S1.6 and Fig. S25). (**b**) Diagram of the microscopy observation cell used in all experiments. The glass cell chamber has a depth of 1 mm and a nominal volume of 0.31 mL and the bottom coverglass surface is 1.25 mm thick.

S1.6 Video Recording and data processing

Sequential images of the two-dimensional suspension of colloidal particles were taken with ThorCam™ Software at a constant frame rate of 5, 10 or 30 frames per second (fps) for 150-500 frames using an exposure time of ≈0.5 ms The images were processed based on the radial symmetry method using the TrackNTrace particle tracking framework,

where the particle centre maximum is detected[3,4]. The localization precision for a static SiO_2 particle during a 100-second measurement at an exposure time of ≈0.5 ms was found to be less than 20 nm, as shown in Fig. S4. In the analysis of experimental images, coordinates of all particle centres were extracted from the recorded frames and the radial distribution function curve $g(r)$ is calculated and averaged over all images. This uncertainty in particle localization adds in quadrature with the uncertainty on the true mean diameter of the subset of the particles in any given experiment. We therefore estimate an overall uncertainty in measured separations in a given measurement at approximately ± 100 nm for silica particles.

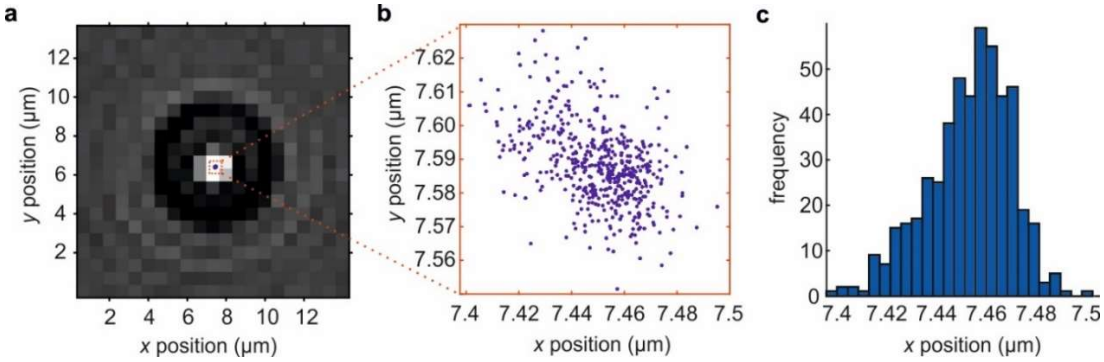


Fig. S4. Spatial localization accuracy of a single immobilized SiO_2 particle. (**a**) Optical microscopy snapshot of a single SiO_2 particle immobilized on the glass surface. (**b**) Scatter plot of particle location determined over 500 frames of imaging using TrackNTrace, with a standard deviation in the x and y dimensions of 16 nm and 12 nm, respectively. (**c**) Histogram of particle location in the x dimension.

Since the interparticle interaction is highly sensitive to pH and salt concentration, and we do not actively control these values in the observation cell, time evolution of the structure of the suspension may be expected. Thus $g(r)$s are calculated and averaged over a short duration at different time intervals (e.g. $t = 5$ mins, 10 mins and 20 mins). Within each time interval, the shape of the $g(r)$ stays relatively constant and is considered to be in steady state. Given the frame size (512 μm × 683 μm) and large number of particles (>2000 counts) available in each frame (see Fig. S26), it is enough to construct a $g(r)$ with as little as 10 consecutive frames for silica particles in DI water ($2R = 4.82$ μm, frame rate = 5 FPS). Additional number of frames do not alter the shape of the $g(r)$ but reduces the noise of the curve. However, we note that the contribution of particle polydispersity can largely affect the shape of the $g(r)$, thus we

may expect variation in the $g(r)$ from different batches of measurement under same experimental conditions (Fig. S6).

In order to clearly distinguish between experiments on particles with different signs of particle charge in three different solvents, the recorded images were digitized and false-coloured (Fig. S3). The digitization process involved extracting the coordinates of all particle centres. Each particle centre was then presented as a disc of diameter corresponding to the nominal particle diameter $2R$. Note that the particle samples have a size distribution (Fig. S1) which is not taken into account in the digitization process since the individual particle sizes are not known with high accuracy. This can occasionally result in overlapping of particles in the digitized images and videos which are provided for illustrative purposes only. Sporadic failure to detect particles in individual raw images can also cause the appearance of "blinking" particles in the digitized videos, which is not present in the raw data (Supplementary Video 1-7). This was found to occur in particular for COOH particles in water due to the lower refractive index of melamine resin compared to silica. The average particle detection efficiency over all experiments was greater than 98%.

S2 Supplementary simulation methods

S2.1 Brownian Dynamics (BD) simulations of interparticle interactions

In Figs. 1, 2, 3 and 5 we have presented forms of the underlying pair interaction potentials $U(x)$ that have been inferred from BD simulations to match the experimentally measured radial probability distribution functions, $g(r)$s. This section provides a description of procedures and further detail on BD simulations. From Table S2 to S12 we provide a comprehensive list of the $U(x)$ parameters used to match simulations to the experimental data. We also present graphs that overlay the experimental and simulated $g(r)$s for experiments shown in Fig. S18 - Fig. S24.

We performed BD simulations of a two-dimensional distribution of interacting spheres using the BROWNIAN package in the Large-scale Atomic/Molecular Massively Parallel Simulator (LAMMPS) software[5]. Example input and necessary simulation files are provided in our Figshare repository.

The relevant timescales for colloidal motion in our BD simulations include a diffusive timescale $\tau_{\text{diff}} \approx \langle \text{MSD} \rangle / 2D$ which is on the order of 1s. In this expression, $\langle \text{MSD} \rangle \approx (0.30 \times 10^{-6}\text{m})^2 \approx 1 \times 10^{-13}\,\text{m}^2$ denotes a typical mean squared displacement in x for a random walker exploring the spatial range of a representative pair interaction potential $U(x)$ in this study, and D ($\approx 1 \times 10^{-13}\,\text{m}^2\text{s}^{-1}$) is the diffusion coefficient in water of a particle of diameter $2R = 4.82\,\mu\text{m}$. Expanding the displacement $\Delta x = x - x_{\text{min}}$ to the lowest order around the potential minimum, x_{min}, we have $U(\Delta x) \approx k\Delta x^2$, which permits us to deduce a viscous relaxation time $\tau_{\text{r}} = \frac{\gamma}{k} \approx 0.01\,\text{s} - 0.1\,\text{s}$. Here, $\gamma = 6\pi\eta R$ denotes the Stokes drag on the particle, where η is the viscosity of the solvent and k denotes a stiffness parameter characterizing the pair interaction potential well. We further have the momentum relaxation time $\tau_{\text{p}} = \frac{m}{\gamma} = 2.5\,\mu\text{s}$ for $4.82\,\mu\text{m}$ diameter silica particles which shows that $\tau_{\text{p}} \ll \tau_{\text{r}}$, placing the problem in the overdamped Langevin or Brownian Dynamics regime.

The overdamped Langevin equation of motion for each colloid can be written as:

$$-\nabla U(x) - \gamma\dot{\vec{x}} + \vec{f}(t) \;=\; 0 \qquad \text{S 1}$$

In this equation, $\vec{f}(t)$ is the random thermal force acting on the particle which has a Gaussian probability distribution with zero mean, $\langle \vec{f}(t) \rangle = 0$, and correlation function $\langle \vec{f}_i(t)\vec{f}_j(t')\rangle = 2\gamma k_{\mathrm{B}}T\delta_{i,j}\delta(t-t')$. The above equation can be integrated in time to obtain particle displacements and trajectories as a function of time. The simulation timestep ($\approx 2.5 \times 10^{-5}\mathrm{s}$) in the integration was chosen to be much smaller than τ_{r}.

In Eq. S 1, $U(x)$ is the total pairwise interaction potential between the colloids, which we assume to be of the form:

$$U(x) \;=\; Ae^{-\kappa_1 x} \;+\; Be^{-\kappa_2 x} \;+\; U_{\mathrm{vdW}} \qquad \text{S 2}$$

Here the first term represents the overall repulsive electrostatic free energy of interaction, $\Delta F_{\mathrm{el}}(x) \;=\; A\exp(-\kappa_1 x)$, with $A \;>\; 0$, and the second term, $\Delta F_{\mathrm{int}}(x) = B\exp(-\kappa_2 x)$, denotes the free energy contribution arising from interfacial solvation[2]. Note that $\kappa_2 < \kappa_1 \approx \kappa$. Importantly the $\Delta F_{\mathrm{int}}(x)$ term implies an attractive contribution to the total free energy for negatively charged particles[6,7]. The third term represents the van der Waals (vdW) attraction between silica particles in solution, for which we have used the expression derived in Ref. 8:

$$U_{\mathrm{vdW}} \;= -\frac{A_{\mathrm{H}}}{12}\left\{\frac{y}{x'^2 + x'y + x'} + \frac{y}{x'^2 + x'y + x' + y} + 2\ln\frac{x'^2 + x'y + x'}{x'^2 + x'y + x' + y}\right\} \qquad \text{S 3}$$

In the above equation, $x' = \frac{x}{2R_1}$ and $y = \frac{R_2}{R_1}$, where R_1 and R_2 are the radii of the corresponding particles. BD simulations were performed on taking into account the experimentally determined polydispersity in particle sizes as shown in Fig. S1. This implies that at simulation level, variable particle radius is taken into account to the lowest level of approximation (i.e., the interaction potential remains fixed and independent of the size of the particles which would not be true in practice). Using a value of the Hamaker constant A_{H} =2.4 zJ (taken from Ref. 9 and which is in agreement with other literature estimates[10]), we found that U_{vdW} made a small contribution ($< -0.5\, k_{\mathrm{B}}T$) to the total interaction energy at large separations, $x \geq 0.2\ \mu\mathrm{m}$, i.e., for the majority of experiments in this work. We emphasize therefore that the vdW interaction cannot be responsible for the strong and long-ranged minima implied by the clusters

observed in experiment. However, for experiments at higher salt concentrations ($c_0 \approx$ 1mM, see Fig. 1d), the vdW interaction can make a more significant contribution ($\approx -1\ k_B T$) to the interaction at separations $x \approx 0.1\ \mu m$, and for this reason it was included in our expression for $U(x)$ in modelling these measurements.

The experimentally measured $g(r)$ curve provides an estimate of the location of the minimum in the pair potential x_{min}. In Eq. S 2, the screening length in solution $\kappa_1^{-1} = \kappa^{-1}$(the Debye length), is known from the measured salt concentration. We then use a trial value of the interaction free energy at the minimum, $U(x_{min}) = w < 0$, to obtain initial values for the parameters A and B as inputs for the pair interaction potential $U(x)$, using the equations:

$$A = -\frac{w\kappa_2 \exp(\kappa_1 x_{min})}{\kappa_1 - \kappa_2}\ ; B = \frac{w\kappa_1 \exp(\kappa_2 x_{min})}{\kappa_1 - \kappa_2} \qquad \text{S 4}$$

where we have taken $\kappa_2/\kappa_1 \approx 0.95$, as suggested in Ref. 7. We note however that this ratio is not a strict requirement and that we may also treat it as a free parameter which yields an alternate set of parameters A, B , κ_1 and κ_2 that can provide equally good qualitative agreement with the experimental data (see e.g. Table S5).

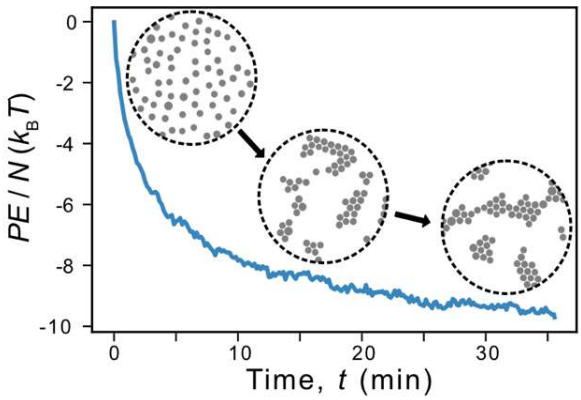


Fig. S5. Convergence of the potential energy per particle, *PE/N*, over the course of a BD simulation. The simulation box measures $200 \times 200\ \mu m^2$ and contains a number of particles, $N \approx 300$, which corresponds to a particle density typical for experiments. The initial configuration of colloids at $t = 0$ involves large average interparticle distances ($x > 1\ \mu m$) so that $PE/N = 0$. In the above case the system is permitted to evolve under the influence of an attractive pair potential $U(x)$ (A =32580, $B = -25848$, κ_1 =13.16, κ_2 =12.5), which has a minimum of $w = -6\ k_B T$ at $x_{min} = 0.43\ \mu m$. The system exhibits the formation of strong, stable and slowly reorganizing clusters within a period of a few minutes, with clusters growing in size over time. In this case, the asymptotic value of $PE/N \approx -10\ k_B T$, which corresponds to an average number of nearest neighbours of ≈ 3.5, as is evident from the cluster configuration at large t. Evolution of the initial configuration of particles (left inset) over time shows the formation of particle clusters

(right inset). Final, converged particle configurations are used to generate $g(r)$ distributions for comparison with experiments.

The BD simulation set-up was validated by comparing the Stokes-Einstein value of the particle diffusion coefficient, $D = k_B T/6\pi\eta R$, with that inferred from a mean squared displacement (MSD) analysis for simulated motion of a single colloid diffusing in 2 dimensions. We also ensured that the pairwise interaction potential $U(x)$ input into a simulation of two interacting particles could be recovered via Boltzmann inversion of the probability distribution of interparticle distances using the procedure described in Section S4.2.

Particle configurations for the BD simulations were initialized via random particle placement in a $200 \times 200\ \mu m^2$ simulation box that reproduced the experimental particle density (≈ 0.008 particles/μm^2). The polydispersity of the simulated colloids was drawn from the manufacturer's size distribution for each particle type, as shown in Fig. S1. Periodic boundaries were applied in the x, y dimensions whilst the z dimension was held finite. The z coordinate of the colloids were fixed at a constant height throughout the simulation, ensuring a 2D system, mimicking experiment. Convergence of the potential energy (PE) per particle in our BD simulations was monitored over time (Fig. S5). Particle positions used for the calculation of the final simulated $g(r)$s were collected once the value of the potential energy reached a stationary value, after approximately 30 minutes of simulation time in a simulation involving a strongly attractive $U(x)$ of a well depth of several $k_B T$ (Fig. S5).

Agreement between the simulated and the experimental $g(r)$s was assessed for a trial input pair interaction potential $U(x)$ and the value of the well depth w adjusted in subsequent BD simulations if required, in order to attain a final simulated best match to the experimental data. This procedure permitted us to infer the functional form of an underlying pair interaction potential $U(x)$. These BD simulations assume the interactions between the particles may be regarded as pairwise additive. As discussed in the main text and Section S3.4, a pair potential inferred from BD is not expected to accurately reflect the true pair potential of the system particularly in the light of factors

such as particle polydispersity which exert substantial influence on the extracted $g(r)$ profile (Fig. S6). In fact given the enormous variability in particle properties, a true pair potential may in fact constitute an idealisation that cannot be probed in practice.

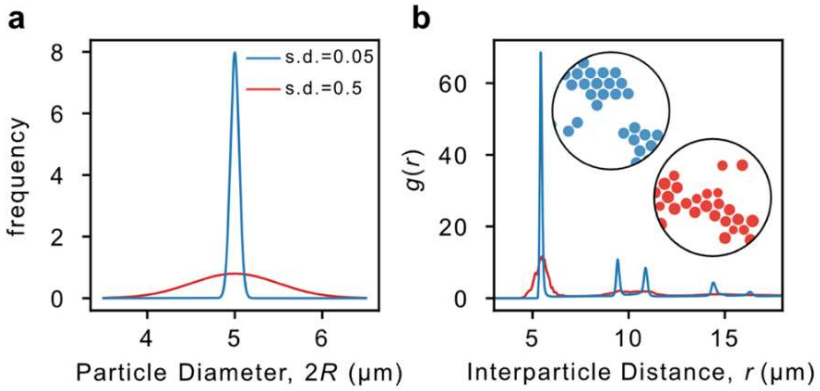


Fig. S6. Influence of the particle polydispersity on the $g(r)$ inferred from a BD simulation. (**a**) Two normally distributed particle size distributions with mean 5 μm and standard deviations of $\mathrm{s.d.} = 0.05$ and 0.5 (blue and red curves respectively). Particle radii drawn from these size distributions were fed into independent BD simulations and allowed to evolve under the influence the same attractive pair potential $U(x)$ (A =27150, $B = -21540$, κ_1 =13.2, κ_2 =12.5), which has a minimum of $w = -5\ k_B T$ at $x_{\min} = 0.43$ μm. (**b**) $g(r)$s determined from BD simulations of the two particle size distributions in (a), clearly showing a high sensitivity of the $g(r)$ to the particle polydispersity. The $g(r)$ corresponding to the narrow size distribution ($\sigma = 0.05$, shown in blue) is characterised by tall, sharp peaks. The majority of clusters formed are arranged in a perfect hexagonal pattern (blue particles, shown inset). The $g(r)$ corresponding to the larger size distribution ($\sigma = 0.5$, shown in red) on the other hand, is characterized by broad, noisy peaks of much smaller height. In simulations of particles with a broader size distribution the clusters display less crystalline order (red particles, shown inset). Our experimental data also clearly demonstrates the role of particle polydispersity, with COOH particles (which have a narrow particle size distribution, see Fig. S1) displaying tall, sharp peaks in the experimental $g(r)$s (see Fig. S21), in contrast to SiO_2 particles which have a broader size distribution and broader $g(r)$ peaks (see Fig. S20).

S2.2 Molecular Dynamics (MD) simulations of alcohols at interfaces

The excess electrical potential due to the orientation of solvent molecules at an interface, φ_{int} is required as an input to interfacial solvation model in order to calculate theoretical $U(x)$ curves (see Section S3.2). In order to estimate $\varphi_{\mathrm{int}}(\sigma)$ as a function of surface electrical charge, σ, we performed molecular dynamics (MD) simulations with the GROMACS MD code[11]. We examined the behaviour of a solvent phase in contact with a model surface composed of oxygen atoms in a parallel plate capacitor setup, as described extensively in previous work[6,12]. Example input files, force field parameters and

code for the analysis of the simulations performed in this study are available in our Figshare repository: https://doi.org/10.6084/m9.figshare.c.6132003.

Prior to running MD simulations in the capacitor setup, we first ran preliminary simulations of a box of 7500 isopropanol molecules, without the capacitor wall atoms, under constant pressure, maintained with the Parrinello-Rahman pressure coupling method. The length of the box in z was allowed to fluctuate, whilst keeping the x, y dimensions fixed to those of the capacitor walls of fixed area. This equilibrated slab of solvent was then sandwiched between capacitor plates comprised of positionally restrained oxygen atoms that only support Lennard-Jones interactions (see Fig. S7). In our simulations, isopropanol and ethanol molecules were both parametrized with the CHARMM36 forcefield[13]. As in previous work, the plates are $\approx 10 \times 10$ nm^2 in area and are separated by approximately 8 nm of solvent medium in the z-direction[6,12]. This ensures that any oscillations in the solvent density or dipole moment profiles attain bulk-like properties at a location z_{mid} in the middle of the capacitor. A subset of the atoms belonging to the first layer in each wall (in direct contact with the solvent) were randomly assigned a positive (left plate) or a negative charge (right plate) in order to generate an electric field of specific strength in the box whilst maintaining electroneutrality within the box. The capacitor system simultaneously yields estimates of $\varphi_{\mathrm{int}}(\sigma)$ for both positive and negative values of σ and provides a well-defined system for comparing solvation at a macroscopic surface with a continuum electrostatics model.

Next, a second round of equilibration was carried out for the entire capacitor system, including the capacitor walls, and consisted of a short NVT run with a v-rescale thermostat, followed by 500 ps in an NPT ensemble where only the z-dimension of the box was allowed to fluctuate, keeping the the x, y dimensions fixed. This ensured that solvent molecules were maintained at the correct density throughout the simulation box. Following this procedure, production MD runs of 20ns duration were performed in an NVT ensemble, with trajectory frames written every 20 ps. The particle mesh Ewald (PME) method was used to evaluate the long-range electrostatic interactions using a 1 Å grid spacing and a short-range cut-off of 12 Å. The Lennard-Jones interactions were

smoothed over the range of $10 - 12$ Å using the force-based switching function. We scaled the z-dimension of the box by a factor 2 for Ewald summation only and applied the 3dc correction of Yeh and Berkowitz to remove artificial polarization induced by neighbouring image dipoles[14].

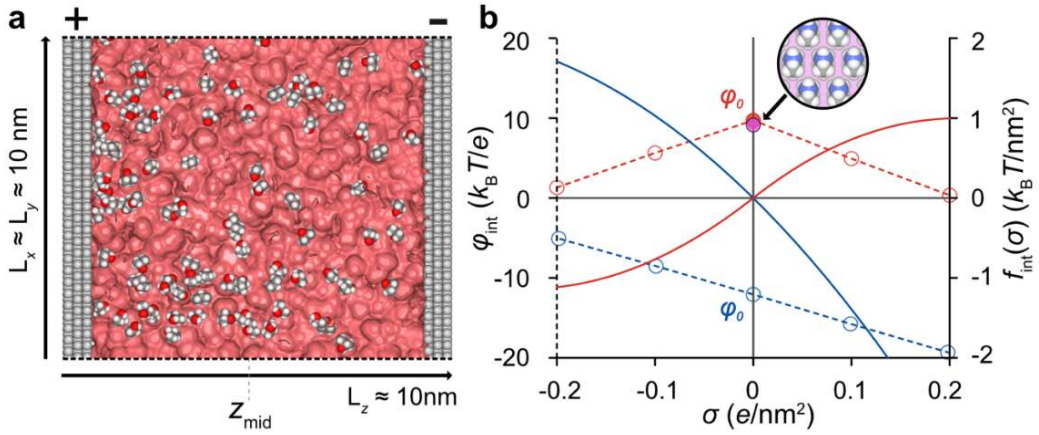


Fig. S7. MD simulations of isopropanol in a capacitor setup: calculation of $\varphi_{int}(\sigma)$ for an alcohol at an interface (**a**) Schematic representation of a simulation cell corresponding to the "capacitor system" used to calculate the excess interfacial potential $\varphi_{int}(\sigma)$ that arises due to symmetry broken orientational behaviour of solvent molecules at an interface. Solvent molecules are confined between two plates of dimensions $\approx 10 \times 10$ nm^2, each made up of three layers of hexagonally packed, positionally restrained oxygen atoms, separated by ≈ 8 nm along the z-direction. A subset of the interfacial wall atoms on the left and right plates are randomly assigned integer charge of $+1e$ (left plate) and $-1e$ (right plate) in order to generate an overall charge density of $\pm\sigma$ on the respective plates. (**b**) The excess interfacial potential $\varphi_{int}(\sigma)$ (left axis, dashed lines and circle markers) and the corresponding excess free energy of interfacial solvation $f_{int}(\sigma)$ (right axis, solid curves) for isopropanol and water for comparison (shown in red and blue respectively). The reorientation of IPA molecules at an O-atom surface that increases in charge density causes φ_{int} to decrease in magnitude, go through zero, and turn increasingly negative. Note that surface chemistry can have a substantial impact on the behaviour of the solvation potential (φ_{int}) in organic solvents[12]. That said, the value of φ_0 for isopropanol molecules in contact with a surface patterned with amine groups (circle inset) is also shown (pink data point), confirming that the sign and magnitude of φ_0 for a more realistic model surface remain unchanged from the O-atom-surface value.

S3 Supplementary calculation methods

S3.1 A brief overview of the interfacial solvation model of interparticle interactions

Our present understanding of the physical mechanism underpinning the proposed interaction is founded in the fact that a solvent molecule at an interface, e.g., that between a charged particle and the fluid, displays orientational behaviour that is different from its counterpart in the bulk. Like dipoles in the bulk fluid, the net orientation of interfacial solvent molecules depends on the local electrical field, but unlike molecules in the bulk, the average orientation of interfacial molecules has additional character due to the broken symmetry created by an interface. This orientational behaviour induced by the interface is associated with an 'excess' contribution to the free energy that is not included in continuum descriptions of electrostatic interactions on which the DLVO theory is based. The assumption that the solvent may be treated as a dielectric continuum does not admit a molecular-level description of the medium and cannot therefore predict any free energy contribution arising from orientational behaviour of interfacial solvent molecules. Furthermore, simulation studies that seek to account for finite ion size and other experimental aspects in greater detail, and yet work with a 'primitive model' of the solvent, which treats water as a smooth continuum, would not be expected to capture our experimentally observed long-ranged attraction between like-charged particles. Our working model of the interfacially induced interaction - described in Refs. 6,7- thus goes beyond PB theory to explain the experimental observations and will be outlined in this section.

When two like-charged particles approach each other in a fluid their net charge decreases via a process called 'charge regulation', minimising the free energy of the system[15]. Nonetheless, the interparticle interaction remains net repulsive. The reduction in particle charge however entails an 'excess' orientational free energy contribution from interfacial solvent molecules. Our current working model of the overall interaction assumes that this excess, interfacial contribution to the free energy superimposes on the

traditional electrostatic free energy. The result is a pair interaction potential that can depart strongly from the continuum expectation, turning attractive or repulsive at long range depending on the experimental conditions.

Notably, although our proposed interfacial free energy arises from solvent molecules located within about 0.5-1 nm from an interface, it can in fact make substantial contributions to the total free energy at large interparticle separations. This is because charge regulation – the underlying phenomenon which triggers the free energy contribution – is long ranged. We emphasize that at present our proposed mechanism does not invoke long-range correlations in or ordering of solvent molecules in the bulk electrolyte[16]. Furthermore, at small distances from the interface, both interfacial spectroscopy measurements and molecular simulations on neat water are in unequivocal agreement concerning surface charge dependent molecular orientation[17-20]. We point out that the interaction mechanism we propose shares some features with, but is substantially different from the well-established *short-range* "hydration force" which manifests at very small separations, typically < 3 nm, between surfaces[21].

We now summarise the main ingredients of an effective model of interparticle interactions in solution. We write the total interparticle interaction potential between two particles in solution as the sum of the van der Waals (vdW) contribution, U_{vdW}, the mean field electrostatic contribution, ΔF_{el}, and an interfacial free energy contribution, ΔF_{int}, as follows

$$U^{*}_{\mathrm{tot}}(x) = U_{\mathrm{vdW}}(x) + \Delta F_{\mathrm{el}}(x) + \Delta F_{\mathrm{int}}(x) = U_{\mathrm{DLVO}}(x) + \Delta F_{\mathrm{int}}(x) \qquad \text{S 5}$$

In Eq. S 5, $U_{\mathrm{DLVO}} = U_{\mathrm{vdW}} + \Delta F_{\mathrm{el}}$ represents the total interparticle interaction potential as postulated in the DLVO theory. For large spheres at large distances from each other (say $\kappa x > 2$), $U_{\mathrm{vdW}}(x)$ may be ignored and the interaction potential may be written as

$$U_{\mathrm{tot}}(x) = \Delta F_{\mathrm{el}}(x) + \Delta F_{\mathrm{int}}(x) \approx A\exp(-\kappa_1 x) + B\exp(-\kappa_2 x) \qquad \text{S 6}$$

here A and B can be treated as constants, $\kappa^{-1} \approx \frac{0.304}{\sqrt{c_0}}$ nm is the Debye length in an aqueous electrolyte containing monovalent salt at a concentration of c_0 moles/litre, and represents the length scale on which electrostatic interactions are screened by counterions in solution[7]. Furthermore, $\kappa_1 \approx \kappa$ is the effective inverse decay length of the electrostatic free energy (ΔF_{el}) term, and we have $\kappa_1 > \kappa_2 \approx 0.95\,\kappa_1$[7]. Note that the condition $\kappa_1 > \kappa_2$ plays a key role in the appearance of a minimum and, within our model, arises from examining the spatial dependence of the calculated interfacial free energy term, $\Delta F_{\mathrm{int}}(x)$. However, further details of the microscopic physical origin of this additional effective screening length κ_2^{-1} and the relationship $\kappa_1 > \kappa_2$ may be further explored in future work. The interfacial solvation model[7] further suggests that

$$B \propto ez\varphi_{\mathrm{int}}\Gamma R^2 \frac{\mathrm{d}\alpha}{\mathrm{d}\psi_{\mathrm{s},\infty}}\psi_{\mathrm{s},\infty} \qquad \text{S 7}$$

where

$$\alpha = \frac{1}{1 + 10^{z(\mathrm{p}H - \mathrm{p}K)}\exp\left(z\psi_{\mathrm{s},\infty}\right)} \qquad \text{S 8}$$

is the ionisation probability of a surface ionisable group of valence $z = \pm 1$ in the ionized state[15], which in turn implies

$$z\frac{\mathrm{d}\alpha}{\mathrm{d}\psi_{\mathrm{s},\infty}} = \frac{-10^{z(\mathrm{p}H - \mathrm{p}K)}\exp\left(z\psi_{\mathrm{s},\infty}\right)}{\left[1 + 10^{z(\mathrm{p}H - \mathrm{p}K)}\exp\left(z\psi_{\mathrm{s},\infty}\right)\right]^2} \leq 0 \qquad \text{S 9}$$

Eqs. S 8 - S 9 above capture the phenomenon of charge regulation. Here, Γ denotes the number density of ionisable groups in the particle, while $\mathrm{p}H$ and $\mathrm{p}K$ denote the negative decadic logarithm of the proton concentration in solution and the equilibrium constant of proton dissociation of the groups respectively. In turn, $\psi_{\mathrm{s},\infty} = \frac{e\phi_{\mathrm{s},\infty}}{k_{\mathrm{B}}T}$ is the dimensionless electrical potential $\phi_{\mathrm{s},\infty}$ created at the surface of an isolated charged object by the ion distribution in the electrolyte, and e is the elementary charge.

In contrast to ϕ which is the electrical potential due to the ions in the system, φ_{int} represents an excess electrical potential created at a planar interface by dipoles representing solvent molecules in the vicinity[22]. Crucially, even at uncharged surface, this interfacial electrical potential, φ_0, is generally not zero and can take a positive or a

negative sign depending on the solvent and the chemistry of the surface[6,12]. In general we may take $\varphi_{\mathrm{int}} \approx \varphi_0$, and as Eq. S 7 shows, the sign of φ_{int} can dramatically modify the form of the interparticle interaction potential, turning it attractive or repulsive at long range. Molecular simulation studies provide estimates of $\varphi_0 \approx -0.5$ to $-0.1\,\mathrm{V} < 0$ for an interface immersed in water with respect to the bulk phase[6,12,19,22-24]. Simulations further suggest $\varphi_0 \approx +0.2\,\mathrm{V} > 0$ for surfaces immersed in alcohols such as ethanol (EtOH) and isopropanol (IPA). Note that the quantity φ_0, the solvent-induced electrical potential at a neutral interface in our work, is similar to "the potential of zero charge" in electrochemistry and interface science, as well as the air-liquid interfacial potential[25,26].

The main experimental trends suggested by Eqs. S 5 - S 9 are: (1) the breaking of charge reversal symmetry in interparticle interactions (e.g., negatively charged particles are characterised by $B < 0$ in water and may therefore attract, whereas positive particles imply $B > 0$, and should therefore repel), (2) use of a solvent in which the sign of φ_0 is opposite to that of water may reverse this trend (i.e., positive particles may attract whereas negatives repel), and (3) the magnitude of the solvation contribution to the interparticle interaction should depend strongly on the $\mathrm{p}H$ in solution. Importantly, when $\frac{\mathrm{d}\alpha}{\mathrm{d}\psi_{\mathrm{s},\infty}} \to 0$, which occurs outside the range of $\mathrm{p}H$ given approximately by $\mathrm{p}K + 0.2 \lesssim \mathrm{p}H \lesssim \mathrm{p}K + 2.5$, the electrostatic contribution to the free energy, $\Delta F_{\mathrm{el}}(x)$, should be the only surviving term in Eq. S 6. Here we expect to obtain $U^*_{\mathrm{tot}} \cong U_{\mathrm{DLVO}}$ and the total interaction potential should revert to a form that agrees with the DLVO prediction.

It is worth noting here that although our theoretical results for interfacial solvation properties utilise molecular dynamics (MD) simulation data for model oxygen-atom surfaces, recent MD simulation studies on water orientation at a variety of more realistic surfaces whose chemistry ranges from that of inorganic silica to polymeric surfaces clearly reveal that essential features of interfacial water orientation, and the sign of the associated interfacial potential, φ_0, are preserved across these materials[12]. It is possible that the dominant role played by hydrogen bonding in water is responsible for the comparative indifference of qualitative aspects of the orientational behaviour of water at an interface to specific surface chemistry[12,22,23]. Interfaces with organic solvents may

however be expected to show significant dependence of molecular orientation - and hence a dependence of both the sign and magnitude of φ_0 on surface chemistry[12].

S3.2 Summary of the approach to calculating the total interparticle interaction

Figs. 1, 2 and 5 display pair interaction potentials, $U_{\mathrm{tot}}(x)$, calculated using our interfacial solvation model as described previously[6,7]. The essential details of the model are recapitulated below. We solve the PB equation

$$\nabla^2\psi(\boldsymbol{r}) = \kappa^2 \sinh\psi(\boldsymbol{r}) \qquad \text{S 10}$$

for two hollow, identical spheres of radius R and surface charge density, σ, at a variable intersurface separation, x, immersed in an electrolyte with a concentration of monovalent salt c_0. Here ψ is the dimensionless electrical potential in the electrolyte and $\kappa = \sqrt{\frac{2e^2c_0}{\varepsilon\varepsilon_0 k_{\mathrm{B}}T}}$ is the inverse of the Debye length - a measure of the distance over which the electrical potential decays from its surface value ψ_{s}, due to screening by the cloud of oppositely charged counterions in solution. Furthermore, e is the elementary charge, k_{B} is Boltzmann's constant, and ε is the relative permittivity of the electrolyte medium ($\varepsilon = 78.5$ for water at temperature $T = 298\,K$). We calculate the potential distribution everywhere in the system subject to the boundary condition applied to the surface of each particle:

$$\sigma(R) = z\alpha(R)\Gamma e \qquad \text{S 11}$$

where $z = \pm 1$ denotes the sign of charge of the ionized group (e.g., $z = -1$ for an acidic group) and Γ is the number density of ionisable groups on the surface of the particle. In this equation, α is the ionisation probability of a group on the surface of the particle and is given by Eq. S 8 [15,27].

Having obtained the distribution of electrical potential ψ in the entire system, we then evaluate the following free energy functional for the electrostatic free energy as described previously[27-30]. Thus we have:

$$F_{\mathrm{el}}(x) = -\int_V \left\{\frac{\varepsilon\varepsilon_0}{2}\, E(\boldsymbol{r};x).E(\boldsymbol{r};x) + 2c_0k_{\mathrm{B}}T(\cosh\psi(\boldsymbol{r};x) - 1)\right\} \mathrm{d}V + \cdots \qquad \text{S 12}$$

$$\Gamma k_B T \int_S \ln \frac{1-\alpha(R;\, x)}{1-\alpha(R;\, \infty)} \mathrm{d}A$$

where $E(r; x)$ denotes the electric field at a point r in the electrolyte for an interparticle surface separation, x. Subtracting the value of the integral at very large separation say, $x = 20\,\kappa^{-1}$, gives the electrostatic interaction free energy, i.e., $\Delta F_{\mathrm{el}}(x) = F_{\mathrm{el}}(x) - F_{\mathrm{el}}(x = 20\,\kappa^{-1})$. We have also previously shown that the electrostatic interaction energy which takes the general screened Coulombic form given by $\Delta F_{\mathrm{el}} \propto \frac{\exp(-\kappa r)}{r}$ can be well approximated by a simple exponential for the large spheres and the comparatively small separations range in our experiments, i.e., we work with $\Delta F_{\mathrm{el}}(x) = A\exp(-\kappa x)$ since $x < R \gg \kappa^{-1}$, where $A > 0$ for like-charged particles[7].

Our model then introduces an interfacial free energy term, $F_{\mathrm{int}}(x)$, which represents a free energy contribution from the orientational behaviour of the interfacial solvent molecules. This term is calculated using MD simulation results for the excess electrical potential at interface $\varphi_{\mathrm{int}}(\sigma)$ as function of σ. Integration of the $\varphi_{\mathrm{int}}(\sigma)$ vs. σ relationship for a given surface type and solvent gives the solvation free energy $f_{\mathrm{int}}(\sigma) = \int_0^{\sigma} \varphi_{\mathrm{int}}(\sigma)\mathrm{d}\sigma$ per unit area of interface (Fig. S8).

Owing to charge regulation, the charge density σ at any point of the particle surface is a function of the inter-surface separation, x. As a result, $f(\sigma)$ becomes a function of interparticle separation. Thus, for a given value of x, the total interfacial free energy, F_{int}, can be calculated via the surface integral

$$F_{\mathrm{int}}(x) = \int_S f_{\mathrm{int}}(\sigma(R, x))\, \mathrm{d}A \qquad \text{S 13}$$

Similar to the evaluation of ΔF_{el} we determine ΔF_{int} by evaluating the integral for each location x and subtracting the value at large separation $x = 20\,\kappa^{-1}$, i.e., $\Delta F_{\mathrm{int}}(x) = F_{\mathrm{int}}(x) - F_{\mathrm{int}}(x = 20\,\kappa^{-1})$. We further find that for the interaction of large particles in solution ($R > \kappa^{-1}$), the interfacial solvation free energy at long range can also be well approximated by an expression of the form $\Delta F_{\mathrm{int}}(x) = B\exp(-\kappa_2 x)$, where $\kappa_2 < \kappa$ (Ref. 7) .

In contrast to $\Delta F_{\mathrm{el}}(x)$, which is generally always positive in the interaction of like-charged objects, the sign of B is governed by both that of the sign of the charge of

the particles and that of the solvation potential, φ_{int}, as displayed by Eq. S 7 (Ref. 7). We obtain the total interaction potential between a pair of particles by adding the two contributions to the free energy. Thus we have:

$$U_{\mathrm{tot}}(x) = \Delta F_{\mathrm{el}}(x) + \Delta F_{\mathrm{int}}(x) \qquad \text{S 14}$$

The assumption of free-energy additivity we invoke in writing Eq. S 14 has a long history. Dating back at least to the Derjaguin-Landau-Verwey-Overbeek (DLVO) theory, such assumptions are widely used in colloid science[31,32]. The assumption of superposition of hydration and electrostatic forces, for instance, has been explicitly tested in atomistic simulations and found to hold within accuracy limits under the relevant conditions[33].

Importantly, a value of $B < 0$ in Eq. S 6 implies an attractive contribution to the pair potential from the interfacial term, ΔF_{int}, which is opposite in sign to and therefore counteracts the interparticle electrostatic repulsion, ΔF_{el}. Conversely, $B > 0$ implies that ΔF_{int} is a positive quantity that increases monotonically with decreasing separation, reinforcing ΔF_{el}. Since $A > 0$ in the interaction of like charged objects, Eq. S 6 thus implies the possible occurrence of a long-ranged minimum in $U_{\mathrm{tot}}(x)$ when $B < 0$, provided that $A/|B| > 1$. If on the other hand $A/|B| \gg 1$ or $\ll 1$, we expect monotonically repulsive or attractive interaction potentials at long range, respectively.

Furthermore, under conditions where $z\frac{\mathrm{d}\alpha}{\mathrm{d}\psi_{\mathrm{s}}} < 0$, Eq. S 7 demonstrates that the overall sign of B is determined by the signs of φ_{int} and $\psi_{\mathrm{s},\infty}$. Thus for $\frac{\mathrm{d}\alpha}{\mathrm{d}\psi_{\mathrm{s}}} \neq 0$, our model suggests that $\Delta F_{\mathrm{int}} < 0$ for weakly negatively charged particles in water, since both φ_0 and $\psi_{\mathrm{s},\infty} < 0$. Whereas for positively charged particles where $\psi_{\mathrm{s},\infty} > 0$, we have $\Delta F_{\mathrm{int}} > 0$. Therefore, for a particle with a given sign of charge, the sign of B, which governs its interactions with a similar neighbour, may be said to be determined by that of φ_0. In practice, surfaces in solution rarely exceed a charge density magnitude of 0.3 e/nm^2 (Fig. S8a, bottom panel). Consequently, for objects in water we generally expect $\varphi_{\mathrm{int}} < 0$ and for weakly charged surfaces we may make the approximation $\varphi_{\mathrm{int}} \approx \varphi_0 = \varphi(\sigma = 0)$. Eq. S 7 implies that the interfacial contribution generates an attractive long-ranged force between negatively charged particles and a repulsive force for positively charged

particles. We expect the converse to hold for a solvent where $\varphi_0 > 0$, i.e., positive particles should attract.

We further note that $0 \lesssim \left|z\frac{\mathrm{d}\alpha}{\mathrm{d}\psi_s}\right| \lesssim 0.25$ depending on the pH in solution. Eq. S 7 shows that when $\left|\frac{\mathrm{d}\alpha}{\mathrm{d}\psi_s}\right|$ is large, the interfacial term can be substantial, implying significant qualitative and quantitative departure from standing theories. This departure is expected to occur when the pH is in the vicinity of the pK of the ionizable groups, or more precisely, when $10^{z(\mathrm{p}H-\mathrm{p}K)}\exp(z\psi_{s,\infty}) \approx 1$. Thus, for anionic groups with $z = -1$ and nominal values of $\psi_{s,\infty} \approx -0.5$ to -6 at low and high pH respectively, we may expect $\left|\frac{\mathrm{d}\alpha}{\mathrm{d}\psi_s}\right|$, and therefore ΔF_{int}, to be large in the range of pH given by $\mathrm{p}K + 0.2 \lesssim \mathrm{p}H \lesssim \mathrm{p}K + 2.5$ (Fig. 2d). Conversely when $\frac{\mathrm{d}\alpha}{\mathrm{d}\psi_s} \to 0$, which occurs well outside the above indicated pH range, Eq. S 7 suggests no contribution at all from the interfacial term, i.e., $\Delta F_{\mathrm{int}} \to 0$.

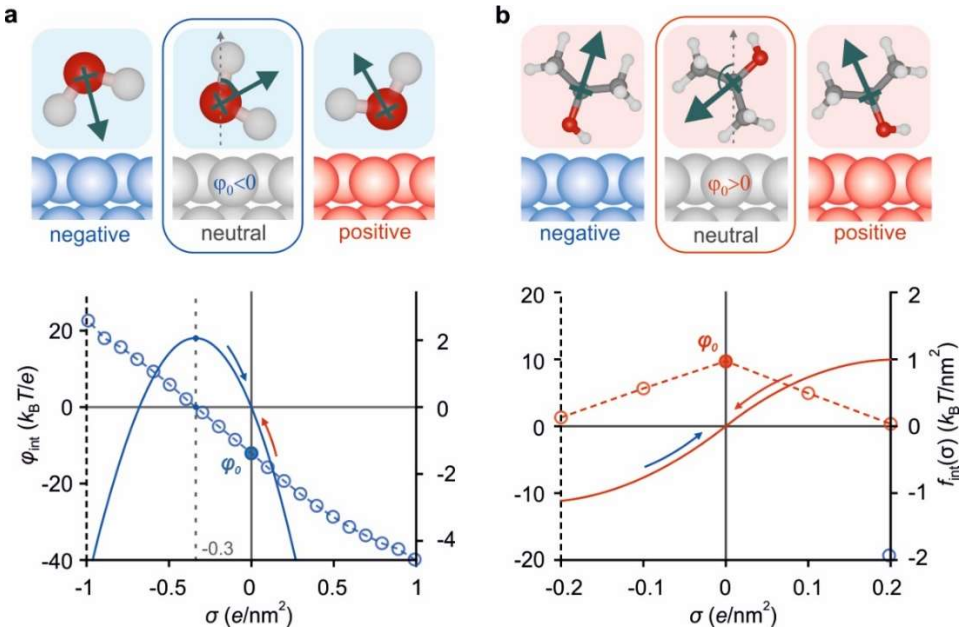


Fig. S8. Schematic depiction of the qualitative average orientation of a solvent molecule at the solid-liquid interface. (**a**) Top: Schematic representation of the dominant orientation of water molecules close to a neutral interface. On average, a molecule close to the interface points its oxygen atom slightly towards the interface and hydrogen atoms towards the bulk, giving a net dipole moment (green arrow) whose z-component points away from the interface and towards the bulk. Dashed vertical arrow depicts the surface normal. This symmetry-breaking in average orientation gives rise to an interfacial electrical potential (or solvation potential) with negative sign, i.e., $\varphi_0 < 0$ (centre panel). At a positively charged surface the average molecular orientation is reinforced giving a more strongly negative value of φ_{int} (right panel). At a strongly negatively charged surface the water molecule flips around, pointing its hydrogen atoms and its

dipole strongly towards the interface (left panel). The re-orientation of water at a negatively charged surface results in a gradual increase in φ_{int} with increasing magnitude of negative surface charge, going through 0 and turning positive as the hydrogen atoms increasingly point towards the interface (open symbols, bottom panel). The plots in the lower panels depict the dependence of φ_{int} on surface charge density, σ as obtained from MD simulations of SPC water at a model surface composed of oxygen atoms[6,12] (open symbols). The integral $f_{\mathrm{int}}(\sigma) = \int_0^{\sigma} \varphi_{\mathrm{int}}(\sigma)\mathrm{d}\sigma$ gives the interfacial solvation free energy per unit area (solid line)[6,12]. When two like charged particles approach each other, charge regulation reduces the magnitude of the charge on the particles in general, regardless of whether the particle is positively or negatively charged. The blue and red arrows depict the impact of charge regulation on the interfacial free energy contribution in water. The approach of negatively charged particles is accompanied by a reduction in interfacial free energy implying an attraction (downward pointing blue arrow) that can mitigate and even overwhelm the electrostatic repulsion, ΔF_{el}. The converse is true for the approach of positively charged particles, where the interfacial solvation contribution implies an additional repulsion that reinforces ΔF_{el} (upward pointing red arrow). (**b**) MD simulations of isopropanol (IPA) at a model neutral oxygen atom surface show that the IPA molecule points its oxygen atom away from the surface giving rise to $\varphi_0 > 0$ (top row). Contrary to the behaviour of water at an O-atom interface, we find that regardless of whether the surface charge turns increasingly positive or negative, the IPA molecule flips around, pointing its dipole away from the surface (green arrow), giving a reduction in φ_{int} compared to φ_0. The reorientation of IPA at a charged interface thus causes φ_{int} to go through zero and turn increasingly negative as the oxygen atom points more strongly towards the surface. Note however that surface chemistry can have a substantial impact on the behaviour of the solvation potential in organic solvents[12]. Regardless, for weakly charged surfaces, typical in experiments, the behaviour of the interfacial free energy is governed by the sign and magnitude of φ_0. Assuming the O-atom surface accurately captures the sign of φ_0, we expect that f_{int} provides a decreasing, attractive contribution to the pair interaction energy (downward pointing red arrow) for the approach of positively charged particles, and vice versa for the interaction of negatively charged particles (upward pointing blue arrow). All dipole moment vectors for illustrative purposes only.

S3.3 Discussion on parameter values used in the theoretical modelling of the experimentally inferred interaction potentials

The input parameters in the theoretical model of the interfacial free energy include the radius of the particles, R, the dielectric constant of the bulk solvent phase, the concentration of monovalent salt in solution, c_0, the number density of the surface ionisable groups, and the parameter $p = z(\mathrm{p}H - \mathrm{p}K)$. R is known from measurement. We fix the values of all other parameters to the values displayed in Table S1 and vary the value of p to obtain calculated pair interaction potentials characterized by values of w and x_{min}that agree with the experimentally inferred potentials.

Ionizable group density, Γ: For silica surfaces we assume $\Gamma = 1$ nm^{-2}, which is a typical value for silica[17,34]. We take $\Gamma \approx 0.1$ nm^{-2} for the COOH and NH_2 functionalized

particles. Here we have assumed that chemically functionalized particles are likely to have approximately an order of magnitude lower group density than amorphous solids such as silica. The precise value of Γ is not very important to the final modelling results since a different value of Γ will require a slightly different value of p to give a similar pair potential. Given the uncertainty in $\mathrm{p}K$ value of at least 1-2 units, the calculated results may be regarded as not particularly sensitive to the exact value of Γ. We therefore hold Γ constant for a given material and vary the value of p in the calculations to obtain a pair potential that captures the experimentally inferred profile.

Salt concentration, c_0: All other parameters remaining constant, salt concentration strongly affects the form of the calculated pair potential by directly influencing the screening length, κ^{-1}. Values of c_0 quoted in the experimental data denote nominal salt concentrations inferred from electrical conductivity measurements of the background electrolyte solution used to produce particle suspensions (see Section S1.2). These concentration measurements may not accurately reflect *in situ* values of concentration in the experimental microscopy chamber which can be different. In general, when modelling experiments on positive particles (both in water and in organic solvents) we found that the best agreement with measurements was obtained for c_0 values in the model that were about 0.04-0.1 mM larger than the nominal, measured bulk electrolyte values (Table S1). We attribute this observation to the fact that the silica chamber walls were chemically functionalized with positively charged polyelectrolytes for all experiments with positively charged particles. This additional chemical processing is likely to alter the ionic strength of the suspension added to the chamber. However, for experiments with negatively charged particles, and for experiments at higher salt concentrations, the disparity between nominal measured concentration values and those used in the modelling procedure was generally small (Table S1). Note that experiments performed without any added salt, in "deionised" water, can in general carry larger uncertainties on the estimated ionic strength. This is due in part to CO_2 dissolution from the air, and the general susceptibility of a pure solvent to impurities from contact with other phases including experimental surfaces.

Modelling silica: For experiments on silica at various salt concentrations and $\mathrm{p}H$ in the range 5.5-6.5 shown in Fig. 1, we model pair interactions with a single value of p (implying a single $\mathrm{p}K$ value in the range 4-6.5). Clearly, this is a significant oversimplification given the variety of $\mathrm{p}K$s known to describe the system[34,35]. But the implication in doing so is that the overall behaviour can be captured by a single effective $\mathrm{p}K$ value representing groups whose $\mathrm{p}K$s lie in the vicinity of the single nominal $\mathrm{p}K$. Groups with $\mathrm{p}K > 6$, higher than the nominal effective $\mathrm{p}K$, are assumed not to contribute to the interaction as they can be regarded as effectively completely discharged. Groups with more acidic $\mathrm{p}K$s ($\mathrm{p}K < 4$) are captured using a small fraction ($f_1 = 0.5\%$) of a highly acidic, permanently ionized species of $\mathrm{p}K$ characterised by $p_1 = \mathrm{p}K - \mathrm{p}H = -5$. This approach permits us to construct a coarse-grained model for silica behaviour in the experiments described in Fig. 1. Note that given the large number of poorly controlled parameters involved in describing the silica surface we do not attempt to provide calculated $U(x)$ profiles as a function of $\mathrm{p}H$ for silica (experiments in Fig. 2).

Modelling interactions in alcohols - salt concentration and $\mathrm{p}K$ *values*: In our PB electrostatics model we treat both isopropanol and ethanol as media with a dielectric constant $\varepsilon = 20$. We use a value of $\varphi_0 = +0.2$ V for the interfacial solvation potential in calculating the interfacial free energy term.

Similar to the experiments on positive particles in water, we use a value of c_0 larger by about 0.075 mM compared to the nominal experimental salt concentration. Furthermore, conversion of measured electrical conductivities to salt concentration in alcohols involves poorly controlled assumptions on the ionic species in solution and the corresponding ionic radii (see Section S1.2). As a result, we may expect that the inferred experimental salt concentrations may carry an error as large as a factor of 2. Experimental uncertainties notwithstanding, the theoretically modelled curves are based on c_0 values close to the experimentally measured nominal values (Table S1).

Note that calculations of $U_{\mathrm{tot}}(x)$ for alcohols (presented in Fig. 5) assume the same value of $\varphi_0 = +0.2$ V for both neutral COOH and NH_2 surfaces in IPA (Fig. 5a). But there is no reason for these values to be the same, since surface chemistry can

influence the magnitude and even the sign of φ_0 for a given solvent[12]. In the present study, qualitative arguments concerning the orientation of alcohols at model oxygen atom surfaces would suggest that the sign of φ_0 is preserved. But the magnitude of φ_0 could be very different for the two (real) surfaces and this will influence the calculated $U_{\mathrm{tot}}(x)$ curves. The calculated $U_{\mathrm{tot}}(x)$ curves in Fig. 5 thus serve the purpose of qualitative comparison with experimental observations.

Furthermore, pK values for ionisable groups in organic solvents are not known accurately. Our previous work on charge measurements on silica in polar and non-polar solvents suggested an upward shift in the effective pK of silica of ≈3.5 units in ethanol[1]. This estimated shift was based on simple solvation energy estimates and was found to agree with experiments. Applying similar considerations to COOH and NH_2 surfaces in the experiments, we expected an upward shift of the pK of carboxylic acid groups to $\mathrm{p}K > 8$ and a downward shift of basic NH_2 group pK values to $\mathrm{p}K < 7$ in alcohols. The values of p obtained in the modelling procedure for COOH particles (Table S1) however imply a rather large upward shift of pK of approximately $6-7$ units to about $\mathrm{p}K = 11-13$ for COOH particles and not much of a shift for amino groups, i.e., $\mathrm{p}K \approx 8$ for NH_2 groups in ethanol. Remarkably, our inferred values of pK for COOH groups and NH_2 groups in ethanol, listed in Table S1 are found to be in good agreement with the literature values for carboxylic acids such as acetic and benzoic acids in ethanol ($\mathrm{p}K > 10$) and a range of aliphatic amines in ethanol ($7 < \mathrm{p}K < 9$)[36,37]. Note that for carboxyl particles we have attempted to match the repulsion measured in the experiment. Interestingly, from the present parameter values, the dominant contribution to the repulsive $U_{\mathrm{tot}}(x)$ appears to stem mainly from the $\Delta F_{\mathrm{int}}(x)$ term rather than from the $\Delta F_{\mathrm{el}}(x)$ term as one might intuitively expect. This balance will of course alter for a (different) value of $\varphi_0 < +0.2$ V. Therefore, the present set of results provide only qualitative indications of the expected behaviour, but the trends that emerge are all physically plausible.

S3.4 Considerations in comparing the results of pair-interaction-based theory and simulation procedures with an experiment involving an ensemble of interacting particles

Pairwise additivity of interaction energies is a simplifying assumption

A significant caveat on the presented combined experiment-theory approach is that we attempt to map a collective interaction between heterogeneous particles on to a pair-interaction calculated for an isolated pair of identical particles. This procedure should at best warrant qualitative comparisons between experimentally inferred and theoretically calculated potentials as outlined in the next section. Furthermore, in our BD simulation-based modelling of the experimentally observed interactions, we assume pairwise additivity of interparticle interactions. This is a simplifying approximation and unlikely to be rigorously true in experiments[38]. Interaction potentials inferred from our BD simulations thus represent a pair potential that could give rise to the experimentally observed $g(r)$ structure in a situation where collective interactions can be described in a strictly pairwise additive manner. Although these inferred potentials are likely to provide a good approximation of the pair potential in experiment, they cannot be taken to accurately represent the "true pair potential". Pair potentials may indeed be accessed in measurements on interactions of isolated pairs of particles as shown in Fig. S12. But in such experiments, the uncertainty on the size and properties of the individual particles in each measured pair interaction can impede quantitative comparison to a theoretical calculation. Note that in the present cluster experiments we average over a large number of particles which suggests that we may reasonably expect the size distribution of particles in the measurement to approach that of the particle sample. We further account for particle size variation by incorporating the known 'ensemble-level' size distribution as an input into the BD simulation (see Fig. S1 and Fig. S17). Accurately accounting for the particle size distribution is likely to pose a challenge in relating direct pair-potential measurements to theoretical calculations.

Experimental variability in parameters of interest

Next, the experiments inherently contain a degree of variability and perturbation that are hard, if not impossible to control and account for. A few of these include: (1) average

particle size in an experiment which may not correspond to the nominal mean value characterizing the sample, (2) particle-to-particle variability in surface properties, such as group density, $\mathrm{p}K$ values and their distribution, charge density, and particle size (3) change in surface chemistry (e.g., $\mathrm{p}K$) as a function of electrolyte composition (4) drifts in $\mathrm{p}H$ and ionic strength as a function of time, which can influence the surface properties and therefore the stability of clusters. As a result of numerous sources of drift and variability in measurements, qualitative agreement between the theoretical model and the pair potential inferred from the $g(r)$ measurements is the best that can be expected in most cases.

Scope for improvement of the present theoretical model

The above caveats and considerations notwithstanding, there appear to be two aspects of the present theoretical model that suggest the need for further improvement in future work:

(1) One shortcoming of the present rudimentary theoretical model is that it often suggests a strong interparticle attraction to contact under conditions where the experiments clearly display dominance of the repulsion over the attraction at short range. In general, we find that the model does well at capturing the total interaction and the appearance of minima at large separations ($x > 200$ nm). However for experiments on negatively charged particles at ionic strengths $c_0 \gtrsim 0.1$ mM, the present model of the total pairwise interparticle interaction over-estimates the magnitude of the attractive interfacial contribution, ΔF_{int}, at smaller separations, $x < 200$ nm (Fig. 2c, middle panel), often implying attraction to contact where the experiments show stable crystalline clusters with large intersurface separations. In other words, in the present model the ΔF_{int} term appears to grow too strongly in magnitude at smaller intersurface separations. Assuming that at these separations the electrostatic part of the interaction, ΔF_{el}, is accurately given by PB theory including charge regulation, the experimental observations could be seen to imply a damping of the growth of the ΔF_{int} term at shorter range. At present there is no mechanism in the model that would provide such a damping. But future improvements to the modelling approach, such as a more integrated

theory of electrostatics and solvation at an interface, or alternatively, a model that incorporates aspects of the interfacial behaviour of the solvent that are not captured in present molecular simulations may resolve this discrepancy[16].

(2) Secondly, as pointed out in previous work, in calculating $U_{\mathrm{tot}}(x)$ we observe an over-reliance of the depth and location of the minimum (i.e., w and x_{min}) on the precise input value of p (Ref 6). Currently we believe that much of this dependence could be attributed to our attempt to capture an experimentally measured average response arising from numerous sources of experimental variability and temporal drift (particle size, charge, $\mathrm{p}H$, $\mathrm{p}K$, salt concentration) by varying a single parameter, p, in the calculation. However, it is entirely possible that a more in-depth theoretical treatment is likely to free our calculated results from their strong dependence on p. Again, inclusion of additional effects such as the influence of ions on the interfacial solvation structure may well alter the final calculated results, possibly enabling our modelling procedure to capture experimental observations more accurately and broadly[16]. These preliminary indications provide fertile ground for the advancement of an in-depth understanding of the contribution of the interfacial electrolyte to interparticle and intermolecular interactions in solution.

S3.5 Analysing the pH response of particle cluster formation

Comparing the $\mathrm{p}H$ response of the well depth, w, with the qualitative indications from the theoretical model enables us to test for the presence of a key signature of charge regulation in the interfacial free energy term, as shown in Fig. 2. The expression for the interfacial free energy displayed in Eq. S 7, gives the amplitude of the ΔF_{int} term as follows: $B \propto ez\varphi_{\mathrm{int}} \frac{\mathrm{d}\alpha}{\mathrm{d}\psi_{\mathrm{s},\infty}} \psi_{\mathrm{s},\infty} \Gamma R^2$.

We expect the magnitude of the well depth w to show qualitative correlation with that of $\left|\frac{\mathrm{d}\alpha}{\mathrm{d}\psi_{\mathrm{s},\infty}}\right|$ which is expected to change substantially as a function of $\mathrm{p}H$. Depending on $\mathrm{p}H$, we expect $0 \lesssim \left|\frac{\mathrm{d}\alpha}{\mathrm{d}\psi_{\mathrm{s},\infty}}\right| \lesssim 0.25$, which suggests that when $|\mathrm{p}K - \mathrm{p}H| \gg 0$, the interfacial contribution $\Delta F_{\mathrm{int}} \to 0$, and the interparticle attraction between

negative particles should vanish altogether. Note that other quantities in Eq. S 7 – namely, φ_{int} and $\psi_{\mathrm{s},\infty}$– do depend on the surface charge density, σ, but they can be assumed not to change as *substantially* as $\left|\frac{\mathrm{d}\alpha}{\mathrm{d}\psi_{\mathrm{s},\infty}}\right|$ as a function of $\mathrm{p}H$. For anionic surface groups, σ increases in magnitude with increasing $\mathrm{p}H$. The surface electrical potential $\psi_{\mathrm{s},\infty}$ therefore increases in magnitude with increasing $\mathrm{p}H$, whereas the interfacial potential φ_{int} decreases in magnitude with increasing $\mathrm{p}H$ for low charge densities typically encountered in experimental systems (Fig. S8). Therefore, for the purpose of this analysis we treat the product $\varphi_{\mathrm{int}}\psi_{\mathrm{s},\infty}$ as remaining effectively constant in relation to the large variation expected in $\left|\frac{\mathrm{d}\alpha}{\mathrm{d}\psi_{\mathrm{s},\infty}}\right|$ as a function of $\mathrm{p}H$. The dependence of $\psi_{\mathrm{s},\infty}$ on $\mathrm{p}H$ is denoted as $\psi_{\mathrm{s},\infty}(\mathrm{p}H)$ in Eq. S 15.

Figure 2d plots measured values of w as symbols together with dashed lines for the value of $\frac{\mathrm{d}\alpha}{\mathrm{d}\psi_{\mathrm{s},\infty}}$ as given by Eq. S 9, repeated below for convenience:

$$\frac{\mathrm{d}\alpha}{\mathrm{d}\psi_{\mathrm{s},\infty}} = \frac{-z10^{z(\mathrm{p}H-\mathrm{p}K)}\exp\left[z\psi_{\mathrm{s},\infty}(\mathrm{p}H)\right]}{\left\{1+10^{z(\mathrm{p}H-\mathrm{p}K)}\exp\left[z\psi_{\mathrm{s},\infty}(\mathrm{p}H)\right]\right\}^2} = -z\left[1-\alpha\left(\psi_{\mathrm{s},\infty}\right)\right]\alpha\left(\psi_{\mathrm{s},\infty}\right) \qquad \text{S 15}$$

For anionic groups where $z=-1$, we have $\frac{\mathrm{d}\alpha}{\mathrm{d}\psi_{\mathrm{s},\infty}}>0$, whereas for cationic groups where $z=+1$, we have $\frac{\mathrm{d}\alpha}{\mathrm{d}\psi_{\mathrm{s},\infty}}<0$. In the above equation for $\frac{\mathrm{d}\alpha}{\mathrm{d}\psi_{\mathrm{s},\infty}}$, the experimental $\mathrm{p}H$ is known from measurement, and nominal values of $\mathrm{p}K$ of the ionizable groups are known for the COOH and NH_2 particles. For silica, a range of $\mathrm{p}K$s of the surface groups is available from reports in the literature[34,35]. In order to estimate $\psi_{\mathrm{s},\infty}$, the only remaining unknown in the expression, we may refer to zeta (ζ) potential measurements which provide indicative values for $\psi_{\mathrm{s},\infty}$ that are however not quantitatively exact. We emphasize that $\psi_{\mathrm{s},\infty}$ and ζ are themselves functions of $\mathrm{p}H$, which in fact underpins the overall $\mathrm{p}H$ dependence of $\frac{\mathrm{d}\alpha}{\mathrm{d}\psi_{\mathrm{s},\infty}}$. Details used to generate the theoretical expected curves in Fig. 2d for the three types of particles are provided below.

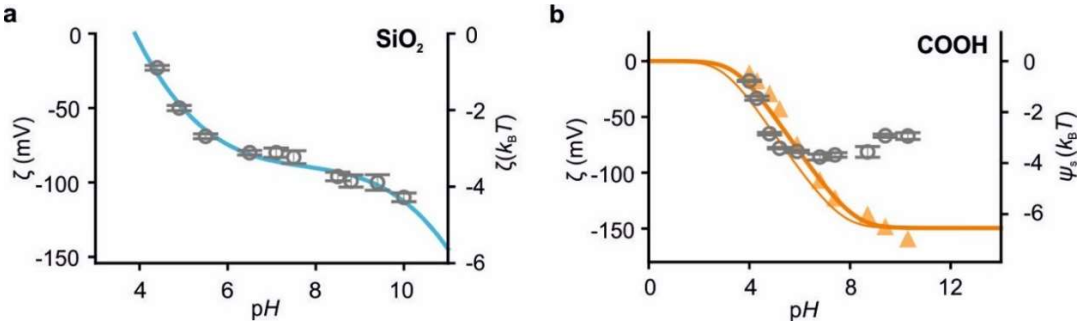


Fig. S9. ζ potentials for SiO_2 and COOH particles (**a**) Measured values of ζ (pH) for SiO_2 particles used as ψ_s (pH) in Eq. S 15 (grey circles). The blue curve shows a fit function $\psi_s = 0.0479pH^3 - 1.1178pH^2 + 8.8668pH - 20.405$ and is provided as a guide to the eye. (**b**) Measured ζ potentials for COOH particles (grey circles). Orange triangles denote values of the surface potential, $\psi_s(pH)$, used in Eq. S 15. At higher pH (>5) these values agree well with ψ_s vs. pH trends calculated for COOH particles using $\Gamma = 0.15$ nm^{-2} and $pK = 4.5$ (thick solid line), and $pK = 5$ (thin solid line.) At low $pH < 5$, the values are similar to both measured ζ potentials as well as the calculated ψ_s values. All ζ potentials represent mean values ± S.D. from 3 sets of measurements.

Silica particles

Because the silica surface carries a variety of ionizable species with pK values ranging from 2 to 11, we use a generalized form of Eq. S 9 applicable for a system with multiple pK values[34,35]. In particular we have

$$\frac{d\alpha}{d\psi_{s,\infty}} = \sum_i f_i \frac{d\alpha_i}{d\psi_{s,\infty}} = -z \sum_i f_i [1 - \alpha_i(\psi_{s,\infty})]\alpha_i(\psi_{s,\infty}) \qquad \text{S 16}$$

where f_i is the fractional preponderance of the i th species of pK value pK_i. As stated in Eq. S 8, the ionization probability of a group of species i may be written as

$$\alpha_i = \frac{1}{1 + 10^{z(pH - pK_i)} \exp(z\psi_{s,\infty})} \qquad \text{S 17}$$

In the analysis for silica shown in Fig. 2d we apply Eqs. S 16-S 17 above, setting $\psi_{s,\infty} = \zeta$, the measured zeta potential values at each pH (grey circles, Fig. S9a). We further assume 7 species of ionizable surface groups of pK values $pK_1 = 3$, $pK_2 = 3.8$, $pK_3 = 5$, $pK_4 = 6$, $pK_5 = 7$, $pK_6 = 9$, $pK_7 = 10$ of nearly equal preponderance (i.e., $f_1 = f_2 = 0.2, f_3 = f_4 = f_5 = 0.15, f_6 = 0.1$ and $f_7 = 0.05$.)

Because the surface chemistry and properties of silica are so complex, and the values of the parameters involved not sufficiently accurately known, it is not meaningful in our view to attempt more detailed modelling of the silica response. It is interesting to note however that shallow minima in the pair-potential ($|w| \approx 2\ k_B T$), which imply

attractions arising from the ΔF_{int} term in our model, remain measurable all the way up to the highest $\mathrm{p}H$ values. Within our model, such behaviour points to the presence of charge regulating groups with $\mathrm{p}K > 9$ which is well known to be the case for silica[35]. Note that this broad response of silica is markedly different from particles carrying a single ionizable chemical species of well-defined $\mathrm{p}K$ as described further below. Finally, the present comparison of the trends for the $\frac{\mathrm{d}\alpha}{\mathrm{d}\psi_{\mathrm{s},\infty}}$ term with the measured values of well depth w, can only be regarded as qualitative as we ignore the variation of the ΔF_{el} term with $\mathrm{p}H$. For acidic groups such as silanols and carboxyls, ΔF_{el} is expected to increase in magnitude with increasing $\mathrm{p}H$ and thus independently contribute to a lowering in magnitude of w. That the interparticle attraction is observed to persist at very high $\mathrm{p}H$ for silica, even in the face of an increasing electrostatic repulsion, provides further strong of evidence of a lingering, albeit diminishing attractive contribution. The observations align well with the expectation, based on our model, of an interfacial solvation contribution arising from a small population of very weakly acidic groups ($\mathrm{p}K > 9$) known to populate the silica surface.

Carboxyl particles (-COOH groups)

Modelling the $\mathrm{p}H$ response of the carboxylated melamine particles permits us to attempt a more quantitative comparison of experimental trends with model predictions. We assume that the surface of our carboxyl particles may be described by a single ionizable species of $\mathrm{p}K = 4.5$, similar to acetic acid. A quantitative calculation of $\frac{\mathrm{d}\alpha}{\mathrm{d}\psi_{\mathrm{s},\infty}}$, would require values of $\psi_{\mathrm{s},\infty}$ as a function of $\mathrm{p}H$ at a greater accuracy that that provided by ζ potential measurements. It is well known that the zeta potential does not accurately capture the value of the electrical potential at the surface of a charged particle due to the high non-linearity of the PB equation in the regime of high potentials. We therefore use an assumed trend for the $\psi_{\mathrm{s},\infty}$ vs. $\mathrm{p}H$ relationship shown in Fig. S9 (orange triangles). This trend in $\psi_{\mathrm{s},\infty}$ reflects the behavior of ζ at low surface potentials as expected (Fig. S9), but $\psi_{\mathrm{s},\infty}$ exceeds ζ in magnitude at $\mathrm{p}H > 5$ where the surface is expected to be strongly ionised. We point out that our assumed trend in $\psi_{\mathrm{s},\infty}$ vs $\mathrm{p}H$ agrees well with a

PB calculation for particles with a group density of $\Gamma = 0.15$ nm^{-2} and $\mathrm{p}K$ values 4.5 and 5 (solid lines, Fig. S9).

Amino-silica particles (-NH_2 groups)

In modelling the aminated-silica particles we assume a single protonatable species of $\mathrm{p}K = 9.5$. We assume behavior that is qualitatively analogous to COOH particles, where $|\psi_{s,\infty}|$ vs $\mathrm{p}H$ qualitatively follows the carboxyl response except that it is reflected and shifted to larger $\mathrm{p}H$ values as shown in the ζ potential measurements presented in Fig. 2b. As a result, the response in $\left|\frac{d\alpha}{d\psi_{s,\infty}}\right|$ is mirrored and shifted to larger $\mathrm{p}H$ values as shown in Fig. 2d. According to our model, the experimental observation for the interaction of positive particles would correspond to *enhanced repulsions* in the regime $\frac{d\alpha}{d\psi_{s,\infty}} \neq 0$. The present experiments are not sensitive enough to quantitatively measure and reliably distinguish between the strength of repulsive interactions in different experiments, but the data clearly show that attractive long-ranged minima are never observed in the pair potentials, as suggested by the model (i.e., the data are consistent with $B \propto \varphi_0 \frac{d\alpha}{d\psi_{s,\infty}} \geq 0$). Because the inferred pair potentials consistently indicate monotonic repulsive pair potentials, we have $w = 0$ for all values of $\mathrm{p}H$. The above analysis demonstrates that the measured trends in w for both positively and negatively charged particles are well captured in the magnitude and sign of $\frac{d\alpha}{d\psi_{s,\infty}}$, providing a crucial test of the predictions of the interfacial solvation model and of Eq. S 7 in particular.

On a related note, it is worth pointing out that in general at low salt concentrations, we expect an upward shift of bulk $\mathrm{p}H$ at which clustering occurs in anionic particles, relative to the nominal $\mathrm{p}K$ value of an isolated, acidic ionisable group. The reason for this shift is related to the increase in magnitude of $\psi_{s,\infty}$ with increasing $\mathrm{p}H$ for anionic particles. The up-shift of the "clustering $\mathrm{p}H$" may be viewed as a simple consequence of the elevation of electrical potential at a charged surface with a lowering of salt concentration which directly influences the bulk $\mathrm{p}H$ value at which the ionization probability changes strongly (i.e., $\left|\frac{d\alpha}{d\psi_{s,\infty}}\right|$ is large) as shown in Eq. S 8. The phenomenon

is sometimes referred to as a "pKa shift" has been broadly recognised and reported in a range of studies on charged molecules surfaces such as DNA, lipid bilayers and polyelectrolyte coatings[39]. For a negatively charged surface, the $\exp(-\psi_{s,\infty})$ term in Eq. S 8 and Eq. S 17 suggest that we may view the effective pH in the vicinity of the surface as lower than in the bulk. Thus as a consequence, in experiments that monitor the bulk pH, the pH value at which half-maximal ionization probability is obtained shifts to larger values. This up-shift is frequently interpreted as an apparent upward shift in pK of the groups themselves. For positively charged surfaces a converse downward shift in effective pK is expected[39]. But such shifts are primarily a consequence of a collective electrostatic effect arising from the interaction of neighbouring charges in a dense arrangement of ionizable groups, typical of macromolecules and polyelectrolytes, with the pK of the group *per se* not requiring to be different at a surface from the value in isolation. Such an 'electrostatic shift' of pK in a charged object could be contrasted with shifts in intrinsic pK values that might arise from electronic, dielectric or solvation effects in the immediate environment of the group, altering the effective pK of a group at a surface or buried in a protein[40,41].

S3.6 Cluster formation in mixtures of chemically dissimilar particles

In the interaction of two particles of identical radius and dissimilar surface chemistry, the prefactor of the exponential term that gives the free energy due to interfacial solvation in Eq. S 6 which may be written as follows:

$$B_{ij} \propto ezR^2 \left[\varphi_{\mathrm{int},i}\, \Gamma_i \left(\frac{\mathrm{d}\alpha}{\mathrm{d}\psi_{s,\infty}} \right)_i \psi_{s,\infty,j} + \varphi_{\mathrm{int},j}\, \Gamma_j \left(\frac{\mathrm{d}\alpha}{\mathrm{d}\psi_{s,\infty}} \right)_j \psi_{s,\infty,i} \right] \qquad \text{S 18}$$

where the subscripts "$i = 1$" and "$j = 2$" denote the corresponding values of quantities for particles "1" and "2" in the interaction. Particle 1 may belong to species A whose chemistry is different from that of particle 2 of species B. In the present analysis, we ignore variations in φ_{int} between different types of surfaces, but we may assume the value remains constant for a specific set of solution conditions. We then have two major quantities that could significantly affect the magnitude of B, namely $\left(\frac{\mathrm{d}\alpha}{\mathrm{d}\psi_{s,\infty}}\right)$ and $\psi_{s,\infty}$,

each characterising a different particle of the two engaged in a pair interaction. Of the two quantities, the one that displays the largest variation depending on solution conditions is $\left(\frac{\mathrm{d}\alpha}{\mathrm{d}\psi_{\mathrm{s},\infty}}\right)$.

Thus, when the values of $\left(\frac{\mathrm{d}\alpha}{\mathrm{d}\psi_{\mathrm{s},\infty}}\right)$ for both species (and implicitly, values of $\psi_{\mathrm{s},\infty}$ for both species) are reasonably large, we expect B to be large for both cross-species (B_{ij}) and same-species (B_{ii}, B_{jj}) pair interactions. Therefore particle clusters that form in mixtures of different types of particle should contain both species. Similarly, when $\left(\frac{\mathrm{d}\alpha}{\mathrm{d}\psi_{\mathrm{s},\infty}}\right) \to 0$ for both species (typically occurring at extremes of $\mathrm{p}H$) and for similar values of $\psi_{\mathrm{s},\infty}$, clusters form neither in pure suspensions nor in mixtures of the two species, since both terms in Eq. S 18 are small. Under solution conditions where, e.g., $\left(\frac{\mathrm{d}\alpha}{\mathrm{d}\psi_{\mathrm{s},\infty}}\right)_2$ is small – i.e., the value of $\left(\frac{\mathrm{d}\alpha}{\mathrm{d}\psi_{\mathrm{s},\infty}}\right)$ of particle #2 in the interaction (e.g., COOH particles in Fig. 4) is small - same-species clusters in species B generally do not form. This is because $\left(\frac{\mathrm{d}\alpha}{\mathrm{d}\psi_{\mathrm{s},\infty}}\right)_2 \to 0$ for both partners in a COOH pair at the relevant $\mathrm{p}H$, which snuffs out B, and therefore the attractive interfacial term altogether. But the value of $\psi_{\mathrm{s},\infty,2}$ can nonetheless be large enough to produce a substantial perturbation of surface potential on particle 1 of species A (SiO_2), since $\Delta\psi_{\mathrm{s},1} \propto \psi_{\mathrm{s},2}$ (Ref. 7). This perturbation of electrical perturbation can couple with a significant $\left(\frac{\mathrm{d}\alpha}{\mathrm{d}\psi_{\mathrm{s},\infty}}\right)_1$ value on particle #1 to give a net B_{12} value that is large enough for an experimentally observable (and favourable) total interfacial free energy contribution. In other words, under specific conditions, the quantities in one of the terms in Eq. S 18 can remain large enough to give a substantial total B_{12} value despite the fact that the other term tends to zero. This can manifest as an attraction and cluster formation for dissimilar negatively charged particles in water in a situation where one species forms clusters on its own (species A in our example) and the other does not (species B). Thus, a reasonable value of $\left(\frac{\mathrm{d}\alpha}{\mathrm{d}\psi_{\mathrm{s},\infty}}\right)$ on one species of particle can be sufficient for an attractive pair interaction between dissimilar particles. This results in an 'OR' type of "truth-table" for a binarised value of

$\left(\frac{\mathrm{d}\alpha}{\mathrm{d}\psi_{\mathrm{s},\infty}}\right)$ characterising cluster formation in mixtures of particles, where "0" represents $\frac{\mathrm{d}\alpha}{\mathrm{d}\psi_{\mathrm{s},\infty}} \to 0$ and "1" implies $\frac{\mathrm{d}\alpha}{\mathrm{d}\psi_{\mathrm{s},\infty}} > 0$ for anionic particles. Note that we omit detailed discussion of the influence of surface potential values, $\psi_{\mathrm{s},\infty,1}$ and $\psi_{\mathrm{s},\infty,2}$, on this set of observations because the measured ζ potentials indicate similar values of $\psi_{\mathrm{s},\infty}$ for both species, particularly in the strongly cluster-forming range of pH 4-8.

S3.7 Protein pair-interaction modelling and calculation of a protein phase separation response as a function of pH and salt concentration

Here we describe an analysis performed in order to obtain a qualitative indication of the ability of a system of identical, electrically charged protein molecules to phase separate depending on the pH and salt concentration in solution. In this analysis we regard droplet formation in proteins as similar to cluster formation in colloidal particles. Analogous to the observations on colloidal interactions we assume that a net attraction in the pair interaction energy is required for individual protein molecules to overcome translational entropy and coalesce into a separate droplet-phase. We consider two different total interaction potentials, $u(x)$: the "canonical DLVO potential" $u_{\mathrm{DLVO}}(x)$, and our proposed pair interaction potential that includes the interfacial solvation contribution to the DLVO interaction energy, i.e., $u^*_{\mathrm{tot}}(x)$.

We consider two spheres of radius $R = 2.5$ nm carrying 5 ionisable Glutamic acid residues (p$K = 4.5$) and calculate the distance dependent pair interaction energy using a procedure identical to that used for colloidal particles (see Section S3.2). The radius and net charge of the spheres in this analysis are characteristic of but not identical to the yeast wild-type protein Sup35 which has recently been shown to undergo phase separation and carries a net excess of 6 acidic amino acids (aspartic and glutamic acids) over the number of basic side chains (lysine and arginine) in the domain that controls its phase segregation response [42].

Thus we calculate both $u_{\mathrm{DLVO}}(x) = u_{\mathrm{vdW}}(x) + \Delta F_{\mathrm{el}}(x)$ as well as $u^*_{\mathrm{tot}}(x) = u_{\mathrm{DLVO}}(x) + \Delta F_{\mathrm{int}}(x)$ as previously described for colloidal particles and outlined in Section S3.2. We approximate the vdW interaction energy using the expression for interacting

spheres of radius $R \sim x$. Thus we have: $u_{\mathrm{vdW}}(x) = -\frac{A_{\mathrm{H}}}{12}\frac{R}{x}$, where we take the Hamaker coefficient $A_{\mathrm{H}} = 3\,k_{\mathrm{B}}T$ in line with the 3-10 $k_{\mathrm{B}}T$ range expected for proteins at $T = 298\,K$ (Ref. 43). We use the sign and magnitude of $u(x)$ at small separations as an indication of the presence or absence of an attractive interaction required to trigger phase segregation or droplet formation in solution. In particular, we examine the value of $u = u(x = 1\,\mathrm{nm})$ in scenarios corresponding to $u_{\mathrm{DLVO}}(x)$ and $u^{*}_{\mathrm{tot}}(x)$, i.e., both with and without the interfacial free energy contribution. In particular, $u_{\mathrm{vdW}} = u_{\mathrm{vdW}}(x = 1\,\mathrm{nm}) \approx -0.6\,k_{\mathrm{B}}T$. Note that an inter-protein spacing of $x = 1\,\mathrm{nm}$ corresponds to a concentration of protein within the droplet of $c_{\mathrm{drop}} \approx 5$ mM, which is a typical value reported in biological phase separation studies[44]. Fig. 6 and Fig. S10 displays two-dimensional plots of both u_{DLVO} and u^{*}_{tot} as a function of pH and salt concentration for the two interacting spheres. A change of sign in u from net repulsive ($u > 0$, red) to attractive behaviour ($u < 0$, blue) is indicative of the possible onset of phase separation.

But clearly the sign of the interaction energy, u, is not the only determinant of phase separation. Although it may be expected that an attractive pair potential is a necessary condition for phase separation, it is by no means sufficient. In order for an attractive pair interaction potential to dominate the overall phase behaviour and result in observable phase separation, the total interaction energy experienced by a molecule within a droplet would need to outweigh the loss in entropy associated with its state in free solution. The (unfavourable) entropic contribution to the free energy for a molecule moving from bulk solution into the droplet may be estimated as $+k_{\mathrm{B}}T\ln\left(\frac{c_{\mathrm{drop}}}{c_{\mathrm{bulk}}}\right)$ per molecule, where c_{drop} denotes the concentration of protein in the droplet/condensate phase and c_{bulk} denotes the concentration of protein in bulk solution.

In other words, at the boundary of stability, we require the chemical potential μ of the protein species in the two phases to equal, i.e.,

$$\mu_{\mathrm{drop}} = \mu_{\mathrm{bulk}} \qquad \text{S 19}$$

We write an expression for the excess free energy of the protein in the droplet as the sum of the entropy of all n molecules in the droplet and an energetic term u_{drop} that is

represented by the sum of all the pairwise of interactions of protein molecules situated at distance given by an estimated interprotein separation in the droplet. Thus we have $F_{\mathrm{drop}} = n[u_{\mathrm{drop}} + k_{\mathrm{B}}T\ln(c_{\mathrm{drop}})]$. Since $\mu = \frac{dF}{dn}$, we have $\mu_{\mathrm{drop}} = u_{\mathrm{drop}} + k_{\mathrm{B}}T\ln(c_{\mathrm{drop}})$. Similarly, in the bulk phase, where there are no nearest neighbour interactions to consider we have $u_{\mathrm{bulk}} = 0$ and therefore $\mu_{\mathrm{bulk}} = k_{\mathrm{B}}T\ln(c_{\mathrm{bulk}})$. Applying Eq. S19 we have

$$u_{\mathrm{drop}} + k_{\mathrm{B}}T\ln(c_{\mathrm{drop}}) = k_{\mathrm{B}}T\ln(c_{\mathrm{bulk}}) \qquad \text{S 20}$$

here u_{drop} is the total (stabilizing) free energy of interaction of a single molecule of protein in the droplet state relative to the bulk state. As a consequence, when stable droplets are observed we may expect the following condition to hold:

$$u_{\mathrm{drop}} < k_{\mathrm{B}}T\ln\left(\frac{c_{\mathrm{bulk}}}{c_{\mathrm{drop}}}\right) \qquad \text{S 21}$$

Taking typical values of $c_{\mathrm{bulk}} \approx 10 - 100\ \mu\mathrm{M}$ and $c_{\mathrm{drop}} = 5$ mM gives $\frac{c_{\mathrm{drop}}}{c_{\mathrm{bulk}}} \lesssim 500$ (Ref. 44). Thus if the energetic contribution satisfies $u_{\mathrm{drop}} \lesssim \ln(500) \cong -6.2\ k_{\mathrm{B}}T$, we may expect phase segregation to occur. We point out that in the present analysis, c_{bulk} is the concentration of protein in the bulk solution at equilibrium with the droplet phase, but this value could be lower than the starting nominal concentration of protein in the experiment.

Importantly, a molecule in a droplet condensate engages in polyvalent interactions with more than one nearest neighbour. Therefore u_{drop} is not the same as the pair interaction energy u (Fig. S10). In order to estimate u_{drop}, we assume a coordination number of ≈ 10 per molecule (which is the average of number of nearest neighbours in body-centered and face-centered close-packing) (Fig. S10i). We also assume that the total interaction energy for a molecule in the droplet state can be regarded as pairwise additive to the first approximation. Thus a total stabilizing interaction energy of $u_{\mathrm{drop}} = -6.2\ k_{\mathrm{B}}T$ for a single molecule in the droplet state corresponds to a pair interaction energy of $u \approx -0.62\ k_{\mathrm{B}}T$ for a single pair of molecules. We may therefore expect phase separation in the region of the diagram where $u < -0.62\ k_{\mathrm{B}}T$.

Fig. S10e displays a coexistence curve in the total interaction energy diagrams corresponding to $\mu_{\mathrm{drop}} = \mu_{\mathrm{bulk}}$, which in this case denotes the condition $u_{\mathrm{c}} = -0.63\ k_{\mathrm{B}}T$.

The coexistence curve separates the parameter space into a region where phase separation (droplet formation) may be expected to occur ($u < u_c$) and another where the suspension may be expected to remain uniformly dispersed ($u > u_c$). Comparing the coexistence curves in the DLVO and in the interfacial solvation free energy diagrams, we note a marked qualitative difference between the two predicted behaviours (Fig. S10g, h). Remarkably the interfacial solvation model is able to qualitatively capture the recently reported pH and salt concentration dependent phase separation behaviour for the wild type Sup35 protein (Fig. S10h, k, l). Here, similar to other observations in the literature, droplet formation is enhanced as the salt concentration is lowered. Droplet formation is also expected to be significant at lower pH, but in fact occurs at pH values significantly higher than the pK values of the ionisable groups, where the molecules retain significant amounts of negative charge and the electrostatic repulsion term ΔF_{el} remains substantial (Fig. S10a,f). Droplet formation vanishes at high pH where the electrostatic repulsion overwhelms all other attractive contributions.

For the same value of $u = u_c$, the DLVO model would suggest no phase separation at all (Fig. S10g, j). The sole source of intermolecular attraction in the DLVO model is the vdW contribution to the pair interaction, $u_{vdW} \approx -0.6\, k_B T$, which we assume to remain constant regardless of pH and salt concentration. In this analysis the vdW contribution alone appears insufficient to overcome the entropy loss due to droplet formation. However, assuming for argument that the vdW contribution were larger and indeed sufficient to sustain a phase separation response on its own (say $u_{vdW} \approx -1\, k_B T$), then the region corresponding to $u \approx 0$ (white band in Fig. S10d) in the DLVO interaction energy diagram presents an approximate contour of a possible coexistence curve. Clearly the pH -salt dependence of such a coexistence curve, is very different to the experimental observations (Fig. S10d). Under the influence of a DLVO type of interaction, phase separation would be expected to occur at higher salt concentrations, regardless of pH, which is not supported by experimental observations on proteins such as Sup35 and Ddx4[42,44] (Fig. S10l).

Finally it is worth noting that for particles carrying mixed acidic and basic groups of different $\mathrm{p}K$ values, such as proteins, where the interacting objects may have a nominal net charge of a given sign, but in fact carry non-uniform patchy regions of charge of either sign, the overall $\mathrm{p}H$ and salt concentration dependence of ΔF_{int}, and therefore the phase separation behavior, could be more complex. Here, the sign of $\frac{\mathrm{d}\alpha}{\mathrm{d}\psi_{\mathrm{s},\infty}}$ for the local charged patches or groups is a decisive factor, and the requirement for $\left|\frac{\mathrm{d}\alpha}{\mathrm{d}\psi_{\mathrm{s},\infty}}\right|$ to be large may be met at more than one $\mathrm{p}H$ value or over a range of $\mathrm{p}H$ values. The present analysis however focuses on the simplest of systems where the objects carry ionizable groups of the same qualitative nature, i.e., acidic.

Ultimately a model of interactions including amino acid residue level detail may be required to provide quantitative calculations of the behaviour expected of proteins within the interfacial solvation model. Future work could examine the use of molecular simulations that incorporate both explicit water and charge regulation of ionisable protein groups in order to construct more accurate models of interaction free energies for a variety of molecular systems[45]. Note that the charge-asymmetry of the interfacial solvation contribution we describe by no means precludes coacervate formation in positively charged molecular systems containing aromatic rings. Here, condensate formation is believed to be driven by an attractive cation-π interaction[46].

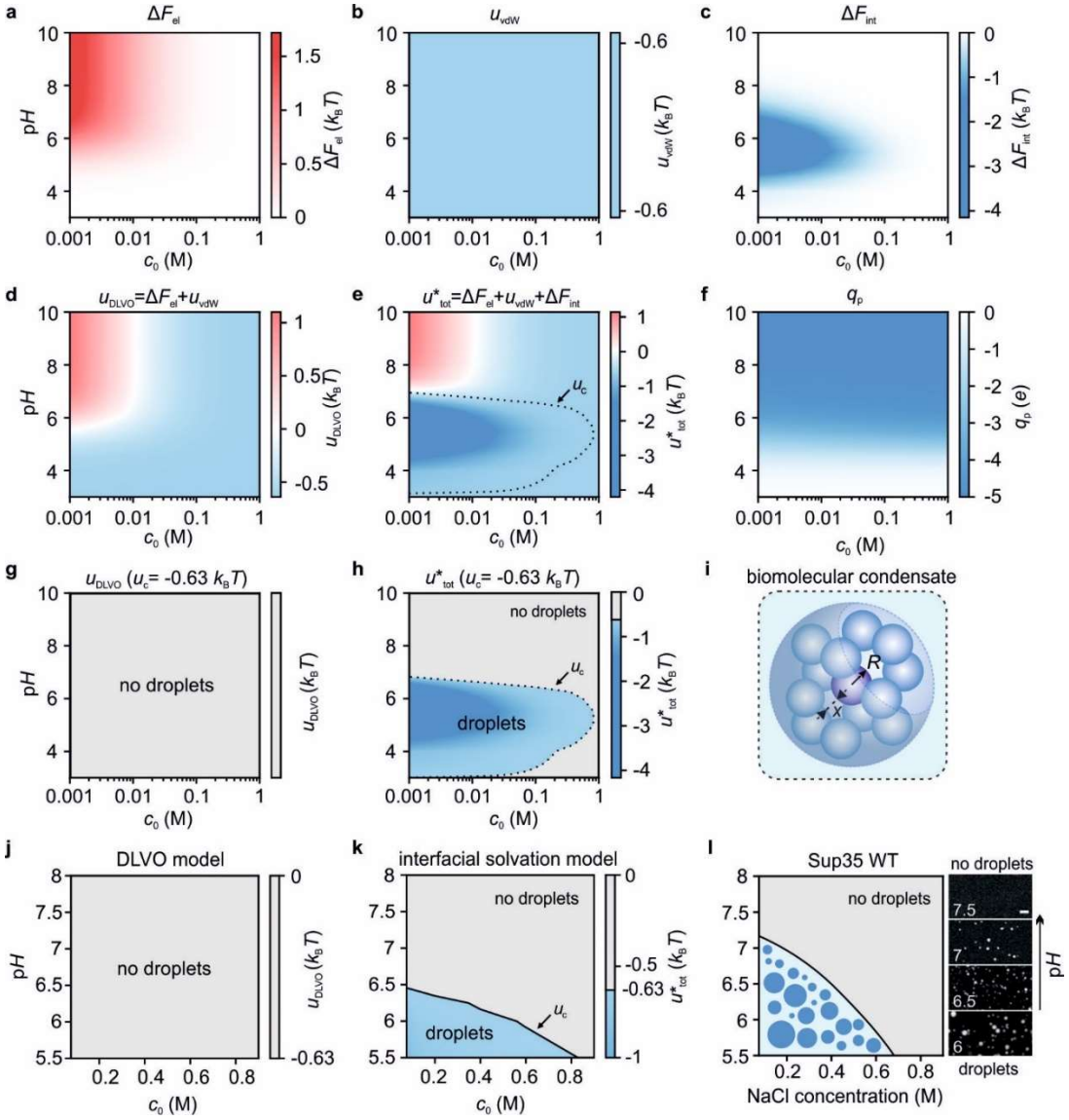


Fig. S10. Biomolecular condensate formation from protein molecules (a-c) Plots of the various contributions to the pair interaction energy $u^*_{\rm tot}(x)$ for a pair of negatively charged protein molecules, calculated as a function of pH and salt concentration c_0 at an intermolecular separation $x = 1$ nm. With the interaction energy referenced to zero at $x = \infty$, positive and negative values of interaction free energies at $x = 1$ nm are indicative of repulsion or attraction respectively. **a**: The electrostatic free energy, $\Delta F_{\rm el}$, is substantial and positive particularly for p$H > 5$, implying a repulsive Coulombic interaction, as expected. **b**: the attractive vdW interaction energy, $u_{\rm vdW} = -0.6\, k_{\rm B}T$, which we assume is not a function of pH or salt concentration. **c**: The interfacial solvation free energy, $\Delta F_{\rm int}$, displays a substantially negative contribution in the range of pH 4 to 7.5 and at lower salt concentrations. (**d**) Total interaction energy $u_{\rm DLVO} = \Delta F_{\rm el} + u_{\rm vdW}$ expected from a DLVO model of interactions. (**e**) Total interaction energy $u^*_{\rm tot} = u_{\rm DLVO} + \Delta F_{\rm int}$ expected following inclusion of the interfacial solvation contribution in the total interaction energy. Black dotted contour denotes the coexistence curve given by $u_{\rm c} = -0.63\, k_{\rm B}T$. (**f**) Calculated protein charge, $q_{\rm p}$, shows that the charge on the molecules remains substantially negative over a wide range pH values. (**g, j**) The DLVO model suggests no phase separation regardless of pH and c_0 with $u_{\rm c} = -0.63\, k_{\rm B}T$, as expected. Setting $u_{\rm c} > -0.5\, k_{\rm B}T$ would in fact support the prediction of phase separation based on this interaction energy diagram, however the contour of the resulting

coexistence curve would be significantly different from experimental observations (see panel (l)), as is evident from the 'white region' in the plot in (d). (**h, k**) Expected dependence of phase separation on $\mathrm{p}H$ and c_0 from the interfacial solvation model. (**i**) Schematic depiction of a phase-separated biomolecular condensate (droplet) showing a single molecule of radius R engaged in interactions with 12 nearest neighbours. (**l**) Measured $\mathrm{p}H$ and salt concentration dependence of the phase separation of yeast wild-type protein Sup35. The region shaded blue depicts conditions that support the formation of droplet condensates. Fluorescence images of condensate formation at a salt concentration of ≈ 0.1 M depict marked reduction and disappearance of droplets at $\mathrm{p}H > 6.5$. Experimental data reproduced with permission from Ref. 42.

We conclude with a few final comments embedding our observations in the broader context of the history of experimental investigation of the interaction between charged objects in solution and the conventional expectation that PB theory, which always predicts repulsions, is expected to hold, especially in solutions containing low concentrations of monovalent ions. Our calculation of the pair interaction potential that arises *when charge regulation couples to the behaviour of interfacial water (*whose properties we have obtained from atomistic MD simulations) shows that there are conditions where like charged particles attract as well as a range of conditions where they repel in accordance with the canonical expectation. From the perspective of the model therefore, it is expected that experiment can and does often show full agreement with PB theory: e.g., our own experiments on positively charged particles in water, as well as negatively charged particles at $\mathrm{p}H$ values reasonably far away from the $\mathrm{p}K$, show behaviour that one would consider in full agreement with PB theory. Note also that it comes as no surprise that theoretical studies that have extensively examined the topic (without considering the effects that we account for in combination) have not reported the possibility of attraction between like-charged particles.

To sum up the observations in our study, the ability to *qualitatively* alter the attractive or repulsive nature of an interparticle interaction at long range by tailoring the surface properties of the particle points to an interfacially governed contribution to the total interaction free energy of a pair of particles in solution. The amenability of the interaction to tuning using the solution $\mathrm{p}H$ and particle $\mathrm{p}K$ strongly suggests that charge regulation plays a defining role in the magnitude of the free energy contribution. The interparticle interaction further displays a stark qualitative asymmetry with respect to

the charge on the particle such that *the sign of the particle charge determines the sign of the force* at long range. Importantly, the type of charge-reversal asymmetry observed in water can be inverted through the use of a solvent with different structural and interaction properties. Our proposed mechanism invoking the excess free energy associated with solvent orientation at an interface captures all these features and explains the experimental observations. The remit of the problem specifically covers pH and salt-concentration dependent cluster or phase formation, as reported in a range of chemical and biochemical processes. Examples of relevant assembly processes range from gelation, coagulation, crystallisation and biological phase segregation to histone-modulated packaging of DNA, virus binding to sulfonated carbohydrates on host cells, biofouling, or indeed any experimental situation where counterintuitive attractions are implicated between suspended entities carrying net electrical charge of the same sign (negative in the aqueous phase).

S4 Supplementary Results

S4.1 Interactions in silica particles in water without prior treatment with NaOH

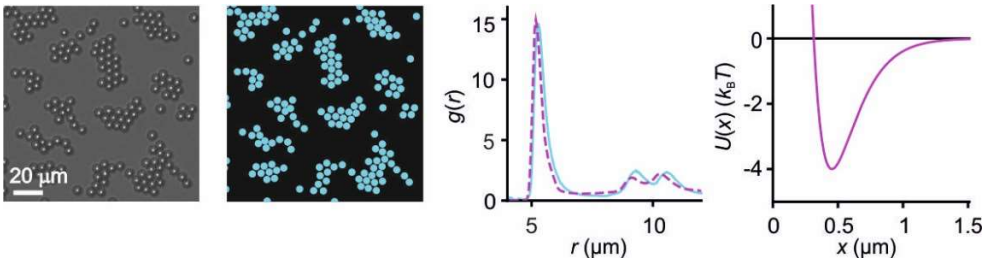


Fig. S11. Interaction of silica particles in deionised (DI) water prepared without prior NaOH treatment. (Left) Experimental and digitised microscopy images of clusters of silica colloids in DI water that had no prior NaOH treatment, as is standard practice for the experiments in this work. The experimental protocol here involved washing the silica particles 5 times in DI water, leaving for 12 hours in DI and then washing again 5 times before being resuspended in the experimental cell. Particles are represented as coloured discs of uniform diameter $2R$ on black background. (Right) Overlays of experimental and simulated $g(r)$ (solid blue and dashed magenta-coloured lines respectively). Also shown is the corresponding inferred pair interaction potential $U(x)$ of the form of Eq. S 6, which is used as an input to a BD simulation to match the experimental data. Parameters corresponding to the inferred $U(x)$ curve are $A = 2137.051$, $B = -1903.887$, $\frac{\kappa_2}{\kappa_1} = 0.95$, and κ_1^{-1} =136 nm.

S4.2 Direct measurements of interaction potentials for pairs of isolated particles

We have further measured the interaction potential between isolated pairs of particles in solution. Fig. S12 presents measurements of the pair potential by single particle tracking of two interacting COOH particles.

In order to directly measure the pair interaction potential $U(x)$ we focused our attention on the behaviour of isolated, diffusing pairs of particles. We define an isolated pair as one where the particles are several particle diameters away from all other neighbouring particles. We examined particle pairs in experiments on COOH particles similar to those shown in Fig. 1. Images were recorded at a frequency of 10 fps using exposure times less than 1 ms. Frame-by-frame tracking of particle centres over a total measurement period of 50 seconds permitted us to construct a histogram of interparticle distances, r. We then converted the measured radial number density function, $N(r)$, into a radial probability density function, $P'(r) = \frac{N(r)}{2\pi\ \Delta r}$, where Δr is the width of a bin in

the histogram. We work with a rescaled probability density function $P(r) = \frac{P\prime(r)}{P'_{\max}(r)}$ where $P'_{\max}(r)$ is the maximum value of the measured radial probability density function, $P'(r)$. Subsequently, we replaced the interparticle distance variable, r, with the intersurface separation, x, using the relation $x = r - 2R$, where $2R = 5.29$ μm is the nominal average diameter of the COOH particle sample. We then obtained a measured pair potential $U(x)$ by Boltzmann inversion of the intersurface probability density function, i.e., $U(x) = -k_B T \ln [P(x)]$. Error bars on the free energy values for each of the measured points are derived from a shot-noise estimate given by $\sqrt{N(r)}$ for each bin of the number density histogram. Note that all measurements of inter-separation, x, in such pair-potential measurements could contain a large systematic uncertainty, of approximately 100 nm for COOH particles, which arises from the absence of information on the true particle radii in the interacting pair of interest.

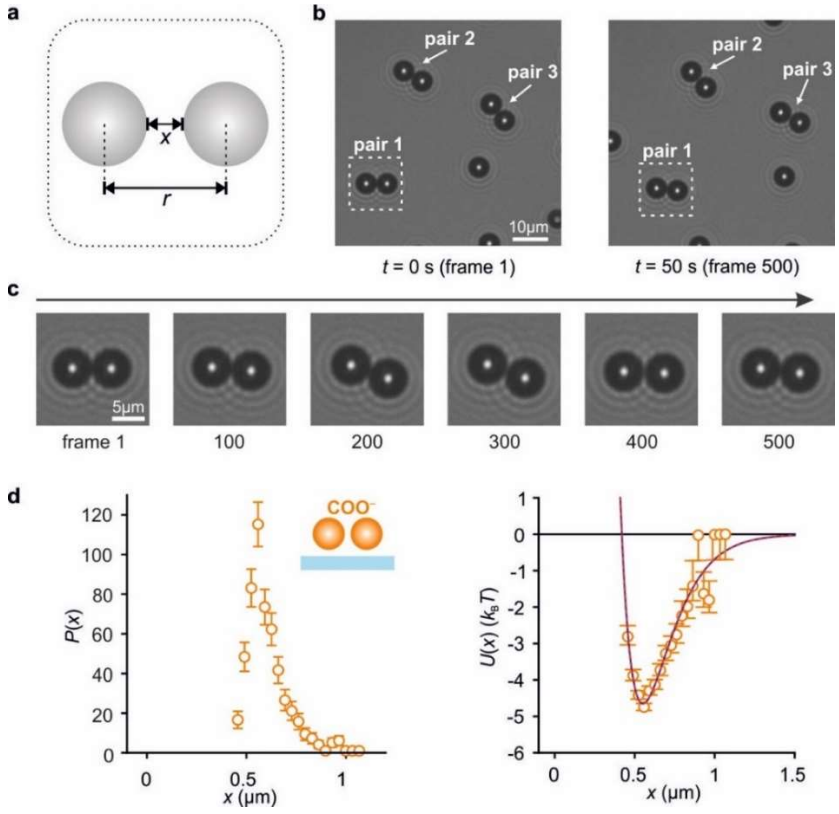


Fig. S12. Direct measurement of pair-interaction potentials for COOH particles. (**a**) Schematic of a pair of colloidal particles with center-to-center distance and intersurface separation of a particle denoted by r and x respectively. (**b**) Experiments on a low concentration of particles (approximately factor 2 lower than for the cluster experiments) under solution conditions that display particle clustering often contain isolated, strongly interacting "bound pairs" of particles

located several micrometers from other neighbouring particles as indicated (top) (**c**) Snapshots in time of an interacting pair of particles (middle panel) over a period of 500 frames corresponding to 50 s. (**d**) Probability density distribution, $P(x)$, (left panel) of the intersurface separation, x, acquired over a typical period of 50 s, and measured pair-interaction energy profile, $U(x)$, (right panel) for a single pair of COOH particles. The measured $U(x)$ data (orange symbols) are presented together with fits to Eq. S 6. In one case we treat A, B and the screening length κ_1^{-1} as free parameters and hold the ratio of the two screening lengths fixed, i.e., $\frac{\kappa_2}{\kappa_1} = 0.95$ (blue dashed line). In the second case, we treat A, B and the ratio of the two screening lengths $\frac{\kappa_2}{\kappa_1}$ as free parameters, holding the Debye length fixed at $\kappa_1^{-1} = 129$ nm, which is the value corresponding to the experimentally measured ionic strength (red dashed line). The fit parameters in each case are as follows: Fit #1 (blue dashed line): $A = 6403$, $B = -5441$, $\kappa_1^{-1} = 129 \pm 9$ nm, $R^2 = 0.83$; Fit #2 (red dashed line): $A = 7139$, $B = -6174$, $\frac{\kappa_2}{\kappa_1} = 0.96 \pm 0.13$, $R^2 = 0.91$. Fit parameter values averaged over 11 different COOH pairs yield: Approach #1: $A = 14882$, $B = -11789$, $\kappa_1^{-1} = 114 \pm 8$ nm, $R^2 = 0.87$, and Approach #2: $A = 1118707$, $B = -1117949$, $\frac{\kappa_2}{\kappa_1} = 0.96 \pm 0.06$, $R^2 = 0.83$. Error bars on $P(x)$ and $U(x)$ values for each of the measured points are derived from a shot-noise estimate given by $\sqrt{N(r)}$, as described in Section S4.2.

S4.3 Optical artifacts in particle tracking do not influence the measurements

Prior work on the measurement of pair interaction potentials between colloidal particles has demonstrated that conventional particle tracking algorithms, which make use of centroid or radial symmetry methods to determine particle location, are prone to errors in particle localisation[47-49]. Errors may be expected especially when particles are in very close proximity with one another and the intensity distribution around each particle is affected by that of its neighbour.

Baumgartl *et al.* pointed out that overlapping of particle images distorts positional information on particles, giving rise to a subtle distortion of a measured interaction potential corresponding to apparent measured minima of 0.2-0.5 $k_\mathrm{B}T$ depth[47]. We measure attractions in the range of 5 $k_\mathrm{B}T$ where the experimental uncertainty on inferred depth is itself of the order of 1 $k_\mathrm{B}T$. Therefore at the outset, we expect that any contribution from optical artifacts to our estimate of minima depths is smaller than the depth of potential measured in most cases, and also smaller than our experimental uncertainty. Furthermore from the literature, the spurious appearance of a minimum in an otherwise purely repulsive interaction would seem to be relevant for smaller particles (2 μm diameter or less). The apparent potential minimum results from a redistribution of probability density as a function of separation. For larger particles of 5 mm diameter

as in our work, Ref. 49 presents a calculation of the error in position determination using conventional centroid based and radial symmetry based tracking methods. Applying the theoretically expected correction as well as the algorithm provided in Yücel *et al.* to correct our particle localisation measurements we obtain the results shown in Fig. S13 below[49]. As expected the corrections due to optical effects are within the errors of the measurement.

The next particle tracking correction method we applied to our data followed the approach outlined in Ref 48. Here, an image of an isolated particle and its associated diffraction pattern is used to construct a series of composite images of particles at a known separation r_t. The 'apparent' separation r_m is then determined by the same image analysis method (the radial symmetry method) used to analyse experimentally acquired images, and the difference $r_t - r_m$ found as a function of r_t (see Fig. S13c). The maximum error in the inferred interparticle distance $r_t - r_m = 37$ nm occurs at an inter-particle separation corresponding to the distance of nearest approach $r_t = 2R$. The functional form of the correction shown in Fig. S13c was linearly interpolated and applied to correct the inter-particle distances measured in an experiment of two interacting COOH particles. These corrected distances were then used to obtain corrected pair interaction potentials $U(x)$ (see Fig. S13b), using the method outlined in the previous section.

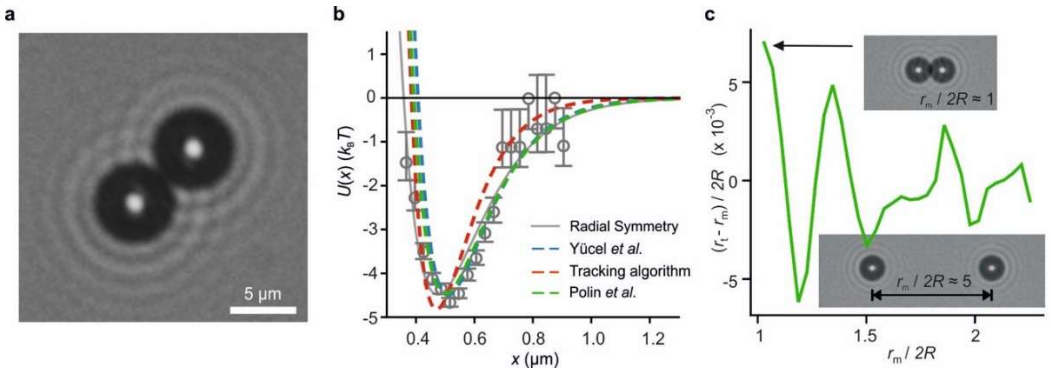


Fig. S13. Application of particle tracking corrections and their effect on the measured pair interaction potentials $U(x)$. (**a**) Digital video microscopy snapshot of a pair of interacting COOH particles, diameter $2R$ = 5.29 μm. The particle images are characterised by a bright intense region at the particle centers, surrounded by a dark ring and associated diffraction pattern. (**b**) Measured pair interaction potentials, $U(x)$, calculated using the method outlined in Section S4.2, and for which the particle center coordinates were determined via the TrackNTrace particle

tracking code employing the radial symmetry method[4] (grey symbols, accompanied by grey fit curve) i.e. the particle tracking method used in all experiments in this work. Fits to $U(x)$ data obtained by applying a correction to the measured distances according to Ref. 49 (blue dashed line), applying the particle tracking algorithm provided in Ref. 49 to our experimental data (red dashed line) and applying a different correction to r as described in Ref. 48 (green dashed line). All fits of $U(x)$ data are to the form to Eq. S 6 and were performed setting $\frac{\kappa_2}{\kappa_1} = 0.95$ in all cases. The parameters are as follows: (1) $A = 5596$, $B = -4779$, $\kappa_1^{-1} = 113$nm (grey) (2) $A = 13926$, $B = -11363$, $\kappa_1^{-1} = 100$ nm (blue) (3) $A = 24819$, $B = -19743$, $\kappa_1^{-1} = 84$ nm (red), and (4) $A = 10166$, $B = -8424$, $\kappa_1^{-1} = 105$ nm (green). The fit error in the quoted Debye lengths, κ_1^{-1}, does not exceed 8 nm for all cases. Good agreement between the various curves shows that particle-tracking correction methods have a negligible effect on the inferred well depth w and $x_{\min}$ values of the underlying pair interaction potential. Error bars on $U(x)$ values for each of the measured points are derived from a shot-noise estimate given by $\sqrt{N(r)}$, as described in section S4.2. (**c**) Plot of the expected difference $r_t - r_m$ between the true and measured interparticle separation as a function of r_t, for our experimental system, using the method of Ref. 48.

S4.4 The long-range attraction is not influenced by surface charge on the neighbouring coverglass surface

In order to examine the role played by the neighbouring, like-charged bounding surface we performed measurements on clusters and bound pairs of particles using a coverglass (as shown in Fig. S3) coated with a thin metal layer that masks the surface charge. We used conformal coatings of 5 nm Chrome as well as surfaces patterned with Cr-Au films (see Fig. S14). Cluster formation occurs regardless of the magnitude and spatial distribution of charge on the underlying surface. Measurements on clusters in the vicinity of metal films yielded pair-potentials whose parameters (Debye length κ_1^{-1} and depth of minimum w) agreed within error with measurements performed using uncoated glass surfaces (Fig. S14a).

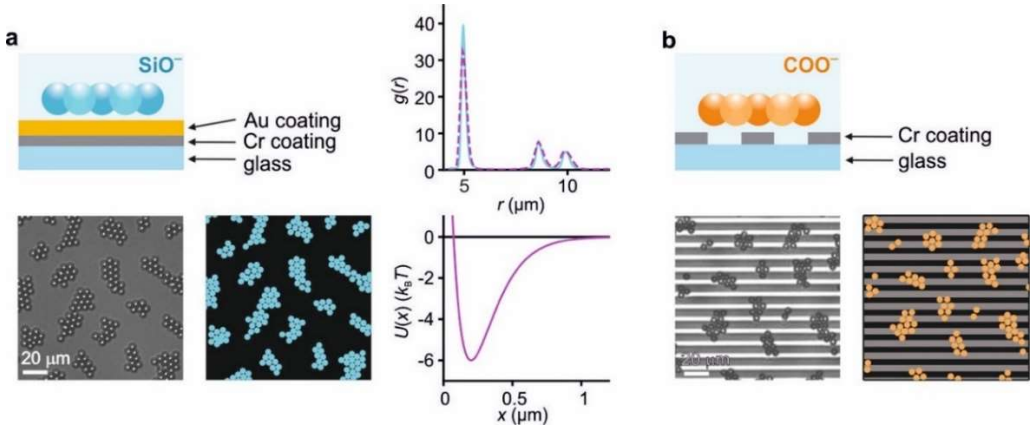


Fig. S14. Examining the effect of coating the underlying coverglass of the experimental cell with thin metal films. (**a**) Schematic representation of the experimental

system displaying a cluster of SiO_2 particles above the underlying coverglass which is coated with a 5 nm thick chrome (Cr) film followed by a 10 nm thick gold (Au) film (top), in order to suppress any electrostatic contribution from the glass, similar to Ref. 48. Experimental and digitised microscopy images of silica colloidal clusters formed above the gold coated surface. Particles are represented as coloured discs of uniform diameter $2R$ on a black background (bottom left). Overlays of experimental and simulated $g(r)$ data (solid blue and dashed magenta-coloured lines respectively) (top right). Corresponding inferred pair interaction potential $U(x)$, used as input to a BD simulation to match the experimental $g(r)$ (bottom right). $U(x)$ has the form of Eq. S 6 where $A = 571.1803$, $B = -554.6975$, $\frac{\kappa_2}{\kappa_1} = 0.95$, and κ_1^{-1} =124 nm which corresponds to the experimentally measured salt concentration. These values maybe compared with a direct pair-potential measurement of $U(x)$ in the same experiment presented in Extended Data Fig. 1d. Here we treat A, B and the screening length κ_1^{-1} as free parameters and hold the ratio of the two screening lengths fixed, i.e., $\frac{\kappa_2}{\kappa_1} = 0.95$. The fit parameters are $A = 928$, $B = -871$, and $\kappa_1^{-1} = 103 \pm 7\text{nm}$ ($r^2 = 0.83$ for the fit). (**b**) Schematic representation of the experimental system in which the coverglass surface is patterned with a 5 nm thick Cr film etched to create a surface with alternating metallised and non-metallised stripes of 5 μm width. (top). Experimental and digitised microscopy images of COOH colloidal clusters formed above the patterned Cr surface (bottom).

S4.5 Ionic strength dependence of cluster formation for COOH particles in aqueous solution

The general trends observed for interactions of COOH particles in response to the variation in solution ionic strength resemble those for SiO_2 particles: the attractions appear strongest at the lowest salt concentrations and gradually weaken with increasing salt concentration (Fig. S15 and Fig. S25c). However, the surface functional group density also plays an important part in the effect, as suggested by Eq. S 7. Carboxylated melamine resin particles in our experiments have nominal carboxyl group densities of 400 μmol/g. Interestingly, a sample of carboxylated polystyrene particles 6.39 μm in diameter (microParticles GmbH) with carboxyl group densities of 15 μmol/g did not display cluster formation behaviour in our experiments. Eq. S 7 clearly shows that the magnitude of the interfacial free energy contribution is proportional to the density of ionizable groups in the particle (Γ), providing a conceivable explanation for the absence of visible cluster formation in particle preparations carrying a low density of ionizable surface groups.

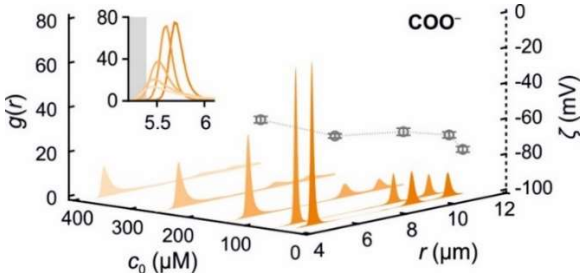


Fig. S15. Ionic strength dependence of the interactions of COOH particles in aqueous electrolyte at p*H*=5.8. The overall trend recapitulates the observations for SiO_2 particles. ζ-potential measurements represent mean values ± S.D from 3 sets of measurements.

S4.6 pH dependence of the interactions of PEI-coated silica particles

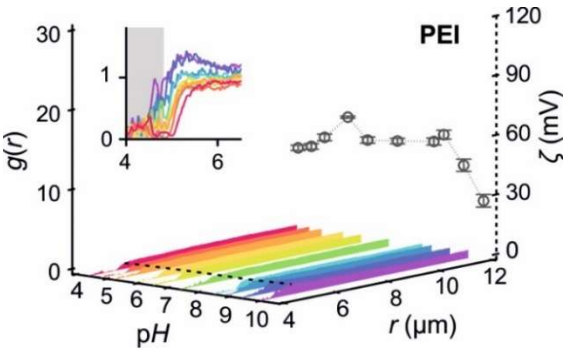


Fig. S16. p*H* dependence of the interactions of PEI-coated silica particles in aqueous electrolyte at constant salt concentration, c_0 ≈ 0.12mM NaCl. Negatively charged silica particles coated with PEI polymer (via the method outlined in Section S1.3) become positively charged over a broad p*H* spectrum, as reflected in the zeta (ζ) potential measured across this range. In accordance with the results shown in Fig. 3 for poly-K and PDADMAC polymers, no clustering is observed for these positively charged (coated) particles in water. Matching of the experimental radial probability distribution functions $g(r)$ with those from BD simulations for a polyelectrolyte coating experiment involving PEI coated particles give inferred pair interaction potentials $U(x)$ that are purely repulsive (see Fig. S23). ζ potential measurements represent mean values ± S.D from 3 sets of measurements

S4.7 Ionic-strength dependent swelling of positively charged polyelectrolyte coatings detected in $g(r)$ measurements

Although the $g(r)$ profile for a system of repulsive particles is relatively featureless, for experiments involving positively charged poly-K and PDADMAC coated particles we observe a markedly different profile for the radial probability distribution functions $g(r)$s when compared to positively charged NH_2-SiO_2 particles (see Fig. S17 and Fig. S23). We found that the slope of the $g(r)$ curve at a location around the nominal particle diameter was significantly smaller for the positively charged polyelectrolyte coated particles, gradually increasing and attaining a value of $g(r) \approx 1$ at an interparticle distance of $r \approx$

$8\ \mu m$ which is much larger than the corresponding value of $r \approx 5\ \mu m$ observed on experiments for NH_2-SiO_2 particles (Fig. S23). This is a significant disparity in behaviour given that the silica particles used for polymer coating experiments are only about 1 μm larger in diameter than the NH_2-SiO_2 particles. On first glance, this might suggest an exceptionally long ranged repulsion in the interparticle interaction. We noted however that varying the prefactor A and setting $B = 0$ in Eq. S 2 and varying the screening length for a purely repulsive pair interaction potential $U(x)$ could not capture the experimentally observed behaviour in a BD simulation. However, we then found that a BD simulation with a particle size distribution whose mean is larger than that of the nominal size distribution by about 1.7 μm was better able to match the experimental $g(r)$s (see Fig. S17). We suggest that the observations likely reflect a contribution to an enlarged effective particle size from swollen and highly repulsive polyelectrolyte brushes attached to the surface of the particles (Fig. S17a). PDADMAC used in the experiment has a molecular weight of 350,000 g/mol and a total contour length, l_{max}, of around 2 μm. Thus, nearly fully extended mutually repulsive polymer chains at the surface could be thought to contribute to a significant increase in the effective particle diameter (Fig. S17).

To further investigate this phenomenon and to test our hypothesis, PDADMAC coated particles were suspended in solutions of different salt concentrations and the corresponding $g(r)$s measured (see Fig. S17). At $c_0 = 0.05$ mM NaCl, the characteristic 'long range' behaviour can be observed in the $g(r)$. The region of the $g(r)$ with gradually increasing slope extended to as far as $r = 10$ µm which cannot be explained with the nominal particle diameter of $2R = 4.98$ µm and the relevant Debye length. We then found that increasing the salt concentration to 0.15 mM and higher, the form of the measured $g(r)$ altered substantially (see Fig. S17), reverting to behaviour that is captured in BD simulations performed using the nominal particle size distribution. We attribute these observations to ionic strength dependent electrostatic swelling and collapse of surface polymer brushes. We observe similar behaviour for poly-K coated spheres, and we model the interaction in a similar fashion.

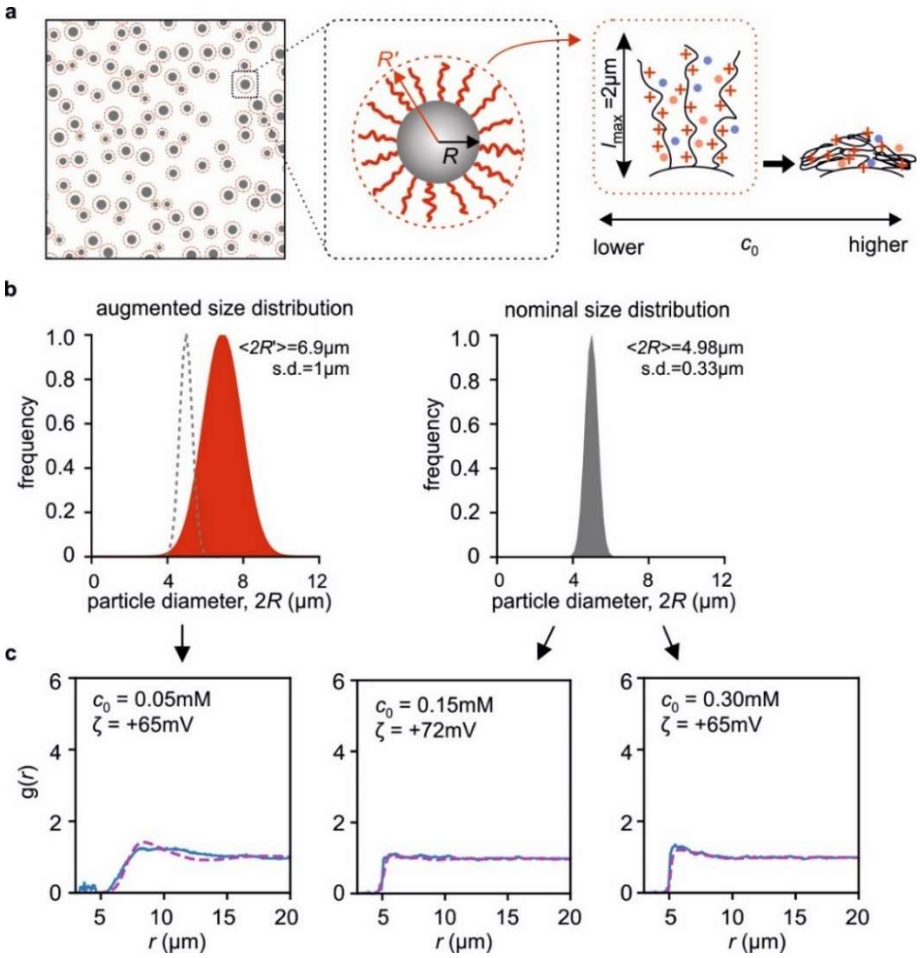


Fig. S17. Interactions of PDADMAC coated silica particles in electrolytes with different salt concentrations. (**a**) Illustration of the swelling and collapse of a positively charged polyelectrolyte brush at low salt and high salt concentrations, inferred from these measurements. Snapshot of a configuration of particles in a BD simulation (left). Silica particles are denoted as grey discs and the red halos around the particles denote an effective "swollen" diameter due to surface attached polyelectrolyte chains. (**b**) Particle size distributions used in BD simulations for polymer coated particles at low salt concentrations, $c_0 < 0.1$ mM (left) and higher salt concentrations (right). (**c**) Overlays of experimentally measured (blue) and simulated (dashed magenta) $g(r)$s for PDADMAC coated particles in solutions of different ionic strength. A particle size distribution with an increased average diameter of $2(R + l_{\mathrm{max}})$ was needed to better capture experiments at lower salt concentrations.

S5 Data Processing & Analysis

S5.1 Matching experimentally measured $g(r)$s with those from BD simulations

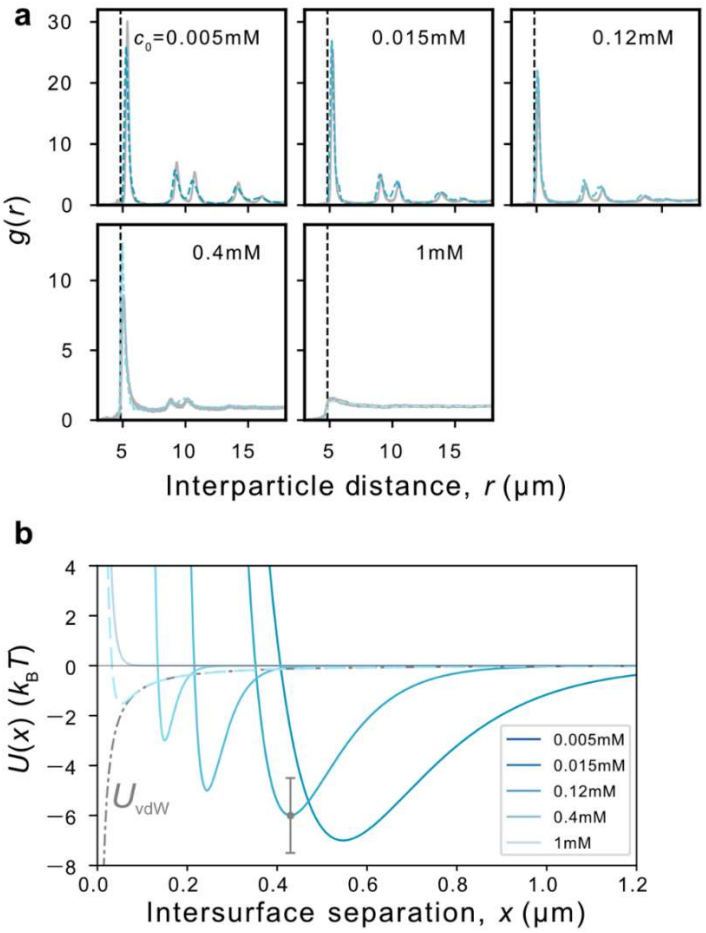


Fig. S18. Matching of the experimental radial probability distribution functions $g(r)$s with those from BD simulations for experiments that vary the salt concentration c_0 for SiO_2 particles in water (shown in Fig. 1). (**a**) The experimental and simulated data (grey and dashed shaded blue lines respectively) are presented overlaid. The black dashed vertical line indicates the nominal particle diameter. (**b**) Corresponding inferred pair interaction potentials $U(x)$. The grey dashed line shows the vdW contribution, which is discussed in detail in Section S2.1. The vertical error bar denotes an estimated uncertainty of $\pm 1.5\ k_B T$ in the overall process, arising from particle size uncertainties and drift in experimental conditions over time that affect cluster properties. The same set of curves presented in the main text figure includes a horizontal error bar on the intersurface separation x. This error bar captures the overall uncertainty in measured interparticle separation (arising from the particle size dispersion and localisation error, see Section S1.6), and is intended to facilitate comparison with a calculated theoretical pair potential where the particle diameter is fixed.

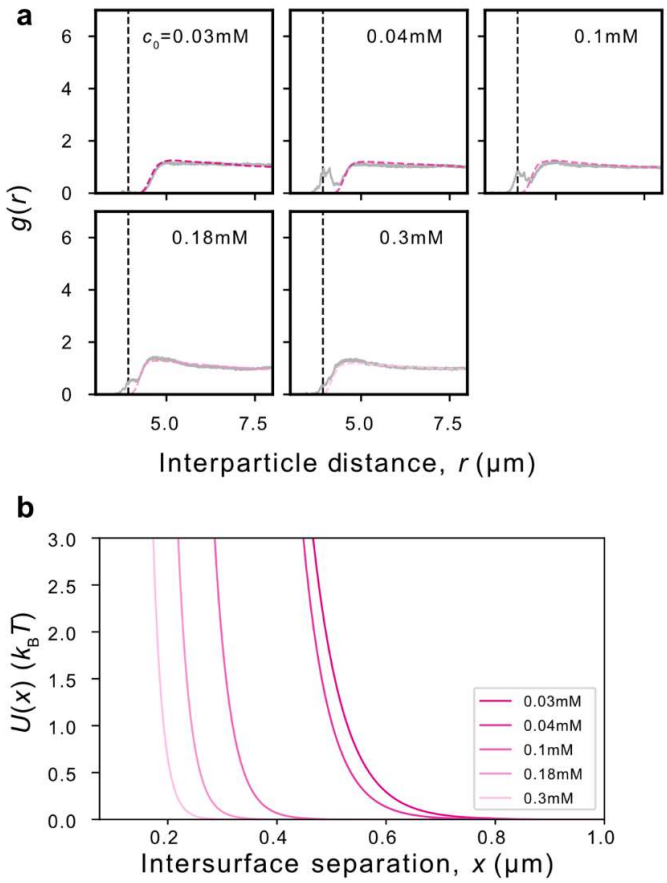


Fig. S19. Matching the experimental radial probability distribution functions $g(r)$s with those from BD simulations for experiments varying the salt concentration for NH_2-SiO_2 particles in water (shown in Fig. 1). (**a**) Overlays of experimental and simulated data (grey and dashed shaded pink lines respectively). The black dashed vertical line indicates the nominal particle diameter. (**b**) Corresponding inferred pair interaction potentials $U(x)$. The same set of curves presented in the main text figure includes a horizontal error bar on the intersurface separation x. This error bar captures the overall uncertainty in measured interparticle separation (arising from the particle size dispersion and localisation error, see Section S1.6), and is intended to facilitate comparison with a calculated theoretical pair potential where the particle diameter is fixed.

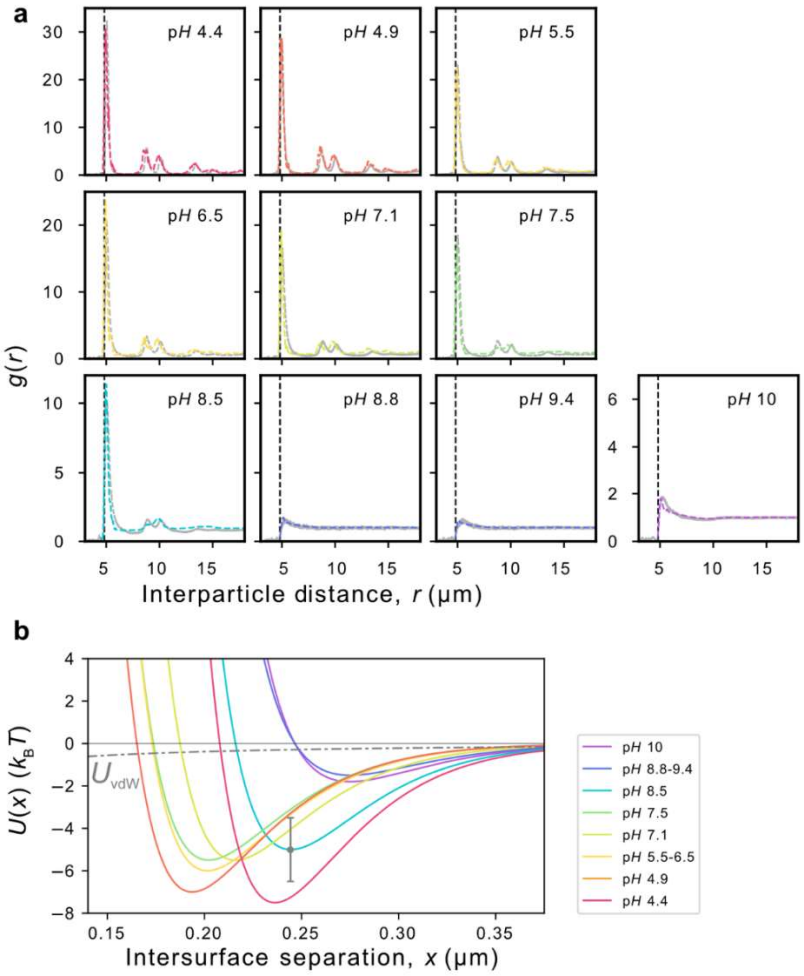


Fig. S20. Matching the experimental radial probability distribution functions $g(r)$s with those from BD simulations for experiments varying the pH for SiO_2 particles in water (shown in Fig. 2). (**a**) Overlays of experimental and simulated data (grey and dashed coloured lines respectively). The black dashed vertical line indicates the nominal particle diameter. (**b**) Corresponding inferred pair interaction potentials $U(x)$. The vertical error bar denotes an estimated uncertainty of $\pm 1.5\, k_B T$ in the overall process, arising from particle size uncertainties and drift in experimental conditions over time that affect cluster properties. The same set of curves presented in the main text figure includes a horizontal error bar on the intersurface separation x. The error bar captures the overall uncertainty in measured interparticle separation (arising from the particle size dispersion and localisation error, see Section S1.6), and is intended to facilitate comparison with a calculated theoretical pair potential where the particle diameter is fixed.

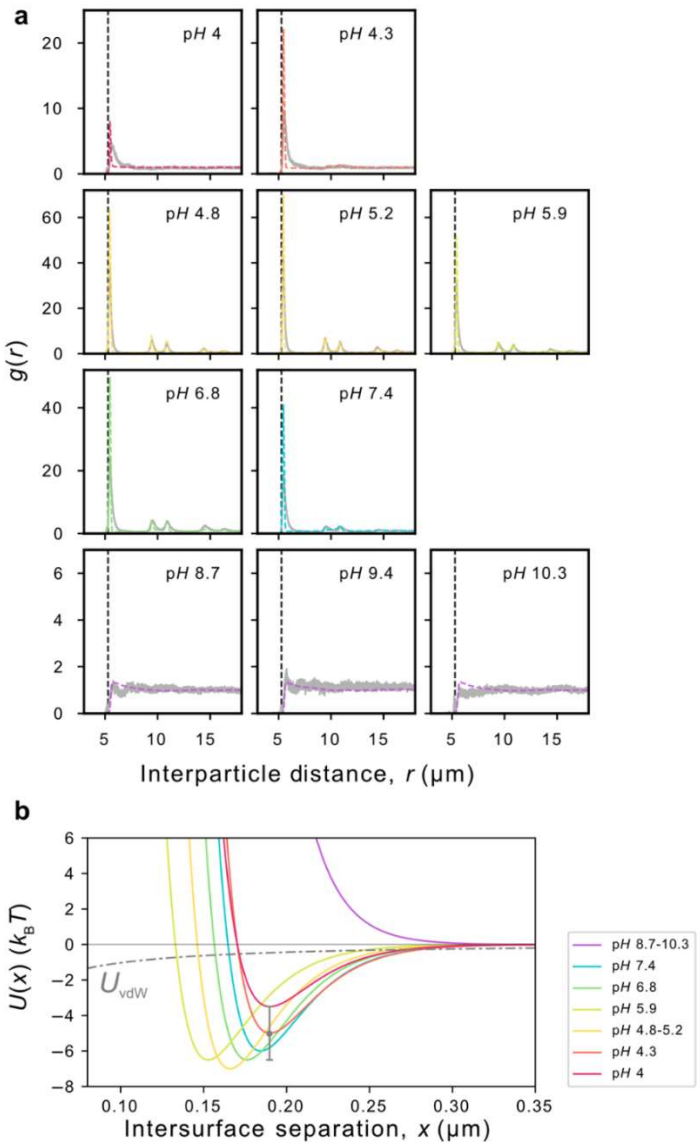


Fig. S21. Matching the experimental radial probability distribution functions $g(r)$s with those from BD simulations for experiments varying the pH for COOH particles in water (shown in Fig. 2). (**a**) Overlays of experimental and simulated data (grey and dashed coloured lines respectively). The black dashed vertical line indicates the nominal particle diameter. (**b**) Corresponding inferred pair interaction potentials $U(x)$. The vertical error bar denotes an estimated uncertainty of $\pm 1.5\, k_B T$ in the overall process, arising from particle size uncertainties and drift in experimental conditions over time that affect cluster properties. The same set of curves presented in the main text figure includes a horizontal error bar on the intersurface separation x. This error bar captures the overall uncertainty in measured interparticle separation (arising from the particle size dispersion and localisation error, see Section S1.6), and is intended to facilitate comparison with a calculated theoretical pair potential where the particle diameter is fixed.

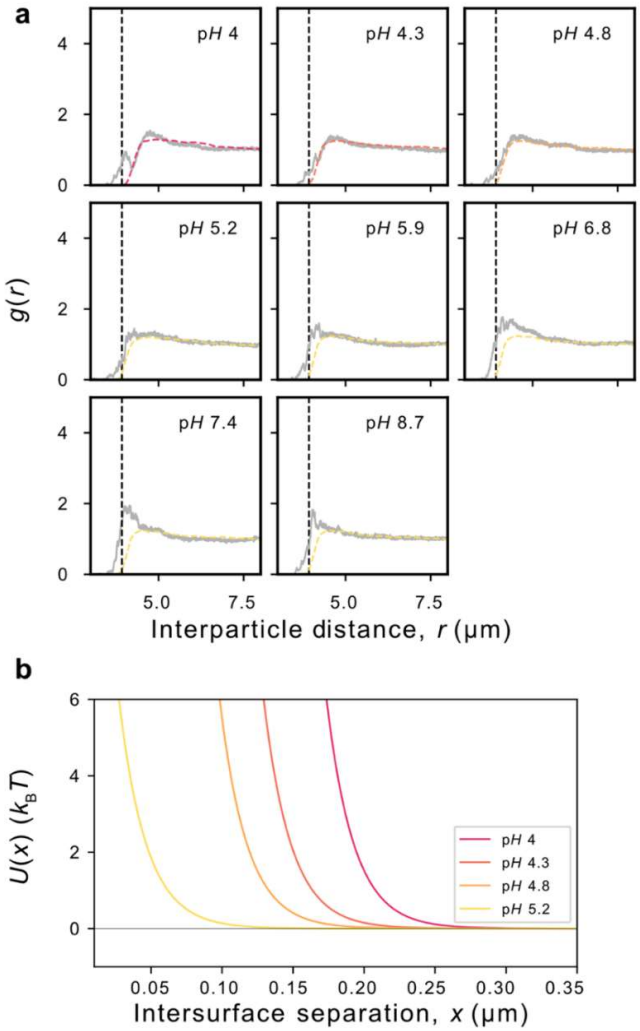


Fig. S22. Matching the experimental radial probability distribution functions $g(r)$s with those from BD simulations experiments varying the pH for NH_2-SiO_2 particles in water (shown in Fig. 2). (**a**) Overlays of experimental and simulated data (grey and dashed coloured lines respectively). The black dashed vertical line indicates the nominal particle diameter. (**b**) Corresponding inferred pair interaction potentials $U(x)$. Experimental data for p$H \geq 5.9$ reveals an increasing proportion of particles stuck particles, presumably in vdW contact with one another. This manifests in a peak in the $g(r)$ plot around the nominal particle diameter. $U(x)$ parameters for these cases cannot be reliably extracted. The same set of curves presented in the main text figure includes a horizontal error bar on the intersurface separation x. This error bar captures the overall uncertainty in measured interparticle separation (arising from the particle size dispersion and localisation error, see Section S1.6), and is intended to facilitate comparison with a calculated theoretical pair potential where the particle diameter is fixed.

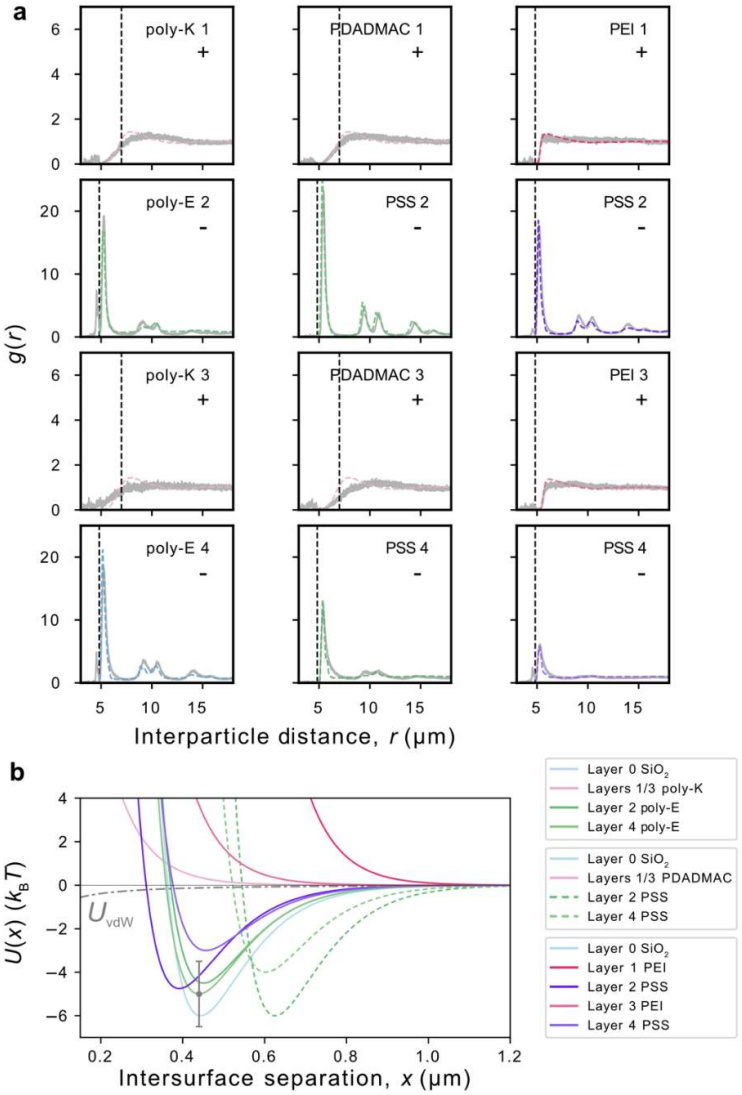


Fig. S23. Matching the experimental radial probability distribution functions $g(r)$s with those from BD simulations for the polyelectrolyte coating experiments (shown in Fig. 3). (**a**) Overlays of experimental and simulated data (grey and dashed coloured lines respectively). The plot inset identifies the polymer coating type in the experiment and the charge of the polymer coating. Each individual experiment is presented column-wise, proceeding from to bottom. Black dashed vertical line indicates the nominal particle diameter. Note that a particle size distribution with an augmented particle diameter was used to fit the data corresponding to layers 1 and 3 of particles coated with poly-K and PDADMAC, as discussed further in Section S4.7. (**b**) Corresponding inferred pair interaction potentials $U(x)$. The vertical error bar denotes an estimated uncertainty of $\pm 1.5\, k_B T$ in the overall process, arising from particle size uncertainties and drift in experimental conditions over time that affect cluster properties. The same set of curves presented in the main text figure includes a horizontal error bar on the intersurface separation x. This error bar captures the overall uncertainty in measured interparticle separation (arising from the particle size dispersion and localisation error, see Section S1.6), and is intended to facilitate comparison with a calculated theoretical pair potential where the particle diameter is fixed.

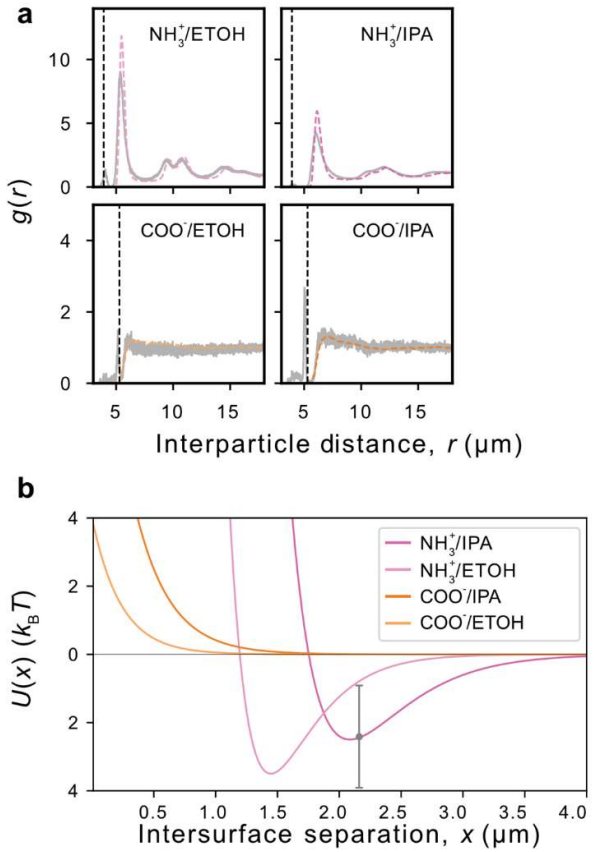
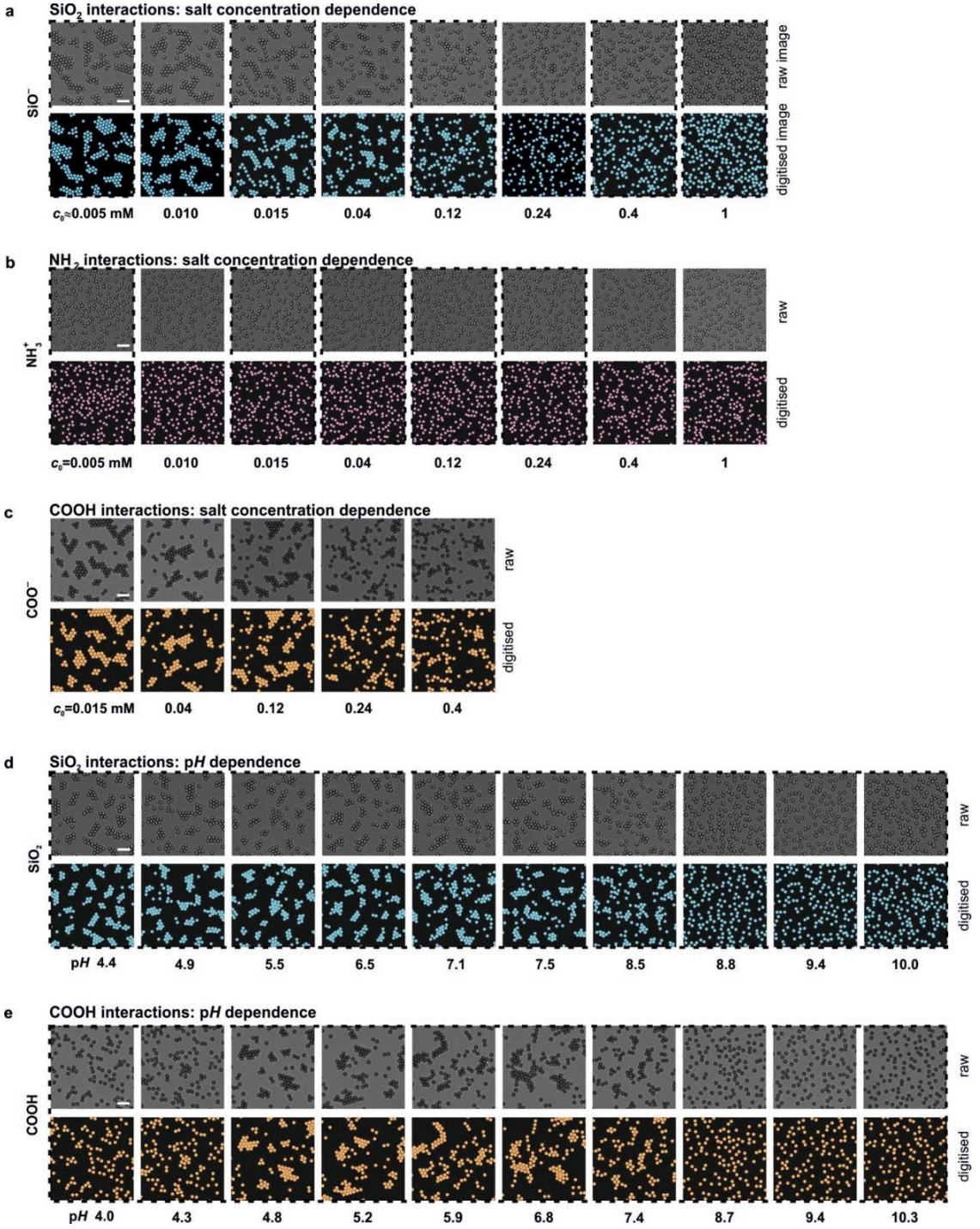
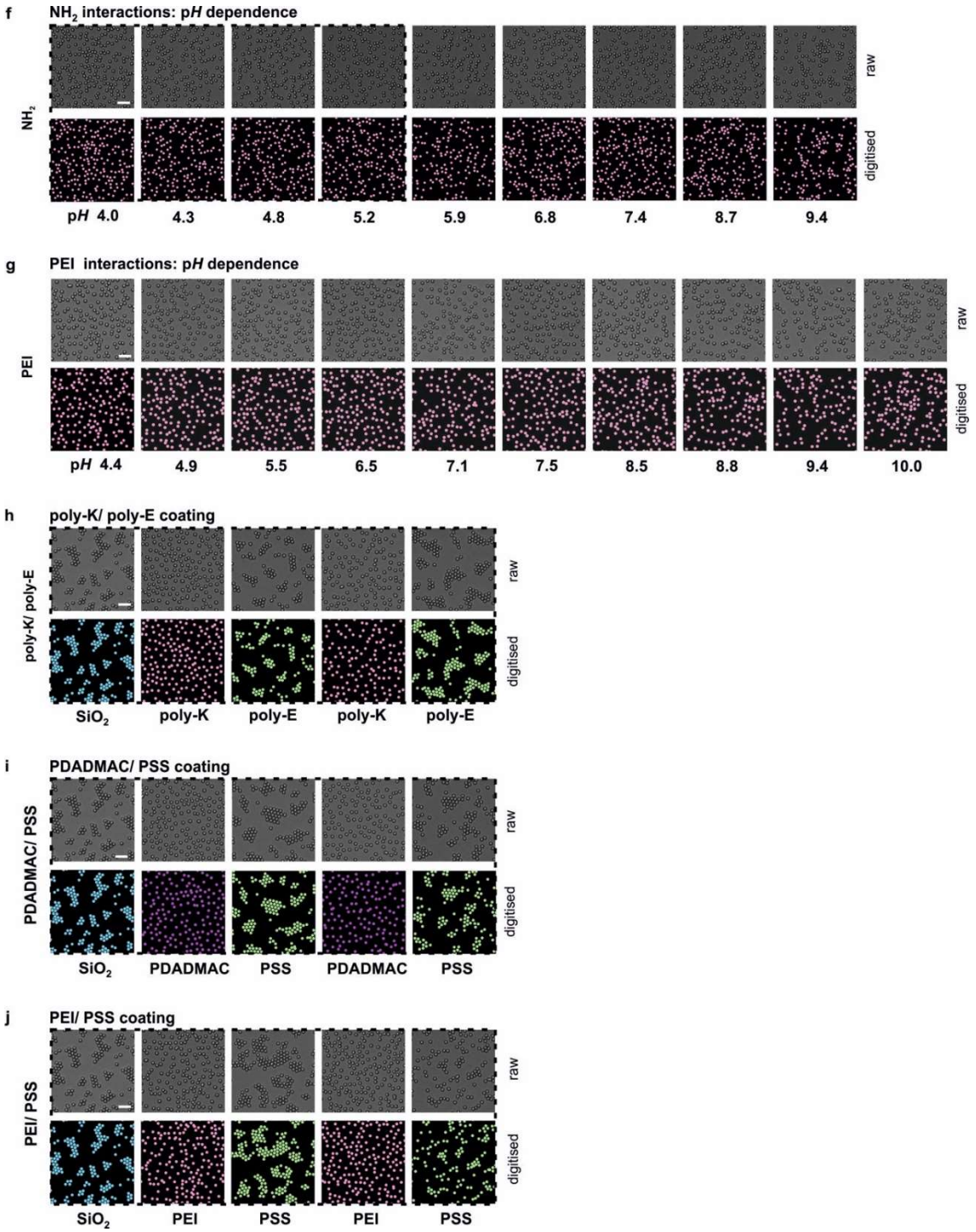


Fig. S24. Matching the experimental radial probability distribution functions $g(r)$s with those from BD simulations for experiments in alcohols (shown in Fig. 5c). (**a**) Overlays of experimental and simulated data (grey and dashed coloured lines respectively). The plot inset the identifies particle type and the solvent in the experiment. The black dashed vertical line indicates the nominal particle diameter. (**b**) Corresponding inferred pair interaction potentials $U(x)$. The vertical error bar denotes an estimated uncertainty of $\pm 1.5\ k_{\mathrm{B}}T$ in the overall process, arising from particle size uncertainties and drift in experimental conditions over time that affect cluster properties. The same set of curves presented in the main text figure includes a horizontal error bar on the intersurface separation x. This error bar captures the overall uncertainty in measured interparticle separation (arising from the particle size dispersion and localisation error, see Section S1.6), and is intended to facilitate comparison with a calculated theoretical pair potential where the particle diameter is fixed.

S5.2 Overview of all experimental snapshots and corresponding digitized images




f
NH2 interactions: pH dependence
NH2
raw
digitised
pH 4.0
4.3
4.8
5.2
5.9
6.8
7.4
8.7
9.4
g
PEI interactions: pH dependence
PEI
raw
digitised
pH 4.4
4.9
5.5
6.5
7.1
7.5
8.5
8.8
9.4
10.0
h
poly-K/ poly-E coating
poly-K/ poly-E
raw
digitised
SiO2
poly-K
poly-E
poly-K
poly-E
i
PDADMAC/ PSS coating
PDADMAC/ PSS
raw
digitised
SiO2
PDADMAC
PSS
PDADMAC
PSS
j
PEI/ PSS coating
PEI/ PSS
raw
digitised
SiO2
PEI
PSS
PEI
PSS

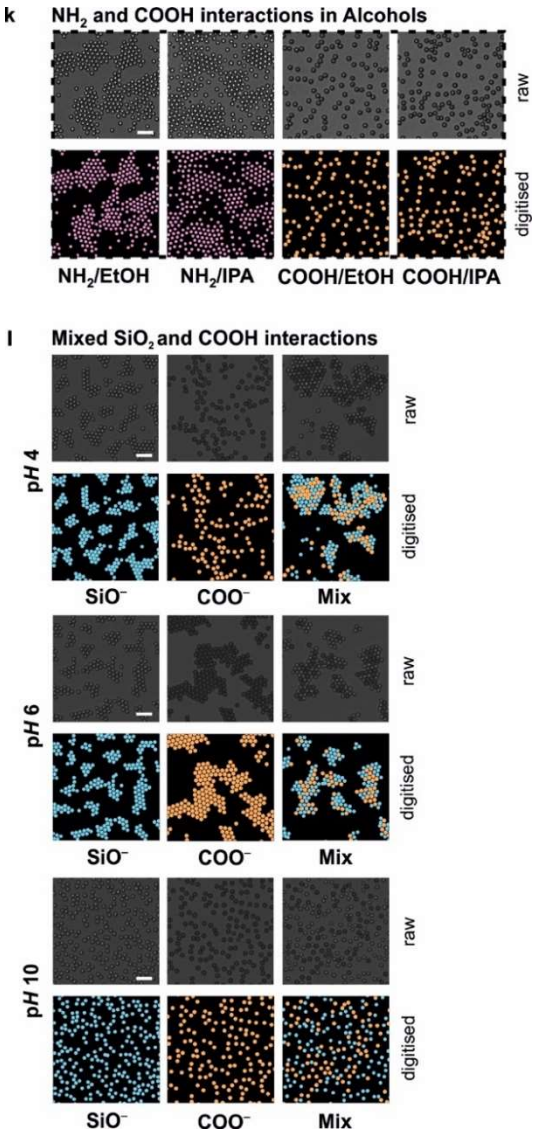


Fig. S25. Overview of all experimental snapshots and corresponding digitized images. Highlighted experiments (black dashed line) are cases accompanied by BD simulation results. Scale bar 20 μm.

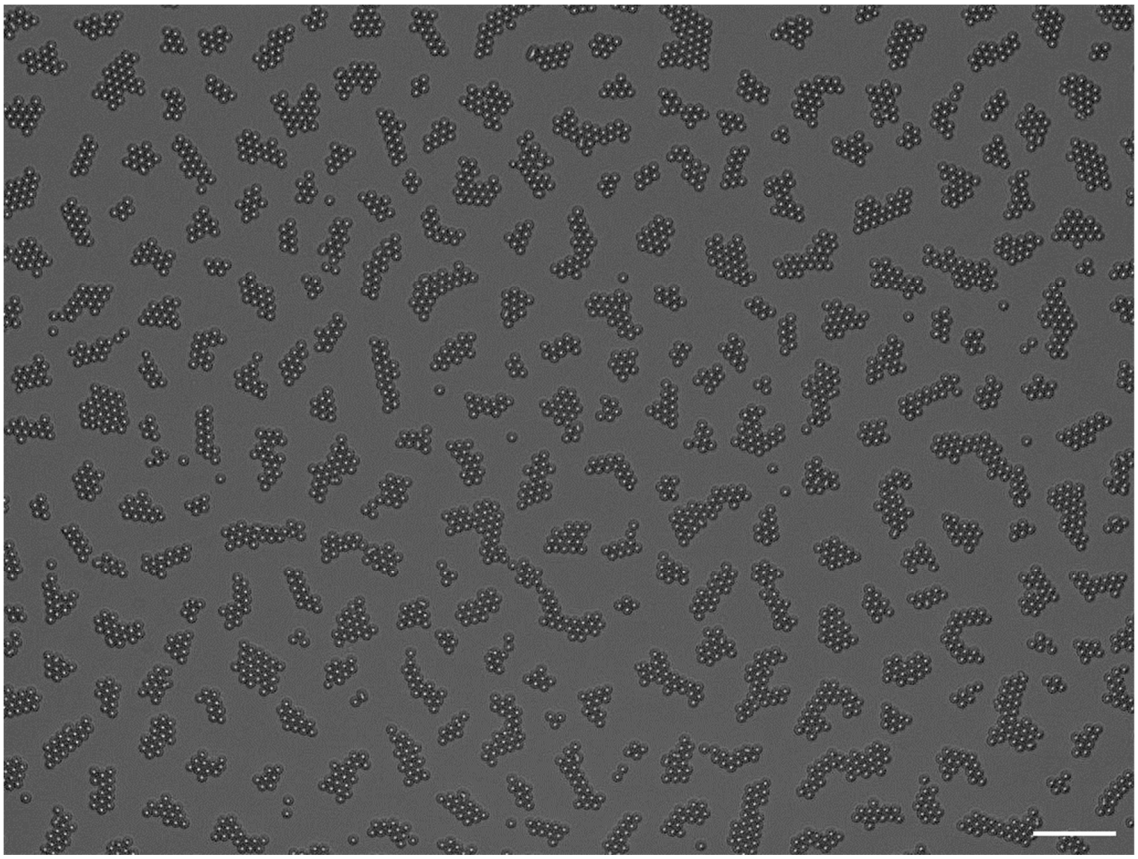


Fig. S26. Full-scale experimental snapshot of silica particles ($2R$=4.82 µm) suspended in DI water. Each frame contains on average >2000 particles with a frame size of 512 µm by 683 µm. Scale bar 50 µm.

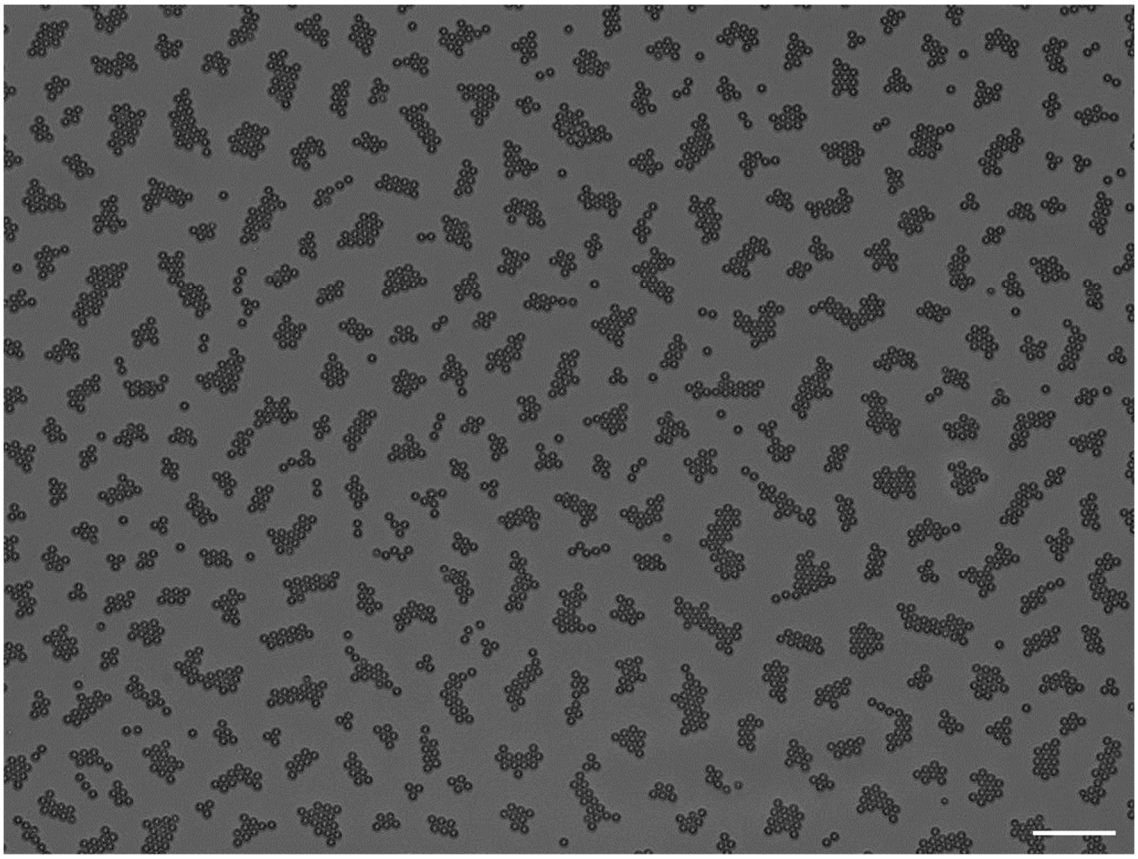


Fig. S27. Full-scale experimental snapshot of carboxylated particles ($2R$=5.29 μm) suspended in DI water. Each frame contains on average >2000 particles with a frame size of 512 μm by 683 μm. Scale bar 50 μm.

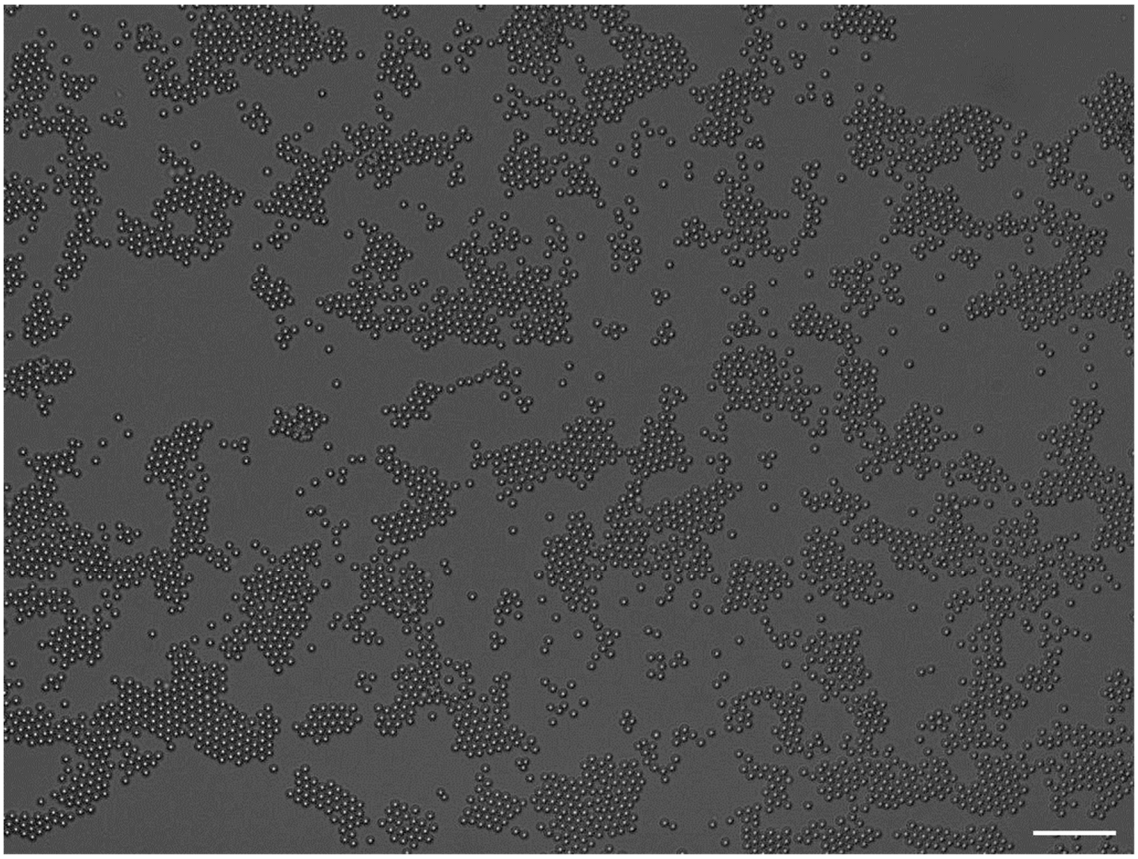


Fig. S28. Full-scale experimental snapshot of aminated silica particles (2R=3.92 µm) suspended in ethanol. Each frame contains on average >2000 particles with a frame size of 512 µm by 683 µm. Scale bar 50 µm.

S6 Supplementary Tables

Table S1. Parameter values used in PB-interfacial solvation model calculations of Utot(x)

			Calculation parameters				Experimental parameters		
FIG. #	Particle	Diameter, $2R$ (μm)	Solvent (ε: dielectric constant)	c_0 (mM)	$p = \mathrm{p}K - \mathrm{p}H$	Γ (nm^{-2})	c_0 (mM)	$\mathrm{p}H$	nominal $\mathrm{p}K$
1 (d)	SiO_2	4.82	H_2O ($\varepsilon = 78.5$)	0.005	0.030	1	0.005	6.4	2-11
			"	0.016	-0.525		0.015	5.5	"
			"	0.12	-0.950		0.12	5.4	"
			"	1.012	-1.500		1	5.4	"
	NH_2	3.92	"	0.04	3.500	0.2	0.005	6.4	9.5
			"	0.1	"		0.04	5.6	"
			"	0.2	"		0.12	5.6	"
			"	0.3	"		0.24	5.4	"
2 (c)	COOH	5.29	"	0.25	1.000 ○	0.1	0.25	4	4.5
			"	"	0.500 ○		0.26	4.3	"
			"	"	-0.500 ○		0.25	5.2	"
			"	"	-1.500 ○		0.25	5.9	"
			"	"	-2.500 ○		0.25	7.4	"
			"	"	-5.000 ○		0.25	10.3	"
	NH_2	3.92	"	0.31	5.000 ○	0.2	0.25	4	9.5
			"	0.18	" □		0.25	4	"
5 (d)	NH_2	3.92	IPA ($\varepsilon = 20$)	0.075	-0.265	0.2	0.0002	8.1	< 7
	COOH	5.29	EtOH ($\varepsilon = 20$)	0.0004	3.500	0.1	0.0004	7.3	$\gtrsim 10$
			IPA ($\varepsilon = 20$)	0.0002	4.500		0.0003	8.1	"

* additional parameters used in SiO_2 calculations: p_1=-5, f_1=0.005 (see Section S3.3)

** colored symbols refer to calculated curves in Fig. 2c

Table S2. BD simulation parameter values used to model experiments that examine the salt concentration dependence of cluster formation for SiO_2 particles in water

			Simulation parameters						Expt. Parameters		
Particle	$2R$ (μm)	Solvent	w (k_BT)	A (k_BT)	B (k_BT)	κ_1 (μm^{-1})	κ_2 (μm^{-1})	A_H (k_BT)	c_0 (mM)	pH	ζ (mV)
SiO_2	4.82	H_2O	7	7433.9	-6399.1	7.4	6.988	-	0.005	6.4	-40
			6	32580.3	-25848.1	13.2	12.5	-	0.015	5.5	-50
			5	623224	-422741	36.0	34.2	-	0.12	5.4	-42
			3	1073860	-690988	65.6	62.3	-	0.4	5.4	-40
			0	100	0	104.6	-	0.6	1	5.4	-26

*values for parameters in experiments are presented on the right for convenience.

Table S3. BD simulation parameter values used to model experiments that examine the salt concentration dependence of interparticle interactions for NH_2-SiO_2 particles in water

			Simulation parameters							Expt. parameters		
Particle	$2R$ (μm)	Solvent	c_0 (mM)*	w (k_BT)	A (k_BT)	B (k_BT)	κ_1 (μm^{-1})	κ_2 (μm^{-1})	A_H (k_BT)	c_0 (mM)	pH	ζ (mV)
NH_2-SiO_2	3.92	H_2O	0.03	0	10000	0	17.4	-	-	0.005	6.4	+57
			0.04	〃	30000	〃	20.5427	-	-	0.015	5.5	+65
			0.10	〃	40000	〃	33.222	-	-	0.04	5.6	+84
			0.18	〃	50000	〃	44.377	-	-	0.12	5.4	+84
			0.30	〃	60000	〃	57.165	-	-	0.24	5.4	+57

* denotes values that are slightly different from the corresponding experimentally measured values as discussed in the text, see Section S3.3.

Table S4. BD simulation parameter values used to model experiments that examine the pH dependence of cluster formation for SiO_2 particles in water

			Simulation parameters						Expt. parameters		
Particle	$2R$ (μm)	Solvent	w (k_BT)	A (k_BT)	B (k_BT)	κ_1 (μm^{-1})	κ_2 (μm^{-1})	A_H (k_BT)	c_0 (mM)	pH	ζ (mV)
SiO_2	4.82	H_2O	1.75	688093	-441309	36.0344	34.2327	-	0.12	10	-110
			1.5	573411	-367757	〃	〃	-	0.11	9.4	-100
			1.5	573411	-367757	〃	〃	-	0.11	8.8	-99
			5	635884	-430895	〃	〃	-	0.12	8.5	-96
			5.5	152267	-111354	〃	〃	-	0.11	7.5	-83
			5.5	249525	-178029	〃	〃	-	0.11	7.1	-80
			6	162493	-118964	〃	〃	-	0.12	6.5	-80
			6	162493	-118964	〃	〃	-	0.11	5.5	-69
			7	142646	-105929	〃	〃	-	0.11	4.9	-50
			7.5	711699	-489383	〃	〃	-	0.12	4.4	-23

Table S5. Alternative set of parameters for the experiments varying pH for SiO_2 particles in water

			Simulation parameters						Expt. parameters		
Particle	$2R$ (μm)	Solvent	w (k_BT)	A (k_BT)	B (k_BT)	κ_1 (μm^{-1})	κ_2 (μm^{-1})	A_H (k_BT)	c_0 (mM)	pH	ζ (mV)
SiO_2	4.82	H_2O	1.5	688093	-441309	36.0344	34.2327	-	0.12	10	-110
			1.75	573411	-367757	〃	34.2327	-	0.11	9.4	-100
			1.75	573411	-367757	〃	34.2327	-	0.11	8.8	-99
			5	444640	-258066	〃	33.512	-	0.12	8.5	-96
			5.5	392688	-346379	〃	35.314	-	0.11	7.5	-83
			5.5	249525	-178029	〃	34.2327	-	0.11	7.1	-80
			6	162493	-118964	〃	34.2327	-	0.12	6.5	-80
			6	162493	-118964	〃	34.2327	-	0.11	5.5	-69
			7	142646	-105929	〃	34.2327	-	0.11	4.9	-50
			7.5	118616	-20216	〃	27.386	-	0.12	4.4	-23

*the parameters capture the increase of A increasing with increasing pH, retaining the same functional form of the pair interaction potentials in Table S4. Here, the value of κ_2 is adjusted to achieve a similar $U(x)$ profile.

Table S6. BD simulation parameter values used to model experiments that examine the pH dependence of cluster formation for COOH particles in water

			Simulation parameters						Expt. parameters		
Particle	$2R$ (μm)	Solvent	w (k_BT)	A (k_BT)	B (k_BT)	κ_1 (μm^{-1})	κ_2 (μm^{-1})	A_H (k_BT)	c_0 (mM)	pH	ζ (mV)
COOH	5.29	H_2O	0	500000	0	52.0111	49.4106	-	0.25	10.3	-67
			0	500000	0	〃	〃	-	0.24	9.4	-67
			0	500000	0	〃	〃	-	0.24	8.7	-81
			6	1667860	-1086860	〃	〃	-	0.25	7.4	-84
			6.5	1177800	-784111	〃	〃	-	0.25	6.8	-86
			6.5	347454	-245874	〃	〃	-	0.25	5.9	-81
			7	743406	-508316	〃	〃	-	0.25	5.2	-78
			7	743406	-508316	〃	〃	-	0.25	4.8	-65
			5	1859830	-1194430	〃	〃	-	0.26	4.3	-33
			3.5	1301880	-836103	〃	〃	-	0.25	4.0	-18

Table S7. Alternative set of parameters for the experiments varying the pH for COOH particles in water

			Simulation parameters						Expt. parameters		
Particle	$2R$ (μm)	Solvent	w (k_BT)	A (k_BT)	B (k_BT)	κ_1 (μm^{-1})	κ_2 (μm^{-1})	A_H (k_BT)	c_0 (mM)	pH	ζ (mV)
COOH	5.29	H_2O	0	500000	0	52.0111	49.4106	-	0.25	10.3	-67
			0	500000	0	〃	49.4106	-	0.24	9.4	-67
			0	500000	0	〃	49.4106	-	0.24	8.7	-81
			6	427943	-101001	〃	43.169	-	0.25	7.4	-84
			6.5	380792	-122764	〃	44.7	-	0.25	6.8	-86
			6.5	347454	-245874	〃	49.4106	-	0.25	5.9	-81
			7	261545	-97934	〃	45.25	-	0.25	5.2	-78
			7	261545	-97934	〃	45.25	-	0.25	4.8	-65
			5	201716	-9417	〃	33.8	-	0.26	4.3	-33
			3.5	141201	-6592	〃	33.8	-	0.25	4	-18

*the parameters capture the increase of A increasing with increasing pH, retaining the same functional form of the pair interaction potentials in Table S6. Here, the value of κ_2 is adjusted to achieve a similar $U(x)$ profile.

Table S8. BD simulation parameter values used to model experiments that examine the pH dependence of interparticle interactions for NH_2-SiO_2 particles in water

			Simulation parameters						Expt. parameters		
Particle	$2R$ (μm)	Solvent	w (k_BT)	A (k_BT)	B (k_BT)	κ_1 (μm^{-1})	κ_2 (μm^{-1})	A_H (k_BT)	c_0 (mM)	pH	ζ (mV)
NH_2	3.92	H_2O	0	25	0	52.0111	-	-	0.25	5.2	+92
			〃	1000	〃	〃	-	-	0.25	4.8	+93
			〃	5000	〃	〃	-	-	0.26	4.3	+90
			〃	50000	〃	〃	-	-	0.25	4	+94

Table S9. BD simulation parameter values used to model experiments that examine the dependence of cluster formation on the charge of the polypeptide coating layer (poly-K/poly-E) displayed in Fig. 3c

			Simulation parameters						Expt. parameters		
Particle	$2R$ (μm)	Solvent	w (k_BT)	A (k_BT)	B (k_BT)	κ_1 (μm^{-1})	κ_2 (μm^{-1})	A_H (k_BT)	c_0 (mM)	pH	ζ (mV)
SiO_2	4.82	H_2O	6	32580	-25848	12.7401	12.1031	-	0.02	5.5	-50
poly-K	*6.5		0	100	0	〃	〃	-	〃	〃	+56
poly-E	4.82		4.5	26845	-21198	〃	〃	-	〃	〃	-39
poly-K	*6.5		0	100	0	〃	〃	-	〃	〃	+52
poly-E	4.82		5	25759	-20490	〃	〃	-	〃	〃	-31

* augmented average particle diameter. See Section S4.7 for details.

Table S10. BD simulation parameter values used to model experiments that examine the dependence of cluster formation on the charge of the polyelectrolyte coating layer (PDADMAC/PSS) displayed in Fig. 3c

			Simulation parameters						Expt. parameters		
Particle	$2R$ (μm)	Solvent	w (k_BT)	A (k_BT)	B (k_BT)	κ_1 (μm^{-1})	κ_2 (μm^{-1})	A_H (k_BT)	c_0 (mM)	pH	ζ (mV)
SiO_2	4.82	H_2O	6	32580	-25848	12.7401	12.1031	-	0.02	5.5	-50
PDADMAC	*6.5		0	100	0	〃	〃	-	〃	〃	+39
PSS	4.82		6	329989	-233183	〃	〃	-	〃	〃	-67
PDADMAC	*6.5		0	100	0	〃	〃	-	〃	〃	+62
PSS	4.82		4	163116	-117001	〃	〃	-	〃	〃	-62

* augmented average particle diameter. See Section S4.7 for details.

Table S11. BD simulation parameter values used to model experiments that examine the dependence of cluster formation on the charge of the polyelectrolyte coating layer (PEI/PSS)

			Simulation parameters						Expt. parameters		
Particle	$2R$ (μm)	Solvent	w (k_BT)	A (k_BT)	B (k_BT)	κ_1 (μm^{-1})	κ_2 (μm^{-1})	A_H (k_BT)	c_0 (mM)	pH	ζ (mV)
SiO_2	4.82	H_2O	6	32580	-25848	12.7401	12.1031	-	0.02	5.5	-50
PEI	4.82		0	1000	0	〃	〃	-	〃	〃	+71
PSS	4.82		4.75	13201	-10830	〃	〃	-	〃	〃	-37
PEI	4.82		0	35000	0	〃	〃	-	〃	〃	+43
PSS	4.82		3	19199	-15107	〃	〃	-	〃	〃	-78

Data not presented in main manuscript.

Table S12. BD simulation parameter values used to model experiments that examine the dependence of cluster formation on the sign of the charge of the particle in ethanol and isopropanol

			Simulation parameters						Expt. parameters		
Particle	$2R$ (μm)	Solvent	w (k_BT)	A (k_BT)	B (k_BT)	κ_1 (μm^{-1})	κ_2 (μm^{-1})	A_H (k_BT)	c_0 (mM)	pH	ζ (mV)
NH_2	3.92	ethanol	3.5	24179.2	-18953.4	4.0766	3.8728	-	0.0004	7.3	+66
		isopropanol	2.5	29115.9	-22234.9	3.077	2.923	-	0.0002	8.1	+55
COOH	5.29	ethanol	0	4	0	4.3	-	-	0.0004	7.3	-49
		isopropanol	0	15	0	3.6	-	-	0.0003	8.1	-22

References

1 Kokot, G., Bespalova, M. I. & Krishnan, M. Measured electrical charge of SiO2 in polar and nonpolar media. *Journal of Chemical Physics* **145** (2016).

2 Masterton, W. L., Bolocofsky, D. & Lee, T. P. Ionic radii from scaled particle theory of the salt effect. *The Journal of Physical Chemistry* **75**, 2809-2815 (1971).

3 Parthasarathy, R. Rapid, accurate particle tracking by calculation of radial symmetry centers. *Nature Methods* **9**, 724-726 (2012).

4 Stein, S. C. & Thiart, J. TrackNTrace: A simple and extendable open-source framework for developing single-molecule localization and tracking algorithms. *Scientific Reports* **6**, 37947 (2016).

5 Thompson, A. P. *et al.* LAMMPS - a flexible simulation tool for particle-based materials modeling at the atomic, meso, and continuum scales. *Computer Physics Communications* **271**, 108171 (2022).

6 Kubincová, A., Hünenberger, P. H. & Krishnan, M. Interfacial solvation can explain attraction between like-charged objects in aqueous solution. *Journal of Chemical Physics* **152**, 104713 (2020).

7 Behjatian, A., Walker-Gibbons, R., Schekochihin, A. A. & Krishnan, M. Nonmonotonic Pair Potentials in the Interaction of Like-Charged Objects in Solution. *Langmuir* **38**, 786-800 (2022).

8 Hamaker, H. C. The London—van der Waals attraction between spherical particles. *Physica* **4**, 1058-1072 (1937).

9 Valmacco, V. *et al.* Dispersion forces acting between silica particles across water: influence of nanoscale roughness. *Nanoscale Horizons* **1**, 325-330 (2016).

10 Ackler, H. D., French, R. H. & Chiang, Y.-M. Comparisons of Hamaker Constants for Ceramic Systems with Intervening Vacuum or Water: From Force Laws and Physical Properties. *Journal of Colloid and Interface Science* **179**, 460-469 (1996).

11 Abraham, M. J. *et al.* GROMACS: High performance molecular simulations through multi-level parallelism from laptops to supercomputers. *SoftwareX* **1-2**, 19-25 (2015).

12 Walker-Gibbons, R., Kubincová, A., Hünenberger, P. H. & Krishnan, M. The Role of Surface Chemistry in the Orientational Behavior of Water at an Interface. *The Journal of Physical Chemistry B* **126**, 4697-4710 (2022).

13 Vanommeslaeghe, K. *et al.* CHARMM general force field: A force field for drug-like molecules compatible with the CHARMM all-atom additive biological force fields. *Journal of Computational Chemistry* **31**, 671-690 (2009).

14 Yeh, I.-C. & Wallqvist, A. On the proper calculation of electrostatic interactions in solid-supported bilayer systems. *The Journal of Chemical Physics* **134**, 055109 (2011).

15 Ninham, B. W. & Parsegian, V. A. Electrostatic potential between surfaces bearing ionizable groups in ionic equilibrium with physiologic saline solution. *Journal of Theoretical Biology* **31**, 405-428 (1971).

16 Chen, Y. X. *et al.* Electrolytes induce long-range orientational order and free energy changes in the H-bond network of bulk water. *Science Advances* **2**, e1501891 (2016).

17 Ong, S. W., Zhao, X. L. & Eisenthal, K. B. Polarization of water molecules at a charged interface - 2nd harmonic studies of the silica water interface. *Chemical Physics Letters* **191**, 327-335 (1992).

18 Ye, S., Nihonyanagi, S. & Uosaki, K. Sum frequency generation (SFG) study of the pH-dependent water structure on a fused quartz surface modified by an octadecyltrichlorosilane (OTS) monolayer. *Physical Chemistry Chemical Physics* **3**, 3463-3469 (2001).

19 Bonthuis, D. J., Gekle, S. & Netz, R. R. Profile of the Static Permittivity Tensor of Water at Interfaces: Consequences for Capacitance, Hydration Interaction and Ion Adsorption. *Langmuir* **28**, 7679-7694 (2012).

20 Myalitsin, A., Urashirna, S. H., Nihonyanagi, S., Yamaguchi, S. & Tahara, T. Water Structure at the Buried Silica/Aqueous Interface Studied by Heterodyne-Detected Vibrational Sum-Frequency Generation. *Journal of Physical Chemistry C* **120**, 9357-9363 (2016).

21 Israelachvili, J. & Wennerstrom, H. Role of hydration and water structure in biological and colloidal interactions. *Nature* **379**, 219-225 (1996).

22 Remsing, R. C., Baer, M. D., Schenter, G. K., Mundy, C. J. & Weeks, J. D. The Role of Broken Symmetry in Solvation of a Spherical Cavity in Classical and Quantum Water Models. *The Journal of Physical Chemistry Letters* **5**, 2767-2774 (2014).

23 Cendagorta, J. R. & Ichiye, T. The Surface Potential of the Water–Vapor Interface from Classical Simulations. *The Journal of Physical Chemistry B* **119**, 9114-9122 (2015).

24 Duignan, T. T., Baer, M. D., Schenter, G. K. & Mundy, C. J. Electrostatic solvation free energies of charged hard spheres using molecular dynamics with density functional theory interactions. *The Journal of Chemical Physics* **147**, 161716 (2017).

25 Randles, J. E. B. Structure at the free surface of water and aqueous electrolyte solutions. *Physics and Chemistry of Liquids* **7**, 107-179 (1977).

26 Li, P., Huang, J., Hu, Y. & Chen, S. Establishment of the Potential of Zero Charge of Metals in Aqueous Solutions: Different Faces of Water Revealed by Ab Initio Molecular Dynamics Simulations. *The Journal of Physical Chemistry C* **125**, 3972-3979 (2021).

27 Biesheuvel, P. M. Electrostatic free energy of interacting ionizable double layers. *Journal of Colloid and Interface Science* **275**, 514-522 (2004).

28 Overbeek, J. T. G. The role of energy and entropy in the electrical double layer. *Colloids and Surfaces* **51**, 61-75 (1990).

29 Krishnan, M. Electrostatic free energy for a confined nanoscale object in a fluid. *Journal of Chemical Physics* **138**, 114906 (2013).
30 Krishnan, M. A simple model for electrical charge in globular macromolecules and linear polyelectrolytes in solution. *The Journal of chemical physics* **146**, 205101-205101 (2017).
31 Verwey, E. J. W. & Overbeek, J. T. G. *Theory of the stability of lyophobic colloids.* (Elsevier, 1948).
32 Parsegian, V. A., Rand, R. P. & Fuller, N. L. Direct osmotic-stress measurements of hydration and electrostatic double-layer forces between bilayers of double-chained ammonium acetate surfactants. *Journal of Physical Chemistry* **95**, 4777-4782 (1991).
33 Schlaich, A., dos Santos, A. P. & Netz, R. R. Simulations of Nanoseparated Charged Surfaces Reveal Charge-Induced Water Reorientation and Nonadditivity of Hydration and Mean-Field Electrostatic Repulsion. *Langmuir* **35**, 551-560 (2019).
34 Darlington, A. M. & Gibbs-Davis, J. M. Bimodal or Trimodal? The Influence of Starting pH on Site Identity and Distribution at the Low Salt Aqueous/Silica Interface. *Journal of Physical Chemistry C* **119**, 16560-16567 (2015).
35 Macias-Romero, C., Nahalka, I., Okur, H. I. & Roke, S. Optical imaging of surface chemistry and dynamics in confinement. *Science* **357**, 784-787 (2017).
36 Grunwald, E. & Berkowitz, B. J. The Measurement and Correlation of Acid Dissociation Constants for Carboxylic Acids in the System Ethanol-Water. Activity Coefficients and Empirical Activity Functions. *Journal of the American Chemical Society* **73**, 4939-4944 (1951).
37 Belskii, V. E., Kudryavtseva, L. A., Derstuganova, K. A., Teitelbaum, A. B. & Ivanov, B. E. Basicity of Aliphatic-Amines in Ethanol. *Bulletin of the Academy of Sciences of the USSR Division of Chemical Science* **30**, 736-738 (1981).
38 Brunner, M., Dobnikar, J., von Grunberg, H. H. & Bechinger, C. Direct measurement of three-body interactions amongst charged colloids. *Physical Review Letters* **92**, 078301 (2004).
39 del Castillo, G. F. D., Hailes, R. L. N. & Dahlin, A. Large Changes in Protonation of Weak Polyelectrolyte Brushes with Salt Concentration-Implications for Protein Immobilization. *Journal of Physical Chemistry Letters* **11**, 5212-5218 (2020).
40 Isom, D. G., Castaneda, C. A., Cannon, B. R. & Garcia-Moreno, B. E. Large shifts in pK(a) values of lysine residues buried inside a protein. *Proceedings of the National Academy of Sciences of the United States of America* **108**, 5260-5265 (2011).
41 Dong, H. T., Du, H. B., Wickramasinghe, S. R. & Qian, X. H. The Effects of Chemical Substitution and Polymerization on the pK(a) Values of Sulfonic Acids. *Journal of Physical Chemistry B* **113**, 14094-14101 (2009).
42 Franzmann, T. M. *et al.* Phase separation of a yeast prion protein promotes cellular fitness. *Science* **359**, 47-54 (2018).

43 Lund, M. & Jonsson, B. A mesoscopic model for protein-protein interactions in solution. *Biophysical Journal* **85**, 2940-2947 (2003).

44 Nott, T. J. *et al.* Phase Transition of a Disordered Nuage Protein Generates Environmentally Responsive Membraneless Organelles. *Molecular Cell* **57**, 936-947 (2015).

45 Radak, B. K. *et al.* Constant-pH Molecular Dynamics Simulations for Large Biomolecular Systems. *Journal of Chemical Theory and Computation* **13**, 5933-5944 (2017).

46 Kim, S. *et al.* Complexation and coacervation of like-charged polyelectrolytes inspired by mussels. *Proceedings of the National Academy of Sciences of the United States of America* **113**, E847-E853 (2016).

47 Baumgartl, J. R., Arauz-Lara, J. L. & Bechinger, C. Like-charge attraction in confinement: myth or truth? *Soft Matter* **2**, 631 (2006).

48 Polin, M., Grier, D. G. & Han, Y. Colloidal electrostatic interactions near a conducting surface. *Physical Review E* **76** (2007).

49 Yücel, H. & Okumuşoğlu, N. T. A new tracking algorithm for multiple colloidal particles close to contact. *Journal of Physics: Condensed Matter* **29**, 465101 (2017).

Statement of Authorship for joint/multi-authored papers for PGR thesis
To appear at the end of each thesis chapter submitted as an article/paper

The statement shall describe the candidate's and co-authors' independent research contributions in the thesis publications. For each publication there should exist a complete statement that is to be filled out and signed by the candidate and supervisor **(only required where there isn't already a statement of contribution within the paper itself).**

Title of Paper	A charge-dependent long-ranged force drives tailored assembly of matter in solution
Publication Status	☒ Published □ Accepted for Publication □ Submitted for Publication □ Unpublished and unsubmitted work written in a manuscript style
Publication Details	Wang, S., Walker-Gibbons, R., Watkins, B., Flynn, M. & Krishnan. M. A charge-dependent long-ranged force drives tailored assembly of matter in solution. Nat. Nanotechnol. 19, 485–493 (2024). https://doi.org/10.1038/s41565-024-01621-5

Student Confirmation

Student Name:	Sida Wang		
Contribution to the Paper	S.W. performed all experiments, participated in data analysis and manuscript preparation.		
Signature	Sida Wang	Date	20/09/2024

Supervisor Confirmation

By signing the Statement of Authorship, you are certifying that the candidate made a substantial contribution to the publication, and that the description described above is accurate.

Supervisor name and title: Professor Madhavi Krishnan			
Supervisor comments			
Signature		Date	20/09/2024

This completed form should be included in the thesis, at the end of the relevant chapter.

3

Chemical control of colloidal self-assembly driven by the electrosolvation force

This chapter presents a recently accepted manuscript "*Chemical control of colloidal self-assembly driven by the electrosolvation force*". In this study, we further investigate the mechanism of the proposed electrosolvation force. The previous chapter demonstrated that the long-ranged attraction between like-charged particles depends on the interplay between particle surface charge and the nature of the solvent. Specifically, we showed that in aqueous solutions, negatively charged particles attract at long range while positively charged particles repel, whereas positively charged particles attract in short-chain alcohols while negatively charged particles repel. To gain further molecular-level insight into the long-ranged attractive force and to understand how microscopic interfacial processes can dominate the interaction between macromolecules and particles at long range, we examined a diverse range of solvents and co-solvents of interest.

Examining a broader range of solvent and solvent mixtures not only expands the scope of the long-ranged attraction but also provides hints to the origin of the electrosolvation force. With the aid of MD simulations, we are able to correlate the response of interfacial molecular structure (solvent molecules and surface-active agents like surfactants and osmolytes) with experimental observations. By perturbing the interfacial solvent structure through the addition of surface-active agents we obtain further compelling evidence that the electrosolvation force is indeed governed either by the interfacial dipole moment.

It is of our particular interest to look at osmolytes, inspired by their ability to mediate biomolecular interactions [64-67]. For example, organic osmolytes such as amino acids, trimethylglycine (TMG) and trimethylamine *N*-oxide (TMAO) are known for their appreciable impact on the stability of proteins, yet the fundamental mechanism underlying these effects remain poorly understood [68-71]. These osmolytes are often categorized as 'structure maker' or 'structures breaker', depending on their ability to enhance or disrupt interfacial water structures [71-73]. Interestingly, we observed drastic variations in cluster responses with the introduction of different types of osmolytes. While the addition of micromolar to sub-millimolar concentration of amino acids, such as tyrosine and glycine suppressed attraction between silica particles in aqueous solutions, cluster formation was not disrupted by TMG even at molar concentrations. With the aid of simulation, our observations provide further insight into the origin of the electrosolvation force. The observation could in general be explained either by considering the total net dipole moment density (solvent plus small molecule) or by the net excess dipole orientation density of solvent alone at interfaces. Our findings offer a novel perspective on colloidal stabilities, particularly in the contexts of biomolecular phase septation and protein folding.

manuscript:

Chemical control of colloidal self-assembly driven by the electrosolvation force

Manuscript

Chemical control of colloidal self-assembly driven by the electrosolvation force

Sida Wang†[1], Rowan Walker-Gibbons†[1], Bethany Watkins[1], Binghui Lin[1], & Madhavi Krishnan*[1,2]

† these authors contributed equally
[1]Physical and Theoretical Chemistry Laboratory, Department of Chemistry, University of Oxford, South Parks Road, Oxford OX1 3QZ, United Kingdom
[2]The Kavli Institute for Nanoscience Discovery, Sherrington Road, Oxford OX1 3QU, United Kingdom.
*correspondence to madhavi.krishnan@chem.ox.ac.uk

Abstract

Self-assembly of matter in solution generally relies on attractive interactions that overcome entropy and drive the formation of higher-order molecular and particulate structures. Such interactions play key roles in a variety of molecular processes, e.g., crystallisation, biomolecular folding and condensation, pathological protein aggregation and biofouling. The electrosolvation force introduces a distinct conceptual paradigm into the known palette of interactions that drive the spontaneous accretion and organisation of matter. However, an understanding of the underlying physical chemistry, and therefore the ability to exert control over and tune the interaction, remains incomplete. Here we provide further evidence that this force arises from the structure of the interfacial electrolyte. Neutral molecules such as a different solvent, osmolytes or surfactants, may — even at very low concentrations in the medium — disrupt or reinforce pre-existing interfacial solvent structure, thereby furnishing unanticipated chemical tuning of the ability of matter to self-assemble. The observations present unexpected mechanistic elements that may explain the impact of co-solvents and osmolytes on protein structure, stability and biomolecular condensation. Our findings thus shed light on microscopic mechanisms that drive the emergence of order and structure from molecular to macroscopic scales in the solution phase.

Introduction

Liquids in contact with interfaces play a pivotal role in a range of natural phenomena occurring, e.g., in the atmosphere, in geology, chemistry and biology[1-3]. The solid-liquid interface in particular plays a crucial role in a host of scientific and technological areas such as chromatography, electrochemical energy generation and storage, biological implant design, biofouling, self-assembly, drug delivery and the stability of pharmaceuticals and fine chemicals[4-8]. Molecular level phenomena at an interface with an electrolyte can impact system properties and behaviour at much larger length scales. For instance, interfacial molecular processes underpin the uptake of gases at the ocean/air interface, and the adsorption of surfactants to interfaces determines their practical and therapeutic applications[9] . Furthermore, osmolytes are small, net-neutral soluble compounds that are known to affect the folding, stability, aggregation and condensation of biomolecules, enzymatic activity and surface tension[10-15]. Knowledge of how interfacial processes affect macroscopic system behaviour is therefore central to our ability to understand, design and engineer system properties in phenomena that span a range of length scales in a variety of areas.

Here we provide molecular-level insight into the recently described electrosolvation force, demonstrating routes to chemically tuning and controlling long-ranged interactions that govern accretion, structure formation and self-assembly in suspended matter[16-18]. Specifically, we provide evidence that the electrosolvation force is driven by a significant normal component of molecular dipole moments at an interface. We further suggest that chemical modulation of this interaction via small molecules in the medium may occur by both disruptive and reinforcing effects on the interfacial solvent structure.

The electrosolvation force refers to an electrostatically mediated solvent- or solvation-dependent interparticle interaction that arises from molecular orientational structuring in the electrolyte in the vicinity of a charged surface in contact with a fluid phase[16-19]. It has been previously demonstrated that like-charged particles in solution may attract or repel depending on the nature of the solvent and the sign of charge of the

particle. This counterintuitive long-range attraction therefore effectively breaks the symmetry associated with inversion in the sign of charge in the system, which is characteristic of a canonical Coulombic interaction[18,20,21]. Thus in aqueous solution, negatively charged colloidal particles were observed to attract at long range (5–10 Debye lengths, κ^{-1}) while positively charged particles repelled. Conversely, positively charged particles suspended in short chain alcohols were found to attract whereas negatively charged particles repelled[18]. Here the Debye length $\kappa^{-1} = \sqrt{\epsilon_0 \epsilon_r k_B T/(2\rho_{ion}\, e^2)}$ represents a length scale over which the electrical potential due to a charged object decays exponentially with distance in an electrolyte containing monovalent ions at a number density ρ_{ion} in a medium of dielectric constant ϵ_r. Further, ϵ_0 is the permittivity of free space, e is the elementary charge, k_B is the Boltzmann constant and T is the absolute temperature.

Within the 'interfacial solvation model', the effective interparticle interaction potential, which has been corroborated in experiments, may be written as

$$U_{tot} = \Delta F_{el} + \Delta F_{int} \approx A\exp(-\kappa_1 x) + B\exp(-\kappa_2 x) \quad (1)$$

The first term, $\Delta F_{el} > 0$, represents the familiar repulsive electrostatic interaction free energy between two large like-charged spheres of radius R and intersurface separation x, in the regime $R \gg \kappa^{-1} = \kappa_1^{-1}$. The second term, $\Delta F_{int} \approx B\exp(-\kappa_2 x)$, represents the interfacially generated free-energy contribution to the interaction[16,17]. The model also suggests that $\kappa_2 < \kappa_1 \approx \kappa$, and it can be shown that

$$B \propto z\mu_{av}(\sigma) \quad (2)$$

where z is the sign of the charge of the ionized groups carried by a particle of surface charge density σ. Importantly, in our model, $\mu_{av}(\sigma) \approx \mu_{av}(\sigma = 0)$, which holds for low magnitudes of σ, is the excess normal dipole moment surface density at the interface between the object and the electrolyte, which can be obtained from molecular dynamics (MD) simulations. Importantly, a non-zero average dipole moment density at an interface ($\mu_{av} \neq 0$) implies an additional, previously overlooked contribution to the interparticle interaction energy as indicated in Eqs. (1) and (2). Note that at interfaces in pure solvents, a net orientation of solvent molecules entailing $\mu_{av} \neq 0$ has been reported on

extensively in interfacial spectroscopy experiments, especially for the silica-water interface[22-24]. In previous work we formulated the interfacial free energy contribution in Eqs. (1) and (2) in terms of an interfacial solvation potential, φ_{int} [16-19]. Since $\mu_{\mathrm{av}}(\sigma) = -\varepsilon_0 \varphi_{\mathrm{int}}(\sigma)$, we phrase the discussion in this work in terms of the more intuitively accessible interfacial dipole moment density μ_{av} (MD simulation methods, Suppl. Note. 1). Further, Eq. (1) excludes any contribution from the van der Waals (vdW) force which is negligible at the interparticle separations relevant to these experiments (BD simulations methods).

Thus, depending on the sign and magnitude of B in the electrosolvation or interfacial term in Eq. (2), the interaction between electrically like charged particles in solution may either be net-attractive ($B < 0$) or repulsive ($B \gtrsim 0$) at long range, and in the former case can result in a long-ranged minimum of depth w in the pair-interaction potential (Fig. 1f). Specifically, on a plot of μ_{av} vs. σ, the model would support the appearance of interparticle attraction in the quadrants reflecting opposite signs of the two quantities (coloured regions in Fig. 2e). Pair potentials entailing minima of tunable depth play a crucial role in fostering tailored assembly of large-scale collections of particles[18]. In this work we explore the ability to chemically tune the value of B in particle interactions, based on our understanding of the molecular mechanisms underpinning the electrosolvation force. The study concludes with a comparison of the experimental observations with the indications of the interfacial solvation model.

Results and Discussion

We report on a range of experiments examining the electrosolvation interaction between charged particles of different surface chemistry and charge, suspended in aprotic and protic solvents, in solvent mixtures, as well as in aqueous electrolytes containing varying amounts of co-solvents such as zwitterionic osmolytes and surfactants. We observed the spatial structure of two-dimensional gravity-sedimented suspensions of colloidal particles using bright field microscopy, as described previously[18] (Fig. 1). We worked with two

different samples of silica (SiO_2; diameter $2R$ = 4.82 or 5.17 mm) and a carboxyl-functionalized melamine resin (COOH-MF or COOH; $2R$ = 5.29 mm) representing negatively charged particles, and aminated positively charged silica (NH_2-SiO_2 or NH_2; $2R$ =4.63 mm) microspheres (see experimental methods). Measured radial probability density distributions, $g(r)$, were compared with the results of Brownian dynamics (BD) simulations of a 2-d system of particles to infer the underlying pair-interaction potential, $U(x)$, as previously described (BD simulations methods)[18]. Furthermore, MD simulations of the respective particle surface types in contact with the fluid phase of interest provide microscopic insight into the properties of the interfacial electrolyte, i.e., molecular densities and orientations, as well as estimates of the total dipole moment density, μ_{av}, and of $\mu_{\mathrm{av,w}}$, the dipole moment density due to water alone, under various experimental conditions.

We expect the various experimental conditions tested to alter the interfacial electrolyte structure, influencing the value of μ_{av} or $\mu_{\mathrm{av,w}}$ compared to the pure electrolyte in different ways. Such experiments provide a means to put a core feature of the interfacial solvation model to a systematic test. Values of the surface-averaged excess normal dipole moment surface density inferred from MD simulations provide a theoretically expected sign and approximate magnitude of B in Eq. (2) under various conditions. Experiments reveal either the presence or absence of interparticle attraction, and these outcomes may be compared with qualitative indications of the model (MD simulation methods, Suppl. Note 1)[16-18]. The study concludes with a diagrammatic summary of experimental outcomes, i.e., presence or absence of attraction, as a function of system properties σ and μ_{av}. Owing to the significant challenges associated with experimentally determining estimating μ_{av} at the surface of a microsphere, we use values inferred from molecular simulations in each case. The experimental outcomes largely agree with expectations from the model, lending support to the view that interfacial solvent structuring can play a central role in long-range forces between objects in solution.

The electrosolvation force is observed in many solvents

The solvent itself provides the most direct means to probing the microscopic origins of a putative solvation-governed long-ranged force between suspended particles. We therefore examined interparticle interactions in a range of protic and aprotic solvents namely, water, heavy water, dimethyl sulfoxide (DMSO), methanol, ethanol, 1-propanol, 2-propanol (IPA), 1-butanol, 1-pentanol, 1-hexanol, 1-heptanol, 1-octanol and ethylene glycol (EG) (Figs. 2, 3 and Suppl. Notes 2-4).

Heavy water, D_2O, presents the closest chemical analogue to light water, H_2O – the solvent in which a strong signature of the electrosolvation force was first identified[18]. Possessing highly similar electronic properties to water (such as dipole moment, dielectric constant), D_2O molecules predictably exhibit similar orientational behaviour at interfaces as for H_2O as reported both in MD simulations and in experiments[24-26]. Assuming a value of $\mu_{\mathrm{av}}(\sigma = 0) = \mu_{\mathrm{av}}(0) \approx +0.8$ D nm^{-2}, similar to water, would suggest $B < 0$ for negatively charged particles ($z = -1$) in Eq. (2). Within the electrosolvation view, this would imply interparticle attraction and hence the possibility of formation of stable clusters, similar to water. Indeed, experiments on silica particles in D_2O displayed the formation of stable, slowly reorganizing hexagonally closed packed (hcp) clusters, characterised by an average particle inter-surface separation $x_{\mathrm{min}} \approx 2.5\,\kappa^{-1}$ which is in line with indications from the interfacial solvation model[16-18] (Supplementary Tables 3, 25). On the other hand, for positively charged particles where $z = +1$, a value of $\mu_{\mathrm{av}}(0) > 0$ entails $B > 0$ which in turn implies interparticle repulsions and no cluster formation, capturing the experimental observation for NH_2 particles suspended in D_2O (Fig. 2 and Supplementary Fig. 18).

We then explored interparticle interactions in DMSO, a polar aprotic solvent whose trigonal molecular structure echoes the bent structure of water. Interestingly, in contrast to water, we found that positively charged aminated-silica particles formed clusters in DMSO, albeit in a narrow range of pH, controlled experimentally by varying the amount of HCl added to the pure solvent (Fig. 1, Supplementary Fig. 16 and Supplementary Table 8). On the other hand, silica particle interactions remained

repulsive over a range of added HCl and NaOH concentrations (Supplementary Fig. 16). The observations on NH_2 particles are in fact consistent with the expected orientation of DMSO from MD simulations performed at an O-atom or model NH_2 surface (Fig. 2f)[19]. Here the net orientation of solvent dipoles is inverted compared to water, i.e., $\mu_{\mathrm{av}}(\sigma) < 0$, for surface with a small positive surface charge density, implying interparticle attraction in the interfacial solvation model (Fig. 2e). Simulations at model silica surfaces however indicate that $\mu_{\mathrm{av}}(0)$ depends on the silanol group density, Γ, and may be negative or positive depending on the value of Γ, which is similar to inferences for alcohols[19] (Fig. 2f). But for silica surfaces with $\Gamma \lesssim 1$ nm^{-2} –which may be a realistic value – MD simulations indeed suggest that $\mu_{\mathrm{av}}(0) \lesssim 0$ implying $B \gtrsim 0$. This points to an interparticle interaction that is devoid of a significant attractive contribution for negatively charged silica particles, as observed in experiment (Suppl. Notes 4, 8)[27-29].

Next, we examined interparticle interactions in a range of primary alcohols (Fig. 3). Previous experiments showed that positively charged NH_2 particles readily self-attract and form crystalline clusters in ethanol and IPA, characterized by large interparticle spacings ($x_{\mathrm{min}} \approx 0.5 - 1.5$ μm $= 5 - 11\,\kappa^{-1}$)[18]. In addition to their aliphatic groups of variable length, primary alcohols from methanol to 1-octanol possess a hydroxyl group capable of hydrogen bonding. Similar to previously described MD simulations of ethanol and IPA at an O-atom interface, we expect the likely net orientation of alcohols at a neutral aminated silica surface to entail the hydroxyl group pointing on average more towards the bulk medium, since this orientation presumably favours hydrogen bonding[18,19]. We estimate a net dipole moment surface density $\mu_{\mathrm{av}}(0) = -0.4$ D nm^{-2} for simulations of 1-hexanol at a neutral O-atom wall, similar to both the value expected for other primary alcohols and IPA as well as results for IPA at an amine surface (Fig. 2f). Eq. (2) therefore implies interparticle attraction for NH_2 particles and repulsion for negatively charged particles, which was indeed observed in experiments performed in a range of primary alcohols (Fig. 3). The strength of the interparticle interaction in our experiments is characterized by the depth, w, of the minimum in the inferred pair potential, $U(x)$. Interestingly, similar to cluster formation in water, we found that even

in non-aqueous solvents, w depended strongly on the proton concentration in the medium (Fig. 3, Supplementary Fig. 5, Suppl. Note 2). Note that, similar to DMSO, MD simulations of alcohols at silica surfaces indicate $\mu_{\mathrm{av}}(0)$ values that depend strongly on the silanol group density, Γ, and can point to the possibility of weak cluster formation for silica particles in 1-hexanol, contrary to our experimental observations (Fig. 2f, Suppl. Notes 2, 8).

Given the strong signature of molecular orientational anisotropy of DMSO and primary alcohols at an interface and the apparent impact thereof on interparticle interactions, we set out to examine interparticle interactions in a symmetrical diol, ethylene glycol (1,2-ethanediol — EG). EG has significant conformational complexity compared to water and alcohols: it exists in bulk solution as an 80/20 mix of gauche and trans conformers, where the former conformer has a rather large dipole moment (2.3 D) and the latter an effectively zero dipole moment[30,31]. However, in EG, neither negatively charged SiO_2 nor positively charged NH_2 particles displayed interparticle attraction under either acidic or basic conditions (Fig. 2, Supplementary Fig. 17). Interestingly, our MD simulations of EG at strongly bonding H-bonding silanol surfaces of group densities $\Gamma = 0.5 - 4.7$ OH nm^{-2} show that $\mu_{\mathrm{av}}(0) \approx -0.1$ to $+0.15$ D nm^{-2}, which is significantly smaller in magnitude than the value $\mu_{\mathrm{av}}(0) \approx -0.5$ D nm^{-2} obtained for EG at a hydrophobic O-atom surface (Fig. 2f, MD simulation methods). It is possible that a low magnitude of $|\mu_{\mathrm{av}}(0)| \approx 0.1$ D nm^{-2} is not large enough to support a substantial attractive force required for cluster formation, i.e., $\mu_{\mathrm{av}}(\sigma) \to 0$ would entail $B \to 0$ in Eq. (1) (Suppl. Note 3). EG thus presents an important departure from the other solvent media considered and therefore a significant opportunity for further understanding of the electrosolvation interaction.

Water in alcohol influences the properties of the force

Having examined interparticle interactions in pure solvents, we investigated the nature of the electrosolvation force for positively and negatively charged particles suspended in binary mixtures of water and IPA. NH_2 particles formed stable clusters in pure IPA (pH

$\approx 4-5$) as previously reported, and the addition of small amounts of water up to about 10% (v/v) did not affect the ability of the particles to form clusters (Fig. 4)[18]. For increasing amounts of added water, however, we found that cluster formation was progressively suppressed, with the qualitative structure of the suspensions resembling the results obtained for NH_2 particles in pure water (monotonic repulsions).

Negatively charged particles in water-IPA mixtures displayed inverted trends in cluster formation with increasing water content in the mixture (Fig. 4). We observed no clustering in IPA containing small amounts ($< 1\%$ (v/v)) of water. With increasing fractional content of water however, silica particles formed stable clusters whose structure above 5% (v/v) water qualitatively reflected that observed in pure water (Fig. 4b). The concentration at which the transition from alcohol-like (repulsive) interparticle interactions to water-like (attractive) interactions was found to depend strongly on particle chemistry and was ≈50% for COOH particles (Fig. 4e).

These intriguing observations do in fact find an explanation within the interfacial solvation view which would suggest that the sign of B in Eq. (2) is governed by the sign of the dominant interfacial dipole moment characterising a given solvent mixture. In water-alcohol mixtures containing bulk concentrations of $\approx 10\%$ (v/v) water and larger, the interfacial dipole moment density at the hydrophilic surfaces characteristic of our experiments may be expected to be largely determined by the interfacial character of molecular water[32]. MD simulations of 2% (v/v) water/IPA mixtures indeed showed strong adsorption of water molecules to surface sites bearing silanol groups, indicating an effective concentration enhancement of about a factor 8 compared to the bulk. In contrast, simulations at the same low concentration reveal no substantial surface adsorption of water at a model amine surface which may be viewed as less hydrophilic compared to silica (Fig. 4f and MD simulation methods, Suppl. Note 1). Furthermore, we observed particle-type dependent disparities in the fractional water-content marking the onset of cluster formation in negatively charged polymeric COOH and SiO_2 particles, which may be attributed to the impact of surface chemistry on the composition and structuring of the interfacial electrolyte. Note that estimating molecular orientations and

dipole moment densities from simulations of silica and amine interfaces immersed in solvent mixtures is associated with significant challenges (see MD simulation methods). Therefore we do not infer $\mu_{av}(0)$ values from MD simulations and limit the discussion to a qualitative interpretation of the observed behaviour based on the dominant interfacial solvent species indicated by the simulations.

We also examined a possible role for various monovalent and divalent cations in the interaction between silica particles in water and found no significant influence on the interaction at the low ionic strength (ca. 0.1 mM) tested (Fig. 5).

Chemical gating of the attraction by charge-neutral species

Inspired by the dramatic impact of small amounts of water on the interparticle interaction in binary solvent mixtures, we sought to investigate the influence of net-neutral molecular species such as zwitterionic osmolytes and surfactants added to the medium. Zwitterions and osmolytes are small net-neutral organic molecules, known to play important roles in determining the folded state of proteins, exerting 'protective' and 'disruptive' effects on protein structural stability[33-35]. Zwitterionic surface coatings are also known to display strong anti-fouling properties[36]. While the precise detail underpinning these effects is not entirely clear, universal mechanisms involving osmolyte influence on water structure have attracted substantial attention[12,35,37]. Indeed optical spectroscopy experiments on interfaces immersed in electrolytes containing zwitterions such as amino acids and osmolytes have reported both interfacial adsorption of these species as well as alterations to the interfacial water structure[38,39](Suppl. Notes 5, 6). We therefore examined particle interactions in aqueous electrolytes containing the aromatic L-amino acids tyrosine, tryptophan and phenylalanine, leucine — an aliphatic amino acid, proline, and the polar side-chain amino acids: glutamine, serine and glycine. Silica particles were suspended in aqueous solutions containing amino acids at various bulk concentrations, c_b, up to 1 M for polar amino acids such as glycine. pH and conductivity were measured for all solutions and remained largely unaffected by the addition of amino acids (Supplementary Tables 14-22), confirming their zwitterionic state in solution.

We found that amino acids added to the aqueous phase inhibited the formation of particle clusters at low concentrations ($c_b \approx 10^{-4}$ M) representing ca. 10 ppm in relation to the surrounding water. For example, whilst extremely low tyrosine concentrations of $c_b \approx 10^{-5}$ M had no impact on cluster formation, a significant reduction in the strength of the interparticle attraction was observed at around 0.1 mM (Fig. 6b,c). Concentrations of $c_b \approx 0.5$ mM and above suppressed cluster formation entirely, restoring the canonically expected interparticle repulsion between like-charged particles in aqueous solution. The inferred pair-interaction potentials displayed systematically decreasing depths of minima, w, with $w \to 0$ at $c_b > 0.1$ mM for tyrosine (Fig. 6b-d). For the polar amino acids glycine and serine, and aliphatic proline, however, the transition from attractive to repulsive behaviour was observed at about an order of magnitude higher concentration ($c_b \approx 1$ mM).

Mechanical force measurements have shown some impact of molar concentrations of zwitterionic osmolytes such as glycine and trimethylglycine (TMG) on the magnitude of the electrostatic repulsion between surfaces, and that zwitterions can accumulate and layer at mica interfaces[40,41] . However, at low concentrations ($c_b < 30$ mM), these osmolytes did not influence the magnitude and screening length of the interaction between mica or silica surfaces[40,42]. Along these lines, our measured ζ-potential values showed no significant change with increasing amino acid concentration in solution (Supplementary Tables 14-16). This suggests that the presence of amino acids does not measurably alter the interparticle electrostatic repulsion (ΔF_{el} term in Eq. (1)), but apparently rather dramatically impacts the long-range attraction between negatively charged particles, the likely origin of which is captured within the interfacial solvation view, as elucidated below.

We found that the concentration of amino acid at which particle clustering significantly weakens, and above which it vanishes, follows a trend in interfacial adsorption affinities of the amino acid molecules to the silica surface, values of which have been obtained in previous experimental and MD simulation studies[43-45]. We estimated the magnitude of the pair potential well depths, w, as a function of amino acid

concentration and compared these values with w_{max}, a measure of the electrosolvation interaction strength in pure water devoid of added solutes. In each instance, we determined the bulk concentration of amino acid, $c_{1/2}$, at which the strength of the interparticle attraction given by w/w_{max} was half-maximal (Fig. 6d). Importantly quartz crystal microbalance measurements at silica and polystyrene interfaces have shown that amino acids and polypeptides adsorb to these interfaces substantially[38,39]. The reported extents of adsorption in general agree with u, the value of the minimum energy in the potential of mean force (PMF) for a single amino acid molecule interacting with a silica surface obtained from MD simulations in the literature[38,39,44,46]. We may therefore estimate a surface concentration of amino acid, c_{s}, for a given bulk concentration c_{b} using the Boltzmann relation $c_{\mathrm{s}} = c_{\mathrm{b}} \exp\left(-\frac{u}{\mathrm{k_B}T}\right)$,[44,46]. Assuming constant c_{s}, a plot of $\ln c_{1/2}$ vs. u reveals a linear relationship for the amino acids tested. This suggests that the more strongly adsorbing an amino acid is (larger $|u|$), the lower the bulk concentration c_{b} required to achieve a given surface concentration c_{s} that perturbs the interfacial structure and induces a substantial modulation of the long-ranged attractive interaction (Fig. 6e). Indeed, the different levels of adsorption of such amino acids and the varying impact they have on the interfacial water structure has been reported in SFG experiments studying both hydrophilic silica and hydrophobic polystyrene surfaces [38,39].

Furthermore, MD simulations of water containing a fixed bulk concentration of $c_{\mathrm{b}} = 1$ M amino acid, in contact with a silica surface, permit us to determine the total average dipole moment density, $\mu_{\mathrm{av}}(0)$, which includes the contribution of all interfacial species — solvent and zwitterion — in each case (Fig. 6f, g). Interestingly, simulations reveal that in the presence of amino acid in solution, $\mu_{\mathrm{av}}(0)$ decreases significantly in magnitude from its pure water value, implying a diminished contribution from the interfacial term in Eqs. (1) and (2), and a weakening of cluster formation as an experimental consequence (Fig. 6d, Supplementary Fig. 10). The similarity between the trends of both the experimentally determined $\ln c_{1/2}$ value, and simulation estimates of $\mu_{\mathrm{av}}(0)$, as a function of amino acid surface affinity, quantified by the parameter u,

strongly implicates altered molecular interfacial structuring in the experimentally observed long-range attraction (Fig. 6f).

We then turned our attention to cluster-formation experiments in the presence of methylated zwitterions such as trimethylglycine (TMG) and trimethylamine *N*-oxide (TMAO), which are known to play an important role in stabilizing the folded, more compact structure of proteins under environmental stress, as well as in regulating the formation of phase-separated protein aggregates[11-13,15,47,48]. Infrared and terahertz spectroscopy investigations have shown that TMG and TMAO strengthen the H-bonding network and alter the dynamics of bound hydration water respectively, and these properties have been implicated in their ability to stabilize biomolecular folding[49,50]. We performed experiments on SiO_2 particles suspended in aqueous solutions at increasing concentrations of TMG in an identical manner to experiments with glycine. We found that cluster formation persisted up to a much higher concentration of TMG of $c_b \approx 3$ M compared to the amino acids, and above which the strength of the interparticle attraction diminished (Fig. 7 a-d). Methylation of the amine functionality therefore appears sufficient to dramatically alter the impact of TMG on cluster formation and stability, rendering the $c_{1/2}$ value for TMG four orders of magnitude higher than its unmethylated counterpart. This observation is reminiscent of the progressive impact on water structure of alkylation in osmolytes such as urea and glycine[51,52]. Methylated glycine derivatives have also been demonstrated to adsorb more strongly than glycine to silica nanoparticles[45]. However, in experiments performed in pure water, high concentrations of TMG can result in a significant increase in ionic strength in solution, due to weak protonation at pH 7 (ca. 0.01%) of the carboxyl group whose p$K \approx 3$, which in experiments on colloidal particles generally results in a weakening of the long ranged attractive force[18]. Ionic strength measurements for 4 M TMG in solution indeed indicate $c_0 \approx 0.5$ mM which is substantially higher than $c_0 \approx 10^{-5}$ M value noted for experiments with zwitterionic amino acids (Supplementary Table 11). Thus even at the highest concentration of TMG, the reduced propensity for cluster formation may equally likely stem from an indirect slight increase in ionic strength rather than from a direct

influence of the TMG molecule on the interfacial electrolyte properties[40]. Although the reasons for the stark disparity in impacts of glycine and TMG on interparticle attraction are not immediately clear, it is possible that TMG acts to strengthen the hydrogen bonding network of water, which has been noted in both experimental and computational studies focusing on explaining the effect of TMG and TMAO on protein stability[49-51] (Fig. 8e, Suppl. Note 6).

Similar experiments on TMAO in solution yielded a $c_{1/2}$ value of 50 mM, about two orders of magnitude larger than for glycine, but nearly two orders of magnitude lower than for TMG (Fig. 7d). However, we found significant differences in the pH and ionic strength in solutions of TMAO and TMG of the same concentration. We attribute these observations to the weaker acidity of the amine oxide functionality of TMAO ($pK > 4$) resulting in a lower degree of ionization compared to the carboxyl group of TMG and a loss of zwitterionic (neutral) character as a consequence (Supplementary Table 13). Comparing experiments that controlled for pH and ionic strength, we found the $c_{1/2}$ value for TMG decreased substantially to 1 M, closer to the value obtained for TMAO, but nonetheless about an order of magnitude larger (grey curve in Fig. 7d). The experiments thus indicate that TMAO and TMG are similar in their influence on the electrosolvation interaction and that their quantitative impact on cluster formation, as reflected in $\ln c_{1/2}$ values, is readily distinguishable from the zwitterionic amino acid family.

Importantly, $\mu_{\mathrm{av}}(0)$ values inferred in molecular simulations for aqueous suspensions of osmolytes at a silica surface revealed no apparent differences amongst the all the zwitterions examined, suggesting similar experimental trends in cluster formation and dissolution, which was clearly not observed (Supplementary Fig. 10). However, for electrolyte containing TMG or TMAO, we found that the contribution of the water molecules alone to the excess dipole moment density at the interface, $\mu_{\mathrm{av,w}}(0)$, displayed a large enhancement of the pre-existing molecular dipole orientation characterizing pure water at a silica interface (Fig. 7e and MD simulation methods)[53,54]. At a concentration of $c_{\mathrm{b}} = 3$ M TMG, we noted that $\mu_{\mathrm{av,w}}(0) \approx 2$ D nm^{-2}, which is approximately five times

the value for pure water at the same neutral silica interface (Fig. 7e). This is in stark contrast to the other amino acids, except proline, where in general we estimated rather small changes in the value of $\mu_{\mathrm{av,w}}(0)$ compared to pure water. Thus, as indicated by previous computational and experimental studies, our simulations suggest that TMG and TMAO have a strong ordering effect on interfacial water molecules compared to the other zwitterions considered. This property likely offsets any disruption of the interfacial electrolyte structure caused by their adsorption at the interface and may likely underpin their role in the cluster formation problem (Figs. 7f,g, 8e)[45,48,49,55]. Interestingly, we found that the qualitative effect on $\mu_{\mathrm{av,w}}(0)$ of proline was similar to that of TMG at a silica interface. This not only recapitulates its higher $\ln c_{1/2}$ value compared to the other amino acids (Figs. 6e, 7e), but is also reminiscent of similarities amongst these three zwitterionic species observed in other contexts[42], e.g., the zwitterions TMG, TMAO and proline are considered 'protective osmolytes' for their stabilising effect on the folded state of proteins[12,14,56]. Also, SFG measurements on aqueous solutions of amino acids at silica and polystyrene interfaces show that whilst glycine does not significantly alter the signal attributed to the net orientation of interfacial water, other amino acids such as proline and leucine do change the net orientation of interfacial water considerably[39]. Furthermore, our experiments on COOH particle interactions in the presence of zwitterions in solution shed light on the role of surface chemistry in the electrosolvation interaction (Suppl. Note 9), also echoing the surface-chemistry dependence of interfacial electrolyte structure reported in spectroscopy investigations [23,39,57].

In a final experiment on the role of interfacially active agents, we examined the effect of a popular non-ionic surfactant polysorbate-20 (Tween 20), widely used in biochemical experiments to solubilize proteins and stave off non-specific adsorption to surfaces[58]. In line with its known propensity to form high-density self-organised monolayers at hydrophobic interfaces we found that low concentrations of Tween 20 ($>$ 1% (w/v) or $c_{\mathrm{b}} \approx 8$ mM) abolished stable cluster formation in silica particles (Fig. 8a-d), recapitulating the qualitative impact of this surfactant in a range of practical contexts involving molecule-surface interactions[58]. This behaviour maybe contrasted with the

effect of a simple triol, such as glycerol, known to stabilise folded states of proteins[59]. Glycerol had a non-disruptive influence on cluster formation up to $c_b \approx 1$ M in solution, similar to the water structure-reinforcing osmolytes tested (TMG and TMAO) (Fig. 8). Importantly, unlike for these zwitterionic osmolytes, our MD simulations suggest that glycerol present at $c_b = 1 - 3$ M in an aqueous electrolyte adsorbs to the silica interface, yet leaves both the total net dipole moment density, $\mu_{av}(0)$, and the dipole moment density due to water, $\mu_{av,w}(0)$, relatively unchanged (Supplementary Fig. 10). The implication within the interfacial solvation model is a relatively unaltered value of B in Eq. (2), and therefore the persistence of cluster formation even at relatively high concentrations of glycerol as indeed seen in experiments. A graphical summary of the experimental observations presented on a plot of μ_{av} vs. sign of σ shows that experimentally observed trends largely align with expectations from the interfacial solvation model of interparticle interactions (Fig. 9).

Our study provides more than 40 different experimental instances where the properties of interfacial electrolyte structure – as inferred from MD simulations – correlates with the presence or absence of long-range attraction between electrically like-charged particles in a wide range of particulate systems suspended in a variety of media containing varying amounts of co-solvents and neutral solutes (Fig. 9). The experimental outcomes are summarised in a plot that uses the sign of σ as inferred from electrokinetic (zeta potential) measurements on the particle sample and μ_{av} values from MD simulations (Fig. 9, Supplementary Fig. 2, Supplementary Tables 3-24). We find that the presence or absence of the long-range interparticle attraction can be explained within a view that invokes either the net excess dipole moment surface density in the electrolyte, or that of the solvent alone, in the immediate vicinity of the interface (Figs. 8e, 9). Overall, the findings provide an improved microscopic understanding of the origin of the experimentally observed electrosolvation force. The ability to modulate the long-range attraction using small neutral molecules and surfactants at low concentrations, and the indications that emerge, point to the profoundly important role this force likely plays in mediating colloidal stability of suspensions and possibly in biochemical interactions

involving biomolecular condensation and protein folding. Considered in conjunction with the indications from MD simulations, our experimental observations on the effects of small-molecule additives on interparticle interactions suggest three general mechanistic possibilities: (1) adsorption to interfaces at low bulk concentrations disrupts the pre-existing hydration structure around particles, thereby quelling the electrosolvation attraction and stabilising the suspension against aggregation (colloidal stability), e.g., amino acids and glycerol at > 1 M concentration (Fig. 8e) (2) surface active agents can reinforce the hydration structure around particles and thereby sustain the electrosolvation attraction and concomitant cluster formation up to much larger concentrations (e.g., TMG and TMAO, see Fig. 8e). In the biomolecular context this mechanism could be related to trends involved in the stabilisation of the folded molecular state (folding stability) (3) the additive has a non-disruptive effect on interfacial electrolyte structure, and therefore cluster formation up persists up to high concentrations, e.g., glycerol at ≤ 1 M concentration (Fig. 8e). Although our present theoretical view contains the key ingredients necessary to capture the experimental behaviour, the model does not currently include any long-range effects in the electrolyte, which may well contribute to the final overall picture. Moreover, heterogeneities in particle surface properties – such as σ and $\mu_{\mathbf{av}}$, a characteristic feature of natural systems – may also play an important role in the electrosolvation force[60-62]. Further advances in theoretical modelling of the interaction will likely benefit from renewed scrutiny of the role of electrical fields generated by polarized solvent molecules and dipoles at interfaces immersed in non-local media[63,64].

Methods

Experimental methods

Experimental set-up

A bright-field microscope was constructed in-house to observe colloidal particle suspensions. The microscope consists of a collimated 470-nm light-emitting diode (LED, M470L4, ThorLabs), a 10× objective (Olympus UPlanSApo) and a charge-coupled device camera (CCD, DCU223M, ThorLabs), as illustrated in Fig. 1. A pitch and roll platform (AMA027, ThorLabs) was used to maintain a level plane for the glass observation cell, with planarity monitored using a spirit level (DWL-80E, Digi-Pas).

The glass cell for microscopy (20/C/G/1, Starna Scientific) was cleaned prior to sample loading. The glass surface naturally provides a negatively charged surface for negatively charged particles (SiO_2 and COOH-MF) in solutions. For positively charged particles (NH_2-SiO_2), the glass cell was coated with 1% poly(ethyleneimine) (PEI) polymer solution ($M_n \approx 60$ kg mol^{-1}, $M_w \approx 750$ kg mol^{-1}, analytical standard, P3143, Sigma-Aldrich) to provide a positively charged surface layer. Once the particle suspension was loaded into the cell, the top surface was sealed with a polished cover slide such that the sample was airtight and bubble free.

Data recording and processing

Images of the colloidal suspension were recorded once all particles in solution had settled under gravity to the bottom surface of the cell. This typically required between 1 and 50 min, depending on the density and viscosity of the solvent studied. All experimental observations were repeated between 2 and 10 times. All recordings were performed using exposure times of 0.4 ms at a rate of 5 frames per second (fps) for 150 frames, with recordings performed three times at intervals of 5 min. The recorded images were then analysed using TrackNTrace based localization code to track particle coordinates for further analysis[18,65].

Procedures for preparing particle suspensions

Particles with different surface functionalities examined in this work include silica microspheres (SiO_2, type 1: 4.82 µm diameter, material density 2 g cm^{-3}, Bangs Laboratories; type 2: 5.17 µm diameter, material density 1.85 g cm^{-3}, microParticles GmbH), amino-functionalized silica microspheres (termed 'NH_2-SiO_2' or 'NH_2', 4.63 or 3.92 µm in diameter, NH_2 group content >30 µmol g^{-1}, microParticles GmbH), and carboxyl-functionalized melamine microspheres (termed 'COOH-MF' or 'COOH', 5.29 µm diameter, COOH group content ≈ 400 µmol g^{-1}, microParticles GmbH). The corresponding particle size distributions are shown in Supplementary Fig. 1.

For experiments in aqueous systems, all particles were suspended and centrifuged multiple times in the electrolyte medium of interest until the pH and conductivity of the supernatant converged to the required values. SiO_2 and COOH-MF particles were suspended in 10 mM NaOH (99.99%, Thermo Fisher) for 10 min prior to re-suspension and centrifugation in the final electrolyte. Note this step is not essential for cluster formation, but enhances cluster formation likely by increasing the extent of deprotonation of ionisable surface groups. NH_2-SiO_2 particles were not treated with NaOH prior to experiments.

For experiments in organic solvents including alcohols, DMSO and EG examined in this study, we first prepared aqueous suspensions of colloidal particles which were then centrifuged and resuspended three times in high purity ethanol to minimize moisture content in the final suspension. The particles were then resuspended in the final solvent of interest.

Characterization of particle electrical charge

The sign of particle charge in each sample was determined using electrokinetic measurements of zeta potentials (Zetasizer Nano Z, Malvern Panalytical). Representative zeta potential distributions for the silica and aminated silica particles in our experiments are presented in Supplementary Fig. 2.

Measurement of solvent and electrolyte properties

Non-aqueous solvents were stored under dry nitrogen to limit moisture absorption from ambient air (solvent purity and supplier information provided in Supplementary Table 1). Concentrated solutions of HCl and NaOH in anhydrous 2-propanol (AH-IPA) were used to adjust pH in non-aqueous media to minimise the amount of water introduced into the medium. For all experiments in non-aqueous media, we estimate a final percentage of less than 0.004% (v/v) of water arising from the addition acid and base. Similarly, to vary the ionic strength in experiments performed in IPA, a saturated solution of NaCl in AH-IPA solution was prepared and dilutions subsequently performed with AH-IPA to achieve the desired final concentration in the experiment. pH and conductivity were measured for each case (pH sensor: UltraMicroISM; conductivity sensor: InLab741 ISM; SevenDirect SD23, Mettler Toledo). Failure to properly dry the solvents prior to experiments promotes cluster formation of negatively charged particles in alcohols, as reflected in the water-IPA mixture experiments in the main text. The hygroscopic nature of the solvents considered, combined with the strong propensity of water to adsorb to the hydrophilic silica surface likely generates an interfacial layer of water surrounding the particles which can then dominate the observed the interactions. The ionic strength, c_0, of the various electrolyte solutions in our experiments were inferred by measurements of electrical conductivity, s, using the conductivity meter. An experimentally determined calibration curve of standard solutions with slope $a = \frac{s}{c_0}$, was used for this purpose, where $a \approx 150\ \mu\mathrm{S\ cm^{-1}\ mM^{-1}}$. For water, we may compare this value with a theoretical estimate of the slope, $a = \frac{e^2 \mathrm{N_A}}{6\pi\eta a_\mathrm{h}}$ where $\eta = 0.89\ \mathrm{cP}$ is the viscosity of water at 298 K, a_h is the average hydrodynamic radius of the ions in solution, e the elementary charge and $\mathrm{N_A}$ the Avogadro number[66]. Using ionic radii 1.01 and 1.82 Å for Na^+ and Cl^- ions given in ref.[67], this expression yields a value of $a = 65\ \mu\mathrm{S\ cm^{-1} mM^{-1}}$ which is within about a factor 2 of our calibration result. To convert the measured electrical conductivity to salt concentration in non-aqueous solutions such as longer linear alcohols, DMSO and EG, in which inorganic salts may be poorly soluble, we used the same calibration relationship as for aqueous electrolytes, but corrected the

inferred concentrations for the viscosity of the solvent as in ref.[18]. This procedure assumes that the hydrodynamic radii for the ionic species are identical in both water and alcohols. The uncertainties involved in the conversion of electrical conductivity measurements to salt concentration in organic solvents thus place a limit on the accuracy of experimental estimates of ionic strengths.

For experiments containing low concentrations of added osmolytes and surfactants, inferences of ionic strength were performed by measuring electrical conductivity and converting to c_0 as described above. For experiments involving high concentrations of added osmolytes, e.g., TMG and TMAO, we performed a viscosity correction of electrical conductivity data using the literature relationship, $\frac{\eta}{\eta_0} = 1 + Bc_b + Dc_b^2$, where $\frac{\eta}{\eta_0}$ is the relative viscosity of the solution containing solute at a molarity, c_b, and B and D are constants taken from Pitkänen et al.[68].

Interparticle interactions in other non-aqueous solvents

Although we did examine a broader range of solvents than those discussed in this study, e.g., formamide and dimethylformamide, we only present results for solvents where highly controlled experiments were possible. There are several important considerations that determined experimental feasibility and whether robust conclusions could be drawn from performing experiments in a given solvent. Firstly, controlled investigations require solvents of high purity as reflected in a sufficiently low ionic strength, inferred from conductivity measurements. A typical range of electrical conductivity for strong cluster formation in aqueous solutions is ca. <120 μS cm^{-1}, whereas it tends to be much smaller, <0.5 μS cm^{-1}, for experiments in IPA. Secondly, since the appearance of the long-ranged attraction depends strongly on pH, we require solvents where the addition of small amounts of acid or base does not alter the protonation state of the solvent molecules or derivatives present in the medium. We also require solvents that are non-volatile, stable at room temperature, and do not dissociate into by-products. For example, on exposure to air formamide oxidises to give formic acid. Dimethyl formamide can contain small amounts of protonatable weak base dimethyl amine. Thus, although acetone, dimethyl

formamide and formamide are H-bonding solvents and therefore of intrinsic interest alongside water and heavy water, they did not meet some of the above criteria, and experiments in these media are therefore not considered in this study[69].

MD simulation methods

Solvents in an 'O-atom-wall capacitor'

To estimate the surface averaged dipole moment density, μ_{av}, using molecular simulations, we used a parallel-plate capacitor system. Here, a slab of solvent is sandwiched by model solid surfaces carrying variable amounts of net electrical charge density, σ, as described in refs.[16,19]. Simulation boxes of neat solvents were initialised, energy minimized and subject to a short NVT and NPT equilibration to reach a density corresponding to 1 atm pressure. We used the SPC model for water except for simulations at a silica interface, and the CHARMM36 forcefield for all other solvents in this work, except for EG where we employed the model of Gaur et al.[31]. The pressure was maintained with the Parrinello-Rahman pressure coupling method with only the z-dimension of the simulation box allowed to fluctuate. The equilibrated slabs of neat solvent were then inserted into the parallel-plate capacitor system. The capacitor plates entailed an area $\approx 10\times10$ nm^2, were separated by ≈ 4 - 8 nm in the z-direction, depending on the case simulated, and were composed of positionally restrained oxygen atoms that only support Lennard-Jones (LJ) interactions. The z-dimension of the simulation box was chosen such that any density oscillations of the solvent reached a constant bulk value in the middle of the box. A subset of randomly chosen atoms in the first layer of the left wall (in direct contact with the solvent) was assigned a positive charge (left plate) which was balanced by an equal number of randomly selected atoms assigned a negative charge on the right plate. Hydrogen bonds were constrained with the LINCS algorithm. The 3dc correction of Yeh and Berkowitz was applied to remove artificial polarization induced by neighbouring image dipoles[70].

Solvents and solvent mixtures in contact with a model silica surface

The CHARMM-GUI webserver was used to generate model uncharged silica surfaces with surface group densities ranging from Γ =0.5 to 4.7 OH nm^{-2} and were parametrised with the INTERFACE-FF forcefield description[71,72]. The silica slab was solvated on either side with a slab of solvent of thickness ≈ 3 nm, energy minimized, and then subject to a short NVT equilibration with the v-rescale thermostat at 300 K for 50 ps. Next, an NPT equilibration of 500 ps was performed at 1 atm maintained with the Parrinello-Rahman pressure coupling method, with only the z-dimension of the simulation box allowed to fluctuate. We used the CHARMM TIP3P water model for simulations at a silica interface. For each solvent, the size of the simulation box was around 10×10×10 nm^3, large enough so that any density fluctuations of the solvent could reach a constant bulk value (Supplementary Fig. 3). This initialisation procedure was followed by production MD runs in an NVT ensemble lasting 5-10 ns, with a timestep of 2 fs and with trajectory frames written every 0.2 ps. The particle mesh Ewald (PME) method was used to evaluate the long-range electrostatic interactions, using a 1 Å grid spacing and a short-range cut-off of 12 Å. The LJ interactions were smoothed over the range of 10-12 Å using the force-based switching function. Hydrogen bonds were constrained with the LINCS algorithm.

For simulations involving solutions containing osmolytes, water was described with the CHARMM TIP3P model, and parameters for the osmolyte molecules were taken from the CHARMM36 and CGENFF forcefields. For the zwitterion TMAO however, we used the Shea(m) and Netz models in combination with the SPC/E water model for reasons explained in following sections[53,54]. The simulation protocol was nonetheless similar to that outlined above[54]. Osmolyte-water solutions were generated such that the simulation box approximately attained the desired final osmolyte concentration after the NPT equilibration step. Production MD was performed in an NVT ensemble lasting 20 ns. We note that these simulations employed the same silica forcefield and surface group density as that used in ref.[44] - the study that determined PMF for the interaction of

amino acids with the silica surface. Values of the PMF minima, u, from the study are presented in the plots in Fig. 6f.

We note here that estimating reliable interfacial solvent orientations and dipole moment densities from MD simulations of silica and amine surfaces immersed in binary solvent mixtures is challenging due to the sensitivity of such properties on the balance between the many types of solvent-solvent and solid-solvent interactions present in such systems. These interactions are described by the underlying forcefield parametrisations which may need careful attention to accurately model such complex systems, as noted in refs.[73,74]. In particular, the behaviour of binary solvent mixtures at interfaces can be strikingly different to the bulk behaviour and further additional complexity arises from the possible competition of solvent molecules for surface sites[75]. Therefore, we do not provide estimates of $\mu_{\mathrm{av}}(0)$ for IPA/water mixtures.

Solvents at model amine surfaces

Amine surfaces were modelled by creating a regular repeating arrangement of a small primary amine molecule $CH_3CH_2CH_2NH_2$ in a hexagonal close packed configuration with group density $\Gamma \approx 4$ groups nm^{-2} (Supplementary Fig. 3). The heavy atoms of the amine groups were positionally restrained throughout the simulations with a large force constant of 10,000 kJ mol^{-1} nm^{-2}. The simulations employed the same simulation protocol as for the O-atom capacitor, with LJ walls placed at either end of the simulation cell in the z direction. Solvent molecules were sandwiched between the amine surface and the opposing LJ wall. The LJ wall applies a uniform LJ 12-6 potential corresponding to that of a CG321 atom type and functions to maintain 2d periodicity of the system. Parametrisation for the amine molecules was performed with the CHARMM-GUI webserver. To simulate amine surfaces with a reduced surface group density of $\Gamma \approx 1$ group nm^{-2}, 75% of the amine groups had their atomic charges set to zero, whilst retaining their LJ interaction terms. Although the model amine surfaces generated may not accurately reflect the surface of the aminated silica surfaces of our positively charged nanoparticles, our aim was to capture the surface chemistry to a first approximation,

and to contrast the behaviour of a strongly hydrophilic silanol surface with a chemically different hydrogen-bonding (NH_2) group.

Determining μ_{av} from MD simulations

The excess net normal dipole moment surface-density, μ_{av}, for each MD simulation was estimated according to Eq. (3). The calculation of this quantity is closely related to the that of the excess interfacial electrical potential, φ_{int}, described extensively in refs.[16,19], with the two quantities related as follows:

$$\frac{\mu_{av}(\sigma)}{\varepsilon_0} = \frac{1}{\varepsilon_0}\left[\int_{z_{int}}^{z_{int}+l}\langle\rho(z)\mu_z(z)\rangle\,\mathrm{d}z\Big|_{interface} - \int_{z}^{z+l}\langle\rho(z)\mu_z(z)\rangle\,\mathrm{d}z\Big|_{bulk}\right] = -\varphi_{int}(\sigma) \quad (3)$$

Here, $\mu_z(z) = \vec{\mu}(z).\vec{n}$ represents the normal component of the molecular dipole moment, at a distance z from the interface, in a given simulation snapshot at a given spatial location with respect to the surface normal, $\vec{n}$, evaluated for any surface charge density, σ, of interest. $\rho(z)$ represents the density of the solvent molecules as a function of z, where the thickness of the interfacial layer is given by l, and ε_0 is the permittivity of free space. Furthermore, $\langle\ldots\rangle$ denotes spatiotemporal averaging in the xy plane of the simulation box over the duration of the simulation. The polarization $P(z)$, or the average dipole moment density, $P(z) = \langle\rho(z)\vec{\mu}(z).\vec{n}\rangle|_{bulk}$, calculated at the midplane of the capacitor from the MD simulations, was found to agree well with the value expected for a capacitor with continuum water as the dielectric material of relative permittivity ε as in refs.[16,19]. In the interfacial region however, the average dipole moment density, $\langle\rho(z)\vec{\mu}(z).\vec{n}\rangle|_{interface}$, departs substantially from the continuum value due to symmetry breaking in the orientational behaviour of the solvent induced by the presence of the interface. Integrating the quantity $\langle\rho(z)\vec{\mu}(z).\vec{n}\rangle$ over the interfacial region of thickness l, and subtracting the value of the same integral evaluated over a layer of the same thickness l in the bulk liquid (located in the middle of the capacitor), gives the "excess" net normal dipole moment surface-density, μ_{av}, at any given value of surface charge density, σ. We note here that the spatial binning of the molecular dipole moments was performed using the O-atom coordinate for water molecules and the molecular center of geometry for all other solvent molecules and osmolytes[19]. The spatial extent of the

interfacial region is defined by the parameters z_{int} and l. z_{int} denotes the location of an interfacial plane, which for an O-atom wall is given by the location nearest to the surface where $\langle \rho(z)\vec{\mu}(z).\vec{n} \rangle$ drops below the value in the bulk solvent, as in ref.[16]. The value of l is determined by the distance at which oscillations in $\langle \rho(z)\vec{\mu}(z).\vec{n} \rangle$ decay to yield a constant 'bulk' value (Supplementary Fig. 3). For all systems other than the O-atom capacitor, we determined μ_{av} at a net uncharged surface only, i.e., $\mu_{\mathrm{av}} = \mu_{\mathrm{av}}(0)$, and used the sign and magnitude of this quantity to interpret experimental observations. Since the relevant charge densities in experiments are often expected to be quite small, i.e., $|\sigma| < 0.1\ e$ nm^{-2}, and μ_{av} generally does not depend strongly on σ, except in some cases e.g., DMSO, the value of $\mu_{\mathrm{av}}(0)$ generally proves sufficient to rationalise experimental observations within the interfacial solvation model.

Since our model silica systems have two surfaces in contact with the solution of interest, $\mu_{\mathrm{av}}(0)$ was determined as an average over both interfaces. Furthermore, for simulations involving osmolyte molecules in the solvent phase, $\mu_{\mathrm{av}}(0)$ was found to not converge to a constant value in the bulk liquid, due to the low concentration of zwitterions in the simulation box. The residual uncertainty in $\mu_{\mathrm{av}}(0)$ was estimated by the difference in the value obtained for the two silica interfaces (containing contributions both from the solvent and osmolyte molecules), and was found to be small: $\Delta\mu_{\mathrm{av}} \approx 0.01 - 0.03$ D nm^{-2}. Error bars depicted in Fig. 6f reflect this source of error. The interfacial dipole moment density was integrated over an interfacial region of thickness $l = 1.5$ nm for all simulations involving zwitterionic osmolytes.

Simulations of EG

For all simulations involving EG, we employed the model of Gaur et al.[31]. This model has been developed to correctly reproduce the ratio of gauche and trans conformers of EG in the bulk liquid and at the air/water interface. We performed simulations of EG in contact with a hydrophobic O-atom wall and silica surfaces of various silanol group densities ranging from $\Gamma =$ 0.5 – 4.7 OH nm^{-2}. This yielded $\mu_{\mathrm{av}}(0)$ values of ≈ -0.5 D

nm^{-2} for the O atom wall and a value of significantly lower magnitude, $\mu_{av}(0) = $ -0.1 to +0.15 D nm^{-2}, for the silica surfaces (Suppl. Note 3).

Simulations of TMAO/water solutions

The parametrisation in MD of certain zwitterions such as TMAO is known to be challenging, and it is important to use a model that accurately describes the solvation thermodynamics[54]. In this work we have employed the Shea(m) and Netz models for TMAO, which are optimized forcefields for TMAO that better capture the density and activity coefficient of TMAO-water solutions, and are therefore generally preferred[53,54]. The SPC/E water model was used in the modelling of TMAO-water solutions as in ref.[54]. Forcefield parameters for the TMAO models are compatible with our silica forcefield INTERFACE-FF, which was designed to be thermodynamically consistent with different classes of forcefields with minor adjustment[71,76]. Simulations of TMAO in water using the Shea(m) and Netz models displayed increasing positive values of $\mu_{av,w}(0)$ with increasing concentration of TMAO in the aqueous medium (Fig. 7e). However, the CHARMM model (the forcefield employed for all other zwitterions in this work), resulted in significantly different orientational behaviour of TMAO at a silica interface, and a decrease in in $\mu_{av,w}(0)$ with increasing TMAO concentration such that $\mu_{av,w}(0) \approx 0$ D nm^{-2} at $c_b = 3$ M. This highlights the general importance of accurate forcefield parametrisation in extracting experimentally relevant values of $\mu_{av,w}$. Whilst we cannot rule out that further model parametrisation of MD models may be needed for other zwitterionic osmolytes, we were able to qualitatively capture the general experimental trends for all other osmolytes in this study using the CHARMM models.

Hydrogen bond analysis

In our simulations, we identify a hydrogen-bond based on geometric criteria given by a donor–acceptor distance of less than 3 Å and a donor–H–acceptor angle of over 150°. The MDAnalysis package was used to load and perform hydrogen bond analysis on the simulation trajectories[77]. In particular, we studied the number of hydrogen bonds formed

between TMAO/TMG zwitterions and water molecules both at a silica interface and in bulk solution, as discussed further in Suppl. Note 6.

BD simulation methods

The main text presents forms of the underlying pair-interaction potentials, $U(x)$, that have been inferred from BD simulations to match the experimentally measured radial probability distribution functions, $g(r)$. The procedures underpinning the simulations have been discussed in detail in ref.[18] and will be summarised briefly here. We performed BD simulations of a two-dimensional distribution of interacting spheres using the BROWNIAN package in the Large-scale Atomic/Molecular Massively Parallel Simulator (LAMMPS) software[78].

We use a pair potential $U'(x)$ between two interacting particles of the form:

$$U'(x) = Ae^{-\kappa_1 x} + Be^{-\kappa_2 x} + U_{\mathrm{vdW}} \quad (4)$$

Here the first term represents the overall repulsive electrostatic free energy of interaction, $\Delta F_{\mathrm{el}}(x) = A\exp(-\kappa_1 x)$, with $A > 0$ always, and the second term, $\Delta F_{\mathrm{int}}(x) = B\exp(-\kappa_2 x)$, denotes the free energy contribution arising from interfacial solvation[2], where B may be positive, negative or zero as described previously and briefly in Suppl. Note 1[16,17]. Note that $\kappa_2 < \kappa_1 \approx \kappa$ as shown in ref.[16,17]. Importantly the $\Delta F_{\mathrm{int}}(x)$ term implies an attractive contribution to the total free energy for negatively charged particles in water[16,17]. The third term represents the vdW attraction between silica particles in solution, for which we have used the expression derived in ref.[79] similar to ref.[18].

The simulations account for the experimentally determined polydispersity in particle size (Supplementary Fig. 1) at the lowest level of approximation. Whilst r, the inteparticle separation, accounts for the size of the individual particles the interaction potential, $U'(x)$, remains unaffected and independent of the size of the particle-pair, which would not be accurate in practice. Using a value of the Hamaker constant A_{H} =2.4 zJ (taken from ref.[80] and which is in agreement with other literature estimates[81]), we estimated a rather small contribution for the vdW interaction, $0 \geq U_{\mathrm{vdW}} \gtrsim -0.4\,\mathrm{k_B}T$, to the total interaction energy at large separations, $x \geq 0.2$ μm, which is the relevant

intersurface separation for attractive interactions observed in a majority of experiments in this work. Therefore, the vdW interaction cannot be responsible for the deep and long-ranged minima implied by the clusters observed in experiment. In experiments involving D_2O or aqueous solutions containing high concentrations of TMG, we found average an interparticle separation in clusters of $x_{\mathrm{min}} \approx 0.1$ μm, implying $U_{\mathrm{vdW}} \approx -0.6\,\mathrm{k_B}T$ which is much smaller in magnitude than $|w|$ in these cases. The presented $U(x)$ profiles which are free of the U_{vdW} contribution, that is:

$$U(x) = Ae^{-\kappa_1 x} + Be^{-\kappa_2 x} \tag{5}$$

The experimentally measured $g(r)$ curve provides an initial estimate of the location of the minimum in the pair potential x_{min} which can be used to guide the choice of input parameters to the BD simulation. We generally take $\kappa_1^{-1} = \kappa^{-1}$, the Debye length, which is estimated from the experimentally measured salt concentration. We then use a trial value of the interaction free energy at the minimum, $U(x_{\mathrm{min}}) = w < 0$, to obtain initial values for the parameters A and B as inputs for the pair-interaction potential $U(x)$, using the equations:

$$A = -\frac{w\kappa_2 \exp(\kappa_1 x_{\mathrm{min}})}{\kappa_1 - \kappa_2}\,; B = \frac{w\kappa_1 \exp(\kappa_2 x_{\mathrm{min}})}{\kappa_1 - \kappa_2} \tag{6}$$

where we have taken $\kappa_2/\kappa_1 \approx 0.95$, as suggested in ref.[17].

Particle coordinates for the BD simulations were initialized via random particle placement in a 200×200 μm^2 simulation box at the experimentally measured particle density (≈ 0.008 particles μm^{-2}). Periodic boundaries were applied in the x and y dimensions. The z coordinate of the particles were fixed at a constant height throughout the simulation, ensuring a 2d system of interacting particles mimicking experiment. Convergence of the potential energy per particle in our BD simulations was monitored over time. Particle positions used for the calculation of the final simulated radial probability density distributions, $g(r)$, were collected once the value of the potential energy reached a stationary value. This criterion was typically met after ≈ 30 – 60 min of simulation time in a simulation involving a strongly attractive $U(x)$ with a well depth $|w|$ of several $\mathrm{k_B}T$.

References

1 Lis, D., Backus, E. H. G., Hunger, J., Parekh, S. H. & Bonn, M. Liquid flow along a solid surface reversibly alters interfacial chemistry. *Science* **344**, 1138-1142 (2014).

2 Zhong, J. *et al.* Atmospheric Spectroscopy and Photochemistry at Environmental Water Interfaces. *Annu. Rev. Phys. Chem.* **70**, 45-69 (2019).

3 Gonella, G. *et al.* Water at charged interfaces. *Nat. Rev. Chem.* **5**, 466-485 (2021).

4 Whitesides, G. M., Mathias, J. P. & Seto, C. T. Molecular Self-Assembly and Nanochemistry: a Chemical Strategy for the Synthesis of Nanostructures. *Science* **254**, 1312-1319 (1991).

5 Mann, S. Self-assembly and transformation of hybrid nano-objects and nanostructures under equilibrium and non-equilibrium conditions. *Nat. Mater.* **8**, 781-792 (2009).

6 Zaera, F. Probing Liquid/Solid Interfaces at the Molecular Level. *Chem. Rev.* **112**, 2920-2986 (2012).

7 Björneholm, O. *et al.* Water at Interfaces. *Chem. Rev.* **116**, 7698-7726 (2016).

8 Eder, M., Amini, S. & Fratzl, P. Biological composites—complex structures for functional diversity. *Science* **362**, 543-547 (2018).

9 Kim, M. J., Farmer, D. K. & Bertram, T. H. A controlling role for the air−sea interface in the chemical processing of reactive nitrogen in the coastal marine boundary layer. *Proc. Natl. Acad. Sci. U.S.A* **111**, 3943-3948 (2014).

10 Yancey, P. H., Clark, M. E., Hand, S. C., Bowlus, R. D. & Somero, G. N. Living with Water Stress: Evolution of Osmolyte Systems. *Science* **217**, 1214-1222 (1982).

11 Tanaka, M. *et al.* Trehalose alleviates polyglutamine-mediated pathology in a mouse model of Huntington disease. *Nat. Med.* **10**, 148-154 (2004).

12 Street, T. O., Bolen, D. W. & Rose, G. D. A molecular mechanism for osmolyte-induced protein stability. *Proc. Natl. Acad. Sci. U.S.A* **103**, 13997-14002 (2006).

13 Levine, Z. A., Larini, L., Lapointe, N. E., Feinstein, S. C. & Shea, J.-E. Regulation and aggregation of intrinsically disordered peptides. *Proc. Natl. Acad. Sci. U.S.A* **112**, 2758-2763 (2015).

14 Liao, Y.-T., Manson, A. C., Delyser, M. R., Noid, W. G. & Cremer, P. S. Trimethylamine N-oxide stabilizes proteins via a distinct mechanism compared with betaine and glycine. *Proc. Natl. Acad. Sci. U.S.A* **114**, 2479-2484 (2017).

15 Aravindan, S. *et al.* Osmolytes dynamically regulate mutant Huntingtin aggregation and CREB function in Huntington's disease cell models. *Sci. Rep.* **10**, 15511 (2020).

16 Kubincová, A., Hünenberger, P. H. & Krishnan, M. Interfacial solvation can explain attraction between like-charged objects in aqueous solution. *J. Chem. Phys.* **152**, 104713 (2020).

17 Behjatian, A., Walker-Gibbons, R., Schekochihin, A. A. & Krishnan, M. Nonmonotonic Pair Potentials in the Interaction of Like-Charged Objects in Solution. *Langmuir* **38**, 786−800 (2022).
18 Wang, S., Walker-Gibbons, R., Watkins, B., Flynn, M. & Krishnan, M. A charge-dependent long-ranged force drives tailored assembly of matter in solution. *Nat. Nanotechnol.* **19**, 485–493 (2024).
19 Walker-Gibbons, R., Kubincová, A., Hünenberger, P. H. & Krishnan, M. The Role of Surface Chemistry in the Orientational Behavior of Water at an Interface. *J. Phys. Chem. B* **126**, 4697-4710 (2022).
20 Baksh, M. M., Jaros, M. & Groves, J. T. Detection of molecular interactions at membrane surfaces through colloid phase transitions. *Nature* **427**, 139-141 (2004).
21 Gomez, E. W., Clack, N. G., Wu, H.-J. & Groves, J. T. Like-charge interactions between colloidal particles are asymmetric with respect to sign. *Soft Matter* **5**, 1931–1936 (2009).
22 Ye, S., Nihonyanagi, S. & Uosaki, K. Sum frequency generation (SFG) study of the pH-dependent water structure on a fused quartz surface modified by an octadecyltrichlorosilane (OTS) monolayer. *Phys. Chem. Chem. Phys.* **3**, 3463-3469 (2001).
23 Myalitsin, A., Urashirna, S. H., Nihonyanagi, S., Yamaguchi, S. & Tahara, T. Water Structure at the Buried Silica/Aqueous Interface Studied by Heterodyne-Detected Vibrational Sum-Frequency Generation. *J. Phys. Chem. C* **120**, 9357-9363 (2016).
24 Marchioro, A. *et al.* Surface Characterization of Colloidal Silica Nanoparticles by Second Harmonic Scattering: Quantifying the Surface Potential and Interfacial Water Order. *J. Phys. Chem. C* **123**, 20393-20404 (2019).
25 Nagata, Y., Pool, R. E., Backus, E. H. G. & Bonn, M. Nuclear Quantum Effects Affect Bond Orientation of Water at the Water-Vapor Interface. *Phys. Rev. Lett.* **109**, 226101 (2012).
26 Montenegro, A. *et al.* Field-Dependent Orientation and Free Energy of D2O at an Electrode Surface Observed via SFG Spectroscopy. *J. Phys. Chem. C* **126**, 20831-20839 (2022).
27 Fan, H.-F., Li, F., Zare, R. N. & Lin, K.-C. Characterization of Two Types of Silanol Groups on Fused-Silica Surfaces Using Evanescent-Wave Cavity Ring-Down Spectroscopy. *Anal. Chem.* **79**, 3654-3661 (2007).
28 Lagström, T., Gmür, T. A., Quaroni, L., Goel, A. & Brown, M. A. Surface Vibrational Structure of Colloidal Silica and Its Direct Correlation with Surface Charge Density. *Langmuir* **31**, 3621-3626 (2015).
29 Darlington, A. M. & Gibbs-Davis, J. M. Bimodal or Trimodal? The Influence of Starting pH on Site Identity and Distribution at the Low Salt Aqueous/Silica Interface. *J. Phys. Chem. C* **119**, 16560-16567 (2015).
30 Jindal, A. & Vasudevan, S. Molecular Conformation and Hydrogen Bond Formation in Liquid Ethylene Glycol. *J. Phys. Chem. B* **124**, 9136-9143 (2020).

31 Gaur, A. & Balasubramanian, S. Liquid ethylene glycol: prediction of physical properties, conformer population and interfacial enrichment with a refined non-polarizable force field. *Phys. Chem. Chem. Phys.* **24**, 10985-10992 (2022).
32 Melnikov, S. M., Höltzel, A., Seidel-Morgenstern, A. & Tallarek, U. A Molecular Dynamics Study on the Partitioning Mechanism in Hydrophilic Interaction Chromatography. *Angew. Chem. Int. Ed.* **51**, 6251-6254 (2012).
33 Bolen, D. W. & Baskakov, I. V. The osmophobic effect: natural selection of a thermodynamic force in protein folding 1 1Edited by D. Draper. *J. Mol. Biol.* **310**, 955-963 (2001).
34 Panuszko, A., Adamczak, B., Czub, J., Gojło, E. & Stangret, J. Hydration of amino acids: FTIR spectra and molecular dynamics studies. *Amino Acids* **47**, 2265-2278 (2015).
35 Adamczak, B., Wieczór, M., Kogut, M., Stangret, J. & Czub, J. Molecular basis of the osmolyte effect on protein stability: a lesson from the mechanical unfolding of lysozyme. *Biochem. J.* **473**, 3705-3724 (2016).
36 Mi, L. & Jiang, S. Integrated Antimicrobial and Nonfouling Zwitterionic Polymers. *Angew. Chem. Int. Ed.* **53**, 1746-1754 (2014).
37 Rösgen, J., Pettitt, B. M. & Bolen, D. W. Protein Folding, Stability, and Solvation Structure in Osmolyte Solutions. *Biophys. J.* **89**, 2988-2997 (2005).
38 York, R. L., Holinga, G. J. & Somorjai, G. A. An Investigation of the Influence of Chain Length on the Interfacial Ordering of l-Lysine and l-Proline and Their Homopeptides at Hydrophobic and Hydrophilic Interfaces Studied by Sum Frequency Generation and Quartz Crystal Microbalance. *Langmuir* **25**, 9369-9374 (2009).
39 Holinga, G. J. *et al.* An SFG Study of Interfacial Amino Acids at the Hydrophilic SiO2 and Hydrophobic Deuterated Polystyrene Surfaces. *J. Am. Chem. Soc.* **133**, 6243-6253 (2011).
40 Ridwan, M. G., Shrestha, B. R., Maharjan, N. & Mishra, H. Zwitterions Layer at but Do Not Screen Electrified Interfaces. *J. Phys. Chem. B* **126**, 1852-1860 (2022).
41 Hallett, J. E., Agg, K. J. & Perkin, S. Zwitterions fine-tune interactions in electrolyte solutions. *Proc. Natl. Acad. Sci. U.S.A* **120**, e2215585120 (2023).
42 Govrin, R., Tcherner, S., Obstbaum, T. & Sivan, U. Zwitterionic Osmolytes Resurrect Electrostatic Interactions Screened by Salt. *J. Am. Chem. Soc.* **140**, 14206-14210 (2018).
43 Gao, Q. *et al.* Amino Acid Adsorption on Mesoporous Materials: Influence of Types of Amino Acids, Modification of Mesoporous Materials, and Solution Conditions. *J. Phys. Chem. B* **112**, 2261-2267 (2008).
44 Bag, S. *et al.* Buffer Influence on the Amino Acid Silica Interaction. *Chemphyschem* **21**, 2347-2356 (2020).
45 Xie, M. & Brüschweiler, R. Degree of N-Methylation of Nucleosides and Metabolites Controls Binding Affinity to Pristine Silica Surfaces. *J. Phys. Chem. Lett.* **11**, 10401-10407 (2020).

46 Rimola, A., Costa, D., Sodupe, M., Lambert, J.-F. & Ugliengo, P. Silica Surface Features and Their Role in the Adsorption of Biomolecules: Computational Modeling and Experiments. *Chem. Rev.* **113**, 4216-4313 (2013).
47 Yancey, P. H. Organic osmolytes as compatible, metabolic and counteracting cytoprotectants in high osmolarity and other stresses. *J. Exp. Biol.* **208**, 2819-2830 (2005).
48 Bruździak, P., Panuszko, A. & Stangret, J. Influence of Osmolytes on Protein and Water Structure: A Step To Understanding the Mechanism of Protein Stabilization. *J. Phys. Chem. B* **117**, 11502-11508 (2013).
49 Stasiulewicz, M., Panuszko, A., Bruździak, P. & Stangret, J. Mechanism of Osmolyte Stabilization–Destabilization of Proteins: Experimental Evidence. *J. Phys. Chem. B* **126**, 2990-2999 (2022).
50 Hishida, M., Anjum, R., Anada, T., Murakami, D. & Tanaka, M. Effect of Osmolytes on Water Mobility Correlates with Their Stabilizing Effect on Proteins. *J. Phys. Chem. B* **126**, 2466-2475 (2022).
51 White, A. & Jiang, S. Local and Bulk Hydration of Zwitterionic Glycine and its Analogues through Molecular Simulations. *J. Phys. Chem. B* **115**, 660-667 (2011).
52 Panuszko, A., Bruździak, P., Kaczkowska, E. & Stangret, J. General Mechanism of Osmolytes' Influence on Protein Stability Irrespective of the Type of Osmolyte Cosolvent. *J. Phys. Chem. B* **120**, 11159-11169 (2016).
53 Schneck, E., Horinek, D. & Netz, R. R. Insight into the Molecular Mechanisms of Protein Stabilizing Osmolytes from Global Force-Field Variations. *J. Phys. Chem. B* **117**, 8310-8321 (2013).
54 Ganguly, P., Polák, J., Van Der Vegt, N. F. A., Heyda, J. & Shea, J.-E. Protein Stability in TMAO and Mixed Urea–TMAO Solutions. *J. Phys. Chem. B* **124**, 6181-6197 (2020).
55 Zou, Q., Bennion, B. J., Daggett, V. & Murphy, K. P. The Molecular Mechanism of Stabilization of Proteins by TMAO and Its Ability to Counteract the Effects of Urea. *J. Am. Chem. Soc.* **124**, 1192-1202 (2002).
56 Bozorgmehr, M. R. & Monhemi, H. How Can a Free Amino Acid Stabilize a Protein? Insights from Molecular Dynamics Simulation. *J. Solution Chem.* **44**, 45-53 (2015).
57 Chen, X., Hua, W., Huang, Z. & Allen, H. C. Interfacial Water Structure Associated with Phospholipid Membranes Studied by Phase-Sensitive Vibrational Sum Frequency Generation Spectroscopy. *J. Am. Chem. Soc.* **132**, 11336-11342 (2010).
58 Shen, L., Guo, A. & Zhu, X. Tween surfactants: Adsorption, self-organization, and protein resistance. *Surf. Sci.* **605**, 494-499 (2011).
59 Vagenende, V., Yap, M. G. S. & Trout, B. L. Mechanisms of Protein Stabilization and Prevention of Protein Aggregation by Glycerol. *Biochemistry* **48**, 11084-11096 (2009).

60 Chen, Y. *et al.* Electrolytes induce long-range orientational order and free energy changes in the H-bond network of bulk water. *Sci. Adv.* **2**, e1501891 (2016).

61 Dedic, J., Okur, H. I. & Roke, S. Polyelectrolytes induce water-water correlations that result in dramatic viscosity changes and nuclear quantum effects. *Sci. Adv.* **5**, eaay1443 (2019).

62 Dedic, J., Okur, H. I. & Roke, S. Hyaluronan orders water molecules in its nanoscale extended hydration shells. *Sci. Adv.* **7**, eabf2558 (2021).

63 Gruen, D. W. R. & Marčelja, S. Spatially varying polarization in water. A model for the electric double layer and the hydration force. *J. Chem. Soc., Faraday Trans. 2* **79**, 225-242 (1983).

64 Belaya, M. L., Feigel'Man, M. V. & Levadny, V. G. Structural forces as a result of nonlocal water polarizability. *Langmuir* **3**, 648-654 (1987).

65 Stein, S. C. & Thiart, J. TrackNTrace: A simple and extendable open-source framework for developing single-molecule localization and tracking algorithms. *Sci. Rep.* **6**, 37947 (2016).

66 Kokot, G., Bespalova, M. I. & Krishnan, M. Measured electrical charge of SiO2 in polar and nonpolar media. *Journal of Chemical Physics* **145** (2016).

67 Masterton, W. L., Bolocofsky, D. & Lee, T. P. Ionic radii from scaled particle theory of the salt effect. *J. Phys. Chem.* **75**, 2809-2815 (1971).

68 Pitkänen, I., Suuronen, J. & Nurmi, J. Partial Molar Volume, Ionization, Viscosity and Structure of Glycine Betaine in Aqueous Solutions. *J. Solution Chem.* **39**, 1609-1626 (2010).

69 Buncel, E. & Symons, E. A. The inherent instability of dimethylformamide–water systems containing hydroxide ion. *J. Chem. Soc. D*, 164-165 (1970).

70 Yeh, I.-C. & Wallqvist, A. On the proper calculation of electrostatic interactions in solid-supported bilayer systems. *J. Chem. Phys.* **134**, 055109 (2011).

71 Emami, F. S. *et al.* Force Field and a Surface Model Database for Silica to Simulate Interfacial Properties in Atomic Resolution. *Chem. Mater.* **26**, 2647-2658 (2014).

72 Choi, Y. K. *et al.* CHARMM-GUI Nanomaterial Modeler for Modeling and Simulation of Nanomaterial Systems. *J. Chem. Theory Comput.* **18**, 479–493 (2021).

73 Dai, J. X., Li, X. F., Zhao, L. F. & Sun, H. Enthalpies of mixing predicted using molecular dynamics simulations and OPLS force field. *Fluid Phase Equilib.* **289**, 156-165 (2010).

74 Karnes, J. J. & Benjamin, I. Mechanism and Dynamics of Molecular Exchange at the Silica/Binary Solvent Mixtures Interface. *J. Phys. Chem. A* **119**, 12073-12081 (2015).

75 Gobrogge, E. A. & Walker, R. A. Binary Solvent Organization at Silica/Liquid Interfaces: Preferential Ordering in Acetonitrile–Methanol Mixtures. *J. Phys. Chem. Lett.* **5**, 2688-2693 (2014).

76 Heinz, H., Lin, T.-J., Kishore Mishra, R. & Emami, F. S. Thermodynamically Consistent Force Fields for the Assembly of Inorganic, Organic, and Biological Nanostructures: The INTERFACE Force Field. *Langmuir* **29**, 1754-1765 (2013).

77 Michaud-Agrawal, N., Denning, E. J., Woolf, T. B. & Beckstein, O. MDAnalysis: A toolkit for the analysis of molecular dynamics simulations. *J. Comput. Chem.* **32**, 2319-2327 (2011).

78 Thompson, A. P. *et al.* LAMMPS - a flexible simulation tool for particle-based materials modeling at the atomic, meso, and continuum scales. *Comput. Phys. Commun.* **271**, 108171 (2022).

79 Hamaker, H. C. The London—van der Waals attraction between spherical particles. *Physica* **4**, 1058-1072 (1937).

80 Valmacco, V. *et al.* Dispersion forces acting between silica particles across water: influence of nanoscale roughness. *Nanoscale Horiz.* **1**, 325-330 (2016).

81 Ackler, H. D., French, R. H. & Chiang, Y.-M. Comparisons of Hamaker Constants for Ceramic Systems with Intervening Vacuum or Water: From Force Laws and Physical Properties. *J. Colloid Interface Sci.* **179**, 460-469 (1996).

Acknowledgements

European Research Council (ERC) under the European Union's Horizon 2020 research and innovation programme No 724180 (SW, RWG, MK).

Author Contributions Statement

S.W. performed the experiments. R.W.-G. performed and analysed simulations. S.W. and R.W.-G. analysed the data and participated in manuscript preparation. B.W. and B.L. contributed to experiments. M.K. designed and supervised the study. R.W.-G. and M.K. wrote the manuscript.

Competing Interests Statement

The authors declare no competing interests.

Data availability

The data that support the findings of this study are available from figshare https://doi.org/10.6084/m9.figshare.c.7183569 and from the corresponding authors upon request.

Code availability

The code used in this study are available from figshare https://doi.org/10.6084/m9.figshare.c.7183569 and from the corresponding authors upon request.

Figures

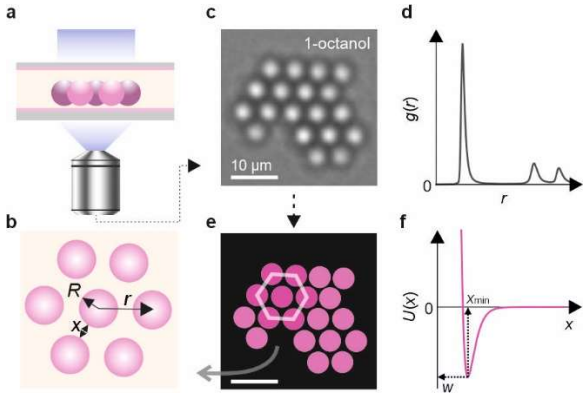


Figure 1. Experimental set-up for inferring interparticle interactions in 2-d colloidal suspensions. a,b Schematic representation of a particle cluster in a gravity-sedimented colloidal suspension, with particles represented as spheres of radius R, engaged in a cluster, levitating above a silica coverglass, at an interparticle separation r and intersurface separation x. Particles are imaged using bright field microscopy (see Experimental methods). **c,d** Particle coordinates are extracted from a microscope image using single particle tracking software[65] and used to generate radial distribution profiles, $g(r)$. **e** Digitised microscopy images where particles are represented as coloured discs of uniform diameter $2R$ on a black background. Like-charged colloidal particles can be observed to form stable, slowly reorganising hexagonally close packed (hcp) clusters in solution. Scale bar 10 µm. **f** Brownian dynamics simulations are used to infer a pair-interaction potential, $U(x)$, characterised by an attractive minimum of depth w, and location x_{min}, capable of reproducing the experimentally observed $g(r)$ (see BD Simulation methods). Typical inferred interaction strengths of $|w| \approx 5\,\mathrm{k_B}T$ are obtained for strongly clustering systems, as shown here for positively charged NH_2 particles suspended in 1-octanol.

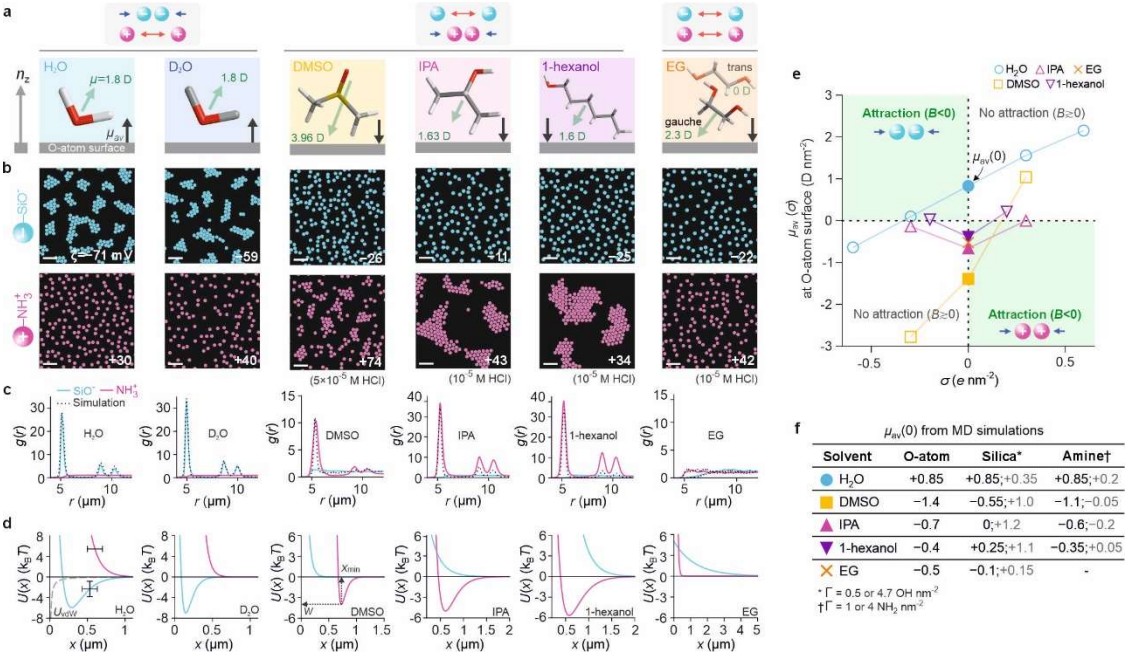


Figure 2. Solvent dependence of charge-asymmetric cluster formation. a Structures and average orientation of solvent molecules at an uncharged O-atom surface (dipole moments - green arrows; surface normal - n_z), as inferred from MD simulations. Normal component of the net interfacial molecular dipole moment, μ_{av}, points slightly away from the surface for H_2O and D_2O and towards the surface for the other cases. **b** Digitised experimental images of negatively charged silica SiO_2 particles (blue, $2R = 4.82$ or 5.17 mm) and positively charged aminated silica NH_2-SiO_2 particles (pink, $2R = 4.63$ mm) suspended in H_2O, D_2O, DMSO, 2-propanol (IPA), 1-hexanol, and ethylene glycol (EG) (Supplementary Fig. 11). Scale bar 20 μm. Stable clusters were observed in H_2O and D_2O for SiO_2 particles, and in DMSO, IPA and in primary and secondary alcohols for NH_2 particles (Fig. 3), but not in EG (Supplementary Fig. 17, Suppl. Note 3). Measured zeta potentials, ζ (in mV) provided in inset. **c** Experimental $g(r)$ for SiO_2 (solid blue lines) and NH_2 particles (solid pink lines), and corresponding simulated $g(r)$ profiles (dashed grey curves) (top row). Ordered clusters produce $g(r)$ profiles with a periodic peak-structure indicating interparticle attraction. **d** Pair-interaction potentials $U(x)$ of the form of Eq. (1), inferred from BD simulations, that best reflect the experimental $g(r)$ profiles for silica (blue) and NH_2 particles (pink), and the negligible vdW contribution, U_{vdW} (grey dashed line) (Supplementary Table 25). Error bars denote estimated uncertainties of ±100 nm on particle diameter and $\pm 1.5\, k_B T$ in w. **e** Excess interfacial dipole moment density $\mu_{av}(\sigma)$ from MD simulations carrying positive and negative surface charge density σ At zero surface charge, $\sigma = 0$, we obtain $\mu_{av}(0) = +0.85$ D nm^{-2} for water and $\mu_{av}(0) < 0$ for other cases (filled symbols). Parameter values in green quadrants of the μ_{av} vs. σ plot support interparticle-attraction and cluster formation between electrically like-charged particles (since $B < 0$ in Eqs. (1) and (2)). **f** $\mu_{av}(0)$ for solvents in contact with a neutral O-atom surface, silica surfaces with varying surface group density ($\Gamma = 0.5$ or 4.7 OH nm^{-2}), and model amine surfaces with varying surface group density ($\Gamma = 1$ or 4 NH_2 nm^{-2}).

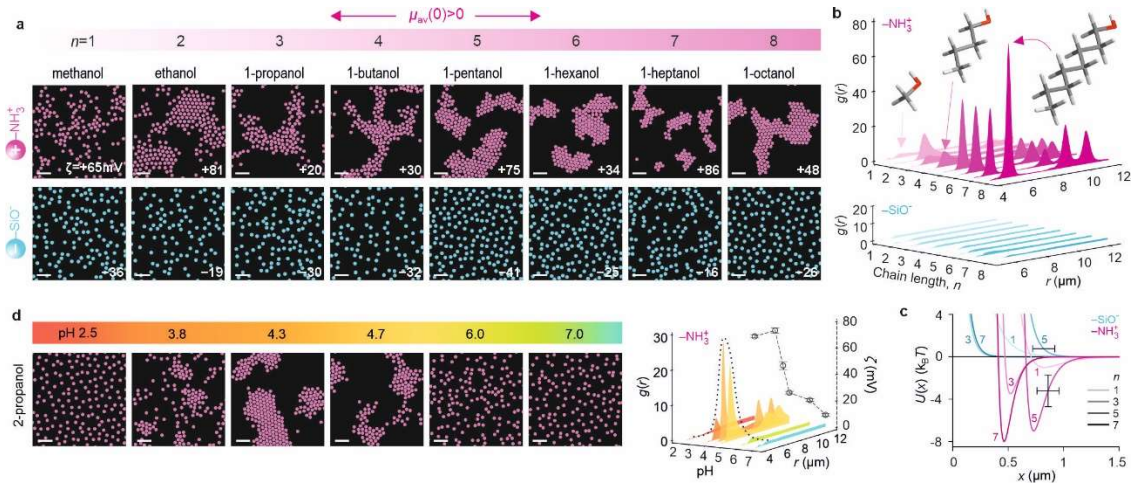


Figure 3. Cluster formation of positively charged particles in primary alcohols. a Representative image of positively charged aminated silica NH_2-SiO_2 particles (pink) and negatively charged SiO_2 particles (blue) in primary alcohols of increasing chain length from methanol ($n = 1$, left) to 1-octanol ($n = 8$, right) (see Supplementary Table 4 for experimental conditions). All amine particle experiments contained 10^{-5} M HCl. Measured zeta potentials (ζ) are noted. **b** Radial probability density distributions as a function of alcohol chain length for the experiments shown in **a**. **c** Inferred pair-interaction potentials, $U(x)$, from BD simulations that best reproduce the experimental $g(r)$s for select cases (see Supplementary Table 26 for parameters). Well depths $|w| \approx 1\,k_BT$ and $\approx 3\,k_BT$ were sufficient to capture the $g(r)$ profile of NH_2 particles in methanol and 1-propanol respectively. Larger values $|w| \approx 7\,k_BT$ were required to capture the strong cluster formation observed in the higher chain alcohols 1-pentanol and 1-heptanol. Purely repulsive pair potentials described interactions of negatively charged SiO_2 particles in alcohols (Supplementary Table 26). Error bars denote estimated uncertainties of ± 100 nm on particle diameter and $\pm 1.5\,k_BT$ in w. **d** Effect of pH on cluster formation, shown for NH_2 particles in 2-propanol (IPA). Negatively charged SiO_2 and COOH particles in IPA display no evidence of interparticle attraction as a function of pH (Supplementary Fig. 5). Scale bars 20 μm.

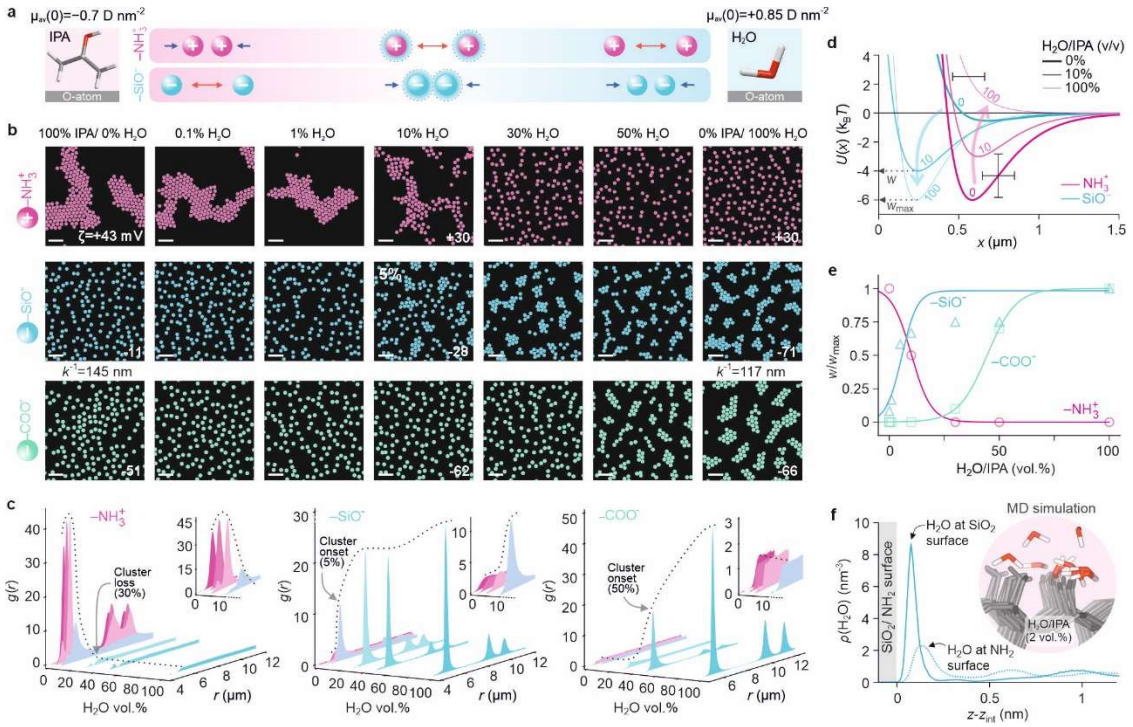


Figure 4. Tuning the strength of the interparticle attraction in water-alcohol mixtures. a Structure of colloidal particle suspensions for positively charged NH_2 (pink), and negatively charged SiO_2 (blue) and COOH particles (green), in water/IPA mixtures of increasing volume percentage of water (left to right). **b** Measured zeta potentials of the particles (ζ) are shown inset. NH_2 particles display attraction and cluster formation in pure IPA containing water at a concentration $\lesssim 10\%$ (v/v). SiO_2 and COOH particle interactions are purely repulsive in pure IPA but the onset of interparticle attraction and cluster formation occurs at around 5 and 50% (v/v) water respectively (Supplementary Table7 for experimental conditions). Scale bar 20 μm. **c** $g(r)$ profiles as a function of water volume percent for the three particle surface types. **d** Inferred pair-interaction potentials, $U(x)$, from BD simulations that match the experimental particle distributions (see Supplementary Table 27 for parameters). Error bars denote estimated uncertainties of ± 100 nm on particle diameter and $\pm 1.5\, k_B T$ in w. **e** Normalised pair-interaction potential well depths, w/w_{max}, as a function of water volume percent. **f** Profiles of interfacial water density, $\rho(H_2O)$ as a function of distance z from the interface, situated at z_{int}, calculated from MD simulations of a 2% (v/v) water/IPA mixture in contact with a silica (solid line) and model amine surface (dashed line) carrying surface group densities $\Gamma \approx 4.7$ and 4 nm^{-2} respectively (see MD simulation methods). Simulations indicate significant water adsorption at the hydrophilic silica surface, in contrast with a model surface composed of amine groups. Inset: molecular dynamics snapshot, with interfacial water molecules in a background medium of IPA (pink) adsorbed to silanol groups on the silica surface.

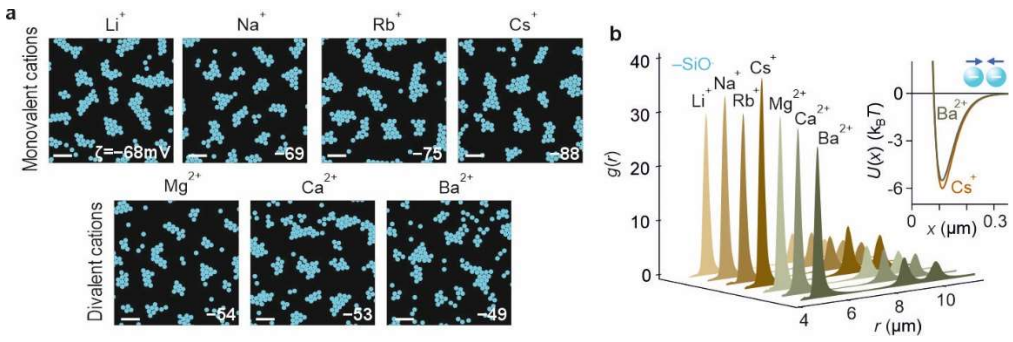


Figure 5. Cluster formation in aqueous electrolytes containing monovalent and divalent cations. a Digitized experimental image of negatively charged SiO_2 colloidal suspensions forming clusters in the presence of LiCl, NaCl, RbCl, CsCl, $MgCl_2$, $CaCl_2$, and $BaCl_2$ at an ionic strength of 0.1 mM. Scale bar represents 20 μm. **b** Measured $g(r)$ profiles in each case, with inferred pair interaction potentials $U(x)$ presented for Cs^+ and Ba^{2+} (inset). Note that at the rather small interparticle separation value $x \approx 0.1$ mm characteristic of these experiments, the estimated attractive contribution to the pair potential from the van der Waals force is $\approx 1\ k_B T$, which is larger than in the rest of the experiments in the study but significantly smaller than the measured minima of depth $w \approx 6\ k_B T$.

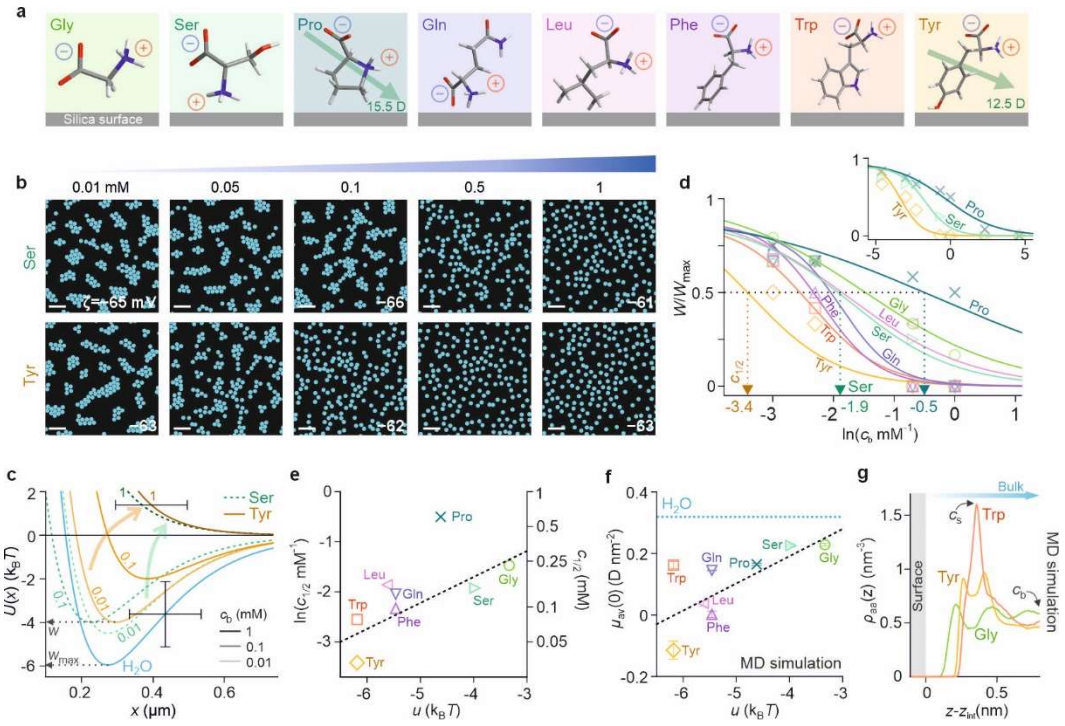


Figure 6. Amino acids can abolish cluster formation at very low concentration. **a** Molecular structure of amino acids investigated. Molecular orientations depict averages observed in MD simulations at a silica interface. Average interfacial dipole moment vectors for proline and tyrosine (green arrows) imply normal components that are oriented opposite to that of pure water at an interface (see Fig. 2a). **b** Digitised images of negatively charged SiO_2 particles suspended in various concentrations of net-neutral amino acids in water, shown here for serine and tyrosine (see Supplementary Fig. 24 for all amino acids studied). The interparticle attraction significantly weakens at $c_b = 0.5$ mM for serine and 0.1 mM for tyrosine, and vanishes at higher concentrations. Scale bar 20 μm. **c** Inferred pair-interaction potentials $U(x)$ for serine and tyrosine-containing solutions inferred from BD simulations (see Supplementary Table 28 for parameters). Error bars denote estimated uncertainties of ± 100 nm on particle diameter and $\pm 1.5\, k_B T$ in w. **d** Normalised well depths, w/w_{max}, as a function of c_b with sigmoidal fits to the data (coloured lines). At $c_b = c_{1/2}$, the clustering strength is half-maximal, i.e., $w/w_{max} = 0.5$. **e** Plot of measured $\ln c_{1/2}$ vs. PMF minima values, u, taken from MD simulations in ref.[44] (symbols) with a linear fit (black dashed line). **f** Excess interfacial dipole moment densities, $\mu_{av}(0)$, from MD simulations of $c_b = 1$ M aqueous solution of amino acid in contact with a neutral silica surface. Error bars depict uncertainty arising from simulation convergence (see MD simulation methods). $\mu_{av}(0)$ values for the amino acid-containing electrolyte are systematically lower than the pure water value, $\mu_{av}(0) \approx 0.3$ D nm^{-2}, (blue dashed horizontal line) with the magnitude decreasing with increasing surface affinity of the amino acid reflected in $|u|$. **g** Averaged amino acid density profiles in solution, ρ_{aa} (as a function of distance from the silica surface $(z - z_{int})$), for simulations described in **f**, present qualitative trends of the interfacial concentration, c_s, which is highest for tryptophan and lowest for glycine.

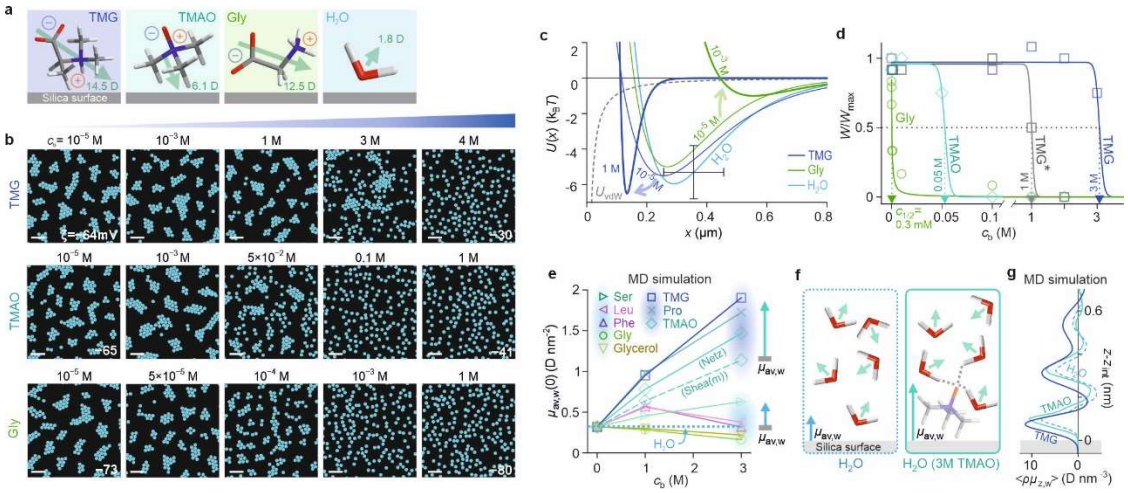


Figure 7. Highly disparate influence of zwitterions on interparticle attraction. **a** Schematic depiction of average TMG and TMAO molecular orientation at a silica surface compared to glycine and water, inferred from MD simulations. **b** Digitised experimental images of colloidal suspension structure for negatively charged SiO_2 particles in aqueous solutions of increasing concentrations, c_b, of TMG, TMAO or glycine. Scale bars 20 μm. **c** Inferred pair-interaction potentials $U(x)$ (see Supplementary Table 29 for parameters) for $c_b = 10^{-5}$ M and 1 M concentrations of zwitterion. Error bars denote estimated uncertainties of ±100 nm on particle diameter and $\pm 1.5\, k_B T$ in w. **d** Normalised pair-interaction potential well depths, w/w_{max}, as a function of zwitterion concentration in solution indicate $c_{1/2} = 3$ M (TMG in water), 1 M (TMG solution with pH and conductivity matched to TMAO solution – TMG*), 50 mM (TMAO in water), and 0.3 mM (glycine in water). **e** Contribution of water alone to the total excess dipole moment density at the interface, $\mu_{av,w}(0)$, in MD simulations of a silica surface with a group density of 4.7 OH nm^{-2} immersed in water containing varying zwitterion concentration (see MD simulation methods). Zwitterions can be grouped into two categories depending on their qualitative effect on the sign and magnitude of $\mu_{av,w}(0)$. TMG, TMAO and proline zwitterions enhance the value of $\mu_{av,w}(0)$ significantly above that of pure water at a silica surface (blue horizontal dashed line). Data corresponding to two TMAO models (Shea(m) and Netz) are presented (see MD simulation methods). **f** Schematic illustration of excess dipole moment density, $\mu_{av,w}$, at a silica surface in pure water, and a solution containing $c_b \approx 3$ M TMAO (see Suppl. Note 6 for detail). **g** Spatial profiles of the water dipole moment density at the interface for TMAO- and TMG-containing aqueous media (solid blue lines) are consistently more positive than the pure water case (blue dashed line), which yields $\mu_{av,w}(c_b = 3\,\mathrm{M}) > \mu_{av,w}(c_b = 0)$.

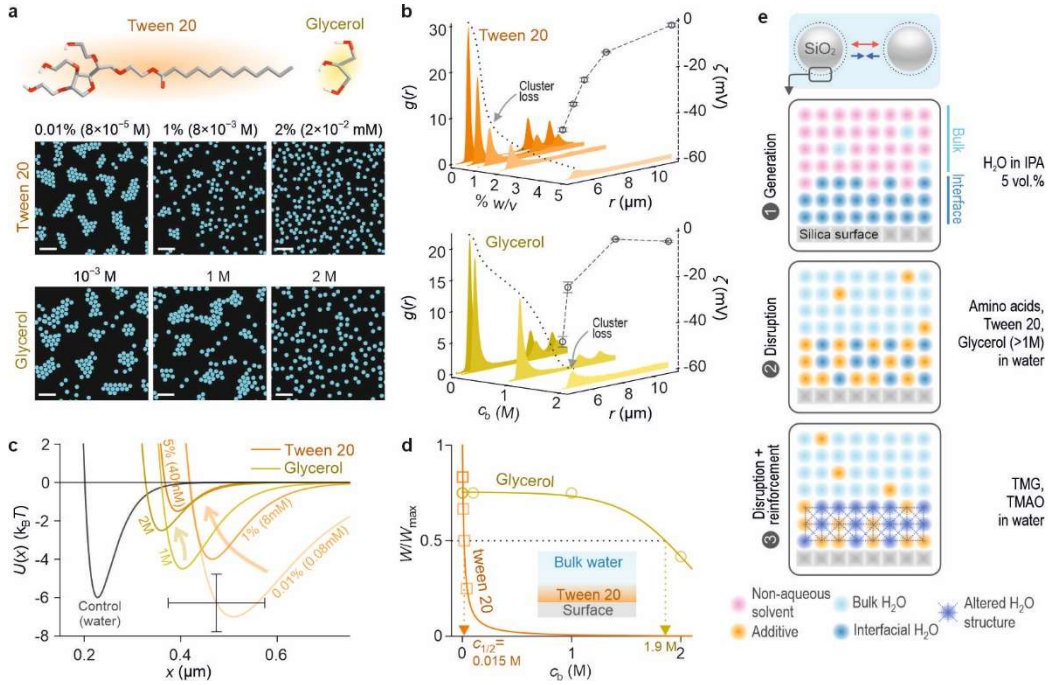


Figure 8. Surfactants suppress cluster formation. a Images of colloidal suspension structure for negatively charged SiO_2 particles suspended in aqueous solution containing increasing concentrations, c_b, of Tween 20 and glycerol. Scale bars 20 μm. **b** $g(r)$ profiles (left axis) and measured zeta potentials (ζ) (right axis) for Tween 20 and glycerol experiments **c** Inferred pair-interaction potentials $U(x)$ as a function of Tween 20 or glycerol concentration (see Supplementary Table 30 for parameters). Control experiment in water with pH and conductivity identical to 5% Tween (grey). Error bars denote estimated uncertainties of ±100 nm on particle diameter and ±1.5 k_BT in w. **d** Normalised pair-interaction potential well depths, w/w_{max}, as a function of additive concentration yield $c_{1/2} = 0.015$ M for Tween 20 and 1.9 M for glycerol. Schematic representation of possible mechanism by which Tween 20 disrupts cluster formation, depicting adsorption of surfactant to the silica surface (inset). **e** Schematic view of how microscopic interfacial structuring drives long-range interparticle forces. Electrosolvation-governed attraction can occur in solvent mixtures when, e.g., trace amounts of surface-associated water generate a thin aqueous interfacial layer (dark blue spheres – case 1). Strongly adsorbing additives (orange) such as amino acids and surfactants may disrupt interfacial water structure thus suppressing the interparticle attraction even at low concentrations c_b (case 2). Additives that potentially entail weaker disruptive effects on interfacial structure, such as glycerol, may have no significant impact on cluster formation up to high concentrations, $c_b \lesssim 1$ M. Surface-adsorbing alkylated zwitterions may reinforce interfacial water orientation (hatched region – case 3), offsetting disruptive effects due to adsorption, thereby sustaining cluster formation up to molar c_b values.

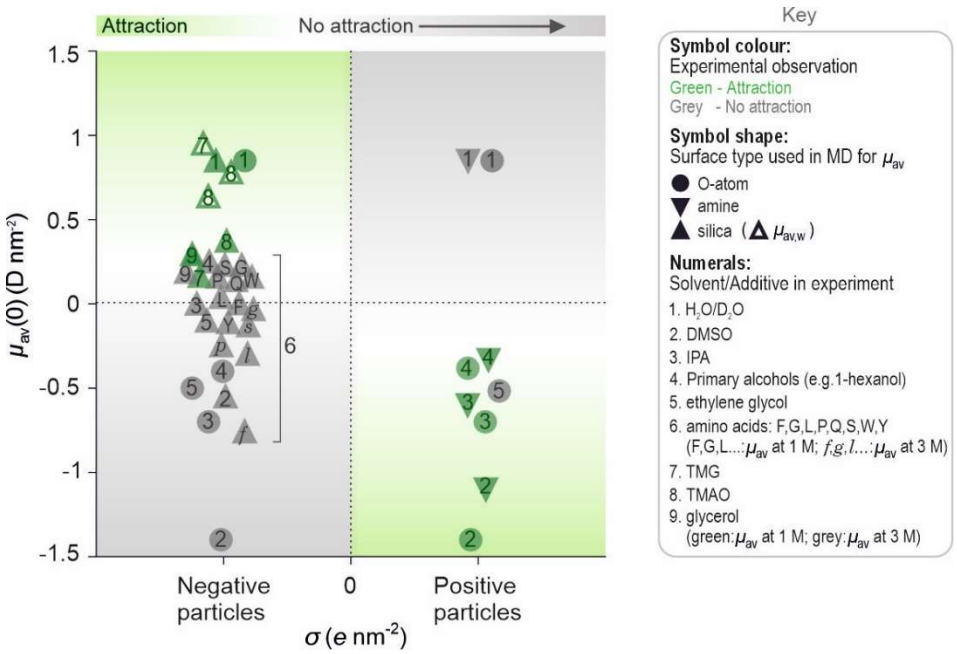


Figure 9. Graphical summary and comparison of the experimental observations with expectations based on the interfacial solvation model. Background colour on the plot presents the qualitative theoretical expectation based on the interfacial solvation model given by Eqs. (1) and (2). For negatively charged particles ($\sigma < 0$), attraction (green area) is expected when the average interfacial dipole moment density is substantial and positive, i.e., $\mu_{av} > 0$, whereas no attraction is expected when $\mu_{av} \lesssim 0$ (grey area). Conversely, for positively charged particles ($\sigma > 0$), attraction is expected when $\mu_{av} < 0$ and no attraction when $\mu_{av} \gtrsim 0$. Qualitative experimental outcomes are presented as coloured symbols on a binarized abscissa specifying the sign of charge of the particle – positive or negative, with the corresponding ordinate value denoting values of μ_{av} (filled symbols) or $\mu_{av,w}$ (open symbols) obtained from MD simulations. Symbol colour denotes the observed experimental outcome: attraction and cluster formation (green symbols) and absence of attraction and cluster formation (grey symbols). The graph presents results describing a total of 37 experimental situations for which μ_{av} values were determined (e.g., μ_{av} for Tween 20 and solvent mixtures at an interface are not available). All depicted dipole moment density values for silica reflect a group density of 1 OH nm^{-2}, except values for the amino acids, TMAG, TMAO and glycerol which entail a group density of 4.7 OH nm^{-2}.

Supplementary Information

Chemical control of colloidal self-assembly driven by the electrosolvation force

Sida Wang†[1], Rowan Walker-Gibbons†[1], Bethany Watkins[1], Binghui Lin[1], & Madhavi Krishnan*[1,2]

† these authors contributed equally
[1]Physical and Theoretical Chemistry Laboratory, Department of Chemistry, University of Oxford, South Parks Road, Oxford OX1 3QZ, United Kingdom
[2]The Kavli Institute for Nanoscience Discovery, Sherrington Road, Oxford OX1 3QU, United Kingdom.
*correspondence to madhavi.krishnan@chem.ox.ac.uk

Table of Contents

Suppl. Note 1. Further discussion of the interfacial solvation model of particle interactions 6
Suppl. Note 2. Further considerations on particle interactions in alcohols 10
Suppl. Note 3. Interactions in EG 12
Suppl. Note 4. Interactions in DMSO 13
Suppl. Note 5. Interactions in electrolytes containing zwitterionic amino acids 14
Suppl. Note 6. Simulation trends for electrolytes containing TMAO and TMG 16
Suppl. Note 7. Further considerations in BD simulations 17
Suppl. Note 8. Discussion of the surface properties of silica 18
Suppl. Note 9. Additional Experiments 20
Supplementary Figures 22
Supplementary Tables 38
References 49

List of Figures

Supplementary Figure 1. Probability distributions of particle diameter for each particle type studied in experiments. 22
Supplementary Figure 2. Particle charge characterization of SiO_2 and NH_2-SiO_2 in aqueous solution, selected solvents and mixtures. 22
Supplementary Figure 3. Simulation setups for studying interfacial solvation at model silica and amine surfaces 23
Supplementary Figure 4. Effect of added salt on cluster formation for NH_2, SiO_2 and COOH particles in 2-propanol 24
Supplementary Figure 5. Effect of pH on interparticle interactions for NH_2, SiO_2 and COOH particles in 2-propanol 25
Supplementary Figure 6. Effect of solvent pH on interparticle interactions for NH_2 and SiO_2 particles suspended in dimethyl sulfoxide 26
Supplementary Figure 7. Zeta potential distribution for SiO_2 particles in water at various pH. 26
Supplementary Figure 8. Improving agreement between simulated and measured $g(r)$ distributions through the incorporation of a weak external flow in BD simulations. 27
Supplementary Figure 9. Matching the measured $g(r)$ profile for negatively charged SiO_2 particles in EG with BD simulations. 28
Supplementary Figure 10. Total excess dipole moment density, $\mu_{av}(0)$, in MD simulations of water/zwitterion solutions of varying zwitterion concentration 29
Supplementary Figure 11. Raw and digitized images of experiments shown in Fig. 2. 30
Supplementary Figure 12. Raw and digitized images of experiments shown in Fig. 3. 30
Supplementary Figure 13. Raw and digitized images of NH_2, SiO_2 and COOH particle interactions in IPA with a variation in added salt. 31
Supplementary Figure 14. Raw and digitized images of NH_2, SiO_2 and COOH particle interactions in IPA with a variation in solution pH. 31
Supplementary Figure 15. Raw and digitized images of NH_2, SiO_2 and COOH particle interactions in water-IPA mixtures 32
Supplementary Figure 16. Raw and digitized images of NH_2 and SiO_2 particle interactions in DMSO with a variation in solution pH. 32
Supplementary Figure 17. Raw and digitized images of NH_2 and SiO_2 particle interactions in EG with variation in solution pH. 33
Supplementary Figure 18. Raw and digitized images of NH_2, SiO_2 and COOH particle interactions in D_2O. 33
Supplementary Figure 19. Raw and digitized images of SiO_2 particle interactions in aqueous solutions containing varying concentrations of Tween 20. 33
Supplementary Figure 20. Raw and digitized images of SiO_2 particle interactions in glycerol solutions with variation in concentration. 34
Supplementary Figure 21. Raw and digitized images of SiO_2, COOH and NH_2 particle interactions in water with a variation in concentration of added TMG. 34

Supplementary Figure 22. Raw and digitized images of SiO_2 particle interactions in TMG-containing water with adjusted pH and conductivity.....35
Supplementary Figure 23. Raw and digitized images of SiO_2 particle interactions in water containing various concentrations of added TMAO.....35
Supplementary Figure 24. Raw and digitized images of SiO_2 particle interactions in water containing various concentrations of added amino acids.....37
Supplementary Figure 25. Raw and digitized images of SiO_2 and COOH particle interactions in water containing various concentrations of added tyrosine.....37

List of Tables

Table S1. Detail on solvents used in the study. 38
Table S2. Detail on additives used in the study. 38
Table S3. List of experimental conditions for experiments shown in Fig. 2. 39
Table S4. List of experimental conditions for experiments shown in Fig. 3. 39
Table S5. Salt concentration variation experiments for NH_2, SiO_2 and COOH particles in IPA. 40
Table S6. pH variation experiments in IPA for NH_2, SiO_2 and COOH particles. 40
Table S7. Water-IPA mixture experiments for NH_2, SiO_2 and COOH particles. 41
Table S8. pH variation experiments in DMSO for NH_2 and SiO_2 particles. 41
Table S9. pH variation experiments in EG for NH_2 and SiO_2 particles. 42
Table S10. List of experimental conditions for NH_2, SiO_2 and COOH particle interactions in D_2O. 42
Table S11. SiO_2 and COOH particle interaction experiments with varying TMG concentration in water. 43
Table S12. pH and conductivity adjusted experiments in TMG-containing water. 43
Table S13. SiO_2 particle interactions in water containing TMAO. 44
Table S14. SiO_2 particle interactions in water containing L-serine. 44
Table S15. SiO_2 particle interactions in water containing glycine. 44
Table S16. SiO_2 and COOH particle interactions in water containing L-tyrosine. 44
Table S17. SiO_2 particle interactions in water containing L-leucine. 45
Table S18. SiO_2 particle interactions in water containing L-phenylalanine. 45
Table S19. SiO_2 particle interactions in water containing L-tryptophan. 45
Table S20. SiO_2 particle interactions in water containing L-glutamine. 45
Table S21. SiO_2 particle interactions in water containing L-proline. 45
Table S22. SiO_2 and COOH particle interactions in water containing L-tyrosine. 46
Table S23. SiO_2 particle interactions in water containing Tween 20. 46
Table S24. SiO_2 particle interactions in water containing glycerol. 46
Table S25. $U(x)$ values used in BD simulations to model experiments in Fig. 2. 46
Table S26. $U(x)$ values modelling experiments in Fig. 3. 47
Table S27. $U(x)$ values modelling the experiments shown in Fig. 4. 47
Table S28. $U(x)$ values modelling experiments shown in Fig. 6. 47
Table S29. $U(x)$ values modelling experiments shown in Fig. 7. 48
Table S30. $U(x)$ values modelling experiments shown in Fig. 8 48

Suppl. Note 1. Further discussion of the interfacial solvation model of particle interactions

Previous studies have described in detail the theoretical basis of a working model of the interfacial solvation-driven interparticle interaction – termed the 'interfacial solvation model'[1-3]. Our interfacial-solvation theoretical framework examines the change in system free energy due to interfacial solvent molecules that occurs in response to a decrease in interparticle separation as two particles approach. The mechanism further relies on the fact that the charge carried by particles depends on the pH in solution and is also a function of interparticle separation via a process known as charge regulation[4]. The coupling of charge regulation with the orientational behaviour of the interfacial solvent gives rise to a free energy contribution, ΔF_{int}, which may be added to the traditional electrostatic free energy of interaction, ΔF_{el}, for two charge-regulating particles. A total free energy composed of a sum of these two contributions was found to successfully describe numerous features of the experiment[1,2]. Thus, in essence, the interfacial solvation model presents an attempt to capture the thermodynamic consequences of the symmetry-broken molecular orientational behaviour at an interface that is manifestly absent from continuum theories of electrostatic interactions in the fluid phase.

Within the interfacial solvation model, the effective interparticle interaction potential may be written as

$$U_{\text{tot}} = \Delta F_{\text{el}} + \Delta F_{\text{int}} \approx A\exp(-\kappa_1 x) + B\exp(-\kappa_2 x) \qquad (1)$$

where $A > 0$ always, and $\kappa \approx \kappa_1 > \kappa_2$. When $B < 0$ we may expect a long-range attractive force between particles which vanishes for $B = 0$ and turns repulsive for $B > 0$. According to Supplementary Eq. (1), a stable minimum in the pair potential occurs when the canonically repulsive first term dominates at short range ($x < \kappa^{-1}$), since typically, $\frac{A}{|B|} > 1$. But at long range, $x \gg \kappa^{-1}$, since $\kappa_1 > \kappa_2$, the attractive second term competes with the first term and can dominate the overall interaction.

In the original formulation of our theoretical model, we determined the required interfacial free energy in Supplementary Eq. (1) by calculating a charging free energy

integral obtained from MD simulations of pure solvents at an interface[1,2]. The simulations relied on inferring the quantity $\varphi_{\mathrm{int}}(\sigma)$, an 'excess' interfacial electrical potential that arises from the solvent alone, for surfaces of various electrical charge density, σ. We then evaluated the interfacial free energy term by integrating the interfacial free energy density over the surface area of two charge-regulating particles whose interaction was analysed using a mean field model of the electrostatics. We thus obtained the following expression for the coefficient of the interfacial free energy term in Supplementary Eq. (1)[1,2]:

$$B \propto ez\varphi_{\mathrm{int}}\Gamma R^2 \frac{\mathrm{d}\alpha}{\mathrm{d}\psi_{\mathrm{s},\infty}}\psi_{\mathrm{s},\infty} \qquad (2)$$

In the above equation, e is the elementary charge, $\psi_{\mathrm{s},\infty}$ is the electrical potential at the surface of an isolated particle due to ions in solution, α represents the ionization probability of the particles' chargeable groups whose number density is Γ, and the groups may carry a charge of $z\,e$ in their ionized states where $z = \pm 1$. Importantly, φ_{int} is an excess electrical potential that develops at a surface immersed in a pure solvent, with reference to the electrical potential in the pure bulk solvent[1,2,5].

At the microscopic level, this solvation-related electrical potential arises from the normal component of the net excess solvent molecular dipole moment at an interface with respect to that expected from a continuum picture of a dielectric medium. The symmetry-broken orientational behaviour of solvent molecules at an interface, which gives rise to a net excess dipole moment relative to the bulk, is caused by the presence of an interface that divides the system into two distinct half-spaces and thus introduces an angular anisotropy in hydrogen bonding or other intermolecular interactions of the interfacial molecules. In fact, it is well known from spectroscopic studies and molecular simulations that solvent molecules such as water have a preferred orientation at an interface, even when the surface has zero surface charge[1,5,6]. For water e.g., this preferred orientation arises from a tendency of interfacial water molecules to directionally hydrogen bond towards the bulk liquid rather than the solid interface. However, there are ambiguities involved in inferring a quantity such as φ_{int} from distance dependent profiles of solvent molecular orientation observed in MD simulations[5-9]. In this work we cast the

interfacial free energy term in Supplementary Eq. (1) in terms of a net normal excess interfacial dipole moment density which is a quantity that is directly observed in and can be unambiguously inferred from molecular simulations and also from independent experimental methods. In the discussion of this study, we therefore replace the excess interfacial electrical potential, φ_{int}, in Supplementary Eq. (1) with an excess net normal dipole moment surface-density, μ_{av}, where the two quantities are directly related to each other as shown in MD simulation methods (Eq.3).

At a given surface charge density, σ, subtraction of the net dipole moment density in the bulk solvent from the corresponding value in the interfacial region yields $\mu_{\mathrm{av}}(\sigma)$ which thus represents the solvent-density-averaged excess normal component of the molecular dipole moment per unit surface area in the interfacial region. Since $\mu_{\mathrm{av}}(\sigma)$ is directly proportional to $-\varphi_{\mathrm{int}}(\sigma)$, the overall sign and approximate magnitude of the prefactor B can be given in simpler form by:

$$B \propto z\mu_{\mathrm{av}}(\sigma) \tag{3}$$

Thus, in the present study we seek to qualitatively relate the presence or absence of an experimentally observed interparticle attraction in various solvents to the sign of $B = z\mu_{\mathrm{av}}(\sigma)$ expected based on MD simulations. Similar to discussions on φ_{int} in previous work, we will find that $\mu_{\mathrm{av}}(0)$, i.e., the excess dipole moment density obtained in simulations for small values of charge density ($\sigma \to 0$), is sufficient to qualitatively describe the observations. Importantly, we point out that although within the interfacial solvation model $B < 0$ is a necessary condition for interparticle attraction it is not sufficient to support the appearance of a stable minimum ($w < -2\,\mathrm{k_B}T$) in the pair potential which underpins the formation of stable crystalline clusters in experiment. According to Supplementary Eq. (1), very large values of $\frac{A}{|B|} \gg 1$ or small values of $A \to 0$ and $B \to 0$ that arise in the strongly and very weakly charged limits respectively, would not support the formation of stable clusters in solution[1,2]. Since pH exerts significant control of the magnitude of charge carried by protonatable ionisable groups, we may expect cluster formation in experiments to display a strong dependence on pH as shown previously and discussed in detail later[3].

Previous studies provided calculations of pair-interaction potentials under various experimental conditions including salt concentration, pH and the type of solvent, and compared the theoretical predictions with experimentally measured pair-potentials[1-3]. In this study, we limit the scope of data interpretation to providing qualitative assessments of observed experimental trends in relation to the proposed theoretical model of the underlying interaction. We have systematically compared the appearance of clusters, and in some cases the strength of the interparticle attractions underpinning cluster formation, with qualitative indications from the interfacial solvation model. We do not attempt to provide calculations of pair potentials using the interfacial solvation model for the range of experimental conditions described in this work for several reasons: (1) in organic solvents, dissociation constants of the surface ionizable groups (pK values) are not well known, (2) in water-alcohol mixtures, in addition to uncertain pK values[10,11], dielectric constants of the intervening medium are not known, and screening lengths are hard to estimate, (3) in experiments involving osmolytes, parameters underpinning the osmolyte-surface interaction are not well known. Despite the myriad uncertainties on experimental parameters in the systems considered, clear trends that align with the qualitative indications of the interfacial solvation model as given by Supplementary Eq. (3) do nonetheless emerge.

Suppl. Note 2. Further considerations on particle interactions in alcohols

When NH_2 particles were suspended in various short and long-chain alcohols we observed in general the formation of strong, stable clusters which are characteristic of systematically longer screening lengths expected for apolar media that entail a reduction in background ionic strength compared to aqueous media, and in agreement with indications of the interfacial solvation model[2] (Fig. 2,3). Experiments show that at high pH (implying low surface charge densities for basic amine groups), cluster formation is abolished which implies that the deep minimum in the interparticle potential vanishes (Fig. 3). This may be attributed to a reduced charge density and surface potential ψ_s of the interacting particles (reflected in the low measured zeta potentials), a reduction in magnitude of charge regulation as reflected in $|\frac{d\alpha}{d\psi}|$, or both, bearing in mind that each of these effects can independently contribute to $B \to 0$ as given by Supplementary Eq. (2). In general, we found the pH range that promoted cluster formation lay in the region of around 5 to 7 across all the alcohols tested (Supplementary Table 3,4). The pK of amine groups in a high dielectric medium such as water is expected to lie around 9 but may shift to lower values of 7-9 in ethanol, and possibly even lower in media of lower dielectric constant such as longer chain alcohols[11]. As described in previous work, pH values in the vicinity of the pK are expected to result in a substantial contribution from the interfacial free energy term, fostering interparticle attraction and the formation of stable clusters for positive particles in solution[1,2]. At the other extreme, corresponding to low pH, we have an increase in ionic strength due to the added acid (Supplementary Table 6) which may on its own result in dissolution of clusters. Regardless, the particle charge density is higher at lower pH, due to basic ionisable groups, as reflected in higher measured zeta potentials (Supplementary Table 6). As a result, not only does ΔF_{el} increase and compete more strongly with the interfacial term at all separations, but in fact $\mu_{av}(\sigma)$ itself, which is molecule-orientation dependent, may simultaneously decrease in magnitude and may even change sign as the interfacial molecules reorient to point

their O atoms preferentially towards an increasingly positively charged surface. This could result in $\mu_{\mathrm{av}}(0) \geq 0$ (Fig. 2e) for large and positive σ, which would further reinforce monotonic interparticle electrostatic repulsion, leading to absence of cluster formation at low pH.

On the other hand, negatively charged SiO_2 particles displayed robust interparticle repulsion in alcohols over a range of acidic and basic pH values and following from Supplementary Eq. (3) would indicate $\mu_{\mathrm{av}}(0) \leq 0$, similar to that required to explain the cluster formation for positively charged particles. Molecular simulations of the alcohol-solid interface however show that over a range of silanol group densities $\Gamma = (0.5 < \Gamma < 4.7$ nm$^{-2})$ we may expect $0 < \mu_{\mathrm{av}}(0) < +1.2$ D nm^{-2} (Fig. 2f). MD simulations of both IPA and1-hexanol at silica surfaces carrying large silanol group densities thus suggest $\mu_{\mathrm{av}}(0) > 0$, whose sign does not agree with that of the results obtained for simulations at an O-atom wall, and in fact points to the possibility of cluster formation for silica particles in alcohols. Our experimental observations however demonstrate the absence of attraction for silica particles in alcohols, indicating either a low magnitude or a negative sign of μ_{av}. The simulation results however do suggest that this condition would be met for net solvent exposed -OH group densities in the range $\Gamma \lesssim 1$ nm^{-2} which may in fact be a reasonable value as discussed in Suppl. Note 5[12-16,17,18].

Suppl. Note 3. Interactions in EG

The balance between gauche and trans conformers in aqueous solutions of EG has been shown to be affected by the dielectric constant of the surrounding medium[19]. Furthermore, ab-initio MD simulations of EG at the air/liquid interface show that EG molecules orient with their hydrophobic methylene groups pointing into the vapour phase[19]. Thus the air/liquid interface is depleted of trans conformers and enriched in gauche conformers with their C-O bonds oriented with the O atom towards the bulk. If the orientational behaviour of molecular EG at the solid/liquid interface were similar to that at the air/liquid interface, we would expect $\mu_{\mathrm{av}}(0) < 0$, similar to the MD simulation result obtained for an O-atom wall. The interfacial solvation model would then suggest attraction between positively charged particles in liquid EG, similar to the results for alcohols (Fig. 2f). Obtaining the correct molecular dipole moment distribution from simulations of EG at the solid/liquid interface would rely crucially on correctly capturing the interfacial conformational and orientational distribution, which in turn is likely to depend strongly on the nature of bonding interactions at the interface. In fact the dramatic difference in sign and magnitude of $\mu_{\mathrm{av}}(0)$ for EG at either O-atom ($\mu_{\mathrm{av}}(0) = -0.5$ D nm^{-2}) or silica surfaces ($\mu_{\mathrm{av}}(0) = -0.1$ to $+0.15$ D nm^{-2}) likely reflects the crucial importance of asymmetric bonding interactions in determining interfacial structural character (Fig. 2f). H-bonding interactions that happen to result in an overall low average value of excess normal dipole moment density, i.e., $\mu_{\mathrm{av}}(\sigma) \to 0$ would entail $B \to 0$ in Supplementary Eq. (1), and therefore the absence of cluster formation for both signs of particle charge.

Suppl. Note 4. Interactions in DMSO

Although there is no significant hydrogen bonding in DMSO, there are strong intermolecular dipole-dipole interactions which can lead to anisotropic molecular orientation at an interface[20]. In general we expect $\mu_{\mathrm{av}}(0) < 0$ for DMSO, but for silanol surfaces with values of $\Gamma > 2$ nm^{-2} MD simulations suggest $\mu_{\mathrm{av}}(0) > 0$, which implies $B < 0$ for negatively charged particles, thereby raising the possibility of an attraction for silica particles in DMSO at high silanol or carboxyl group densities[5]. For $\Gamma < 2$ nm^{-2} however we expect $\mu_{\mathrm{av}}(0) \lesssim 0$ and therefore interparticle repulsion for silica particles. Assuming $\mu_{\mathrm{av}} <0$ to hold for amine surfaces as well, we expect attraction for positively charged particles in DMSO. Note that whilst MD simulations suggest $\mu_{\mathrm{av}}(0) < 0$ for DMSO at aminated surfaces, they also indicate that μ_{av} rapidly decreases in magnitude with increasing positive surface charge density. In fact, surface charge densities $\sigma > 0.15\, e$ nm^{-2} lead to $\mu_{\mathrm{av}} \gtrsim 0$ which would suggest absence of attraction between positively charged particles. These trends are in fact successful in capturing two key features of the experimental observations: (1) relatively weak clustering, since particles typically carry a non-zero net charge density (i.e., $|w|$ is small compared to clustering interactions in other solvents), and (2) that cluster formation occurs over a relatively narrow range of pH compared to alcohols (Supplementary Figure 6).

Suppl. Note 5. Interactions in electrolytes containing zwitterionic amino acids

Amino acids such as phenylalanine, tyrosine, tryptophan and leucine, all carry hydrophobic side chains that are thought to promote adsorption to a silica interface as reported in experiments and MD simulations[22-25] (Fig. 6g). The surface propensity of the hydrophobic amino acids in particular has also been confirmed experimentally using XPS[26]. At the water-air interface, phenylalanine and leucine orient with the hydrophobic moiety towards air and the hydrophilic amino acid functionality exposed to water which favours hydrogen bonding[27]. At the silica-water interface, we may therefore expect a similar driving force for adsorption of these amino acids arising from ordering of the hydrophobic chains at the particle surface away from the bulk water[22,24]. Hydrogen bonding interactions between zwitterionic amino acids and silica surfaces are also known to promote adsorption[28]. Population of the solid-liquid interface by oriented dipolar molecules would immediately suggest an alteration of the net excess interfacial dipole moment. An altered normal component of the excess dipole moment density would be expected to influence the long-range attraction within the interfacial solvation view, potentially furnishing a qualitative explanation of the experimental observations.

In fact, our simulations suggest that not only does $\mu_{\mathrm{av}}(0)$ decrease from its pure-water value and tend to zero with decreasing polarity of the amino acid side chain, but it may even change sign as the polarity of the amino acid side-chain decreases from glycine to tyrosine (Fig. 6f). We note however that the finite size of the simulation box and the need for adequate simulation statistics implies concentrations in our simulations that are 1-2 orders of magnitude higher than the surface concentrations expected based on simulated PMF minima and the experimentally inferred $c_{1/2}$ values (e.g., for tyrosine $c_{\mathrm{s}} = 40$ mM)[23].

Furthermore the study by Bag *et al.* employed a charged silica interface in order to extract the values of the minima in the potentials of mean force, whereas we use a neutral silica surface to infer $\mu_{\mathrm{av}}(0)$ values[23]. Therefore we make use of the PMF values

from the study of ref.[23] in Fig. 6 since these results refer to interactions with more realistic model silica surfaces, and we do not attempt to extract PMF values from our simulations that only focus on uncharged hydroxylated silica surfaces. We therefore invoke $\mu_{\mathrm{av}}(0)$ values from our simulations with the sole purpose of outlining qualitative arguments concerning a possible origin of the amino-acid species dependent impact on the experimental observations.

Along these lines, it is not clear, for instance, if under our experimental conditions, $\mu_{\mathrm{av}}(0)$ may realistically be expected to turn significantly negative for tyrosine adsorption as suggested by MD simulations (Fig. 6f). Importantly, although the simulated $\mu_{\mathrm{av}} < 0$ value obtained for a tyrosine-containing electrolyte at a silica surface might superficially suggest the possibility of an attractive electrosolvation force for positively charged particles, we must also recognize that amino acid adsorption to surfaces is likely to be highly dependent on the chemistry of the surface. Therefore, it does not follow that the adsorption trends expected for silica surfaces and the concomitant impact on μ_{av} could be expected to hold for amine-silica particles. Indeed, clustering of NH_2 particles with amino acids in solution was not observed in experiment (data not shown). Finally, for all simulations involving osmolytes we use a value of $\Gamma =$ 4.7 SiOH groups nm^{-2} in line with ref.[23]. Interestingly our simulations of aqueous media containing glycine and tyrosine in contact with a model silica surface carrying an SiOH density of $\Gamma = 1$ nm^{-2} displayed very similar amino acid surface densities ρ_{aa} for both cases when compared to a silica surface with $\Gamma =$ 4.7 SiOH groups per nm^2 (Fig. 6g).

In summary, analysis of $\mu_{\mathrm{av}}(0)$ in our MD simulations demonstrates that adsorption of osmolytes at the solid-liquid interface can dramatically alter the structure of the interfacial electrolyte. This disruption to the interfacial electrolyte – smallest for glycine and strongest for tyrosine – correlates well with a significant modulation of the long-ranged attraction between particles in solution.

Suppl. Note 6. Simulation trends for electrolytes containing TMAO and TMG

As stated in the main text, molecular simulations displayed an increase in the interfacial dipole moment density due to water alone, $\mu_{\mathrm{av,w}}$, with increasing concentration of TMG/TMAO in solution. Therefore, solutions containing TMG and TMAO zwitterions appear to have a stronger ordering effect on interfacial water molecules compared to the other zwitterions considered. This feature is supported by other computational and experimental studies and may provide insight into the persistence of cluster formation at high TMG and TMAO concentrations observed in our experiments[29,30]. Interestingly, we also found a similar effect on $\mu_{\mathrm{av,w}}$ for proline at the silica interface, wherein clustering persists at higher concentrations of proline than that suggested solely by trends in affinity for the silica surface of the amino acids examined. Cluster formation in solutions containing the other amino acids followed a bulk concentration dependence that was captured well by the trend in their interfacial binding affinities (Fig. 6,7).

An orientational and hydrogen bond analysis for TMG and TMAO at the silica interface in MD simulations presents a physical picture for the strong ordering effect these zwitterions have on interfacial water molecules (MD Simulation methods). Rather than preferentially hydrogen bonding with the hydrophilic silica surface, TMAO and TMG molecules both orient so that their methyl groups point towards the surface. Their O atoms hydrogen bond with interfacial water molecules with which they form on average ≈ 3 hydrogen bonds per zwitterion at $c_{\mathrm{b}} \approx 3$ M (Fig. 7f). The presence of TMG and TMAO at an interface also causes interfacial water molecules to point their O atoms more on average towards the interface than in the absence of these zwitterions, unlike for most of the other amino acids. As a result the dipole moments of interfacial water molecules in solutions containing TMAO and TMG zwitterions at a silica interface were consistently more aligned with the surface normal over an interfacial region of around 1 nm, resulting in a significantly more positive value of $\mu_{\mathrm{av,w}}(0)$, when compared with pure water (Fig. 7e).

Suppl. Note 7. Further considerations in BD simulations

Incorporating the effect of weak external flows into BD simulations

In experiments it can be challenging to rule out the presence of weak external flows that arise from non-planarity of the cell or evaporation during the observation timeframe. This can result in the formation of large clusters whose size is not captured in our BD simulations that generally do not incorporate these additional effects. One example concerns experiments in 1-hexanol (Fig. 2) where incorporation of particle displacement due to background flow at BD simulation level greatly improves the agreement between the size of clusters in simulations and therefore between measured and simulated $g(r)$s (Supplementary Figure 8)

Matching simulated and measured for SiO_2 particles in EG

In Fig. 2, although particles of neither sign of charge displayed a long-ranged attraction in EG, we noted evidence for an apparently much longer ranged repulsion for negative particles than for positive particles. BD simulations suggest that such a signature in the measured $g(r)$ could arise from strongly heterogeneous interparticle interactions, or alternatively that the pair-interaction in fact reflects a much longer-ranged screened Coulombic decay, captured in this case by a screening length that is a factor ≈20 larger than the nominal Debye length, $\kappa^{-1} \approx 50$ nm (Supplementary Figure 9).

Suppl. Note 8. Discussion of the surface properties of silica

Well hydrated amorphous silica is expected to have a maximum density of $\Gamma = 4.7$ silanol groups per nm^2 - a value reported in experiments and used in simulations[18]. However, several experimental reports of the number density of SiOH are much lower ($\Gamma \leq 1$ group nm^{-2}), with the reported number of deprotonatable sites for amorphous silica even at extremely alkaline pH values of 12 entailing only about 20% of the total nominal group density of $\Gamma =$ 4-5 nm^{-2} [14-17,21]. This suggests an effective accessible SiOH density of $\Gamma < 1$ nm^{-2} groups in a range of spectroscopic experiments that probe the state of the silica interface in contact with the electrolyte. Furthermore, surface silanol groups are present in a variety of forms, supporting different degrees of H-bonding with the solvent, depending on their immediate neighbours e.g., vicinal silanols and geminal groups that can H-bond with each other. Silanol centres carrying a single OH group are classified as Q3, whereas the assignment Q4 describes siloxane bridges where the O atom is engaged only in siloxane bridges and the Si centre lacks an OH group. Importantly mesoporous organosilica particles, prepared by chemical synthesis and similar to those used in this work, have silanol group densities that are strongly dependent on the temperature of any post synthesis treatment with reported values lying between $\Gamma = 0.9$ and 3 nm^{-2} (ref. [13]). In fact ref. [13] shows that the number density of SiOH groups for mesoporous silica can be much less than the total number density of all silanols which include a large fraction of Q4 sites that do not bear an OH group. SiOH groups therefore constitute about 25 to 50% of the total number of all sites (which includes Q2, Q3 and Q4) over a number of different silica preparations.

In our simulations, for simplicity we consider a model silica surface carrying a mix of Q3 and Q4 groups, where a density of $\Gamma = 4.7$ OH nm^{-2} implies 100% Q3 SiOH groups. Since Q3 groups are not expected to be present at these densities on mesoporous silica surfaces, it is likely that this model-surface configuration overestimates the H-bonding ability of our silica microsphere surface, and therefore the impact of the surface on interfacial electrolyte structure. The resulting $\mu_{\mathrm{av}}(0)$ values may therefore be regarded as providing an "upper limit" on the impact of surface H-bonding on the interfacial

solvent. Thus, taking into consideration the presence of the various other surface silanol species with different H-bonding character, as well as accounting for the solvent inaccessibility of interior groups that contribute to the total nominal silanol density value, may, together or independently, point to a smaller density of Q3 silanol groups required in our simulation set-up in order to faithfully capture the true net impact of surface chemistry on interfacial solvent structuring relevant to the experiments. Hence we provide $\mu_{\mathrm{av}}(0)$ values for two limiting cases of SiOH group densities in Fig. 2f, namely $\Gamma = 0.5$ and 4.7 OH nm^{-2}, with the trends in our study rather aligning with the indications provided by the lower of the two values.

Suppl. Note 9. Additional Experiments

Cluster formation of COOH particles in osmolyte/water solutions

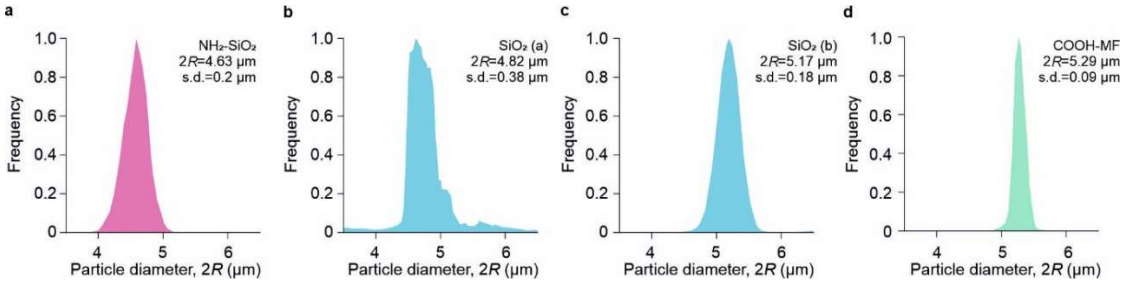
We briefly discuss the role played by zwitterions in cluster formation of COOH particles. TMG was found to influence the interaction of COOH particles in a similar fashion to that observed for SiO_2, with attractive particle clusters persisting up to high concentrations of about 0.5 M, albeit an order of magnitude lower than the $c_{1/2}$ value noted for silica particles (Supplementary Figure 21). Furthermore, we found that whilst COOH particles displayed similar trends to silica particles for some amino acids, we also observed significantly different cluster forming behaviour than for silica, e.g., in response to a small perturbation in pH (Supplementary Figure 25). Within our view of the electrosolvation force outlined above, disparities in cluster formation behaviour in response to osmolytes and co-solvents in solution are to be expected for chemically different particles. This would follow from the fact that adsorption energies of small molecules and their interactions at the interface are likely to be profoundly dependent on intermolecular interactions as well as molecule-surface interactions that are in turn specifically dependent on the particle surface chemistry and any response thereof to solution conditions. Whilst contributing to the richness and complexity of the underlying phenomenology, the dependence of cluster formation on particle properties, such as surface chemistry, in negatively charged particles (e.g., COOH or SiO_2) directly implicates the interface in dictating the magnitude of the attractive electrosolvation force. Note that in these experiments, the remaining system properties, i.e., sign of the particle charge, pH, salt concentration, and solvent composition or osmolyte type and concentration, remain identical, and only the particle chemistry varies.

Sign inversion of zeta potential for negatively charged particles in IPA under acidic conditions

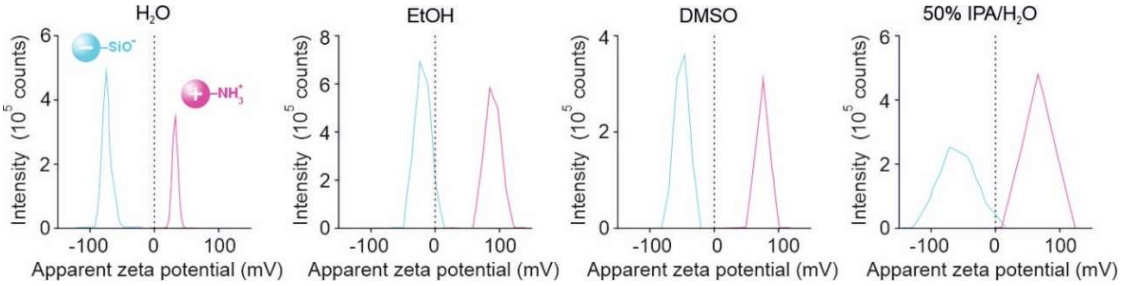
As shown in Supplementary Table 6 and Supplementary Figure 5, for experiments on particle interactions suspended in IPA at acidic pH values ≤5, both SiO_2 and COOH particles displayed a measured positive zeta potential. The origin of this inversion in sign of zeta potential is not clear and could stem from a number of sources, including possible charge reversal, or protonation of the silanol groups due to an increased pK value of silanol groups in alcohols. Counterion governed charge inversion or reversal is traditionally expected in the strong coupling regime which is favoured by multivalent counter-ions and small dielectric constants - conditions which are not met in these experiments[31,32]. In order to indirectly probe the sign of the charge of the particle relevant for an interaction, we studied particle-wall interactions for COOH and SiO_2 particles suspended in IPA containing 0.01 mM HCl. Particle-surface interactions were examined in an observation cell coated with positively charged PEI polymer, generally used when imaging positively charged NH_2 particles. Interestingly, both COOH and SiO_2 particles, that registered positive zeta potentials, stuck to the positively coated cell surface, as expected rather for negatively charged particles interacting with a PEI coated surface.

In contrast, both COOH and SiO_2 particles in protonated IPA diffused freely above an untreated negatively charged glass surface, displaying behaviour typical for negatively charged particles. Taken together, our "surface interaction based" qualitative inference of particle charge suggests that both types of particles in fact most likely carry a negative sign of charge. This observation echoes similar reports on silica particles coated with lipid bilayers of variable sign of charge and density[33]. Furthermore, the same silica particles suspended in water at lower pH ≈ 4 also often displayed a large fraction of particles with positive zeta potentials, although silanol groups are generally not expected to exist in the doubly protonated state ($SiOH_2^+$) at weakly acidic pH (Supplementary Figure 7). Zeta potential measurements therefore likely report on additional electrokinetic or interfacial contributions not necessarily reflecting the electrical charge on the particle exclusively.

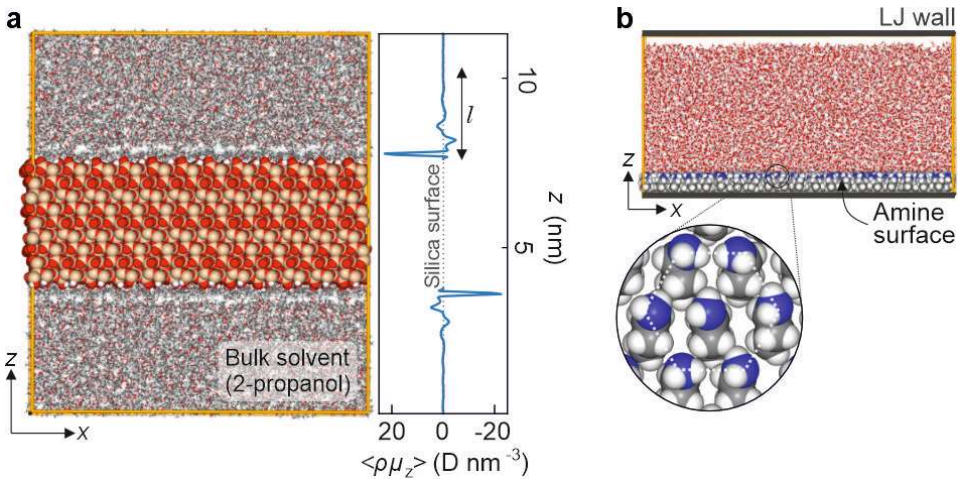
Supplementary Figures



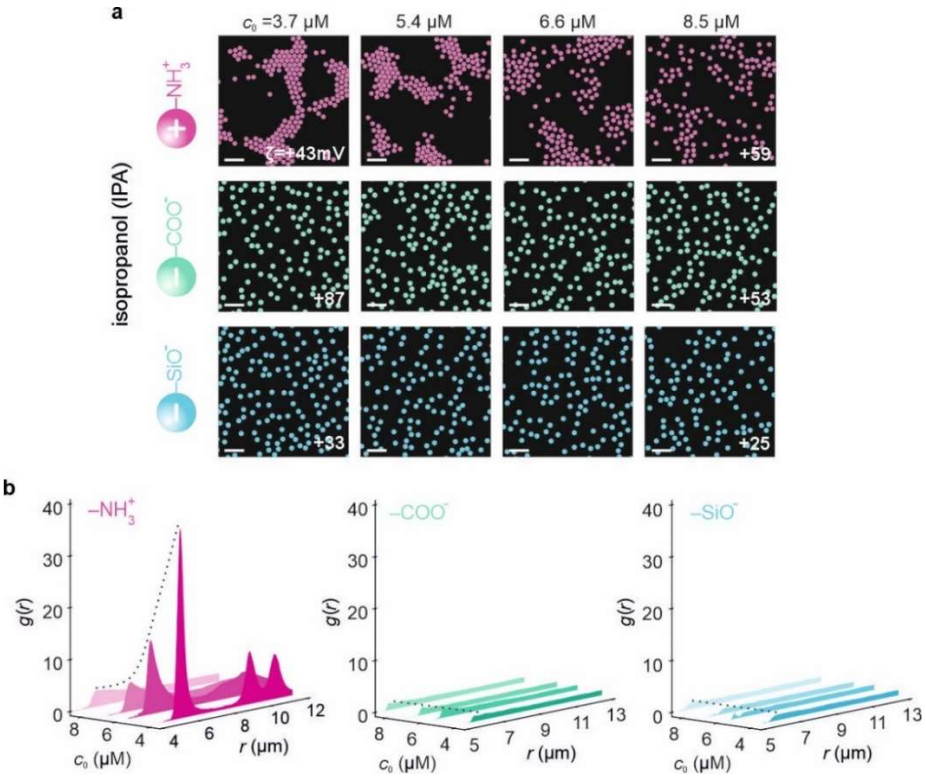
Supplementary Figure 1. Probability distributions of particle diameter for each particle type studied in experiments. a NH_2-SiO_2, **b, c** two types of SiO_2 particles and **d** COOH-MF particles. The distributions were taken from the manufacturer's measurements based on the Coulter principle. The mean and standard deviation (s.d.) of the particle diameter distributions are quoted in the inset.



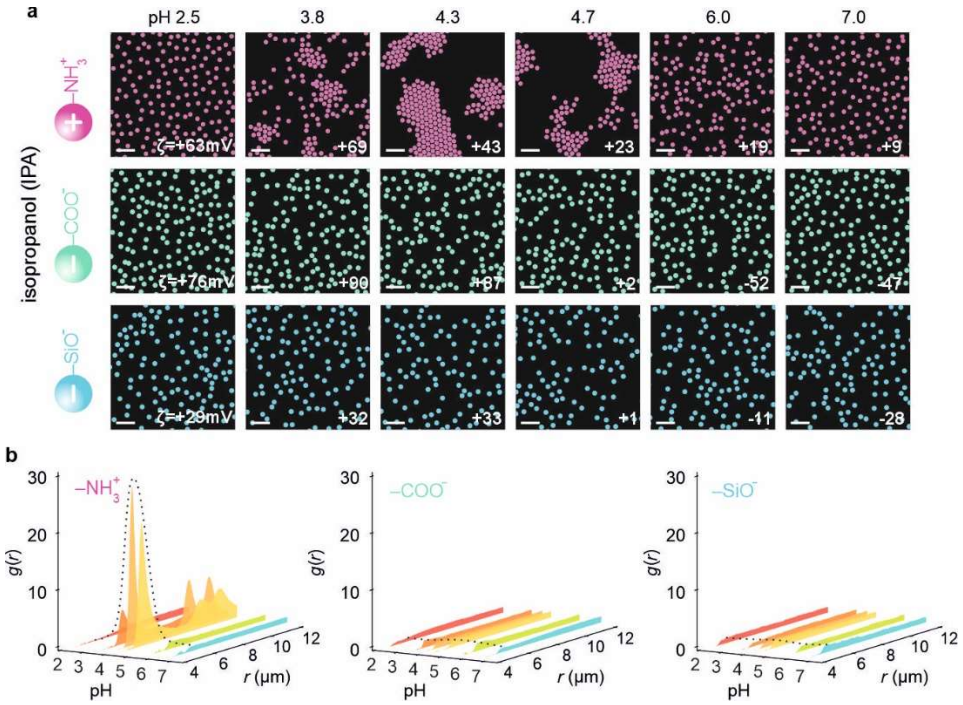
Supplementary Figure 2. Particle charge characterization of SiO_2 and NH_2-SiO_2 in aqueous solution, selected solvents and mixtures. Distribution of zeta potentials measured for particles in H_2O, ethanol, DMSO and 50% IPA/H_2O mixture (left to right). Measurements were performed in the same solution conditions as those used for optical microscopy observation of suspension structures.



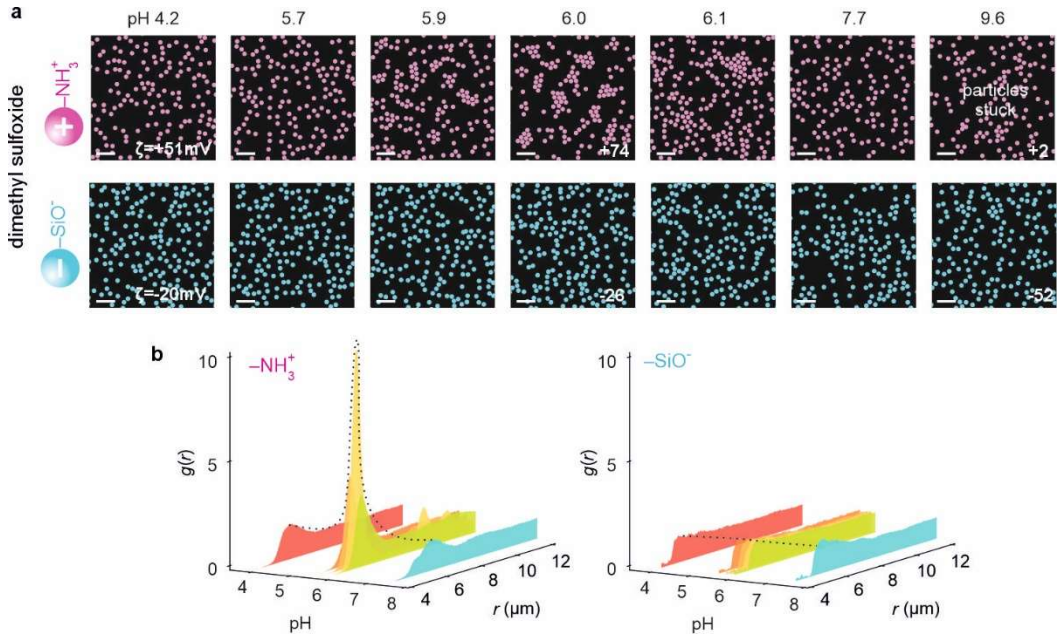
Supplementary Figure 3. Simulation setups for studying interfacial solvation at model silica and amine surfaces. a Simulation cell schematic for all simulations studying the interfacial solvation properties of silica surfaces in this work. An uncharged slab of silica with silanol surface group densities ranging from Γ = 0.5 – 4.7 OH nm^{-2} generated with the CHARMM-GUI webserver, measuring approximately 10×10 nm^2 in area and 4 nm in width, is solvated on both sides with the fluid phase of interest. Periodic boundaries apply in all three dimensions, as indicated by the yellow box edges. At the interface, solvent molecules display a preferential orientation that results in non-zero average values of the dipole moment density $\langle\rho\mu_z\rangle$ shown here for 2-propanol (right). The simulation cell is designed to be large enough in the z dimension such that the profiles of the dipole moment density reach a constant value ($\langle\rho\mu_z\rangle \approx 0$ for an uncharged silica surface in this case) in the bulk liquid, at a distance l which we regard as denoting the approximate thickness of the interfacial region. To calculate $\mu_{av}(0)$, the dipole moment density profile is integrated from a location in the bulk liquid to the silica surface as shown in MD simulation methods Eq. (3) and described in detail below. These values are reported in the main text and Fig. 2f. **b** Simulation cell schematic for all simulations studying the interfacial solvation properties of model amine surfaces. Model amine fragments were patterned in a hexagonally close packed arrangement such that the terminal NH_2 group faced the bulk solvent, and were positionally restrained to form the model surface. This surface is placed in contact with the fluid phase of interest, water in the case pictured. At the other end of the simulation cell in the z direction an 'LJ wall' was placed to confine the solvent molecules. Periodic boundaries apply in the xy directions only. Variable NH_2 surface group densities were realised by switching on or off the atomic partial charges of the amine functional groups, whilst retaining their LJ interaction terms.



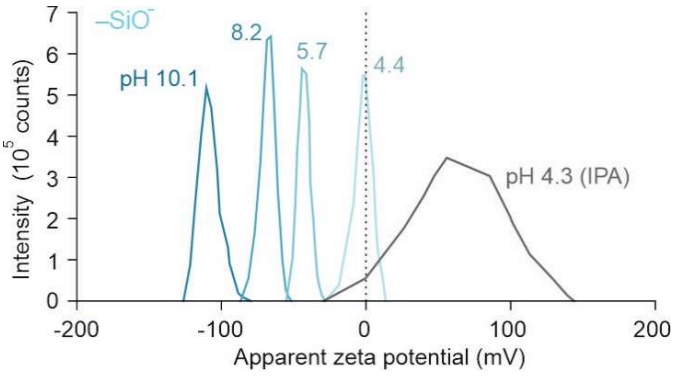
Supplementary Figure 4. Effect of added salt on cluster formation for NH_2, SiO_2 and COOH particles in 2-propanol (IPA). **a** Digitized experimental image of NH_2, SiO_2 and COOH particle interactions as a function of NaCl concentration in IPA (with 0.01mM HCl). **b** Radial distribution density functions, $g(r)$, as a function of salt concentration for three types of particles. Similar to negatively charged particles in water, interparticle attraction is strongest for positively charged NH_2 particles in IPA containing a lower concentration of salt ($c_0 \approx$ 3-5 μM in this case)[3]. Negatively charged SiO_2 and COOH particles display no evidence of interparticle attraction or cluster formation regardless of the salt concentration. Note that in acidic IPA we measure positive values of zeta potentials for SiO2 and COOH particles which is discussed further below.



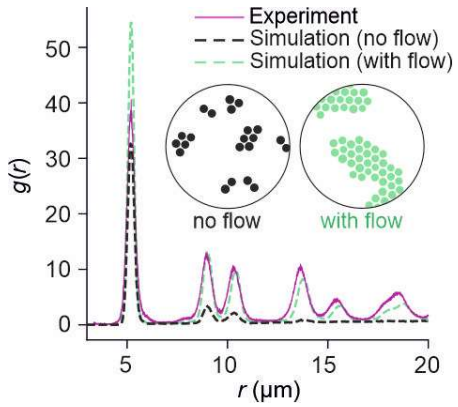
Supplementary Figure 5. Effect of pH on interparticle interactions for NH_2, SiO_2 and COOH particles in 2-propanol (IPA). a Digitized experimental image of NH_2, SiO_2 and COOH particle interactions in IPA as a function of pH. **b** Radial probability density functions, $g(r)$, as a function of pH for three types of particles. We do not maintain constant ionic strength in this set of experiments (Supplementary Table 6). For positively charged NH_2 particles, the strongest interparticle attraction was observed at around pH 4-5. SiO_2 and COOH particles show no evidence of interparticle attraction or cluster formation regardless of pH. Note that for pH<6 we measure positive values of zeta potentials for SiO_2 and COOH particles which is discussed further below.



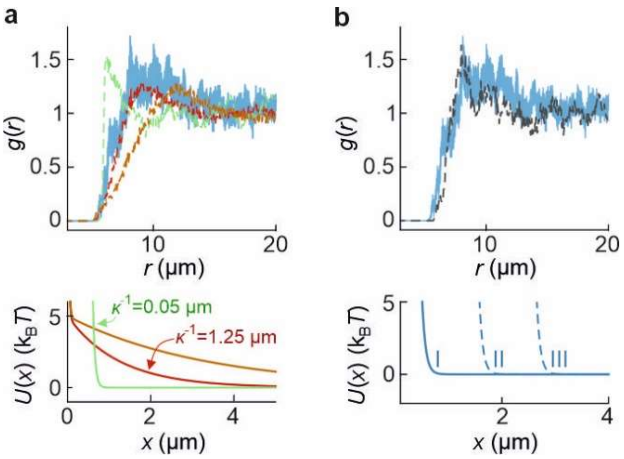
Supplementary Figure 6. Effect of solvent pH on interparticle interactions for NH_2 and SiO_2 particles suspended in dimethyl sulfoxide (DMSO). a Digitized experimental image of NH_2 and SiO_2 particles in DMSO as a function of pH adjusted by the addition of HCl. **b** Radial probability density functions, $g(r)$, as a function of pH for the two types of particles. For positively charged NH_2 particles in DMSO, cluster formation was observed in a narrow range of about 1 pH unit at pH≈ 6. This is in sharp contrast to IPA where cluster formation persisted over a range of ca. 2-3 units of pH (Supplementary Figure 5). No evidence of attraction was found for negatively charged SiO_2 particles in DMSO.



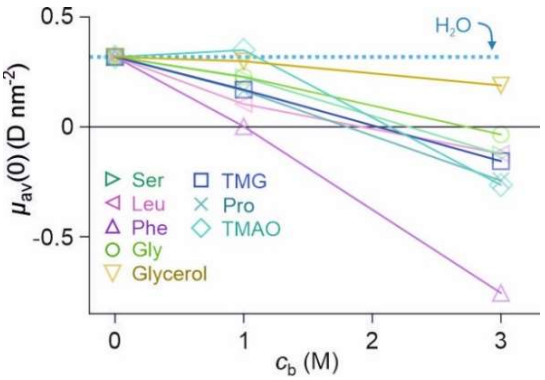
Supplementary Figure 7. Zeta potential distribution for SiO_2 particles in water at various pH. We observe a systematic reduction in zeta potential as pH drops from ≈10 to ≈4. Four curves plotted from left to right indicate zeta potential distributions with an average of -110 mV, -64 mV, -42 mV and -5 mV in solutions of pH 10.1, 8.2, 5.7 and 4.4, adjusted by the addition of Tris or HCl. For the lowest pH case, a significant fraction of particles appears to be characterized by positive values of zeta potential. The grey curve displays the zeta potential distribution of SiO_2 particles suspended in IPA at pH 4.3, and indicates largely positive values.



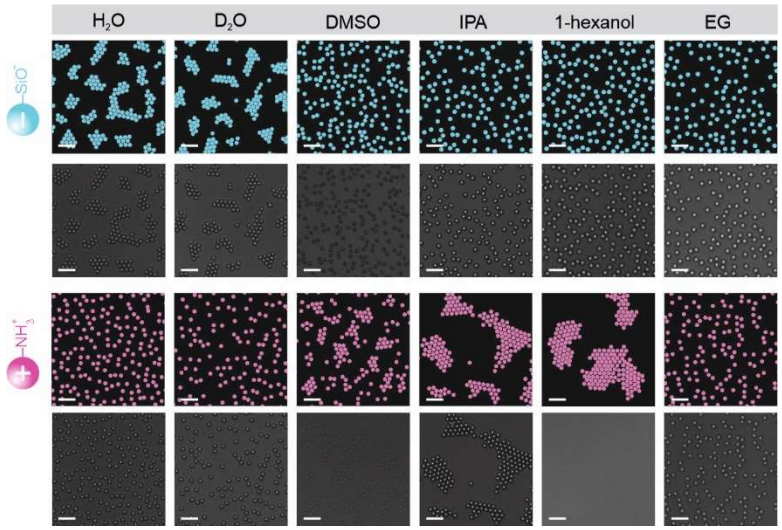
Supplementary Figure 8. Improving agreement between simulated and measured $g(r)$ distributions through the incorporation of a weak external flow in BD simulations. Experimental radial distribution function $g(r)$ for positively charged NH_3^+ particles suspended in 1-hexanol (pink solid line) compared with $g(r)$s outputs from BD simulations that do or do not incorporate the presence of weak external flows (green and grey dashed lines respectively). Snapshots of the simulated suspension structure for the two cases (inset). The pair-interaction potential for both cases is described by Supplementary Eq. (1) with parameters A = 2482.789 k_BT, B = -2240.343 k_BT, κ_1 = 5.405 μm^{-1}, κ_2 = 5.135 μm^{-1}. Particle flow was implemented in the BD simulation by applying a constant force in the x direction of 5 k_BT μm^{-1} (corresponding to a flow velocity of ≈1 μm sec^{-1}) to particles with a total potential energy of interaction greater than -5.5 k_BT. This captures to the first order the influence of weak external flow on cluster formation. Weakly associated or free particles are gradually swept along in the direction of the flow until they encounter a cluster. Here they may engage in strong multivalent nearest-neighbour interactions that anchor them as it were in a growing cluster. In general, this results in the formation of large clusters in simulations, comparable in size to those observed in experiments. The simulated suspension structure then also more closely resembles that seen in experiment (Fig. 2b).



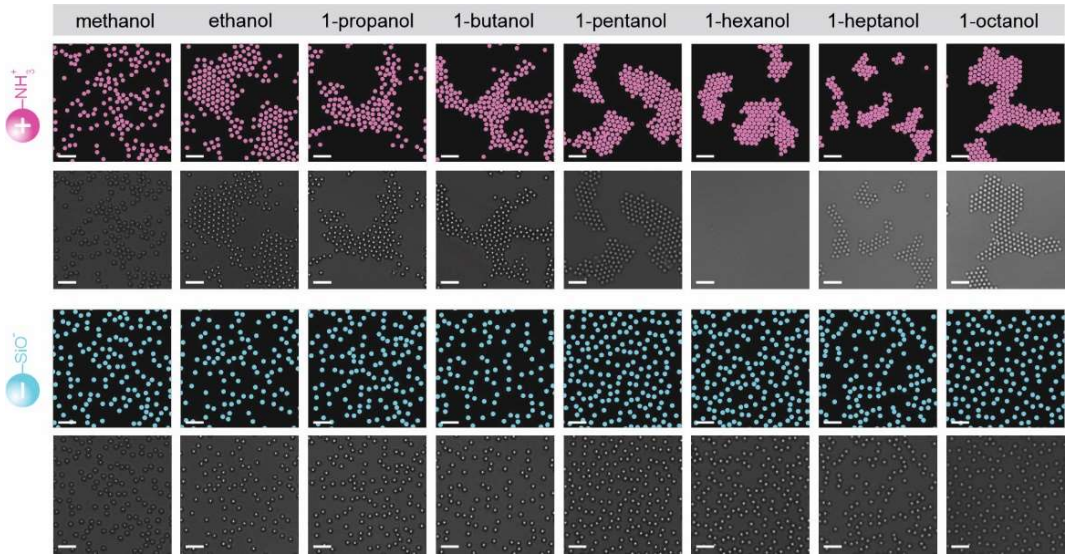
Supplementary Figure 9. Matching the measured $g(r)$ profile for negatively charged SiO_2 particles in EG with BD simulations. a Experimental $g(r)$ for SiO_2 particles ($2R$ = 4.82 μm) suspended in EG (blue line). The $g(r)$ profile slowly increases to a maximum value over a distance of a few microns which is markedly different to those measured in other solvents (Fig. 2) and could not be successfully captured using the standard BD approach ($\kappa_1 = \kappa \approx 20$ μm^{-1}, the nominal inverse Debye length), in $U(x)$ equation (green line, Supplementary Table 25 for parameters). However, it is possible to model these observations by assuming a weak and long-ranged repulsive pair-interaction potential $U(x)$ (A =5 k_BT, κ_1 = 0.8 μm^{-1} and $B = 0$, red line). To prevent particle overlap arising from the weak interparticle repulsion (small A value), a pair potential of the form $U(x) = 30\exp(-50x) + A\exp(-\kappa_1 x)$ is used, where the first term plays the role of a steeply rising repulsive interaction energy mimicking the hard sphere interaction. Another case is presented to highlight the sensitivity of the $g(r)$ to the screening length parameters (A = 5 k_BT, κ_1 =0.3 μm^{-1}, $B = 0$, orange line). **b** Matching of the experimental observations by simulating a system with a distribution of A values (Supplementary Eq. (1)). In the simulation, each particle is assigned a particle type I, II or III characterised by a parameter a' = 1×10^4, 1×10^{11} or 1×10^{18} k_BT respectively. Pairwise interactions between particles of type 1 and 2 were characterised by $A = \sqrt{a'_1 a'_2}\, k_BT$ yielding a pair potential with particle-property-dependent exponential prefactor. Roughly equal numbers of each particle type were present in the simulation. All pair interactions are with a screening of length κ_1 =15 μm^{-1} (inferred from experimental conductivity measurements). Both approaches support the a $g(r)$ profile that slowly increases to a maximum value over the range of a few micrometres in x, and therefore reasonably capture the experimentally observed 'long-range' behaviour. Although there are multiple options to configure BD simulations in a way that enables them to reflect experimental observations, the choice of an appropriate pair potential ultimately depends on knowledge of the underpinning physical mechanisms at play.



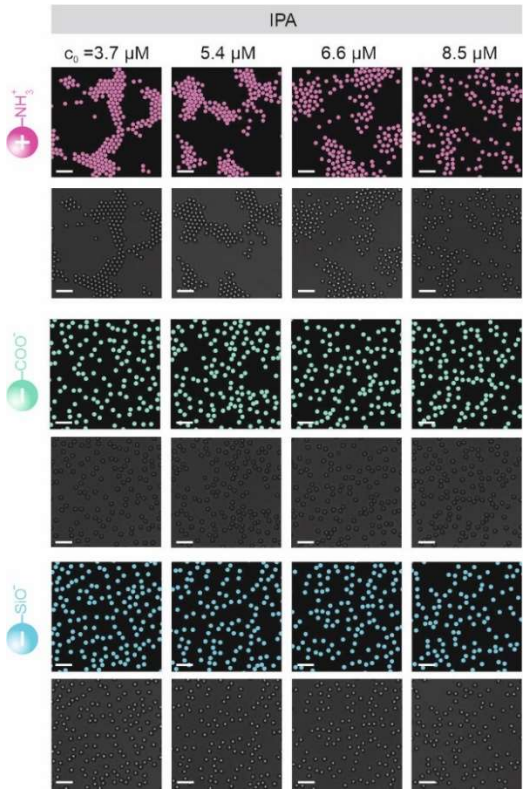
Supplementary Figure 10. Total excess dipole moment density, $\mu_{av}(0)$, in MD simulations of water/zwitterion solutions of varying zwitterion concentration at an uncharged silica surface of silanol group density $\Gamma = 4.7$ OH nm^{-2}. The overall excess dipole moment density includes the contribution of all interfacial molecular species, namely water and osmolyte. Notably, large concentrations of glycerol (up to ca. 1 M) minimally disrupt the value of $\mu_{av}(0)$ such that $\mu_{av}(0) \approx \mu_{av,w}(0)$. Furthermore, the $\mu_{av}(0)$ values characterizing the interfacial electrolyte in solutions containing methylated zwitterions TMAO and TMG show rather similar behaviour to amino acids serine, leucine and glycine. Note however that the $\mu_{av,w}(0)$ values for TMG and TMAO are greatly enhanced compared to their amino acid counterparts (Fig. 7e).



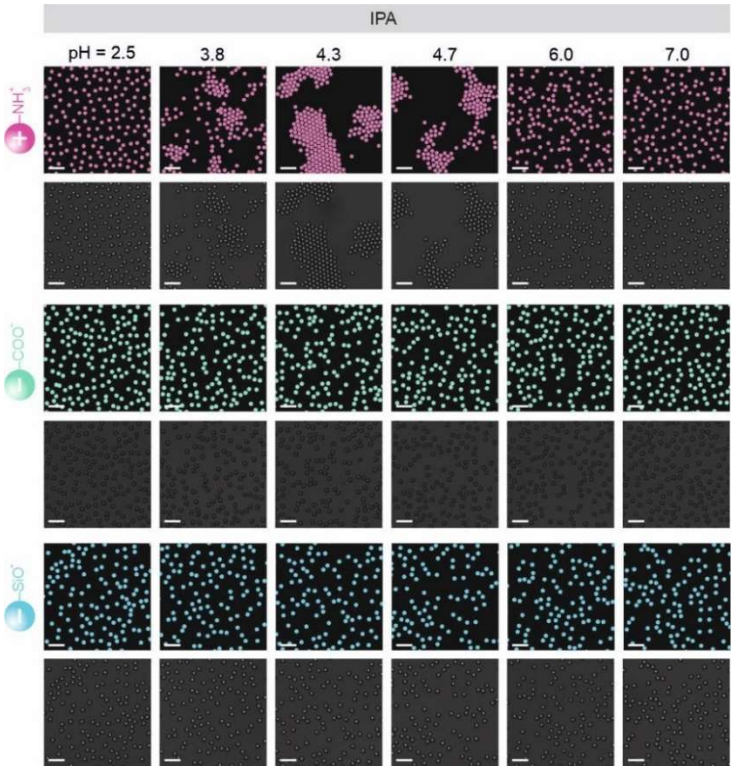
Supplementary Figure 11. Raw and digitized images of experiments shown in Fig. 2.



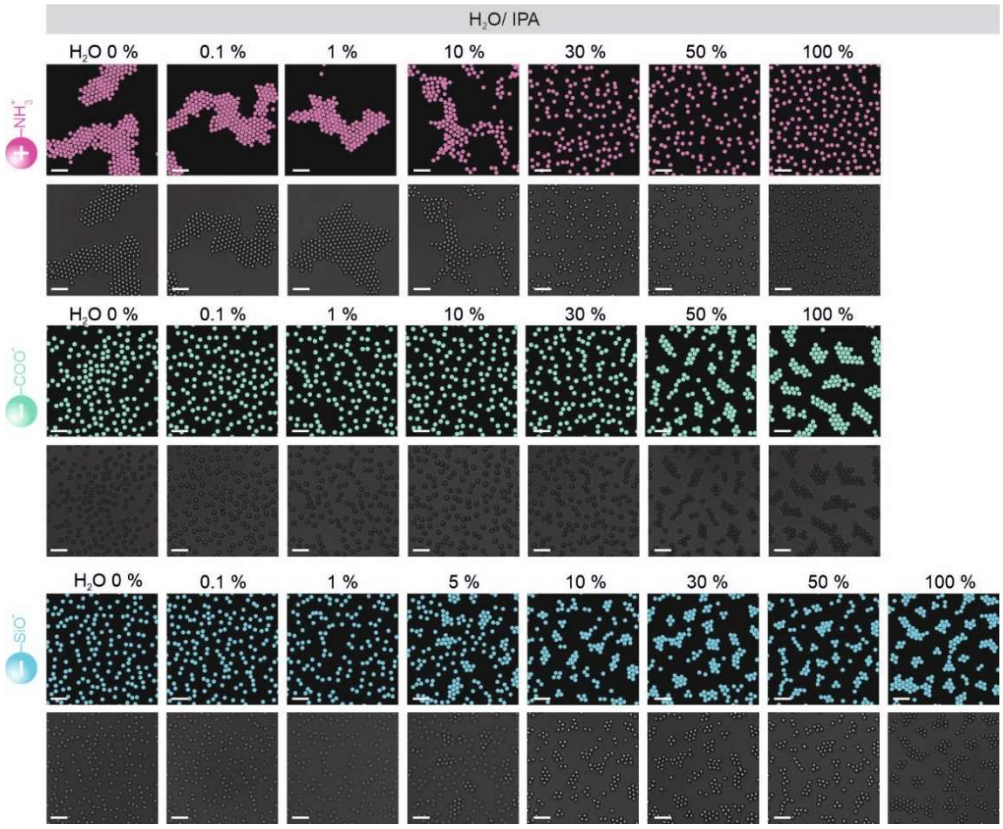
Supplementary Figure 12. Raw and digitized images of experiments shown in Fig. 3.



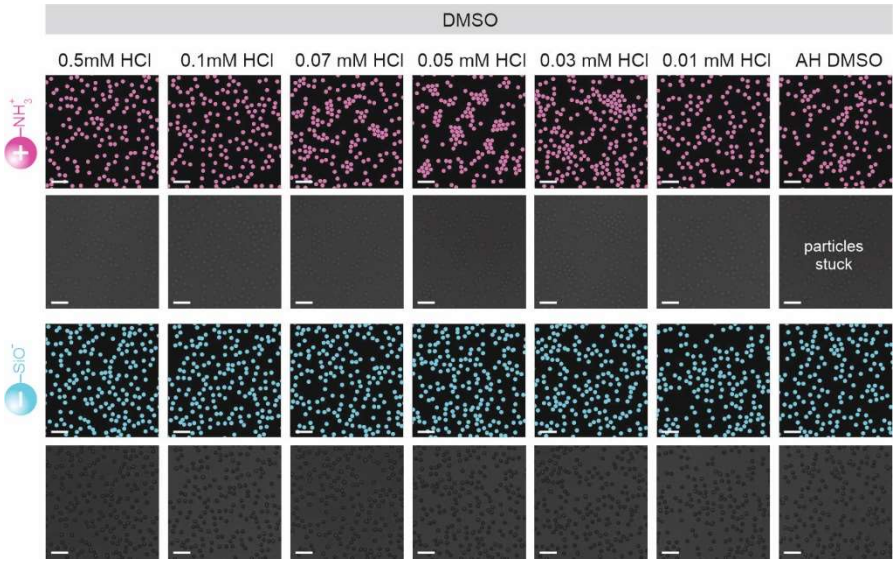
Supplementary Figure 13. Raw and digitized images of NH_2, SiO_2 and COOH particle interactions in IPA with a variation in added salt.



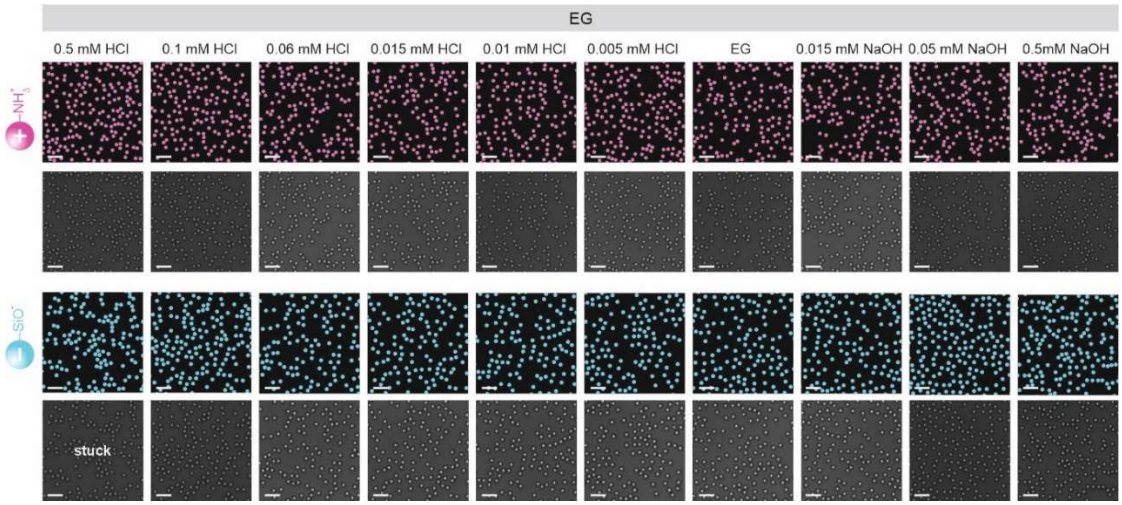
Supplementary Figure 14. Raw and digitized images of NH_2, SiO_2 and COOH particle interactions in IPA with a variation in solution pH.



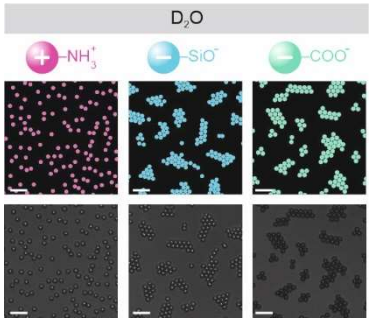
Supplementary Figure 15. Raw and digitized images of NH_2, SiO_2 and COOH particle interactions in water-IPA mixtures (vol.% of H_2O in IPA).



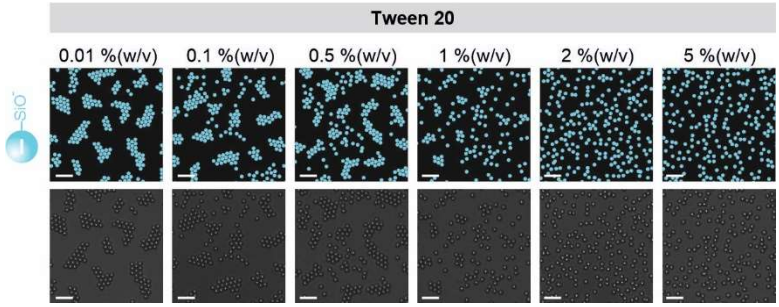
Supplementary Figure 16. Raw and digitized images of NH_2 and SiO_2 particle interactions in DMSO with a variation in solution pH.



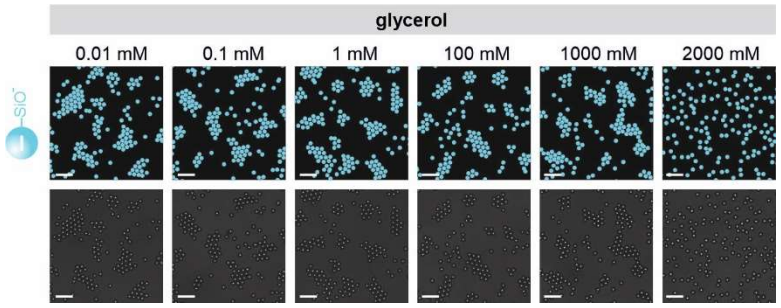
Supplementary Figure 17. Raw and digitized images of NH_2 and SiO_2 particle interactions in EG with variation in solution pH.



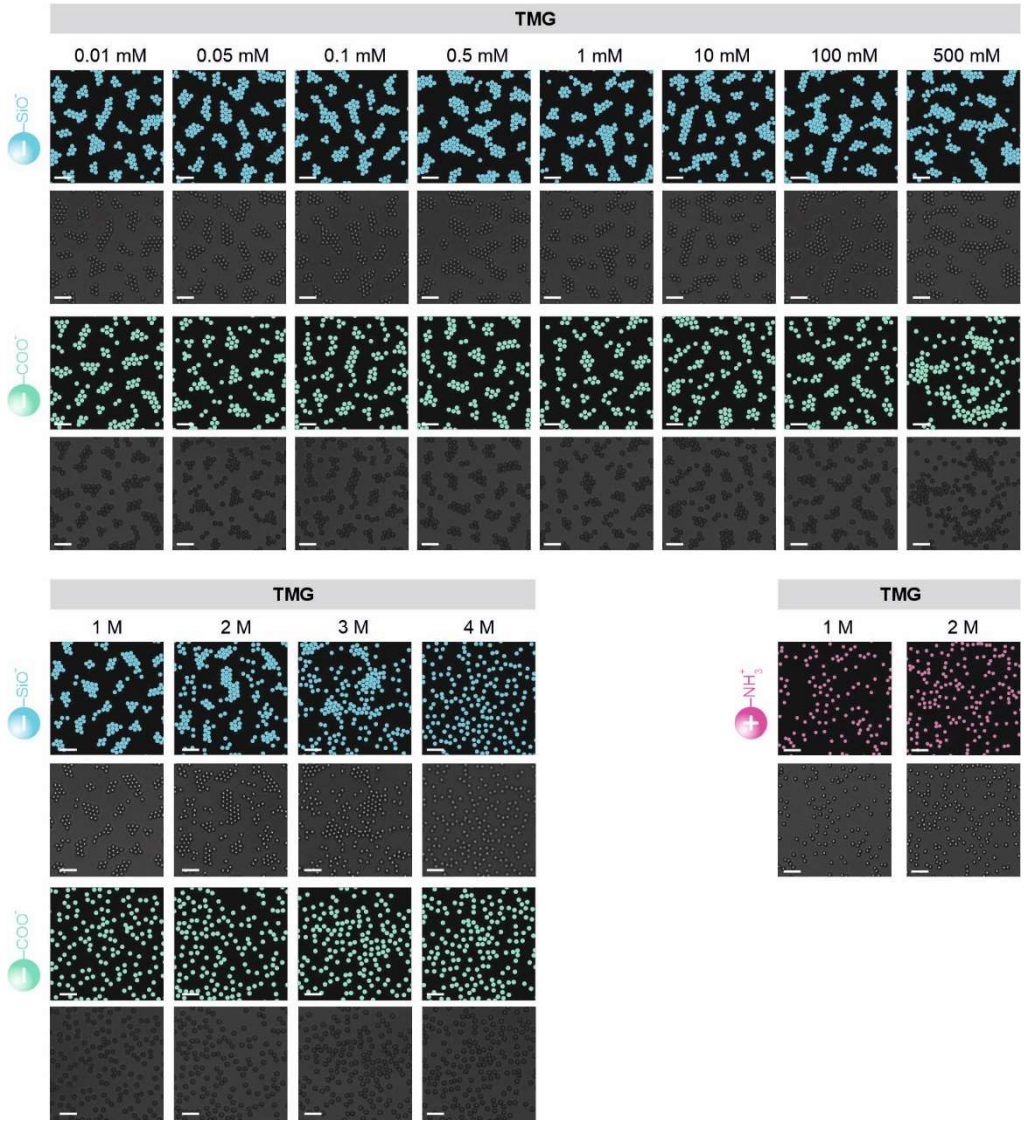
Supplementary Figure 18. Raw and digitized images of NH_2, SiO_2 and COOH particle interactions in D_2O.



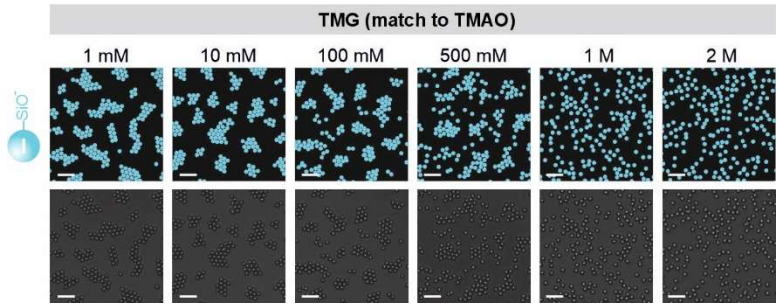
Supplementary Figure 19. Raw and digitized images of SiO_2 particle interactions in aqueous solutions containing varying concentrations of Tween 20 (percentage (w/v) of Tween 20 in water).



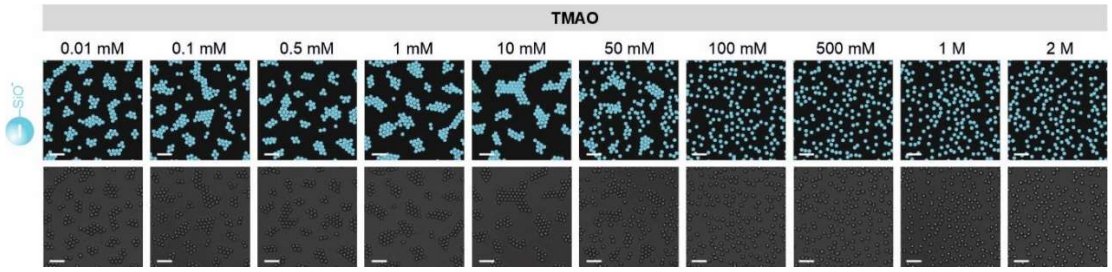
Supplementary Figure 20. Raw and digitized images of SiO_2 particle interactions in glycerol solutions with variation in concentration.



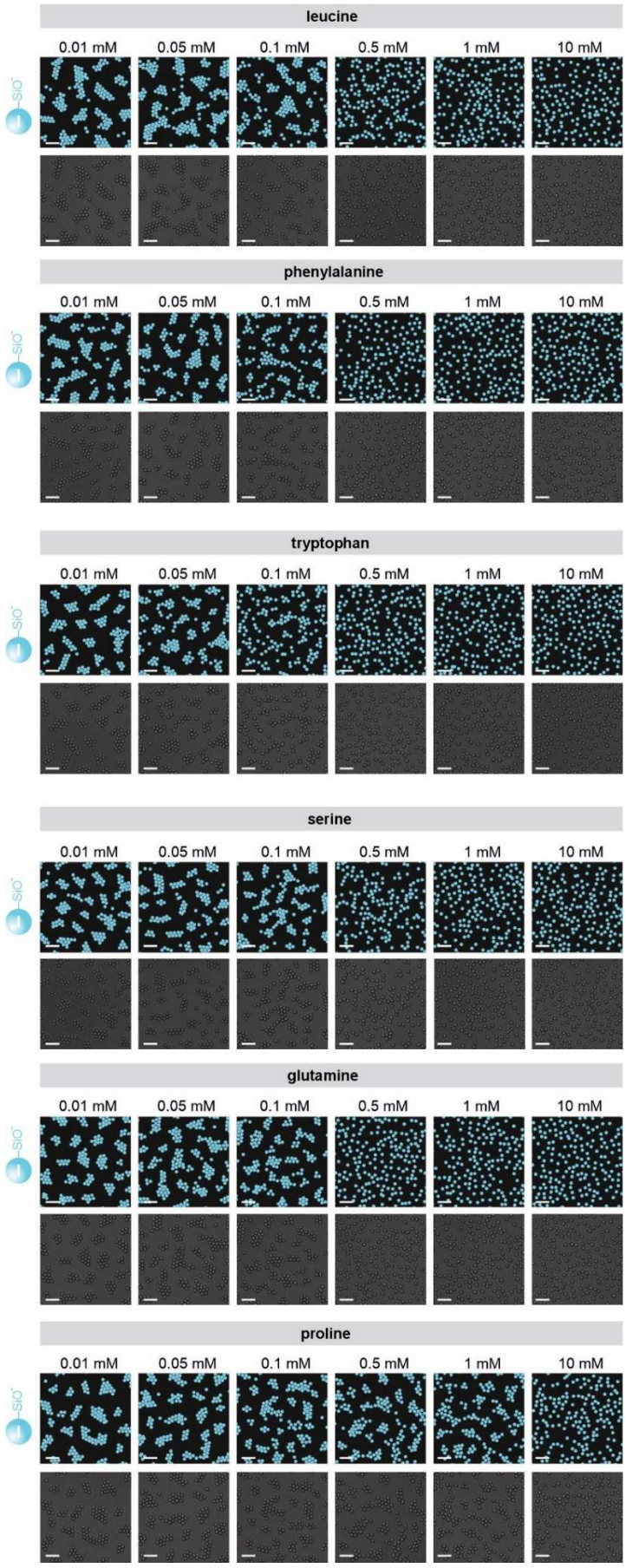
Supplementary Figure 21. Raw and digitized images of SiO_2, COOH and NH_2 particle interactions in water with a variation in concentration of added TMG.

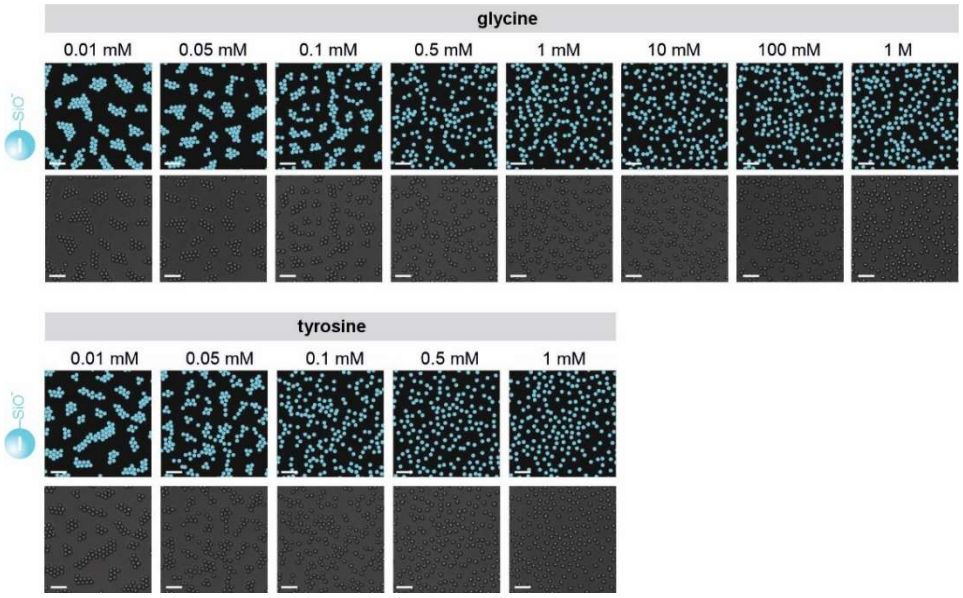


Supplementary Figure 22. Raw and digitized images of SiO_2 particle interactions in TMG-containing water with adjusted pH and conductivity. In each case the pH and conductivity of the TMG-containing electrolyte is adjusted to match that of the corresponding experiment at the same concentration of TMAO (see Supplementary Table 12).

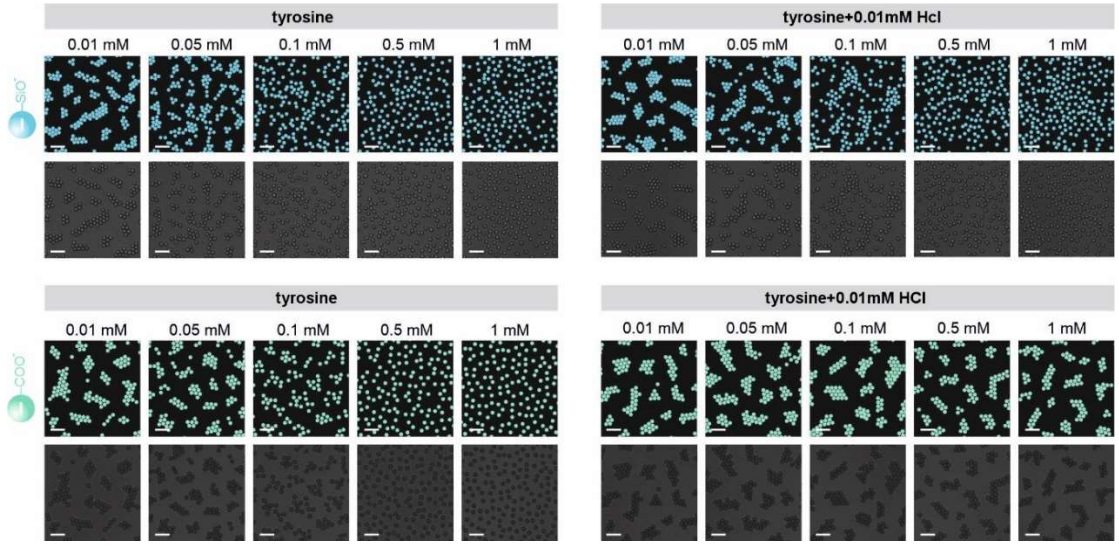


Supplementary Figure 23. Raw and digitized images of SiO_2 particle interactions in water containing various concentrations of added TMAO.


leucine
0.01 mM
0.05 mM
0.1 mM
0.5 mM
1 mM
10 mM
sio
phenylalanine
0.01 mM
0.05 mM
0.1 mM
0.5 mM
1 mM
10 mM
sio
tryptophan
0.01 mM
0.05 mM
0.1 mM
0.5 mM
1 mM
10 mM
sio
serine
0.01 mM
0.05 mM
0.1 mM
0.5 mM
1 mM
10 mM
sio
glutamine
0.01 mM
0.05 mM
0.1 mM
0.5 mM
1 mM
10 mM
sio
proline
0.01 mM
0.05 mM
0.1 mM
0.5 mM
1 mM
10 mM
sio



Supplementary Figure 24. Raw and digitized images of SiO_2 particle interactions in water containing various concentrations of added amino acids.



Supplementary Figure 25. Raw and digitized images of SiO_2 and COOH particle interactions in water containing various concentrations of added tyrosine (with and without pH adjustment by the addition of 0.01 mM HCl).

Supplementary Tables

Supplementary Table 1. Detail on solvents used in the study.

Solvent	Product Number	Supplier	Purity
Methanol	34860	Sigma-Aldrich	≥99.9%
Ethanol	32221-M	Sigma-Aldrich	≥99.8%
2-propanol (IPA)	278475	Sigma-Aldrich	anhydrous, 99.5%
1-propanol	279544	Sigma-Aldrich	anhydrous, 99.7%
1-butanol	281549	Sigma-Aldrich	anhydrous, 99.8%
1-pentanol	138975	Sigma-Aldrich	≥99%
1-hexanol	471402	Sigma-Aldrich	anhydrous, ≥99%
1-heptanol	A12793	Thermo Fisher	99%
1-octanol	297887	Sigma-Aldrich	anhydrous, ≥99%
ethylene glycol	324558	Sigma-Aldrich	anhydrous, 99.8%
dimethyl sulfoxide	276855	Sigma-Aldrich	anhydrous, ≥99.9%
deuterium oxide	613444	Sigma-Aldrich	99.9 at.% D

Supplementary Table 2. Detail on additives used in the study.

Additives	Product Number	Supplier	Purity
L-leucine	L8000	Sigma-Aldrich	≥98%
L-phenylalanine	P2126	Sigma-Aldrich	≥98%
L-tyrosine	93829	Sigma-Aldrich	≥99.0%
L-tryptophan	93659	Sigma-Aldrich	≥99.5%
L-serine	S4500	Sigma-Aldrich	≥99%
Glycine	G7126	Sigma-Aldrich	≥99%
L-glutamine	G3126	Sigma-Aldrich	≥99%
L-proline	A10199	Thermo Fisher	99%
Trimethylglycine (TMG)	101003	MP Biomedicals	≥99%
Trimethylamine N-oxide (TMAO)	92277	Sigma-Aldrich	≥99.0%
Tween 20	655206	Sigma-Aldrich	-
Glycerol	G7893	Sigma-Aldrich	≥99.5%
NaCl	010862	Thermo Fisher	99.998%
HCl	087617	Thermo Fisher	99.999%
NaOH	045780	Thermo Fisher	99.99%

Supplementary Table 3. List of experimental conditions for experiments shown in Fig. 2.

Particle	2*R* (μm)	Solvent	pH	Conductivity (μS cm^{-1})	η (cP)	Equivalent c_0 (mM)	ζ (mV)	Added acid/base
NH_2	4.63	H_2O	5.8	1.00	1.0	0.007	30.2±1.7	-
SiO_2	4.82	H_2O	5.8	1.00	1.0	0.007	-70.9±5.3	-
NH_2	4.63	D_2O	6.0	4.04	1.0	0.027	40.3±8.6	-
SiO_2	4.82	D_2O	6.0	4.04	1.0	0.027	-59.3±1.3	-
NH_2	4.63	DMSO	6.0	2.40	2.0	0.032	73.8±2.6	0.05 mM HCl
SiO_2	4.82	DMSO	9.6	0.60	2.0	0.008	-51.8±1.3	-
NH_2	4.63	IPA	4.3	0.25	2.4	0.004	42.7±2.7	0.01 mM HCl
SiO_2	5.17	IPA	6.1	0.08	2.4	0.001	-11.4±0.4	-
NH_2	4.63	1-hexanol	6.3	0.09	6.0	0.003	33.8±2.3	0.01 mM HCl
SiO_2	5.17	1-hexanol	7.3	0.06	6.0	0.002	-24.5±0.7	-
NH_2	4.63	EG	7.1	0.30	15.5	0.031	41.8±2.0	0.01 mM HCl
SiO_2	5.17	EG	8.0	0.28	15.5	0.029	-22.0±5.9	-

Supplementary Table 4. List of experimental conditions for experiments shown in Fig. 3.

Particle	2*R* (μm)	Solvent	pH	Cond. (μS cm^{-1})	η (cP)	Equiv. c_0 (mM)	ζ (mV)	Added acid/base
NH_2	4.63	methanol	6.3	0.73	0.6	0.0029	64.8±13.3	0.01 mM HCl
NH_2	4.63	ethanol	4.3	0.70	1.2	0.0056	81.3±7.1	
NH_2	4.63	1-propanol	7.5	0.64	2.1	0.0088	20.4±10.2	
NH_2	4.63	1-butanol	6.8	0.36	3.0	0.0072	30.0±0.3	
NH_2	4.63	1-pentanol	4.9	0.14	4.3	0.0040	75.2±1.0	
NH_2	4.63	1-hexanol	6.3	0.09	6.0	0.0035	33.8±2.3	
NH_2	4.63	1-heptanol	5.5	0.11	7.8	0.0055	85.7±1.9	
NH_2	4.63	1-octanol	6.0	0.03	10.1	0.0019	47.5±2.8	
SiO_2	5.17	methanol	6.4	0.56	0.6	0.0021	-35.9±8.8	-
SiO_2	5.17	ethanol	6.2	0.02	1.1	0.0001	-18.8±1.2	-
SiO_2	5.17	1-propanol	7.8	0.57	2.3	0.0087	-30.4±2.6	-
SiO_2	5.17	1-butanol	7.9	0.31	3.0	0.0063	-32.1±3.1	-
SiO_2	5.17	1-pentanol	7.0	0.04	4.0	0.0010	-41.0±1.7	-
SiO_2	5.17	1-hexanol	7.3	0.06	5.9	0.0023	-24.5±0.7	-
SiO_2	5.17	1-heptanol	5.3	0.05	7.4	0.0027	-15.9±1.7	-
SiO_2	5.17	1-octanol	6.5	0.01	7.4	0.0007	-25.7±0.9	-

Supplementary Table 5. Salt concentration variation experiments for NH_2, SiO_2 and COOH particles in IPA.

Particle	2*R* (μm)	Solvent	pH	Cond. (μS cm^{-1})	η (cP)	Equiv. c_0 (mM)	ζ (mV)	Added acid/base
NH_2	4.63	IPA	4.3	0.23	2.4	0.0037	42.7±2.7	0.01 mM HCl
NH_2	4.63	IPA	4.3	0.34	2.4	0.0054	64.5±0.7	
NH_2	4.63	IPA	4.3	0.41	2.4	0.0066	63.2±3.7	
NH_2	4.63	IPA	4.3	0.53	2.4	0.0085	58.6±2.1	
COOH	5.29	IPA	4.3	0.23	2.4	0.0037	87.4±3.5	
COOH	5.29	IPA	4.3	0.34	2.4	0.0054	54.5±1.6	
COOH	5.29	IPA	4.3	0.41	2.4	0.0066	57.0±1.7	
COOH	5.29	IPA	4.3	0.53	2.4	0.0085	53.4±0.8	
SiO_2	5.17	IPA	4.3	0.23	2.4	0.0037	32.6±1.6	
SiO_2	5.17	IPA	4.3	0.34	2.4	0.0054	48.5±2.9	
SiO_2	5.17	IPA	4.3	0.41	2.4	0.0066	42.4±1.7	
SiO_2	5.17	IPA	4.3	0.53	2.4	0.0085	25.2±6.5	

Supplementary Table 6. pH variation experiments in IPA for NH_2, SiO_2 and COOH particles.

Particle	2*R* (μm)	Solvent	pH	Cond. (μS cm^{-1})	η (cP)	Equiv. c_0 (mM)	ζ (mV)	Added acid/base
NH_2	4.63	IPA	2.5	1.54	2.4	0.0246	63±1	0.06 mM HCl
NH_2	4.63	IPA	3.8	0.4	2.4	0.0064	69±2	0.015 mM HCl
NH_2	4.63	IPA	4.3	0.25	2.4	0.0040	43±3	0.01 mM HCl
NH_2	4.63	IPA	4.7	0.11	2.4	0.0018	23±1	0.005 mM HCl
NH_2	4.63	IPA	6.1	0.08	2.4	0.0013	19±1	-
NH_2	4.63	IPA	7	0.18	2.4	0.0029	9±1	0.015 mM NaOH
NH_2*	4.63	IPA	9.3	0.39	2.4	0.0062	-5±2	0.06 mM NaOH
COOH	5.29	IPA	2.5	1.54	2.4	0.0246	76±6	0.06 mM HCl
COOH	5.29	IPA	3.8	0.4	2.4	0.0064	90±4	0.015 mM HCl
COOH	5.29	IPA	4.3	0.25	2.4	0.0040	87±3	0.01 mM HCl
COOH	5.29	IPA	4.7	0.11	2.4	0.0018	2±1	0.005 mM HCl
COOH	5.29	IPA	6.1	0.08	2.4	0.0013	-52±1	-
COOH	5.29	IPA	7	0.18	2.4	0.0029	-47±2	0.015 mM NaOH
COOH	5.29	IPA	9.3	0.39	2.4	0.0062	-43±2	0.06 mM NaOH
SiO_2	5.17	IPA	2.5	1.54	2.4	0.0246	29±15	0.06 mM HCl
SiO_2	5.17	IPA	3.8	0.4	2.4	0.0064	32±5	0.015 mM HCl
SiO_2	5.17	IPA	4.3	0.25	2.4	0.0040	33±2	0.01 mM HCl
SiO_2	5.17	IPA	4.7	0.11	2.4	0.0018	1±7	0.005 mM HCl
SiO_2	5.17	IPA	6.1	0.08	2.4	0.0013	-11±0	-
SiO_2	5.17	IPA	7	0.18	2.4	0.0029	-28±1	0.015 mM NaOH
SiO_2	5.17	IPA	9.3	0.39	2.4	0.0062	-37±1	0.06 mM NaOH

* rows with grey text indicate cases involving particles stuck to the glass surface (data not used)
** note that the listed measured zeta potentials might not reflect the true sign of surface charge of the particle. See Suppl. Note 10 for details

Supplementary Table 7. Water-IPA mixture experiments for NH_2, SiO_2 and COOH particles.

Particle	2*R* (μm)	Solvent	Water% (v/v)	pH	Cond. (μS cm^{-1})	*η* (cP)	Equiv. c_0 (mM)	*ζ* (mV)	Added acid/base
NH_2	4.63	IPA	0	4.3	0.25	2.4	0.0040	43±2.7	0.01 mM HCl IPA
NH_2	4.63/	H_2O/IPA	0.10	5.8	0.21	2.4	0.0034	68±2.4	
NH_2	4.63	H_2O/IPA	1	5.9	0.23	2.4	0.0036	64±1.6	
NH_2	4.63	H_2O/IPA	10	6.2	0.31	2.2	0.0045	30±4.1	
NH_2	4.63	H_2O/IPA	30	6.2	0.48	1.7	0.0054	35±0.9	
NH_2	4.63	H_2O/IPA	50	5.9	0.75	1.2	0.0060	67±1.6	
NH_2	4.63	H_2O	100	5.8	1.00	1.0	0.0067	30±1.7	
SiO_2	4.82	IPA	0	6.1	0.08	2.4	0.0013	-11±0.4	-
SiO_2	4.82	H_2O/IPA	0.10	7.5	0.12	2.4	0.0019	-9±1.6	
SiO_2	4.82	H_2O/IPA	1	7.3	0.14	2.4	0.0022	-24±1.3	
SiO_2	4.82	H_2O/IPA	5	7.5	0.18	2.3	0.0027	-28±1.0	
SiO_2	4.82	H_2O/IPA	10	7.5	0.20	2.2	0.0029	-28±1.0	
SiO_2	4.82	H_2O/IPA	30	7.3	0.21	1.7	0.0024	-41±3.1	
SiO_2	4.82	H_2O/IPA	50	6.0	0.33	1.2	0.0026	-52±5.7	
SiO_2	4.82	H_2O	100	5.8	1.00	1.0	0.0067	-71±5.3	
COOH	5.29	IPA	0	6.1	0.08	2.4	0.0013	-51±1.8	-
COOH	5.29	H_2O/IPA	0.10	7.5	0.12	2.4	0.0019	-54±2.6	
COOH	5.29	H_2O/IPA	1	7.3	0.14	2.4	0.0022	-56±4.7	
COOH	5.29	H_2O/IPA	10	7.5	0.20	2.2	0.0029	-62±3.5	
COOH	5.29	H_2O/IPA	30	7.3	0.21	1.7	0.0024	-56±2.9	
COOH	5.29	H_2O/IPA	50	6.0	0.33	1.2	0.0026	-99±5.5	
COOH	5.29	H_2O	100	5.8	1.00	1.0	0.0067	-66±1.7	

Supplementary Table 8. pH variation experiments in DMSO for NH_2 and SiO_2 particles.

Particle	2*R* (μm)	Solvent	pH	Cond. (μS cm^{-1})	*η* (cP)	Equiv. c_0 (mM)	*ζ* (mV)	Added acid/base
NH_2	4.63	DMSO	4.2	19.6	2.0	0.2613	51±5	0.5 mM HCl
NH_2	4.63	DMSO	5.7	4.3	2.0	0.0573	-	0.1 mM HCl
NH_2	4.63	DMSO	5.9	3.2	2.0	0.0427	-	0.07 mM HCl
NH_2	4.63	DMSO	6.0	2.4	2.0	0.0320	74±3	0.05 mM HCl
NH_2	4.63	DMSO	6.1	1.67	2.0	0.0223	-	0.03 mM HCl
NH_2	4.63	DMSO	7.7	0.86	2.0	0.0115	-	0.01 mM HCl
NH_2	4.63	DMSO	9.6	0.601	2.0	0.0080	2±5	-
SiO_2	4.82	DMSO	4.2	19.6	2.0	0.2613	-20±4	0.5 mM HCl
SiO_2	4.82	DMSO	5.7	4.3	2.0	0.0573	-	0.1 mM HCl
SiO_2	4.82	DMSO	5.9	3.2	2.0	0.0427	-	0.07 mM HCl
SiO_2	4.82	DMSO	6.0	2.4	2.0	0.0320	-26±2	0.05 mM HCl
SiO_2	4.82	DMSO	6.1	1.67	2.0	0.0223	-	0.03 mM HCl
SiO_2	4.82	DMSO	7.7	0.86	2.0	0.0115	-	0.01 mM HCl
SiO_2	4.82	DMSO	9.6	0.601	2.0	0.0080	-52±0	-

* rows with grey text indicate cases involving particles stuck to the surface (data not used)

Supplementary Table 9. pH variation experiments in EG for NH_2 and SiO_2 particles.

Particle	2*R* (μm)	Solvent	pH	Cond. (μS cm^{-1})	η (cP)	Equiv. c_0 (mM)	ζ (mV)	Added acid/base
NH_2	4.63	EG	1.2	13.4	15.5	1.3847	-	0.5 mM HCl
NH_2	4.63	EG	3.0	1.4	15.5	0.1447	-	0.1 mM HCl
NH_2	4.63	EG	5.8	0.48	15.5	0.0496	67±6	0.06 mM HCl
NH_2	4.63	EG	7.4	0.28	15.5	0.0289	-	0.015 mM HCl
NH_2	4.63	EG	7.1	0.3	15.5	0.0310	42±2	0.01 mM HCl
NH_2	4.63	EG	7.9	0.28	15.5	0.0289	-	0.005 mM HCl
NH_2	4.63	EG	8.0	0.28	15.5	0.0289	36±3	-
NH_2	4.63	EG	8.0	0.36	15.5	0.0372	-	0.015 mM NaOH
NH_2	4.63	EG	8.3	0.77	15.5	0.0796	27±2	0.05 mM NaOH
NH_2	4.63	EG	9.5	6	15.5	0.6200	-	0.5 mM NaOH
SiO_2	5.17	EG	1.2	13.4	15.5	1.3847	-	0.5 mM HCl
SiO_2	5.17	EG	3.0	1.4	15.5	0.1447	-	0.1 mM HCl
SiO_2	5.17	EG	5.8	0.48	15.5	0.0496	-20±4	0.06 mM HCl
SiO_2	5.17	EG	7.4	0.28	15.5	0.0289	-	0.015 mM HCl
SiO_2	5.17	EG	7.1	0.3	15.5	0.0310	-16±2	0.01 mM HCl
SiO_2	5.17	EG	7.9	0.28	15.5	0.0289	-	0.005 mM HCl
SiO_2	5.17	EG	8.0	0.28	15.5	0.0289	-22±6	-
SiO_2	5.17	EG	8.0	0.36	15.5	0.0372	-	0.015 mM NaOH
SiO_2	5.17	EG	8.3	0.77	15.5	0.0796	-19±4	0.05 mM NaOH
SiO_2	5.17	EG	9.5	6	15.5	0.6200	-	0.5 mM NaOH

* rows with grey text indicate cases involving particles stuck to the surface (data not used).

Supplementary Table 10. List of experimental conditions for NH_2, SiO_2 and COOH particle interactions in D_2O.

Particle	2*R* (μm)	Solvent	pH	Cond. (μS cm^{-1})	η (cP)	Equiv. c_0 (mM)	ζ (mV)
NH_2	4.63	D_2O	6	4.04	1.0	0.0269	40.3±8.6
COOH	5.29	D_2O	6	4.04	1.0	0.0269	-77.1±1.4
SiO_2	4.82	D_2O	6	4.04	1.0	0.0269	-59.3±1.3

Supplementary Table 11. SiO_2 and COOH particle interaction experiments with varying TMG concentration in water.

Particle	$2R$ (µm)	Additive	c_b (mM)	pH	Cond. (µS cm^{-1})	η (cP)	Equiv. c_0 (mM)	ζ (mV)
SiO_2	4.82	TMG	0	5.8	1	1.0	0.0050	-51±2
SiO_2	4.82	TMG	0.01	5.3	2.3	1.0	0.0153	-64±2
SiO_2	4.82	TMG	0.05	5.3	2.3	1.0	0.0153	-
SiO_2	4.82	TMG	0.1	5.4	2.2	1.0	0.0147	-
SiO_2	4.82	TMG	0.5	5.3	2.1	1.0	0.0140	-
SiO_2	4.82	TMG	1	5.3	2.1	1.0	0.0140	-64±1
SiO_2	4.82	TMG	10	5.3	2	1.0	0.0134	-
SiO_2	4.82	TMG	100	5.6	3.89	1.0	0.0265	-
SiO_2	4.82	TMG	500	6.3	13.9	1.1	0.1036	-
SiO_2	4.82	TMG	1000	6.5	23.5	1.2	0.1949	-57±1
SiO_2	4.82	TMG	2000	6.8	36.1	1.5	0.3665	-
SiO_2	4.82	TMG	3000	7.1	37.6	1.8	0.4601	-
SiO_2	4.82	TMG	4000	7.5	32.5	2.2	0.4729	-30±2
COOH	5.29	TMG	0	5.8	1	1.0	0.0050	-66±2
COOH	5.29	TMG	0.01	5.3	2.3	1.0	0.0153	-59±1
COOH	5.29	TMG	0.05	5.3	2.3	1.0	0.0153	-
COOH	5.29	TMG	0.1	5.4	2.2	1.0	0.0147	-
COOH	5.29	TMG	0.5	5.3	2.1	1.0	0.0140	-
COOH	5.29	TMG	1	5.3	2.1	1.0	0.0140	-60±1
COOH	5.29	TMG	10	5.3	2	1.0	0.0134	-
COOH	5.29	TMG	100	5.6	3.89	1.0	0.0265	-
COOH	5.29	TMG	500	6.3	13.9	1.1	0.1036	-
COOH	5.29	TMG	1000	6.3	23	1.2	0.1908	-64±1
COOH	5.29	TMG	2000	6.8	36.1	1.5	0.3665	-
COOH	5.29	TMG	3000	7.1	37.6	1.8	0.4601	-
COOH	5.29	TMG	4000	7.5	32.5	2.2	0.4729	-

Supplementary Table 12. pH and conductivity adjusted experiments in TMG-containing water.

Particle	$2R$ (µm)	Additive	c_b (mM)	pH	Cond. (µS cm^{-1})	η (cP)	Equiv. c_0 (mM)	ζ (mV)
SiO_2	4.82	TMG	1	6.3	1.82	1.0	0.012	-65±1
SiO_2	4.82	TMG	10	7	5.6	1.0	0.037	-
SiO_2	4.82	TMG	100	7.3	35	1.0	0.239	-71±1
SiO_2	4.82	TMG	500	7.5	122	1.1	0.909	-
SiO_2	4.82	TMG	1000	7.5	214	1.2	1.775	-57±2
SiO_2	4.82	TMG	2000	8.2	280	1.5	2.843	-

Supplementary Table 13. SiO_2 particle interactions in water containing TMAO.

Particle	2*R* (μm)	Additive	c_b (mM)	pH	Cond. (μS cm^{-1})	η (cP)	Equiv. c_0 (mM)	ζ (mV)
SiO_2	4.82	TMAO	0	5.8	1	1.0	0.005	-51±2
SiO_2	4.82	TMAO	0.01	5.6	1	1.0	0.006	-65±1
SiO_2	4.82	TMAO	0.1	5.7	1	1.0	0.007	-
SiO_2	4.82	TMAO	0.5	6.3	1.3	1.0	0.009	-
SiO_2	4.82	TMAO	1	6.3	1.82	1.0	0.012	-63±2
SiO_2	4.82	TMAO	10	7	5.6	1.0	0.037	-
SiO_2	4.82	TMAO	50	7.4	16.5	1.0	0.111	-
SiO_2	4.82	TMAO	100	7.4	34.5	1.0	0.235	-
SiO_2	4.82	TMAO	500	7.6	124	1.1	0.924	-
SiO_2	4.82	TMAO	1000	7.7	215	1.2	1.783	-41±1
SiO_2	4.82	TMAO	2000	8.2	286	1.5	2.903	-

Supplementary Table 14. SiO_2 particle interactions in water containing L-serine.

Particle	2*R* (μm)	Amino acid	c_b (mM)	pH	Cond. (μS cm^{-1})	η (cP)	Equiv. c_0 (mM)	ζ (mV)
SiO_2	4.82	L-serine	0.01	5.5	1.21	1.0	0.008	-65±0.6
SiO_2	4.82	L-serine	0.05	5.6	1.23	1.0	0.008	-
SiO_2	4.82	L-serine	0.1	5.7	1.20	1.0	0.008	-66±1.1
SiO_2	4.82	L-serine	0.5	5.7	1.18	1.0	0.008	-
SiO_2	4.82	L-serine	1	5.6	1.19	1.0	0.008	-61±0.8
SiO_2	4.82	L-serine	10	5.7	1.24	1.0	0.008	-77±1.6

Supplementary Table 15. SiO_2 particle interactions in water containing glycine.

Particle	2*R* (μm)	Amino acid	c_b (mM)	pH	Cond. (μS/cm)	η (cP)	Equiv. c_0 (mM)	ζ (mV)
SiO_2	4.82	glycine	0.01	5.7	1.11	1.0	0.007	-73±2.2
SiO_2	4.82	glycine	0.05	5.8	1.14	1.0	0.008	-
SiO_2	4.82	glycine	0.1	5.6	1.12	1.0	0.007	-61±1.3
SiO_2	4.82	glycine	0.5	5.8	1.17	1.0	0.008	-
SiO_2	4.82	glycine	1	5.6	1.17	1.0	0.008	-61±1.7
SiO_2	4.82	glycine	10	5.8	1.64	1.0	0.011	-82±2.4
SiO_2	4.82	glycine	100	5.9	9.25	1.0	0.063	-78±1.3
SiO_2	4.82	glycine	1000	6.3	70.8	1.2	0.587	-80±0.9

Supplementary Table 16. SiO_2 and COOH particle interactions in water containing L-tyrosine.

Particle	2*R* (μm)	Amino acid	c_b (mM)	pH	Cond. (μS cm^{-1})	η (cP)	Equiv. c_0 (mM)	ζ (mV)
SiO_2	4.82	L-tyrosine	0.01	5.5	1.17	1.0	0.008	-63±1.5
SiO_2	4.82	L-tyrosine	0.05	5.5	1.22	1.0	0.008	-
SiO_2	4.82	L-tyrosine	0.1	5.5	1.23	1.0	0.008	-62±1.8
SiO_2	4.82	L-tyrosine	0.5	5.5	1.38	1.0	0.009	-
SiO_2	4.82	L-tyrosine	1	5.6	1.50	1.0	0.010	-63±0.9
COOH	5.29	L-tyrosine	0.01	5.5	1.17	1.0	0.008	-67±0.4
COOH	5.29	L-tyrosine	0.05	5.5	1.22	1.0	0.008	-
COOH	5.29	L-tyrosine	0.1	5.5	1.23	1.0	0.008	-63±2.8
COOH	5.29	L-tyrosine	0.5	5.5	1.38	1.0	0.009	-
COOH	5.29	L-tyrosine	1	5.6	1.50	1.0	0.010	-62±1.3

Supplementary Table 17. SiO_2 particle interactions in water containing L-leucine.

Particle	$2R$ (μm)	Amino acid	c_b (mM)	pH	Cond. (μS cm^{-1})	η (cP)	Equiv. c_0 (mM)
SiO_2	4.82	L-leucine	0.01	5.6	1.22	1.0	0.008
SiO_2	4.82	L-leucine	0.05	5.6	1.19	1.0	0.008
SiO_2	4.82	L-leucine	0.1	5.6	1.16	1.0	0.008
SiO_2	4.82	L-leucine	0.5	5.7	1.21	1.0	0.008
SiO_2	4.82	L-leucine	1	5.6	1.16	1.0	0.008
SiO_2	4.82	L-leucine	10	5.6	1.05	1.0	0.007

Supplementary Table 18. SiO_2 particle interactions in water containing L-phenylalanine.

Particle	$2R$ (μm)	Amino acid	c_b (mM)	pH	Cond. (μS cm^{-1})	η (cP)	Equiv. c_0 (mM)
SiO_2	4.82	L-phenylalanine	0.01	5.7	1.18	1.0	0.008
SiO_2	4.82	L-phenylalanine	0.05	5.7	1.19	1.0	0.008
SiO_2	4.82	L-phenylalanine	0.1	5.8	1.21	1.0	0.008
SiO_2	4.82	L-phenylalanine	0.5	5.6	1.20	1.0	0.008
SiO_2	4.82	L-phenylalanine	1	5.5	1.18	1.0	0.008
SiO_2	4.82	L-phenylalanine	10	5.5	1.23	1.0	0.008

Supplementary Table 19. SiO_2 particle interactions in water containing L-tryptophan.

Particle	$2R$ (μm)	Amino acid	c_b (mM)	pH	Cond. (μS/cm)	η (cP)	Equiv. c_0 (mM)
SiO_2	4.82	L-tryptophan	0.01	5.7	1.13	1.0	0.008
SiO_2	4.82	L-tryptophan	0.05	5.7	1.07	1.0	0.007
SiO_2	4.82	L-tryptophan	0.1	5.6	1.24	1.0	0.008
SiO_2	4.82	L-tryptophan	0.5	5.7	1.12	1.0	0.007
SiO_2	4.82	L-tryptophan	1	5.6	1.15	1.0	0.008
SiO_2	4.82	L-tryptophan	10	5.6	1.5	1.0	0.010

Supplementary Table 20. SiO_2 particle interactions in water containing L-glutamine.

Particle	$2R$ (μm)	Amino acid	c_b (mM)	pH	Cond. (μS cm^{-1})	η (cP)	Equiv. c_0 (mM)
SiO_2	4.82	L-glutamine	0.01	5.7	1.19	1.0	0.008
SiO_2	4.82	L-glutamine	0.05	5.6	1.27	1.0	0.008
SiO_2	4.82	L-glutamine	0.1	5.7	1.31	1.0	0.009
SiO_2	4.82	L-glutamine	0.5	5.7	1.37	1.0	0.009
SiO_2	4.82	L-glutamine	1	5.8	1.57	1.0	0.010
SiO_2	4.82	L-glutamine	10	5.7	4.91	1.0	0.033

Supplementary Table 21. SiO_2 particle interactions in water containing L-proline.

Particle	$2R$ (μm)	Amino acid	c_b (mM)	pH	Cond. (μS cm^{-1})	η (cP)	Equiv. c_0 (mM)
SiO_2	4.82	L-proline	0.01	5.8	1.13	1.0	0.008
SiO_2	4.82	L-proline	0.05	5.6	1.18	1.0	0.008
SiO_2	4.82	L-proline	0.1	5.8	1.13	1.0	0.008
SiO_2	4.82	L-proline	0.5	5.8	1.20	1.0	0.008
SiO_2	4.82	L-proline	1	5.9	1.30	1.0	0.009
SiO_2	4.82	L-proline	10	5.9	3.58	1.0	0.024

Supplementary Table 22. SiO_2 and COOH particle interactions in water containing L-tyrosine.

Particle	2*R* (μm)	Amino acid	c_b (mM)	pH	Cond. (μS cm^{-1})	η (cP)	Equiv. c_0 (mM)	Added acid/base
SiO_2	4.82	L-tyrosine	0.01	4.9	5.53	1.0	0.037	0.01 mM HCl
SiO_2	4.82	L-tyrosine	0.05	4.9	5.35	1.0	0.036	
SiO_2	4.82	L-tyrosine	0.1	4.8	5.3	1.0	0.035	
SiO_2	4.82	L-tyrosine	0.5	4.9	5.43	1.0	0.036	
SiO_2	4.82	L-tyrosine	1	4.8	5.93	1.0	0.040	
COOH	5.29	L-tyrosine	0.01	4.9	5.53	1.0	0.037	
COOH	5.29	L-tyrosine	0.05	4.9	5.35	1.0	0.036	
COOH	5.29	L-tyrosine	0.1	4.8	5.3	1.0	0.035	
COOH	5.29	L-tyrosine	0.5	4.9	5.43	1.0	0.036	
COOH	5.29	L-tyrosine	1	4.8	5.93	1.0	0.040	

Supplementary Table 23. SiO_2 particle interactions in water containing Tween 20.

Particle	2*R* (μm)	Additive	c_b % (w/v)	pH	Cond. (μS cm^{-1})	η (cP)	Equiv. c_0 (mM)	ζ (mV)	adjustment
SiO_2	4.82	Tween 20	0.01	5.3	1.85	1.0	0.012	-54.5±0.8	-
SiO_2	4.82	Tween 20	0.1	5.3	2.12	1.0	0.014	-37.8±1.6	-
SiO_2	4.82	Tween 20	0.5	4.7	4.67	1.0	0.031	-42.6±0.7	-
SiO_2	4.82	Tween 20	1	4.6	6.64	1.0	0.044	-31.4±0.9	-
SiO_2	4.82	Tween 20	2	4.6	10.02	1.0	0.067	-18.0±0.3	-
SiO_2	4.82	Tween 20	5	4.5	21.46	1.0	0.143	-2.1±0.8	-
SiO_2	4.82	Tween 20	0	4.6	20.65	1.0	0.138	-19.8±2	Control*

* Conductivity and p*H* matched to 5% Tween 20 for comparison

Supplementary Table 24. SiO_2 particle interactions in water containing glycerol.

Particle	2*R* (μm)	Additive	c_b (mM)	pH	Cond. (μS cm^{-1})	η (cP)	Equiv. c_0 (mM)	ζ (mV)
SiO_2	4.82	glycerol	0.01	5.3	1.24	1.0	1.000	-57.2±0.3
SiO_2	4.82	glycerol	0.1	5.3	1.53	1.0	0.010	-63.2±2.3
SiO_2	4.82	glycerol	1	4.7	1.62	1.0	0.011	-55.4±2.3
SiO_2	4.82	glycerol	100	4.6	2.13	1.0	0.014	-31.4±2.3
SiO_2	4.82	glycerol	1000	4.5	6.50	1.1	0.048	-7.37±0.3
SiO_2	4.82	glycerol	2000	5.9	5.90	1.3	0.051	-5.0±0.4

Supplementary Table 25. $U(x)$ parameter values used in BD simulations to model experiments shown in Fig. 2.

Particle	2*R* (μm)	Solvent	w (k_BT)	A (k_BT)	B (k_BT)	κ_1 (μm^{-1})	κ_2 (μm^{-1})	A_H (k_BT)
SiO_2	4.82	H_2O	-6	3381.47	-3004.5	8.70	8.27	0.6
SiO_2	4.82	D_2O	-7	8656.562	-7395.153	17.09	16.24	0.6
SiO_2	4.82	DMSO	0	100	-	18.61	-	0.6
SiO_2	5.17	IPA	0	25	-	4.65	-	0.6
SiO_2	5.17	1-hexanol	0	300	-	4.41	-	0.6
SiO_2	5.17	EG*	0	1000000	-	19.74	-	0.6
NH_2	4.63	H_2O	0	1000	-	8.7	-	0.6
NH_2	4.63	D_2O	0	10000	-	17.31	-	0.6
NH_2	4.63	DMSO	-4	5.83E7	-3.12E7	18.61	17.68	0.6
NH_2	4.63	IPA	-5	5255.5	-4526.3	6.58	6.25	0.6
NH_2	4.63	1-hexanol	-6	2482.79	-2240.3	5.40	5.14	0.6
NH_2	4.63	EG	0	1000	-	19.74	-	0.6

* EG data not captured with the standard BD approach, see Supplementary Figure 9 for details.

Supplementary Table 26. $U(x)$ parameter values modelling experiments in Fig. 3.

Particle	$2R$ (μm)	Solvent	w (k_BT)	A (k_BT)	B (k_BT)	κ_1 (μm^{-1})	κ_2 (μm^{-1})	A_H (k_BT)
NH_2	4.63	methanol	-1	19808.2	-14730.5	8.393	7.973	0.6
NH_2	4.63	1-propanol	-3.5	2.7E6	-1.7E6	20.395	19.375	0.6
NH_2	4.63	1-pentanol	-7	4.8E6	-3.0E6	14.363	13.646	0.6
NH_2	4.63	1-heptanol	-8	1.2E6	-831574	19.431	18.459	0.6
SiO_2	5.17	methanol	0	100	-	8.393	-	0.6
SiO_2	5.17	1-propanol	0	100	-	20.395	-	0.6
SiO_2	5.17	1-pentanol	0	100000	-	14.363	-	0.6
SiO_2	5.17	1-heptanol	0	100	-	19.431	-	0.6

Supplementary Table 27. $U(x)$ parameter values modelling the experiments shown in Fig. 4.

Particle	$2R$ (μm)	Water% (v/v)	w (k_BT)	A (k_BT)	B (k_BT)	κ_1 (μm^{-1})	κ_2 (μm^{-1})	A_H (k_BT)
SiO_2	4.82	0	-0.5	878.543	-737.458	6.579	6.245	0.6
SiO_2	4.82	1	-1	1125.828	-966.301	6.241	5.929	0.6
SiO_2	4.82	5	-3.5	1026.552	-942.387	5.504	5.229	0.6
SiO_2	4.82	10	-4	423.572	-409.165	6.978	6.629	0.6
SiO_2	4.82	30	-4.5	577.178	-552.229	8.057	7.655	0.6
SiO_2	4.82	50	-4.5	577.178	-552.229	8.057	7.655	0.6
SiO_2	4.82	100	-6	857.616	-816.112	8.515	8.089	0.6
NH_2	4.63	0	-6	5332.595	-4631.410	6.579	6.250	0.6
NH_2	4.63	10	-3	4376.839	-3708.282	6.978	6.629	0.6
NH_2	4.63	30	0	25	-	7.644	-	0.6
NH_2	4.63	50	0	100	-	12.04	-	0.6
NH_2	4.63	100	0	300	-	8.515	-	0.6
COOH	5.29	0	0	25	-	6.579	-	0.6
COOH	5.29	10	0	25	-	6.95	-	0.6
COOH	5.29	30	-0.5	169.236	-154.252	8	7.6	0.0
COOH	5.29	50	-3.5	564.658	-534.089	6.90	6.555	0.6
COOH	5.29	100	-5	7436.824	-6294.782	8.515	8.089	0.6

Supplementary Table 28. $U(x)$ parameter values modelling experiments shown in Fig. 6.

Particle	$2R$ (μm)	Additive	c_b (mM)	w (k_BT)	A (k_BT)	B (k_BT)	κ_1 (μm^{-1})	κ_2 (μm^{-1})	A_H (k_BT)
SiO_2	4.82	L-serine	0.01	-4.5	1277.001	-1174.238	9.304	8.839	0.6
SiO_2	4.82	L-serine	0.05	-4	1308.764	-1194.910	9.304	8.839	0.6
SiO_2	4.82	L-serine	0.1	-4	735.770	-691.389	9.304	8.839	0.6
SiO_2	4.82	L-serine	0.5	-1.5	12058.534	-9380.984	9.304	8.839	0.6
SiO_2	4.82	L-serine	1	0	50	-	9.304	-	0.6
SiO_2	4.82	L-tyrosine	0.01	-4	1386.478	-1262.219	9.304	8.839	0.6
SiO_2	4.82	L-tyrosine	0.05	-3	923.970	-846.146	9.304	8.839	0.6
SiO_2	4.82	L-tyrosine	0.1	-2	1569.120	-1371.320	9.304	8.839	0.6
SiO_2	4.82	L-tyrosine	1	0	100	-	10.402	-	

Supplementary Table 29. $U(x)$ parameter values modelling experiments shown in Fig. 7.

Particle	$2R$ (μm)	Additive	c_b (mM)	w (k_BT)	A (k_BT)	B (k_BT)	κ_1 (μm^{-1})	κ_2 (μm^{-1})	A_H (k_BT)
SiO_2	4.82	TMG	0.01	-5.5	684.884	-656.249	7.355	6.988	0.6
SiO_2	4.82	TMG	1	-5.5	1800.91	-1644.18	12.308	11.693	0.6
SiO_2	4.82	TMG	100	-5.5	3732.97	-3286.13	17.093	16.238	0.6
SiO_2	4.82	TMG	1000	-6.5	58193.6	-45028.9	45.935	43.638	0.6
SiO_2	4.82	TMG	2000	-6	453276	-315258	62.931	59.785	0.6
SiO_2	4.82	TMG	3000	-4.5	9.7E9	-4.0E9	67.575	64.196	0.6
SiO_2	4.82	TMG	4000	0	100	0	66.931	63.584	0.6
SiO_2	4.82	TMAO	0.01	-5.5	721.537	-689.569	8.058	7.654	0.6
SiO_2	4.82	TMAO	1	-5.5	1958.63	-1780.68	11.395	10.825	0.6
SiO_2	4.82	TMAO	10	-6	3360.13	-2986.48	20.009	19.009	0.6
SiO_2	4.82	TMAO	50	-4.5	434091	-298247	34.657	32.924	0.6
SiO_2	4.82	TMAO	100	0	100	0	50.427	47.905	0.6
SiO_2	4.82	TMAO	1000	0	100	0	138.9	131.955	0.6
SiO_2	4.82	TMG*	1	-5.5	1448.13	-1336.6	11.395	10.825	0.6
SiO_2	4.82	TMG*	10	-5.5	9276.36	-7802.63	20.009	19.009	0.6
SiO_2	4.82	TMG*	100	-6	37746.3	-29727.1	50.854	48.311	0.6
SiO_2	4.82	TMG*	1000	-3	4.4E12	-1.3E12	138.59	131.66	0.6
SiO_2	4.82	TMG*	2000	0	100	0	175.39	166.62	0.6

Supplementary Table 30. $U(x)$ parameter values modelling experiments shown in Fig. 8

Particle	$2R$ (μm)	Additive	c_b (% or mM)	w (k_BT)	A (k_BT)	B (k_BT)	κ_1 (μm^{-1})	κ_2 (μm^{-1})	A_H (k_BT)
SiO_2	4.82	Tween 20	0.01%	-7	44336.2	-34905.1	11.395	10.825	0.6
SiO_2	4.82	Tween 20	0.1%	-5	30265.2	-23881.3	12.308	11.693	0.6
SiO_2	4.82	Tween 20	0.5%	-5	165586	-120015	18.315	17.399	0.6
SiO_2	4.82	Tween 20	1%	-4	1.94E6	-1.23E6	21.820	20.729	0.6
SiO_2	4.82	Tween 20	2%	-3	6.40E6	-3.76E6	26.926	25.579	0.6
SiO_2	4.82	Tween 20	5%	-1.5	1.49E8	-7.24E7	39.336	37.370	0.6
SiO_2	4.82	control (water)*	0	-6	755482	-512194	38.643	36.710	0.6
SiO_2	4.82	glycerol	0.01	-4.5	7656.6	-6437.35	10.402	9.8821	0.6
SiO_2	4.82	glycerol	0.1	-4.5	9545.7	-7937.66	10.402	9.8821	0.6
SiO_2	4.82	glycerol	1	-4.5	32609.2	-25500.5	10.402	9.8821	0.6
SiO_2	4.82	glycerol	100	-4.5	39283.1	-30434.8	10.402	9.8821	0.6
SiO_2	4.82	glycerol	1000	-4.5	1.03E6	-676592	23.260	22.097	0.6
SiO_2	4.82	glycerol	2000	-2.5	3.61E6	-2164450	31.207	28.086	0.6

* conductivity and p*H* matched to 5% Tween 20 for comparison.

Reference

1 Kubincová, A., Hünenberger, P. H. & Krishnan, M. Interfacial solvation can explain attraction between like-charged objects in aqueous solution. *J. Chem. Phys.* **152**, 104713 (2020).

2 Behjatian, A., Walker-Gibbons, R., Schekochihin, A. A. & Krishnan, M. Nonmonotonic Pair Potentials in the Interaction of Like-Charged Objects in Solution. *Langmuir* **38**, 786−800 (2022).

3 Wang, S., Walker-Gibbons, R., Watkins, B., Flynn, M. & Krishnan, M. A charge-dependent long-ranged force drives tailored assembly of matter in solution. *Nat. Nanotechnol.* **19**, 485–493 (2024).

4 Ninham, B. W. & Parsegian, V. A. Electrostatic potential between surfaces bearing ionizable groups in ionic equilibrium with physiologic saline solution. *J. Theor. Biol.* **31**, 405-428 (1971).

5 Walker-Gibbons, R., Kubincová, A., Hünenberger, P. H. & Krishnan, M. The Role of Surface Chemistry in the Orientational Behavior of Water at an Interface. *J. Phys. Chem. B* **126**, 4697-4710 (2022).

6 Kathmann, S. M., Kuo, I. F. W., Mundy, C. J. & Schenter, G. K. Understanding the Surface Potential of Water. *J. Phys. Chem. B* **115**, 4369-4377 (2011).

7 Remsing, R. C., Baer, M. D., Schenter, G. K., Mundy, C. J. & Weeks, J. D. The Role of Broken Symmetry in Solvation of a Spherical Cavity in Classical and Quantum Water Models. *J. Phys. Chem. Lett.* **5**, 2767-2774 (2014).

8 Hummer, G., Pratt, L. R., García, A. E., Berne, B. J. & Rick, S. W. Electrostatic Potentials and Free Energies of Solvation of Polar and Charged Molecules. *J. Phys. Chem. B* **101**, 3017-3020 (1997).

9 Cox, S. J., Thorpe, D. G., Shaffer, P. R. & Geissler, P. L. Assessing long-range contributions to the charge asymmetry of ion adsorption at the air–water interface. *Chem. Sci.* **11**, 11791-11800 (2020).

10 Grunwald, E. & Berkowitz, B. J. The Measurement and Correlation of Acid Dissociation Constants for Carboxylic Acids in the System Ethanol-Water. Activity Coefficients and Empirical Activity Functions. *J. Am. Chem. Soc.* **73**, 4939-4944 (1951).

11 Belskii, V. E., Kudryavtseva, L. A., Derstuganova, K. A., Teitelbaum, A. B. & Ivanov, B. E. Basicity of Aliphatic-Amines in Ethanol. *Bulletin of the Academy of Sciences of the USSR Division of Chemical Science* **30**, 736-738 (1981).

12 Emami, F. S. *et al.* Force Field and a Surface Model Database for Silica to Simulate Interfacial Properties in Atomic Resolution. *Chem. Mater.* **26**, 2647-2658 (2014).

13 Ide, M. *et al.* Quantification of silanol sites for the most common mesoporous ordered silicas and organosilicas: total versus accessible silanols. *Phys. Chem. Chem. Phys.* **15**, 642-650 (2013).

14 Darlington, A. M. & Gibbs-Davis, J. M. Bimodal or Trimodal? The Influence of Starting pH on Site Identity and Distribution at the Low Salt Aqueous/Silica Interface. *J. Phys. Chem. C* **119**, 16560-16567 (2015).

15 Fan, H.-F., Li, F., Zare, R. N. & Lin, K.-C. Characterization of Two Types of Silanol Groups on Fused-Silica Surfaces Using Evanescent-Wave Cavity Ring-Down Spectroscopy. *Anal. Chem.* **79**, 3654-3661 (2007).

16 Dong, Y., Pappu, S. V. & Xu, Z. Detection of Local Density Distribution of Isolated Silanol Groups on Planar Silica Surfaces Using Nonlinear Optical Molecular Probes. *Anal. Chem.* **70**, 4730-4735 (1998).

17 Lagström, T., Gmür, T. A., Quaroni, L., Goel, A. & Brown, M. A. Surface Vibrational Structure of Colloidal Silica and Its Direct Correlation with Surface Charge Density. *Langmuir* **31**, 3621-3626 (2015).

18 Zhuravlev, L. T. The surface chemistry of amorphous silica. Zhuravlev model. *Colloids Surf., A* **173**, 1-38 (2000).

19 Gaur, A. & Balasubramanian, S. Liquid ethylene glycol: prediction of physical properties, conformer population and interfacial enrichment with a refined non-polarizable force field. *Phys. Chem. Chem. Phys.* **24**, 10985-10992 (2022).

20 Di Mino, C. *et al.* Weak Interactions in Dimethyl Sulfoxide (DMSO)–Tertiary Amide Solutions: The Versatility of DMSO as a Solvent. *J. Phys. Chem. B* **127**, 1357-1366 (2023).

21 Ong, S., Zhao, X. & Eisenthal, K. B. Polarization of water molecules at a charged interface: second harmonic studies of the silica/water interface. *Chem. Phys. Lett.* **191**, 327-335 (1992).

22 Rimola, A., Costa, D., Sodupe, M., Lambert, J.-F. & Ugliengo, P. Silica Surface Features and Their Role in the Adsorption of Biomolecules: Computational Modeling and Experiments. *Chem. Rev.* **113**, 4216-4313 (2013).

23 Bag, S. *et al.* Buffer Influence on the Amino Acid Silica Interaction. *Chemphyschem* **21**, 2347-2356 (2020).

24 Gao, Q. *et al.* Amino Acid Adsorption on Mesoporous Materials: Influence of Types of Amino Acids, Modification of Mesoporous Materials, and Solution Conditions. *J. Phys. Chem. B* **112**, 2261-2267 (2008).

25 Xie, M. & Brüschweiler, R. Degree of N-Methylation of Nucleosides and Metabolites Controls Binding Affinity to Pristine Silica Surfaces. *J. Phys. Chem. Lett.* **11**, 10401-10407 (2020).

26 Mocellin, A., Gomes, A. H. d. A., Araújo, O. C., de Brito, A. N. & Björneholm, O. Surface Propensity of Atmospherically Relevant Amino Acids Studied by XPS. *J. Phys. Chem. B* **121**, 4220-4225 (2017).

27 Herboth, R., Gopakumar, G., Caleman, C. & Wohlert, M. Charge State Dependence of Amino Acid Propensity at Water Surface: Mechanisms Elucidated by Molecular Dynamics Simulations. *J. Phys. Chem. A* **125**, 4705-4714 (2021).

28 Abadian, H. *et al.* Leucine on Silica: A Combined Experimental and Modeling Study of a System Relevant for Origins of Life, and the Role of Water Coadsorption. *Langmuir* **38**, 8038-8053 (2022).

29 Zou, Q., Bennion, B. J., Daggett, V. & Murphy, K. P. The Molecular Mechanism of Stabilization of Proteins by TMAO and Its Ability to Counteract the Effects of Urea. *J. Am. Chem. Soc.* **124**, 1192-1202 (2002).

30 Stasiulewicz, M., Panuszko, A., Bruździak, P. & Stangret, J. Mechanism of Osmolyte Stabilization–Destabilization of Proteins: Experimental Evidence. *J. Phys. Chem. B* **126**, 2990-2999 (2022).

31 Levin, Y. Electrostatic correlations: from plasma to biology. *Rep. Prog. Phys.* **65**, 1577-1632 (2002).

32 Diehl, A. & Levin, Y. Colloidal charge reversal: Dependence on the ionic size and the electrolyte concentration. *J. Chem. Phys.* **129**, 124506 (2008).

33 Winter, E. M. & Groves, J. T. Surface binding affinity measurements from order transitions of lipid membrane-coated colloidal particles. *Anal. Chem.* **78**, 174-180 (2006).

Statement of Authorship for joint/multi-authored papers for PGR thesis

To appear at the end of each thesis chapter submitted as an article/paper

The statement shall describe the candidate's and co-authors' independent research contributions in the thesis publications. For each publication there should exist a complete statement that is to be filled out and signed by the candidate and supervisor **(only required where there isn't already a statement of contribution within the paper itself).**

Title of Paper	Chemical control of self-assembly by the electrosolvation force
Publication Status	□Published □ Accepted for Publication XSubmitted for Publication □Unpublished and unsubmitted work written in a manuscript style
Publication Details	Wang, S., Walker-Gibbons, R., Watkins, B., Lin, B. & Krishnan, M. Chemical control of self-assembly by the electrosolvation force.

Student Confirmation

Student Name:	Sida Wang		
Contribution to the Paper	S.W. performed experiments, participated in simulation, data analysis and manuscript preparation.		
Signature	Sida Wang	Date	20/09/2024

Supervisor Confirmation

By signing the Statement of Authorship, you are certifying that the candidate made a substantial contribution to the publication, and that the description described above is accurate.

Supervisor name and title: Professor Madhavi Krishnan			
Supervisor comments			
Signature		Date	20/09/2024

This completed form should be included in the thesis, at the end of the relevant chapter.

4

Strongly attractive pair potentials between like-charged particles in fluids

In the previous chapters, we have demonstrated the generality of the like-charge attraction phenomenon by examining various solvents, electrolytes and particle surface chemistries. While gaining insights into the origin of the proposed electrosolvation force, we established methods for controlling and fine-tuning this long-ranged attraction through cluster formation and disruption. Previous theoretical work has suggested the possibility that pair interactions may be influenced by the presence of another object or many-body effects. Although there have been some prior reports in the literature on attractive pairwise interactions measured in bulk solution, the question of whether like-charge attraction exists between an isolated pair of particles is worth exploring rigorously [74-77]. Previous attempts to measure pair interaction potentials between two isolated particles using techniques such as optical tweezers have frequently faced challenges of experimental artifacts [34,35,37,39,78]. To address this issue and gain a deeper understanding of the electrosolvation force, we shift our experimental focus from clusters to isolated pairs of particles for further examination.

This chapter presents an unpublished manuscript titled "*Strongly attractive pair potentials between like-charged particles in fluids*". In this study, we provide direct evidence of a strong and long-ranged attractive pair potentials between like-charged particles, for both negatively charged particles in aqueous solution and positively charged particles in alcohol. Through single particle tracking of isolated pairs, we obtained the general form of the pair potential along with its quantitative features, such as the depth of the minimum in the pair potential and the screening length. Remarkably, our measurements indicate a rather long-ranged attraction, with the measured screening length being an order of magnitude larger than the nominal Debye length. We also found evidence for a dependence of this screening length on the size of the interacting particles. Our study suggests a significant departure between experimental observations and the traditional view of the solvent as a continuum medium. A more comprehensive description of the fluid medium that accounts for 'non-local' effect is currently under development.

manuscript:

Strongly attractive pair potentials between like-charged particles in fluids

Strongly attractive pair potentials between like-charged particles in fluids

Sida Wang,[1] Rowan Walker-Gibbons,[1] and Madhavi Krishnan[1,2,*]

[1] *Physical and Theoretical Chemistry Laboratory, Department of Chemistry, University of Oxford, South Parks Road, Oxford OX1 3QZ, UK.*

[2] *The Kavli Institute for Nanoscience Discovery, Sherrington Road, Oxford OX1 3QU, UK.*

Direct measurement of the pair interaction potential between electrically like-charged particles in aqueous and apolar media reveals a strong and long-ranged attractive force. The rate of decay of the attraction is about an order of magnitude larger than the Debye screening length expected to characterize electrostatic interactions in dilute aqueous electrolytes. The observations point to significant departures from current thinking and the need for a model of interparticle interactions that accounts for effects due to the molecular nature of the solvent, namely its interfacial behaviour and polarization correlations.

From atomic to astrophysical scales, the emergence of structure depends on the distance-dependent interaction between the fundamental building blocks that constitute a system. The pair interaction potential describes the interaction free energy of two isolated entities as a function of their separation, and is therefore central to understanding and predicting collective behaviour. Electrically charged objects interacting in fluids play a crucial role in a range of natural contexts. Textbook theories anticipate a monotonically decaying screened Coulombic potential, or the Yukawa potential, $U(r) \propto q^2 \exp(-\kappa r)/r$ for a pair of particles of charge q separated by a centre-to-centre distance r, where $\kappa = \sqrt{2e^2 N_A c/\varepsilon\varepsilon_0 k_B T}$ is the inverse Debye screening length. Here ε is the dielectric constant of a medium containing monovalent ions at a molarity c, and e, N_A, ε_0, k_B, and T denote the elementary charge, Avogadro's number, permittivity of free space, Boltzmann's constant and absolute temperature, respectively [1, 2].

Whilst experiments have indeed confirmed this general expectation for charged macroscopic surfaces, reports on particles and macromolecules in solution have pointed to major qualitative departures from theory for many decades [3–10]. Several studies have suggested the possibility of a long-ranged attraction between electrically like-charged particles, and evidence continues to accumulate notwithstanding indications that some early measurements may have been confounded by artifacts [11–15]. Recent experiments on lipid-bilayer coated particles have revealed a further striking divergence from the canon: negatively charged particles in solution displayed strong long-range attraction, forming stable, slowly reorganising, crystalline structures in water, while positively charged particles repelled as expected [10, 13, 14]. Such behavior cannot be explained by the Poisson-Boltzmann continuum-dielectric theory, and therefore the microscopic origins of the observed attraction, and that of the arguably even more intriguing breaking of "charge-inversion symmetry" in the sign of the interparticle force, remained unexplained until very recently.

We recently suggested that the observed strong and long-ranged attraction between negatively charged par-

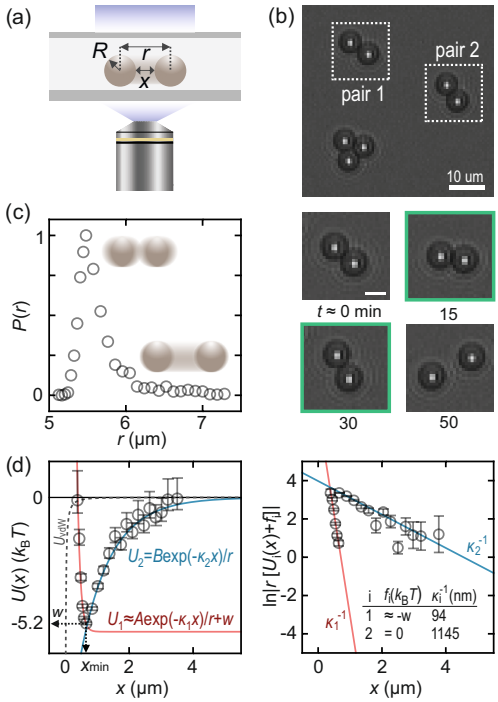


FIG. 1. Experimental setup and procedure for pair-potential measurements. (a) Schematic representation of two interacting microspheres of radius R, at an interparticle distance r, and intersurface separation $x = r - 2R$ observed using bright-field microscopy. (b) Above: Snapshot of well separated pairs of negatively charged SiO_2 particles of radius $R = 2.4\mu$m in DI water ($c \approx 10^{-5}$ M), engaged "bound-states" (white dashed boxes); below: Time-series of pair #1 displaying bound (green outline) and "free" states. Scale bar: 5 μm. (c) Rescaled radial probability density function, $P(r)$, measured for a typical pair of interacting particles. (d) Left: The corresponding pair potential determined using $U(x) = -k_B T \ln P(x)$, displaying the depth, w, and location, x_{min}, of the minimum, and fitted with two-piecewise single exponentials, U_1 and U_2, indicating the repulsive (red) and attractive (blue) regions of the interaction, respectively. van der Waals (U_{vdW}) contribution to the total pair interaction (dashed grey line) calculated as described in Refs. [15, 16]. Right: Log-linear plot of measured data and corresponding fit-functions U_1 and U_2 in (d).

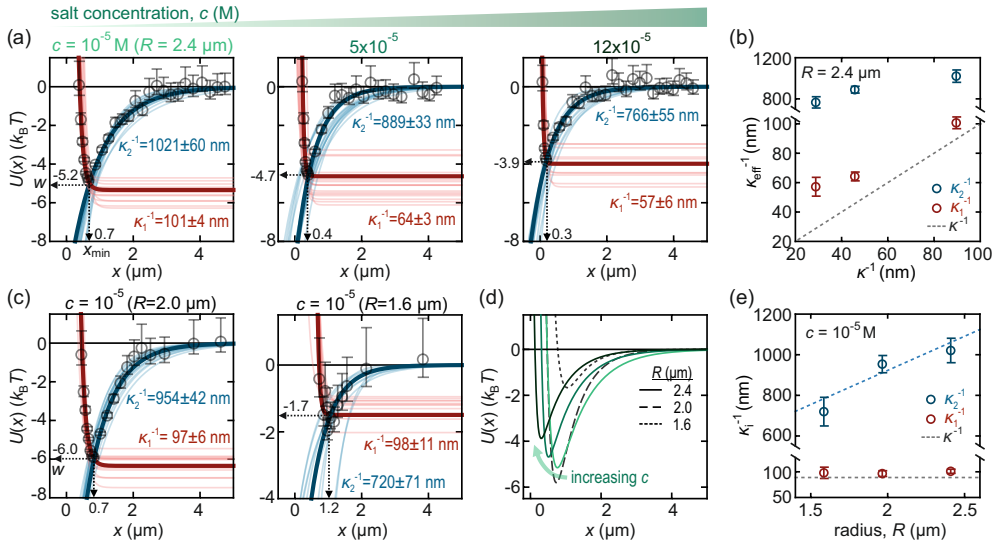


FIG. 2. Salt concentration and particle size-dependence of the pair interaction potential. (a) Measured pair potentials $U(x)$ for ca. 15 pairs of $R = 2.4$ μm silica particles (thin red and blue lines) in aqueous solution for salt concentration c ranging from 10^{-5} M to 1.2×10^{-4} M, showing representative measurements on individual pairs (symbols) and the corredsponding piecewise fits (thick lines). Averaged values of κ_1^{-1} and κ_2^{-1} fitted are noted. (b) Plot of averaged measured screening lengths κ_1^{-1} and κ_2^{-1} compared with the Debye screening length κ^{-1} (dashed grey line). (c) Interaction potentials measured on ca. 12 pairs of $R = 2.0$ μm (left) and 1.6 μm (right) silica particles in water ($c \approx 10^{-5}$ M). Smaller particles ($R = 1.6$ μm) display a significant decrease in $|w|$ and κ_2^{-1} under the same experimental conditions. (d) Bi-exponential fits to averaged pair potential data from measurements in (a) and (c) display systematic shifts of both $x_{\min}$ and well depth w to lower values, with increasing salt concentration. (e) The two measured screening lengths respond differently to changes in particle size: $\kappa_1^{-1} \approx 100$ nm remains relatively constant, similar to the nominal Debye length $\kappa^{-1} \approx 90$ nm (grey dashed line). In contrast, κ_2^{-1} is always significantly larger than κ^{-1} and decreases with decreasing particle radius. Zeta potentials of ≈ -50mV were measured for all particle sizes under the stated solution conditions.

ticles in water – as well as the cognate repulsion between positively charged particles – could be explained by invoking "asymmetric solvation" at an interface between an object and the fluid medium [15]. According to our model, broken orientational symmetry of solvent molecules at an interface gives rise to an excess interfacial free energy that is absent in conventional continuum models of the electrostatic interaction [15, 17, 18]. Refs. [17] and [18] suggested that this "excess" interfacial free energy may be expected to follow the relation $\Delta F_{\rm int} = B \exp(-\kappa_2 r)/r$, and to contribute in addition to the traditional electrostatic free energy of repulsion given by $\Delta F_{\rm el} = A \exp(-\kappa_1 r)/r$. Whilst $A > 0$, in line with the intuitive expectation, $B \propto z\mu_{\rm av} R^2$ can be either positive or negative depending on the sign of the particle charge, z, and of the interfacial polarization or the solvent dipole moment density, $\mu_{\rm av}$, at the interface. In fact a recent experimental study has further tested this idea and shown, e.g., that neutral molecules that are known to alter the structure of interfacial water, can even at low concentrations, strongly perturb the attraction attributed to what we henceforth refer to as an "electrosolvation" force [19].

Concerning the precise form of the pair-potential in the electrosolvation attraction, our model suggested that the relevant inverse screening lengths follow the relation $\kappa_2 < \kappa_1 \approx \kappa$, due to which the interfacial contribution to the interaction is longer ranged than the traditional Coulombic repulsion. Thus the overall sign and magnitude of B can result in a pair-potential for like-charged particles that displays both an attraction and a minimum at long range. We note that the van der Waals contribution to the interaction is small ($\sim 0.5 k_{\rm B}T$) over the separation range of interest, and is therefore ignored in this work [15, 16] (Fig. 1d). Importantly, the magnitude of, and factors contributing to, the two suggested screening lengths κ_1 and κ_2 – which are crucial to gaining more complete insight into the underlying physics – have not been experimentally examined to date.

Experimental work on the electrosolvation interaction has thus far focussed on many-body cluster-formation, providing inferences on the approximate form of the pair-potential but no rigorous direct measurements thereof [15, 19]. Although it has been suggested that a bulk phase instability may result in colloidal condensation in mutually repulsive particles, such behaviour does not explain observations where the colloid-colloid pair distribution function displays a peak signifying an attractive pair-potential characteristic of our previous work [20]. Prior experimental and theoretical studies have nonetheless shown that the interaction between a pair of repulsive particles can be modified by the presence of other particles or surfaces in the vicinity [21, 22]. While the over-

all repulsion between like-charged particles may clearly weaken on account of the presence of a third body, evidence for outright attraction driven by many-body effects, in a system of particles that are mutually Coulombically repulsive at pairwise level, remains scanty [22]. Indeed, PB theory does not admit attraction between two particles due to the proximity of a third body – be it an additional particle or a surface [22–24]. Nonetheless, many-body interactions can give rise to effective potentials that depend on the state of the system and are therefore not the same as the "true" pair interaction potential. Therefore, given the evidence of the electrosolvation attraction derived from cluster-formation experiments [10, 13–15, 19], a direct measurement of the pair potential would not only address the question of whether an attraction indeed exists between two isolated particles, but also provide access to the qualitative and quantitative features of the pair-potential. This study in fact shows that the screening length that captures the electrosolvation attraction can in fact be significantly larger (by nearly a factor 10) than the nominal Debye length even at very low salt concentrations $c \sim 10^{-5}$ M, contrary to experimental or theoretical suggestions to date.

We set out to measure pair interaction potentials between isolated pairs of negatively charged particles under the same solution conditions that result in ordered multi-particle clusters when particles are present at higher number density [15] (Fig. 1) (see End Matter). The measured pair-potentials revealed deep and long-ranged minima at an intersurface separation $x_{\min}$, and were fit to piecewise screened Coulombic functions such that $U_1(x) \approx A\exp(-\kappa_1 x)/r + w$ for $x \leq x_{\min}$, and $U_2(x) = B\exp(-\kappa_2 x)/r$ otherwise, as shown in Fig. 1d (see End matter).

Fig. 2a displays pair potentials inferred from measurements of the radial probability density function $P(r)$ on particles of radius $R = 2.4\mu$m. We performed measurements at three different ionic strength values which differ in the amount of NaCl added to deionized (DI) water characterized by a background ionic strength corresponding to $c \approx 10^{-5}$ M. In addition to the piecewise fits to the measured data of the form of $U_1(x)$ and $U_2(x)$, we also fit the measured data to a bi-exponential function $U(x) = A\exp(-\kappa_1' x) + B\exp(-\kappa_2' x)$ as proposed in Refs. [15, 18] (Fig. 2d). A bi-exponential function not only provides a satisfactory description of the data but also supplies Brownian Dynamics (BD) simulations with a convenient analytical input for computational validation of the experimental observations as discussed later.

Pair potentials measured as a function of increasing ionic strength were on first glance qualitatively similar to inferences from cluster formation experiments, displaying a gradual shift of the location of the minimum from $x_{\min} \approx 0.8$ to 0.3 μm accompanied by a reduction in depth of the minimum from $|w| \approx 5.2$ to 3.9 $k_{\mathrm{B}}T$ (Fig. 2d) [15]. Importantly we found that both fitted screening lengths κ_1^{-1} and κ_2^{-1} were larger than the nominal Debye length, $\kappa^{-1} = 30 - 90$ nm (Fig. 2b). This is particularly surprising given the fact that the conditions of the experiment – characterised by low concentrations of monovalent salt in a medium of high dielectric constant – are formally considered to lie decidedly within the remit of PB theory according to which the force between like-charged particles is always repulsive and spatially screened at a rate given by the Debye length. First, we note that the screening length describing the repulsion, $\kappa_1^{-1} \approx 60 - 100$ nm, is larger than, but nonetheless of the same order of magnitude as the estimated Debye length, κ^{-1}, which lies in the range of $30 - 90$ nm, depending on the salt concentration in the experiment. But surprisingly we found $\kappa_2^{-1} \approx 0.7 - 1\mu$m to be around an order of magnitude larger than κ^{-1}, i.e., $\kappa_2 \ll \kappa_1$ in contrast to $\kappa_2 < \kappa_1$ suggested by [17]. Furthermore κ_2 was only weakly responsive to an order of magnitude change in ionic strength (Fig. 2b). In fact, rather than reflecting the Debye length, the screening length κ_2^{-1} may be seen as comparable to the particle radius, R, which is one other obvious length scale in the system.

We therefore examined the role of particle size in the problem. The expected area-dependence (R^2) of the attractive interfacial free energy contribution, ΔF_{int}, and the measurement range of $|w| \approx 2 - 6k_{\mathrm{B}}T$ offered by the equilibrium approach, would together suggest that the technique can reliably probe only fairly modest changes in R of about a factor of 1.5 [13, 17, 18]. We therefore performed measurements on $R = 1.6$ and 2.0 μm silica particles of the same chemistry as the larger $R = 2.4$ μm particles in DI water (Fig. 2c). Measurements on approximately 15 pairs of particles in each case displayed $\kappa_1^{-1} \approx 100$ nm $\simeq \kappa^{-1}$, similar to the values measured for the larger particles. However, we observed an approximate factor of 1.5 reduction in the value of κ_2^{-1} to 720 ± 71 nm for the smallest particles compared to 1021 ± 60 nm in the largest case (Fig. 2e). Taken together these data appear to suggest a role for a particle property – related directly or indirectly to particle size – in determining the range of decay of the attractive contribution.

Measurements of interaction potentials can be fraught with possible sources of errors arising from motion "blur", incorrect temporal sampling, poor precision of particle localization, insufficient sampling statistics, etc., all of which can contribute to inaccurate estimates of the underlying parameters [25–27]. Given our goal of accurately measuring the parameters characaterizing the underlying pair potentials, namely $x_{\min}$ and w, and the screening lengths κ_1^{-1} and κ_2^{-1} in particular, we vetted our measurements using BD simulations (set-up details described previously [15]). Simulations were performed on pairs of particles interacting via a variety of input potentials, including the measured pair potentials, using the same imaging and sampling conditions as in the experiments. We treated the simulated spatial-position traces

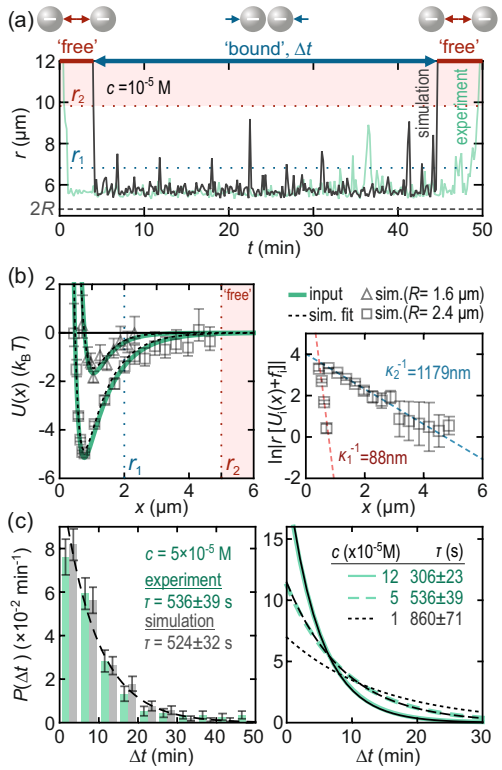


FIG. 3. Validation of measured pair-potentials and bound-state lifetimes using BD simulations. (a) Time trace of measured interparticle separation in a typical experiment (green). Representative time-trace (grey) from a BD simulation performed using the measured $U(x)$ as input. Schematics depict "bound" and "free" states for the simulated pair, defined by cut-off separations $r_1 \leq 6.8$ μm ("bound" state) and $r_2 \geq 9.8$ μm ("free" state). (b) Left: Overlay of average experimentally measured biexponential $U(x)$ functions (green lines) with data from BD simulations (symbols) using as inputs measured $U(x)$ functions for two particle sizes $R = 1.6$ μm (triangles) and 2.4 μm (squares). Bi-exponential fits (black dotted lines) of the simulated data agree well with measured potentials. Right: Log-linear plot of simulated data and piecewise fits for the $R = 2.4$ μm case shown on the left. (c) Left: Probability density data, $P(\Delta t)$, of bound state duration, Δt, measured for a pair of $R = 2.4$ μm particles, are fit to a function $P(\Delta t) \propto \exp(-t/\tau)/\tau$ (black dashed line) to extract an average bound-state lifetime, τ for ≈ 200 bound events (green bars), displayed alongside corresponding simulated data (grey bars). Right: $P(\Delta t)$ fit functions for experiments (green curves) agree well with simulations (black curves). Inset presents experimentally inferred τ for the higher salt concentrations, and a simulated value at the lowest salt concentration. The average bound-state lifetime τ increases as salt concentration decreases.

in a manner identical to measurements and fit the data with equations for U_1 and U_2. In general, we found that the mean fitted values of κ_1^{-1}, κ_2^{-1}, $x_{\min}$, and w inferred from simulations recapitulated within $\approx 10\%$ the ground-truth values specifying the input potentials – spanning a range of $2 - 14\%$ in inaccuracy – similar to the uncertainties on the experimental fit parameters. This confirms that the experimental measurements may indeed be expected to capture the screening lengths describing the underlying pair potentials with reasonable accuracy.

We then performed an independent experimental test of the depths w of the inferred pair-potential minima by measuring the average lifetime of bound states. Here we examined time-traces of interparticle separation and defined distance threshold values r_1 and r_2 such that particles were considered to be engaged in a bound-state for average separations $r < r_1$, and non-interacting for $r > r_2$ (Fig. 3a). We also examined time-dependent interparticle separation data from BD simulations relying on the experimentally measured potentials as inputs. Analysing both the experimental and the simulated data in the same fashion, we constructed residence time histograms $P(\Delta t)$ of the bound state and fit these to the form $P(\Delta t) \propto \exp(-t/\tau)$ where τ is the average lifetime over all pairs of particles considered. For a given average measured pair potential, we obtained excellent agreement between the measured and simulated τ values (Fig. 3c), yielding further independent confirmation of the veracity of the measurements.

The electrosolvation attraction has been demonstrated to occur in a range of solvents, notably primary alcohols [15, 19]. We examined pair-interactions of positively charged aminated silica particles in 1-heptanol, which is about two orders of magnitude less volatile shorter chain length alcohols permitting long-duration measurements on stable bound states (Fig. 4)[15]. However, the attractive interaction between aminated particles in heptanol was so strong that bound pairs once formed rarely separated over hours of observation (Fig. 4a). The highly stable bound states observed implied inferred well depths of $|w| \gtrsim 10$ $k_{\mathrm{B}}T$ which precluded both accurate spatial mapping of the underlying pair-potential as well as lifetime measurements discussed above. The data did, however, permit a reconstruction of the potential around the region of the minimum (Fig. 4b). We found an average value of $x_{\min} \approx 0.7$ μm, which is comparable with the DI water measurement on negatively charged silica particles. Since measurements of electrical conductivity suggest $\kappa^{-1} \approx 70$ nm for heptanol, this observation is compatible with previous experiments and the theoretical model, which indicate $x_{\min} = 5$ - $10\ \kappa_1^{-1}$.

In this study, we have (1) verified the presence of strong attractive interactions between isolated pairs of electrically like-charged particles in solution, (2) measured the form of the pair potential, and (3) demonstrated that an attraction is present at pair-interaction level between negatively charged particles in water and between positively charged particles in an alcohol.

Importantly, the suggested dependence of the electrosolvation attraction on interfacial polarization shown in previous work [15, 19], combined with the present evidence for long screening lengths, points to the require-

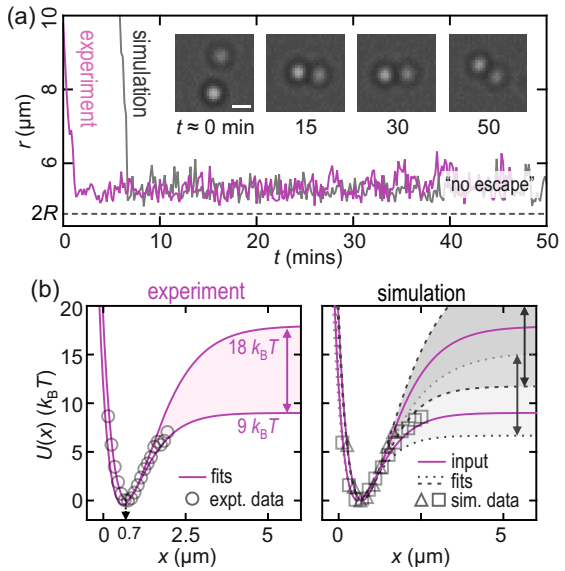


FIG. 4. Strong attraction measured for positively charged aminated silica particles in 1-heptanol. (a) Time-trace of interparticle separation over a period of $t = 50$ min in experiment (pink) and in a BD simulation (grey) with $w = -9k_BT$, beginning with particles in the "free" state and displaying very long-lived bound states (lifetime > 1 h). Inset displays snapshots of bound pairs in heptanol. Scale bar: 5 μm. (b) Left: Measured $U(x)$ data (circles) acquired over a period of 50 min for a representative particle pair. Data on 4 different pairs indicate a range of pair potential functions $U(x)$ (lines) characterized by large differences in fit-equation parameters due to poor sampling of the region outside the minimum. Right: Simulated data (squares and triangles) obtained using the two input potentials shown in the left plot (solid pink lines) are essentially indistinguishable and do not yield unique pair potential fit functions. Grey dotted lines display possible fits to the square symbols and black dashed lines present fits to triangular symbols. Zeta potentials of $\approx +50$ mV were measured for aminated silica particles in 1-heptanol.

ment of a more sophisticated view of the intervening electrolyte than that offerred by a dispersion-free, single-valued dielectric constant [28]. Models of non-local electrostatics, discussed since the 1970s, invoke a wave-vector dependent dielectric function and have raised the possibility of additional length scales in the screening of the electrical potential due to a charged object in solution [29]. It has also been suggested that the relevant length scales in an interaction may well be influenced by the properties of the objects suspended in the medium, including, e.g., surface structural wavelengths [30, 31]. Object-property related, and therefore non-universal, governing length scales would indicate that the electrostatic interaction in the fluid phase may be far more elaborate in character than previously anticipated.

The authors gratefully acknowledge funding from the European Research Council (ERC) under the European Union's Horizon 2020 research and innovation programme (No 724180).

* madhavi.krishnan@chem.ox.ac.uk

[1] B. V. Derjaguin and L. Landau, Theory of the stability of strongly charged lyophobic sols and of the adhesion of strongly charged particles in solutions of electrolytes, Acta Physicochimica (USSR) **14**, 30 (1941).
[2] E. J. W. Verwey and J. T. G. Overbeek, *Theory of the stability of lyophobic colloids* (Elsevier, Amsterdam, 1948).
[3] I. Langmuir, The role of attractive and repulsive forces in the formation of tactoids, thixotropic gels, protein crystals and coacervates, The Journal of Chemical Physics **6**, 873 (1938).
[4] A. Klug, R. E. Franklin, and S. Humphreys-Owen, The crystal structure of tipula iridescent virus as determined by bragg reflection of visible light, Biochimica et biophysica acta **32**, 203 (1959).
[5] A. Kose, M. Ozaki, K. Takano, Kobayash.Y, and S. Hachisu, Direct observation of ordered latex suspension by metallurgical microscope, Journal of Colloid and Interface Science **44**, 330 (1973).
[6] G. M. Kepler and S. Fraden, Attractive potential between confined colloids at low ionic strength, Physical Review Letters **73**, 356 (1994).
[7] K. Ito, H. Yoshida, and N. Ise, Void structure in colloidal dispersions, Science **263**, 66 (1994).
[8] M. D. CarbajalTinoco, F. CastroRoman, and J. L. AraujzLara, Static properties of confined colloidal suspensions, Physical Review E **53**, 3745 (1996).
[9] A. E. Larsen and D. G. Grier, Like-charge attractions in metastable colloidal crystallites, Nature **385**, 230 (1997).
[10] M. M. Baksh, M. Jaros, and J. T. Groves, Detection of molecular interactions at membrane surfaces through colloid phase transitions, Nature **427**, 139 (2004).
[11] J. Baumgartl, J. L. Arauz-Lara, and C. Bechinger, Like-charge attraction in confinement: myth or truth?, Soft Matter **2**, 631 (2006).
[12] M. Polin, D. G. Grier, and Y. Han, Colloidal electrostatic interactions near a conducting surface, Physical Review E **76**, 041406 (2007).
[13] E. M. Winter and J. T. Groves, Surface binding affinity measurements from order transitions of lipid membrane-coated colloidal particles, Analytical Chemistry **78**, 174 (2006).
[14] E. W. Gomez, N. G. Clack, H. J. Wu, and J. T. Groves, Like-charge interactions between colloidal particles are asymmetric with respect to sign, Soft Matter **5**, 1931 (2009).
[15] S. Wang, R. Walker-Gibbons, B. Watkins, M. Flynn, and M. Krishnan, A charge-dependent long-ranged force drives tailored assembly of matter in solution, Nature Nanotechnology **19**, 485 (2024).
[16] H. C. Hamaker, The london—van der waals attraction between spherical particles, Physica **4**, 1058 (1937).
[17] A. Kubincová, P. H. Hunenberger, and M. Krishnan, Interfacial solvation can explain attraction between like-charged objects in aqueous solution, Journal of Chemical Physics **152**, 104713 (2020).
[18] A. Behjatian, R. Walker-Gibbons, A. A. Schekochihin, and M. Krishnan, Nonmonotonic pair potentials in the interaction of like-charged objects in solution, Langmuir **38**, 786 (2022).

[19] S. Wang, R. Walker-Gibbons, B. Watkins, B. Lin, and M. Krishnan, Chemical control of self-assembly by the electrosolvation force, Nature Communications (to appear) https://doi.org/10.48550/arXiv.2410.23920v2 (2025).
[20] P. Attard, Recent advances in the electric double layer in colloid science, Current Opinion in Colloid & Interface Science **6**, 366 (2001).
[21] M. Ospeck and S. Fraden, Solving the poisson-boltzmann equation to obtain interaction energies between confined, like-charged cylinders, Journal of Chemical Physics **109**, 9166 (1998).
[22] J. Dobnikar, M. Brunner, H. H. von Grünberg, and C. Bechinger, Three-body interactions in colloidal systems, Physical Review E **69**, 031402 (2004).
[23] J. C. Neu, Wall-mediated forces between like-charged bodies in an electrolyte, Physical Review Letters **82**, 1072 (1999).
[24] J. E. Sader and D. Y. C. Chan, Long-range electrostatic attractions between identically charged particles in confined geometries and the poisson-boltzmann theory, Langmuir **16**, 324 (2000).
[25] W. P. Wong and K. Halvorsen, The effect of integration time on fluctuation measurements: calibrating an optical trap in the presence of motion blur, Optics Express **14**, 12517 (2006).
[26] N. Mojarad and M. Krishnan, Measuring the size and charge of single nanoscale objects in solution using an electrostatic fluidic trap, Nature Nanotechnology **7**, 448 (2012).
[27] N. Mojarad, V. Sandoghdar, and M. Krishnan, Measuring three-dimensional interaction potentials using optical interference, Optics express **21**, 9377 (2013).
[28] A. Behjatian, R. Blossey, and M. Krishnan, Surface polarization strongly influences electrostatics in a nonlocal medium, The Journal of Chemical Physics **162**, 064901 (2025).
[29] A. A. Kornyshev, A. I. Rubinshtein, and M. A. Vorotyntsev, Model nonlocal electrostatics .1., Journal of Physics C-Solid State Physics **11**, 3307 (1978).
[30] A. A. Kornyshev and S. Leikin, Fluctuation theory of hydration forces - the dramatic effects of inhomogeneous boundary-conditions, Physical Review A **40**, 6431 (1989).
[31] A. Schlaich, J. O. Daldrop, B. Kowalik, M. Kanduc, E. Schneck, and R. R. Netz, Water structuring induces nonuniversal hydration repulsion between polar surfaces: Quantitative comparison between molecular simulations, theory, and experiments, Langmuir **40**, 7896 (2024).

End Matter

Appendix—Experimental methods: In our experiments we used particle number densities $\sim 0.002/\mu\text{m}^2$ that are about 5 times lower than in cluster-formation experiments. This ensures the formation of a number of particle pairs engaged in attractive "bound states", spatially well-isolated from other similar pairs, as shown in Fig. 1b. We observed these bound states using a bright field microscope constructed using a 470 nm collimated light-emitting diode light source (LED, M470L4, ThorLabs), a 10× 0.4 NA objective (UPlanSApo, Olympus) and a charge-coupled device camera (CCD, DCU223M, ThorLabs) as described previously [15] (Fig. 1a). We identified bound particle pairs and tracked the coordinates of both particles over a long period of time using a single particle tracking program. Time series of snapshots of particle pairs were taken at a rate of 10 frames per second (fps) with an exposure time $t_{\text{exp}} \approx 0.1$ ms for 50 mins. Relaxation times were estimated to be $t_{\text{r}} \approx 0.05 - 0.2$ s for the steep repulsive arm of the potential and $\approx 30 - 40$ s for the attractive section for a typical SiO_2 particle ($R = 2.4$ μm) in water. The condition $t_{\text{exp}} \ll t_{\text{r}}$ ensures that the form of the potential well may be faithfully reconstructed without the influence of motion-blur effects [25]. The pair interaction potential, $U(x)$, was then obtained using the Boltzmann relation, $U(x) = -k_{\text{B}}T \ln P(x)$, where $P(x)$ is a separation-dependent probability density function rescaled such that $P(x_{\text{min}}) = 1$. We then shifted the data by a constant and fit the repulsive and attractive parts of the interaction to piecewise screened Coulombic functions such that $U_1(x) \approx A\exp(-\kappa_1 x)/r + w$ for $x \leq x_{\text{min}}$, and $U_2(x) = B\exp(-\kappa_2 x)/r$ otherwise, as shown in Fig. 1d.

We considered the interactions of (1) negatively charged silica (SiO_2) particles of three different radii $R =$ 1.6, 2.0, and 2.4 μm (Bangs Laboratories, Inc.) in water, and (2) positively charged aminated silica particles ($R =$ 2.3 μm, microParticles GmbH) in 1-heptanol. In general, all systems displayed minima of significant depth ($|w| >$ 5 $k_{\text{B}}T$) at an intersurface separation $x_{\text{min}} \approx 0.5 - 1\mu$m, and were characterized by average bound-state lifetimes of $\tau \gtrsim 15$ min. Importantly, the experimental conditions provided by a pure solvent medium (water or alcohols), with little added salt ($10^{-5} < c < 10^{-4}$ M in aqueous media), support accurate measurements of long-range attractive pair potentials for the following reasons. Deep minima in the pair potentials ($|w| \approx 5$ $k_{\text{B}}T$) yield long lifetimes of the bound state and support substantial statistical spatial sampling of the interparticle potential. Large well depths also render the measurement less susceptible to image processing artifacts that can contribute to small measurement inaccuracies of <1 $k_{\text{B}}T$ at small separations [11]. Furthermore, the low concentrations or indeed the total absence of added ions in the solvent media imply large screening lengths of $\kappa^{-1} \approx 100$ nm, which in turn entail significant average interparticle spacings. At an interparticle separation $x \geq 0.3$ μm, a typical range of interest for these experiments, we do not expect interference effects from bright field optical imaging to distort measurements of the spatial dependence of an interaction potential as previously discussed [11, 15].

Supplementary Information

Strongly attractive pair potentials between like-charged particles in fluids

Sida Wang[1], Rowan Walker-Gibbons[1] & Madhavi Krishnan*[1,2]

[1]Physical and Theoretical Chemistry Laboratory, Department of Chemistry, University of Oxford, South Parks Road, Oxford OX1 3QZ, United Kingdom
[2]The Kavli Institute for Nanoscience Discovery, Sherrington Road, Oxford OX1 3QU, United Kingdom.
*correspondence to madhavi.krishnan@chem.ox.ac.uk

Methods

Experimental set-up

The experimental method is similar to that described in our previous studies, and details can be found in ref. (*1, 2*). To examine the colloidal particle interactions, a bright-field microscope was constructed, consisted of a collimated light-emitting diode (LED, M470L4, ThorLabs), a 10× objective (Olympus UPlanSApo) and a charge-coupled device camera (CCD, DCU223M, ThorLabs). The observation cell sits on a levelled pitch and roll platform (AMA027, ThorLabs), carefully calibrated using a spirit level (DWL-80E, Digi-Pas) to reduce particle drift during long observations.

Particle suspensions preparation

Two types of microspheres are examined in this study: negatively charged silica microspheres (SiO_2, $2R$= 4.82±0.39 μm and 3.17±0.32 μm in diameter, Bangs Laboratories), and positively charged amino-functionalized silica microspheres (NH_2-SiO_2, $2R$= 4.63±0.20 μm in diameter, microParticles GmbH).

To prepare colloidal particle suspension in aqueous solutions, SiO_2 particles were suspended in 10 mM NaOH for 10 minutes. Before the final re-suspension in the target electrolyte, particles were re-suspended multiple times in deionized water (DI) for 30 mins and sonicated to remove potential impurities. The solution was further degassed before loading into the cell to eliminate micro-bubbles. To prepare colloidal particle suspensions in 1-heptanol, NH_2-SiO_2 particles were suspended in DI first, then centrifuged and re-suspended multiple times in high purity ethanol to minimize moisture content. Particles were finally re-suspended in 1-heptanol multiple times and degassed before loading into cell.

The ionic strength, c, of the solutions were inferred from an experimentally determined correlation curve, $c = s/a$, where s is the average measured conductivity (EC-33, Horiba) of the particle solution before and after image recordings, and $a \approx 129\ \mu S\ cm^{-1} mM^{-1}$.

A quartz microscopy cell (20/C/Q/1, Starna Scientific) was cleaned carefully before loading the particle suspension. The quartz surface naturally provides a negatively charged surface for negatively charged SiO_2 particles in aqueous solutions. To load positively charged NH_2-SiO_2 particles, the entire cell was coated with a thin layer of poly(ethyleneimine) (PEI) polymer (P3143, Sigma-Aldrich) to provide a positively charged surface. Once the particle suspension was loaded into the cell, the top surface was sealed with a polished quartz cover slide. The final loaded cell should be airtight and free from bubbles.

Image recording and processing

consecutive images of particle interactions were recorded once all particles in solution had settled under gravity to the bottom surface of the cell. Images were recorded at 10 frames per second (fps) for 30,000 frames, or 50 minutes, with an exposure of ≤0.1 ms. Particle coordinates were tracked using TrackNTrace based localization code (*3, 4*) for further analysis.

The localization error of each type of particles is determined by calculating the standard deviation of particle center to center distances, r, by measuring a stationary pair of particles in solution. The localization accuracy for both 1.6 µm and 2.4 µm SiO_2 particles were found to be ~10 nm, and ~50 nm for 2.3 µm NH_2-SiO_2 particles. The larger localization error of NH_2-SiO_2 particle is likely due to the similarity of refractive index between the particle and solvent.

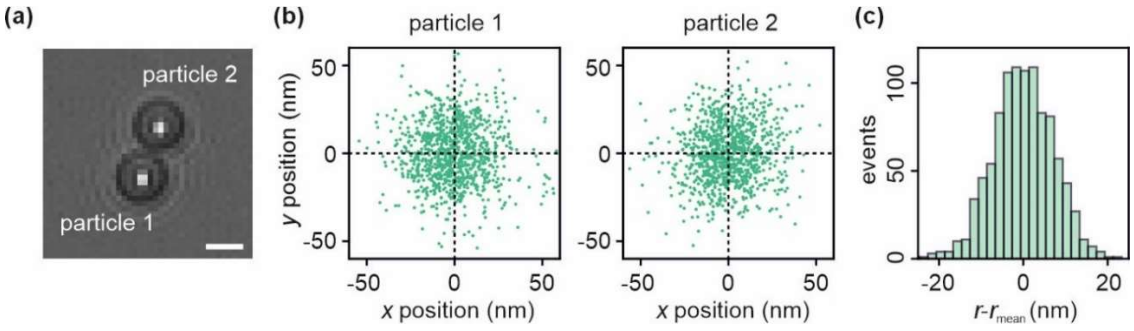


Figure S1. Example of localization error of a pair of stationary SiO_2 particles in water. (a) microscopic image showing a pair of stuck 2.4 µm SiO2 particle. Scale bar 5 µm. (b) localization of particle center for each individual particles. The standard

deviation of particle 1 in x and y position was found to be 17.4 nm and 16.8 nm. The standard deviation of particle 2 in x and y position was 15.5 nm and 16.8 nm. (c) distribution of particle center to center distances of the pair, *r*, with a standard deviation of 7.3 nm.

Brownian dynamics simulations

The Brownian dynamic (BD) simulation was conducted in a similar way that was described in detail in the previous studies (*1, 2*). To recapitulate, the BROWNIAN package from the Large-scale Atomic/Molecular Massively Parallel Simulator (LAMMPS) software (*5*) was used to simulate a pair of interacting identical spheres. The underlying potential is in the following form:

$$U(x) = Ae^{-\kappa_1 x} + Be^{-\kappa_2 x} \quad \text{(S1)}$$

where the first term represents the overall repulsive electrostatic free energy of interaction and the second term represents the electrosolvation free energy (*1*). Values of A, B, κ_1 and κ_2 can be obtained from the averaged fits of the experimentally measured pair potentials in double exponential forms (Eq. S1).

In the BD simulation setup, two identical particles with diameters equal to the experimental average were placed apart in a large simulation box ($\geq 50 \times 50\ \mu m^2$) such that the box size is much larger than the particle diameter. The material density of the particles and the viscosity of the solvents were set to match the experiments. Periodic boundaries were applied in the x and y dimensions. The z coordinate of the particles were fixed, mimicking the 2-dimensional interaction in experiments. Particles coordinates were saved at a rate equal to the frame rate of the experiments (10 FPS).

The diffusion coefficient of a typical SiO_2 particle ($2R \approx 3-5$ μm) in water exhibiting Brownian motion is around $1 \times 10^{-13}\ m^2 s^{-1}$. Examining the measured pair potential, we are able to deduce the corresponding viscous relaxation time $\tau_r = \frac{\gamma}{k}$, where $\gamma = 6\pi\eta R$ is the drag coefficient and k is the stiffness constant where $U(\Delta x) \approx k\Delta x^2$. $\Delta x = x - x_{min}$ is the displacement from position x to the potential minimum. The viscous relaxation time for the repulsive part of the potential is found to be around 0.05 to 0.5 s, and 20 to 50 s for the attractive part. The momentum relaxation time, $\tau_p = \frac{m}{\gamma}$

is about 1-3 μs, indicating $\tau_p \ll \tau_r$. Note the simulation timestep ($\approx 2.5 \times 10^{-5}\, s$) is chosen to be much smaller than τ_r.

The parameters A, B, κ_1 and κ_2 in the input potential (Eq. S1) were chosen based on the averaged fits of experimentally measured pair potentials. To determine the recovery accuracy of the input potentials, pairs potentials of simulated pairs were measured in a similar fashion as the experiments. It is expected that an error of ~10% for the recovery of κ_1 , κ_2 and U.

Additional results

Alternative fitting of pair potentials in double exponential form

We also performed fitting to the measured pair potential data in the double exponential form, shown in Eq. S1, for comparison with values fitted to the single exponential form. In the example below, parameters A, B, κ_1 and κ_2 were fitted in the double exponential form for the same set of experimental data as displayed in Fig. 2a, for silica particle pairs in various measured salt concentrations.

The results indicated that parameters κ_1^{-1}, κ_2^{-1}, U and $x_{\min}$, fitted to the double exponential, follow the same trend across salt concentration c as observed for fitting to the single exponential forms, i.e. all parameter values decrease as salt concentration increases. However, we do note slight variation between the two methods in the average fitted κ_1^{-1} and κ_2^{-1} values, where κ_1^{-1} tends to be slightly larger, and κ_2^{-1} tends to be slightly smaller than values obtained from single exponential fitting. Nonetheless, κ_2^{-1} values which are approximately an order of magnitude larger than the nominal Debye length were measured in all cases, confirming the findings obtained by fitting to the single exponential form.

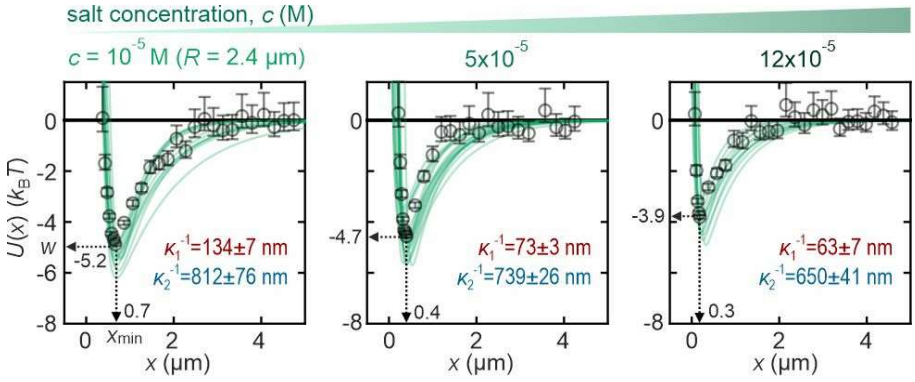


Figure S2. Salt concentration dependence of the pair interaction potential fitted in double exponential form. Measured pair potentials $U(x)$ for ca. 15 pairs of $R = 2.4\,\mu m$ silica particles fitted to double exponential form (Eq. S1) in aqueous solution for salt concentration c ranging from 10^{-5} M to 1.2×10^{-4} M, showing representative measurements on individual pairs (symbols). Averaged values of fitted κ_1^{-1}, κ_2^{-1}, well depth U and $x_{\min}$ are noted.

Table S1. BD simulation in determining fitting accuracy of pair potentials. Input parameters are compared with the averaged fitted parameters κ_1^{-1}, κ_2^{-1}, and U from equations Eq. S1.

Particle	c_0 (mM)	Input κ_1^{-1} (nm)	Fitted κ_1^{-1} (nm)	err.	Input κ_2^{-1} (nm)	Fitted κ_2^{-1} (nm)	err.	Input U (kT)	Fitted U (kT)	err.
2.4 μm SiO2	0.013	91.7	83.1±2.3	10%	1019.8	1140.3±53.3	11%	5.2	5.0±0.2	4%
	0.049	59.3	57.7±2.7	3%	888.6	962.6±41.7	8%	4.7	4.7±0.1	1%
	0.124	54.2	53.4±3.1	1%	765.4	777.8±38.8	2%	3.9	3.8±0.1	2%
1.6 μm SiO2	0.013	92.7	90.3±12.9	3%	721.4	786.2±112.1	8%	1.7	1.8±0.1	6%

References

1. S. Wang, R. Walker-Gibbons, B. Watkins, M. Flynn, M. Krishnan, A charge-dependent long-ranged force drives tailored assembly of matter in solution. *Nature Nanotechnology* **19**, 485–493 (2024).
2. R. W.-G. Sida Wang, Bethany Watkins, Binghui Lin, Madhavi Krishnan, Chemical control of self-assembly by the electrosolvation force. *arXiv*, (2024).
3. S. C. Stein, J. Thiart, TrackNTrace: A simple and extendable open-source framework for developing single-molecule localization and tracking algorithms. *Scientific Reports* **6**, 37947 (2016).
4. R. Parthasarathy, Rapid, accurate particle tracking by calculation of radial symmetry centers. *Nat Methods* **9**, 724-726 (2012).
5. A. P. Thompson *et al.*, LAMMPS - a flexible simulation tool for particle-based materials modeling at the atomic, meso, and continuum scales. *Computer Physics Communications* **271**, 108171 (2022).

Statement of Authorship for joint/multi-authored papers for PGR thesis
To appear at the end of each thesis chapter submitted as an article/paper

The statement shall describe the candidate's and co-authors' independent research contributions in the thesis publications. For each publication there should exist a complete statement that is to be filled out and signed by the candidate and supervisor **(only required where there isn't already a statement of contribution within the paper itself).**

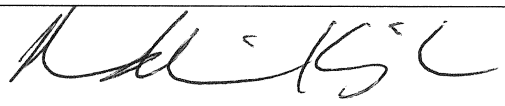
Title of Paper	Strongly attractive pair potentials between like-charged particles in fluids
Publication Status	□Published □ Accepted for Publication □Submitted for Publication ☒Unpublished and unsubmitted work written in a manuscript style
Publication Details	Wang, S., Walker-Gibbons & Krishnan, M. Strongly attractive pair potentials between like-charged particles in fluids.

Student Confirmation

Student Name:	Sida Wang		
Contribution to the Paper	S.W. performed all experiments, conducted simulations, analyzed data and participated in manuscript preparation.		
Signature	Sida Wang	Date	20/09/2024

Supervisor Confirmation

By signing the Statement of Authorship, you are certifying that the candidate made a substantial contribution to the publication, and that the description described above is accurate.

Supervisor name and title: Professor Madhavi Krishnan			
Supervisor comments			
Signature		Date	20/09/2024

This completed form should be included in the thesis, at the end of the relevant chapter.

5

Conclusion

This thesis presented a novel perspective on interparticle interactions through the study of the long-debated like-charge attraction problem. A series of experimental and simulational studies were conducted on two-dimensional suspensions of colloidal particles in solutions. The interparticle interactions were examined under a range of conditions, including various particle surface chemistries, types of solvents and the addition of salts, osmolytes and surfactants to solvent medium. The study revealed compelling evidence for the existence of an asymmetrical long-ranged attractive component, or the electrosolvation force, between particles of the same sign of charge. The findings are organized in three main chapters in this thesis, summarized below.

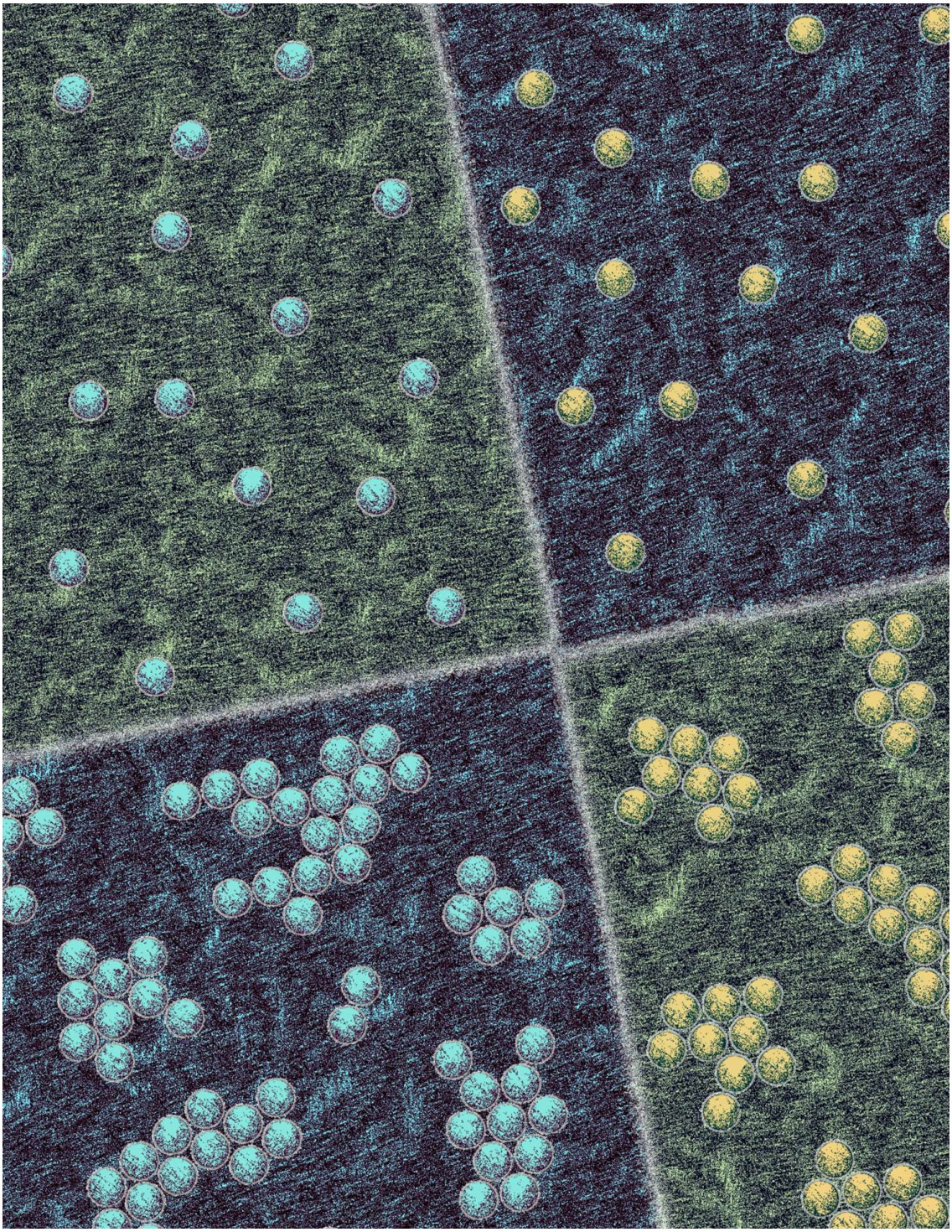


Figure 6. An artwork summarizing the asymmetry property of the like-charge attraction. Attraction is dependent on both the sign of charge of the particle and solvent molecular structure at interface. For example, particles carrying negative charge (e.g., SiO^-, light blue spheres) attract and form ordered clusters in water (dark blue background) whereas positively charged particles (e.g., NH_3^+, yellow spheres) repel. On the contrary, positively charged particles attract in alcohols (green background) but negatively charged particles repel.

In chapter two, a series of experiments were conducted to examine the previously proposed 'interfacial solvation' model, a working model that describes the solvation-driven interparticle interactions [58,59]. The model examines the change in the system's free energy resulting from the response of interfacial solvent molecules when two like-charged particles approach each other. Charge regulation is essential to the model, where the surface charge of the particle is influenced by the interparticle separation due to pH-dependent ionizable surface groups [60]. By accounting for both the orientational response of interfacial solvent molecules and charge regulation, we identify an excess amount of free energy between like-charged particles.

To explore these interactions, we observed two-dimensional structures of colloidal particle suspensions carrying a wide range of surface chemistries, including silanol, carboxyl, amino, polypeptides and polyelectrolytes. Utilizing optical microscope and single-particle tracking, we constructed radial distribution function and inferred the underlying pair interaction potential through simulations. For negatively charged particles in low ionic strength solutions, we observed the formation of slowly self-organizing, hexagonally packed clusters characterized by large interparticle spacings—five to ten times larger than the nominal Debye length. These lattice-like clusters indicated the presence of a strong, long-ranged attractive component between like-charged particles. In contrast, positively charged particles remained randomly dispersed, signifying a net repulsive interaction. We further investigated the effect of pH on particles carrying different functional groups. The trends observed in interparticle interaction in response to change in pH exhibit distinct signatures that align with the interfacial solvation mechanism. Additionally, by examining the interparticle interaction between chemically dissimilar surfaces such as silica and carboxylated particles, we emphasize the importance of the charge-state of the particle, which is a reflection of the ionization degree of the surface functional groups. Remarkably, we observed stable and long-ranged cluster formation between positively charged aminated particles suspended in ethanol and isopropanol, while negatively charged carboxylated particles remained dispersed, consistent with the predictions of the interfacial solvation model. Finally, we

demonstrated the application of our model in describing smaller-scale processes, such as protein phase separation [26]. We introduced the term 'electrosolvation' to describe the attractive component observed between like-charged particles.

In chapter three, we further investigated the properties of the electrosolvation force by examining particle interactions across a broader range of solvents and co-solvents. To better incorporate the orientational effect of interfacial solvent molecules into the electrosolvation framework, we quantify the net interfacial dipole moment density term, μ_{av}, that interrelates with the established excess interfacial electrical potential, φ_{int} [58,59].

Similar to water, negatively charged particles formed stable and reorganizing clusters in D_2O, which exhibits interfacial behaviour similar to H_2O, as suggested by simulation. In solvents such as DMSO and primary alcohols, we observed the formation of strong, stable clusters between positively charged aminated particles. Extending beyond pure solvents, we conducted experiments in the water-isopropanol mixture — two representative solvents exhibiting opposite signs in their interfacial dipole moment at charged surfaces. As the proportion of water increased from the pure isopropanol state, positively charged particle clusters were observed to gradually vanish whereas negatively charged particle clusters began to emerge, continuing until all isopropanol molecules were replaced by water. These experimental observations align well with the electrosolvation picture where the dominant interfacial dipole moment plays a governing role.

Inspired by our findings in binary mixture experiments, we examined the effect of small neutral molecules, including zwitterionic osmolytes and surfactants, on cluster formation between negatively charged silica particles in aqueous solutions. Specifically, we demonstrated that the addition of small amounts ($\approx 10^{-4}$ M) of amino acids such as tyrosine and glycine suppressed cluster formation. In contrast, clusters persisted at concentrations several orders of magnitude higher when adding TMAO or TMG, a methylated glycine derivative. Inspecting the averaged dipole moment density of water molecules at the interface, $\mu_{\mathrm{av,w}}(0)$, we noticed a significant reinforcement of dipole orientation from the original pure water state with the presence of TMG and TMAO

compared to amino acids. Additionally, we observed the suppression of clusters with the addition of a small amount of polysorbate-20, a classic non-ionic surfactant, highlighting the importance of interfacial adsorption. Overall, this study points to the critical role of interfacial molecular dipole moment in electrosolvation and provides insights into controlling biochemical related interactions.

Chapter four focused on the interactions between isolated pairs of colloidal particles through direct measurement using optical microscopy. Pair interaction potentials were obtained through Boltzmann inversion of the measured probability density function of separation and validated in BD simulations. Our results confirmed the presence of a long-ranged, strongly attractive component between negatively charged particle pairs in water as well as between positively charged pairs in alcohol. These findings established that the long-range attraction is present at the pair-potential level and does not arise from many-body effects (due to the presence of neighbouring particles).

Interestingly, the experimentally measured screening length, particularly for the attractive component, is significantly longer — approximately one order of magnitude larger than the nominal Debye length. Traditionally one would consider such screening length measured in dilute 1:1 electrolyte solution to be well captured by Debye length from the Debye–Hückel theory which now clearly fails. Furthermore, measurements conducted for different diameters of particles in the same experimental condition indicated a screening length of the repulsive part of the interaction commensurate with the Debye length. However, the screening length governing the attraction suggests a longer length scale at play connected to the size of the particle. Additionally, we verified the measured well depth of the pair potentials by extracting pair lifetime and corroborated through simulations.

We note that although our proposed electrosolvation model qualitatively captures the long-ranged attraction and its distinct features, certain details such as the discrepancy between attractive and repulsive screening length require additional explanations, such as non-local electrostatics. Future studies could benefit from

examining pair potentials in three-dimensional solutions further away from surfaces, which may more accurately replicate interactions found in biologically relevant systems.

Finally, this thesis presented direct and compelling evidence for like-charge attraction, challenging conventional electrostatic models. The observed unanticipated long-ranged screening lengths point to the complex nature of solvent that deviated significantly from traditional continuum electrostatics. We offer an alternative approach in understanding and controlling interparticle interactions in solution. Our proposed electrosolvation model effectively captures the distinctive properties of this strong and long-ranged attractive component between like-charged particles. The electrosolvation perspective of molecular interactions at interfaces provides valuable insight in understanding complex mechanisms underlying relevant biological processes such as phase separation, crystallization, biomolecular folding and condensation.

Further experiments could delve deeper into the role of interfacial molecular orientation in interparticle interaction with alternative techniques. By applying particle coatings such as lipid bilayers which carry zwitterionic headgroups, we can carefully probe the relative contributions of charge and indeed, headgroup dipole moment density to the interaction. Additionally, while we have demonstrated the effect of salts in controlling the long-ranged attraction, it would be valuable to study how various ionic species influence interaction, along the lines of the well-known Hofmeister series.

Furthermore, we have already demonstrated through careful experimentation that the underlying coverglass surface does not play a role in the interaction. Indeed, cluster formation and pair attraction have been shown to be unaffected by the surface chemistry of the underlying coverglass regardless of whether it is polymer-coated, gold-coated or surface patterned with evaporated metal. Nonetheless, moving forward, it would be beneficial to examine cluster formation and pair interaction in three-dimensional solution to explore the strength of the interaction in the bulk phase and to firmly establish its broad and general relevance. This can be achieved by density matching of solvent and selecting lighter particles.

Additionally, particle-geometry or surface pattern-generated effects in the interaction could bring further insight into the interaction and motivate its relevance in self-assembly applications. For example, the spatial arrangement of clusters can be explored using rod-shaped or other non-spherical particles. Janus microspheres with contrasting surface chemistries between two hemispheres could offer an asymmetry in charge and surface chemical properties that may be uniquely harnessed to drive the formation of various types of crystal lattices, opening up a new dimension in the field of self-assembly. The ultimate frontier is, of course, to demonstrate that this newly discovered interaction is relevant in the broadest sense in biological packaging, compartmentalization and self-assembly. Valuable insights have already been gained by studying pH-controlled interactions of particles coated with biologically relevant materials, such as polypeptides. Performing cluster formation studies using proteins as interacting objects rather than colloidal microspheres will directly address this important question in future.

References

[1] M. Gouy, J. Phys. Theor. Appl. **9**, 457 (1910).

[2] D. L. Chapman, The London, Edinburgh, and Dublin philosophical magazine and journal of science **25**, 475 (1913).

[3] H. C. Hamaker, Physica **4**, 1058 (1937).

[4] B. V. Derjaguin and L. Landau, Acta Physicochimica (USSR) **14**, 30 (1941).

[5] E. J. W. Verwey and J. T. G. Overbeek, *Theory of the stability of lyophobic colloids* (Elsevier, Amsterdam, 1948).

[6] I. JN, Intermolecular and surface forces, 3rd edn. Academic Press, San Diego, 291 (2011).

[7] E. Trizac and J. L. Raimbault, Physical Review E **60**, 6530 (1999).

[8] J. E. Sader and D. Y. C. Chan, Journal of Colloid and Interface Science **213**, 268 (1999).

[9] J. C. Neu, Physical Review Letters **82**, 1072 (1999).

[10] J. E. Sader and D. Y. C. Chan, Langmuir **16**, 324 (2000).

[11] H. Zocher, Z. Anorg. Allg. Chem. **147**, 91 (1925).

[12] W. M. Stanley, Science **81**, 644 (1935).

[13] N. W. P. F. C. BAWDEN, J. D. BERNAL & I. FANKUCHEN Nature **138**, 1051 (1936).

[14] J. D. B. I. FANKUCHEN, Nature **139**, pages923 (1937).

[15] P. Bergmann, P. Low-Beer, and H. Zocher, Phys. Chem **181**, 301 (1938).

[16] I. Langmuir, Journal of Chemical Physics **6**, 873 (1938).

[17] A. Klug, R. E. Franklin, and S. P. F. Humphreysowen, Biochimica Et Biophysica Acta **32**, 203 (1959).

[18] J. P. Cotton and M. Moan, J Phys Lett-Paris **37**, L75 (1976).

[19] M. Nierlich *et al.*, J Phys-Paris **40**, 701 (1979).

[20] N. Ise, T. Okubo, Y. Hiragi, H. Kawai, T. Hashimoto, M. Fujimura, A. Nakajima, and H. Hayashi, Journal of the American Chemical Society **101**, 5836 (1979).

[21] H. Matsuoka, D. Schwahn, and N. Ise, Macromolecules **24**, 4227 (1991).

[22] C. Haro-Pérez, L. F. Rojas-Ochoa, R. Castañeda-Priego, M. Quesada-Pérez, J. Callejas-Fernández, R. Hidalgo-Alvarez, and V. Trappe, Physical Review Letters **102** (2009).

[23] A. Patkowski, E. Gulari, and B. Chu, The Journal of Chemical Physics **73**, 4178 (1980).

[24] M. Krishnan, I. Mönch, and P. Schwille, Nano Letters **7**, 1270 (2007).

[25] M. U. Musheev, M. Kanoatov, C. Retif, and S. N. Krylov, Analytical Chemistry **85**, 10004 (2013).
[26] T. M. Franzmann *et al.*, Science **359** (2018).
[27] G. Goldfinger, *Clean surfaces: their preparation and characterization for interfacial studies.* (Marcel Dekker Inc., 1970).
[28] A. Kose, M. Ozaki, K. Takano, Kobayash.Y, and S. Hachisu, Journal of Colloid and Interface Science **44**, 330 (1973).
[29] N. Ise, T. Okubo, M. Sugimura, K. Ito, and H. J. Nolte, The Journal of Chemical Physics **78**, 536 (1983).
[30] K. Furusawa and N. Tomotsu, Journal of Colloid and Interface Science **93**, 504 (1983).
[31] R. Kesavamoorthy, M. Rajalakshmi, and C. B. Rao, Journal of Physics-Condensed Matter **1**, 7149 (1989).
[32] K. Ito, H. Yoshida, and N. Ise, Science **263**, 66 (1994).
[33] G. M. Kepler and S. Fraden, Physical Review Letters **73**, 356 (1994).
[34] J. C. Crocker and D. G. Grier, Physical Review Letters **77**, 1897 (1996).
[35] A. E. Larsen and D. G. Grier, Nature **385**, 230 (1997).
[36] D. G. Grier, Nature **393**, 621 (1998).
[37] Y. L. Han and D. G. Grier, Physical Review Letters **91** (2003).
[38] J. Baumgartl and C. Bechinger, Europhysics Letters **71**, 487 (2005).
[39] J. Baumgartl, J. L. Arauz-Lara, and C. Bechinger, Soft Matter **2**, 631 (2006).
[40] M. Polin, D. G. Grier, and Y. Han, Physical Review E **76** (2007).
[41] I. Sogami, Phys Lett A **96**, 199 (1983).
[42] B. J. Jancovici, Journal of Statistical Physics **29**, 263 (1982).
[43] P. Attard, R. Kjellander, D. J. Mitchell, and B. Jönsson, The Journal of chemical physics **89**, 1664 (1988).
[44] L. Guldbrand, B. Jonsson, H. Wennerstrom, and P. Linse, Journal of Chemical Physics **80**, 2221 (1984).
[45] P. Attard, D. J. Mitchell, and B. W. Ninham, The Journal of chemical physics **88**, 4987 (1988).
[46] P. Attard, D. J. Mitchell, and B. W. Ninham, The Journal of chemical physics **89**, 4358 (1988).
[47] M. Kardar and R. Golestanian, Reviews of Modern Physics **71**, 1233 (1999).
[48] S. Tandon, R. Kesavamoorthy, and S. A. Asher, Journal of Chemical Physics **109**, 6490 (1998).
[49] T. M. Squires and M. P. Brenner, Physical Review Letters **85**, 4976 (2000).
[50] Y. O. Popov, Journal of Colloid and Interface Science **252**, 320 (2002).
[51] A. Gopinathan, T. Zhou, S. N. Coppersmith, L. P. Kadanoff, and D. G. Grier, Europhysics Letters **57**, 451 (2002).
[52] M. Brunner, C. Bechinger, W. Strepp, V. Lobaskin, and H. H. von Grünberg, Europhysics Letters **58**, 926 (2002).
[53] M. D. Carbajal-Tinoco and P. González-Mozuelos, Journal of Chemical Physics **117**, 2344 (2002).
[54] A. P. dos Santos and Y. Levin, Physical Review Letters **122** (2019).

[55] M. M. Baksh, M. Jaros, and J. T. Groves, Nature **427**, 139 (2004).
[56] E. M. Winter and J. T. Groves, Analytical Chemistry **78**, 174 (2006).
[57] E. W. Gomez, N. G. Clack, H. J. Wu, and J. T. Groves, Soft Matter **5**, 1931 (2009).
[58] A. Kubincová, P. H. Hunenberger, and M. Krishnan, Journal of Chemical Physics **152** (2020).
[59] A. Behjatian, R. Walker-Gibbons, A. A. Schekochihin, and M. Krishnan, Langmuir **38**, 786 (2022).
[60] B. W. Ninham and V. A. Parsegian, Journal of theoretical biology **31**, 405 (1971).
[61] R. Parthasarathy, Nature Methods **9**, 724 (2012).
[62] S. C. Stein and J. Thiart, Sci Rep **6**, 37947 (2016).
[63] A. P. Thompson *et al.*, Computer Physics Communications **271** (2022).
[64] P. H. Yancey, M. E. Clark, S. C. Hand, R. D. Bowlus, and G. N. Somero, Science **217**, 1214 (1982).
[65] P. H. Yancey, Am Zool **41**, 699 (2001).
[66] D. W. Bolen and I. V. Baskakov, Journal of Molecular Biology **310**, 955 (2001).
[67] J. E. Hallett, K. J. Agg, and S. Perkin, Proceedings of the National Academy of Sciences of the United States of America **120** (2023).
[68] J. Rösgen, B. M. Pettitt, and D. W. Bolen, Biophysical Journal **89**, 2988 (2005).
[69] T. O. Street, D. W. Bolen, and G. D. Rose, Proceedings of the National Academy of Sciences of the United States of America **103**, 13997 (2006).
[70] A. Panuszko, B. Adamczak, J. Czub, E. Gojlo, and J. Stangret, Amino Acids **47**, 2265 (2015).
[71] B. Adamczak, M. Wieczór, M. Kogut, J. Stangret, and J. Czub, Biochemical Journal **473**, 3705 (2016).
[72] D. Bandyopadhyay, S. Mohan, S. K. Ghosh, and N. Choudhury, The Journal of Physical Chemistry B **117**, 8831 (2013).
[73] D. Bandyopadhyay, K. Bhanja, S. Mohan, S. K. Ghosh, and N. Choudhury, The Journal of Physical Chemistry B **119**, 11262 (2015).
[74] M. Ospeck and S. Fraden, Journal of Chemical Physics **109**, 9166 (1998).
[75] D. G. Grier, Journal of Physics-Condensed Matter **12**, A85 (2000).
[76] J. Dobnikar, M. Brunner, H. H. von Grünberg, and C. Bechinger, Physical Review E **69** (2004).
[77] B. V. R. Tata, P. S. Mohanty, and M. C. Valsakumar, Solid State Communications **147**, 360 (2008).
[78] J. C. Crocker and D. G. Grier, Physical Review Letters **73**, 352 (1994).